UNIVERSITY OF GRANADA

DEPARTMENT OF INORGANIC CHEMISTRY

DOCTORAL PROGRAMME IN CHEMISTRY

DOCTORAL THESIS

STABLE LANTHANIDE SINGLE ION MAGNETS WITH LUMINESCENT PROPERTIES

Doctoral Thesis supervised by: María Ángeles Palacios López
María del Mar Quesada Moreno

Hadjer Allia

Granada, 2025

Editor: Universidad de Granada. Tesis Doctorales
Autor: Hadjer Allia
ISBN: 978-84-1195-969-8
URI: https://hdl.handle.net/10481/110585

STABLE LANTHANIDE SINGLE ION MAGNETS WITH LUMINESCENT PROPERTIES

Doctoral Thesis submitted by **Hadjer Allia** to get a PhD in Chemistry from the University of Granada, within the Doctoral Programme in Chemistry.

Granada, May 2025

Sig.: Allia Hadjer

THESIS SUPERVISORS

Sig.: María Ángeles Palacios López

Sig.: María del Mar Quesada Moreno

Acknowledgements

In the name of Allah, the most Beneficent, the most Merciful.

I Thank God for making the completion of my PhD programme and of this project conceivable.

My journey through the doctoral programme has now come to an end. It has been a path characterised by dedication, learning, and unforgettable experiences in a beautiful country. I am deeply grateful for all the moments that have shaped this chapter of my life. Living and studing in Granada has been one of the most enriching aspects of this journey. The warmth of the city, reflected in its people, culture, and everyday life, made it a truly welcoming place. Its rich history, stunning architecture, and vibrant traditions not only provided inspiration but also a deep sense of connection. Granada has become a place that I will always carry in my heart.

Completing this dissertation has been a journey marked by professional challenges and personal adversities. I am profoundly grateful for the unwavering support of my tutor, Enrique, and my supervisors, María Ángeles and María del Mar. Their steadfast belief in my abilities and academic potential inspired me to persevere, even in my most difficult moments. Their guidance served as a beacon of light in times of doubt, and without their expertise and direction, I truly believe this work would not have come to fruition. I offer my deepest gratitude and appreciation for all of your support, kindness, and invaluable assistance.

I would like to express my sincere gratitude to all my colleagues in the department for their support and encouragement throughout my doctoral journey. To Juanma, thank you for always checking in on me and asking about the progress of my results, your genuine interest and encouragement meant a great deal to me. To Aritz, thank you for accompanying me throughout my doctoral studies, your presence and insights were a constant source of motivation. To Juanra, I am deeply thankful for your unwavering support and generous help. I am truly honoured to have collaborated with you on my first research article. To Yating, I am especially grateful for the memorable days we spent in the laboratory. We not only worked hard but also shared many moments of laughter, which made the experience even more enjoyable. To Pedro, I am truly grateful for your help in the laboratory. Your presence and support were invaluable, especially during the challenging moments. Heartfelt thanks to all my colleagues in the department; your kindness, collaboration, and support have made this journey richer and more rewarding.

In bringing this effort to life, I must pay love and respect to the precious gifts given to me, my parents who were the candles that lit my way throughout my life. Without their endless love, sacrifices, prayers and financial support, during unexpected personal challenges, this work would not have been possible. There are no words to express my deepest gratitude and love for you. To my brothers and my little sister Meryem. I can see the smiles on your faces. You also deserve my wholehearted gratitude.

The presence of many friends "Loubna, Linda, Khairieh, Asma" has helped me through these difficult years. Their support and care have been invaluable. I extend my heartfelt gratitude to all my friends and colleagues.

I would like to express my heartfelt gratitude to everyone I may have unintentionally forgotten to thank, especially those who are no longer with us. I will never forget the impact you have had on my life.

Finally, I would like to express my gratitude to all the people who listened, supported, helped and shared the events with me during these years.

To all whom I may have missed thanking.

Thank you

ÍNDICE

ABBREVIATIONS AND ACRONYMS

Abbreviations and acronyms	
MM	Molecular magnets
SCM	Single chain magnets
SMMs	Single molecule magnets
SIMs	Single ion magnets
SOC	Spin-orbit coupling
FC	Field-cooling
ZFC	Zero-field-cooling
ZFS	Zero field splitting
QTM	Quantum tunneling of magnetisation
TA-QTM	Thermally assisted quantum tunneling of magnetisation
T_B	Blocking temperature
U	Energy barrier
U_{eff}	Effective energy barrier
M_{sat}	Saturation magnetization
H	Applied magnetic field (T or Oe)
S	Spin angular momentum
J	Total angular momentum
L	Orbital angular momentum
ET	Energy transfer
D	Axial anisotropy parameter
K_B	Boltzmann constant
τ^{-1}	Relaxation rate
τ	Relaxation time
dc	Direct current
ac	alternating current
χ_M	Molar magnetic susceptibility
χ''_M	Out-of-phase ac magnetic susceptibility
KD	Kramer's doublet
PBPY-7	Pentagonal bipyramid polyhedron
OC-6	Ideal octahedron
ES	Excited state
GS	Ground state
S_n	Singlet excited state

T	Triplet state
g_{lum}	Dissymmetry factor for luminescence
f	Oscillator strength
MChD	Magneto-chiral dichroism
CPL	Circularly polarized luminescence
Naph	Naphthyl
H_2bbpen	*N*,*N*'-bis(2hydroxybenzyl)-*N*,*N*-bis(2-methylpyridyl)ethylenediamine)
O^{t}Bu	*Tert*-butoxide
Py	Pyridine
Cy_3PO	Tricyclohexyl phosphine oxide
HMPA	Hexamethylphosphoramide
OPAd_2Bz	Di(1-adamantyl)benzylphosphine oxide
CyPh_2PO	Cyclohexyl(diphenyl)phosphine oxide
Hfac$^-$	1,1,1,5,5,5-hexafluoroacetylacetonate
Tta$^-$	2-tenoyl-trifluoroacetylacetonate
BArF$^-$	Tetrakis[3,5-bis(trifluoromethyl)phenyl]borate
Pc	Phthalocyanine
THF	Tetrahydrofuran
HOMO	Highest occupied molecular orbital
LUMO	Lowest unoccupied molecular orbital
NIR	Near-infrared
UV	Ultraviolet
IR	Infrared
RMN	Nuclear magnetic resonance
CASSCF	Complete active space self-consistent field
DFT	Density functional theory
TD-DFT	Time-dependent density functional theory
MMFF	Molecular mechanics force field

RESUMEN

RESUMEN

En las últimas décadas ha surgido una nueva disciplina: el Magnetismo Molecular. Esta disciplina ha realizado numerosas aportaciones a la comunidad científica, entre ellas el descubrimiento de los imanes unimoleculares (SMMs, del inglés *Single Molecule Magnets*). Esta línea de investigación ha experimentado un notable y rápido desarrollo en las últimas tres décadas. La presente tesis doctoral se enmarca en este contexto, centrándose en el área del Magnetismo Molecular y la Fotoquímica. Los objetivos principales de esta tesis doctoral son el diseño, preparación y caracterización de compuestos de coordinación multifuncionales mononucleares y trinucleares basados en iones lantánidos, con ligandos tipo óxido de fosfina y ligandos quirales tipo base de Mannich, respectivamente, así como el estudio experimental y teórico de sus propiedades magnéticas y luminiscentes. Toda esta investigación fundamental tiene como objetivo aportar nuevos conocimientos para diseñar SMM multifuncionales con propiedades mejoradas. En la actualidad, podemos afirmar que ésta es una de las áreas más activas dentro de la química y la ciencia de materiales debido a las potenciales aplicaciones de los SMMs en campos tan diversos como la espintrónica molecular, el almacenamiento de información de alta densidad y la computación molecular.

En la introducción (**Capítulo 1)** se abordan aspectos de gran interés relacionados con el Magnetismo Molecular y, más concretamente, con los SMMs, tales como: (a) su relación con la Química de la Coordinación; (b) la evolución que han experimentado los SMMs; (c) el estado actual de esta disciplina, en la que destacan tanto los SMMs basados en iones lantánidos como los basados en iones de metales de transición; (d) la necesidad de sintetizar compuestos no sólo con altas barreras de energía efectiva sino que también sean estables; (e) la importancia de la simetría axial para eliminar el túnel cuántico de la magnetización (QTM, del inglés *Quantum Tunnelling of Magnetisation*). Este mecanismo de relajación es muy

rápido y, en la mayoría de los casos, reduce el valor de la temperatura de bloqueo (T_B), es decir, la temperatura por debajo de la cual el compuesto presenta comportamiento SMM; (f) El efecto de las vibraciones moleculares en la relajación de la magnetización, que limita la temperatura de bloqueo, etc; g) Se hará especial hincapié en los SMMs basados, por una parte, en complejos mononucleares de iones lantánidos con geometría bipirámide pentagonal y, en particular, con ligandos tipo óxido de fosfina y, por otra, en complejos hetero-trinucleares Zn^{II}-Ln^{III}-Zn^{II} a partir de ligandos quirales tipo base de Mannich. Estos compuestos suelen presentar relajación lenta de la magnetización a campo cero y son, generalmente, estables al aire, la humedad y la luz; h) La última sección trata de los materiales multifuncionales y, más concretamente, de los SMMs luminiscentes y/o quirales basados en iones lantánidos.

En el capítulo **(2)** se indican los objetivos generales y específicos de esta tesis doctoral.

El capítulo **(3)**, el primero dedicado a los resultados obtenidos en esta tesis doctoral, describe el diseño, síntesis, caracterización espectroscópica y estructural por difracción de rayos X de monocristal, análisis de las medidas magnéticas y cálculos teóricos *ab initio* (para apoyar los resultados experimentales) de 7 complejos mononucleares de iones Ln^{III}. Estos compuestos presentan geometría bipirámide pentagonal (D_{5h}) u octaédrica (O_h) dependiendo del procedimiento de síntesis empleado, síntesis solvotermal o reflujo en atmósfera inerte, respectivamente. Estos complejos contienen Dy^{III} (**1** y **5**), Yb^{III} (**2**), Tb^{III} (**3**), Gd^{III} (**4** y **7**) y Eu^{III} (**6**). En el plano ecuatorial, los compuestos con geometría bipirámide pentagonal contienen un átomo de cloro y cuatro moléculas de agua, y los octaédricos, una molécula de disolvente y tres cloruros, mientras que el ligando óxido de di(1-adamantil)bencilfosfina se encuentra ocupando las posiciones axiales

en todos ellos. Los primeros compuestos son catiónicos, cuyas cargas se equilibran por aniones cloruro, mientras que los segundos son neutros.

Estos ligandos se han escogido por el impedimento estérico que generan, por lo que sólo dos de estos ligandos se coordinan en las posiciones *trans*, favoreciendo una fuerte anisotropía axial en el estado fundamental y, en consecuencia, el comportamiento SMM. Además, los grupos sigma dadores fuertes y voluminosos (adamantilos) aumentan la densidad electrónica en el átomo de oxígeno del óxido de fosfina, lo que favorece la unión a los iones Ln^{III}. El grupo fenilo presente en el ligando pretende sensibilizar a los iones lantánidos para observar la luminiscencia de los mismos.

Se realizaron medidas de susceptibilidad magnética en campo alterno (*ac*) de los complejos **1**, **2**, **3** y **5** en función tanto de la frecuencia como de la temperatura. Para los complejos **2** (Yb^{III}, D_{5h}) y **3** (Tb^{III}, D_{5h}), no se observa relajación lenta de la magnetización por encima de 2 K a campo cero, lo que indica o bien una barrera muy pequeña o la existencia de QTM. Bajo un campo magnético externo de 1000 Oe, se observa relajación lenta de la magnetización para **3**, pero sin máximos definidos en las señales fuera de fase incluso a 10000 Hz. Sin embargo, el complejo **2** muestra relajación lenta de la magnetización bajo un campo magnético *dc* de 1000 Oe. El ajuste de los tiempos de relajación indica que la relajación magnética tiene lugar a través de los procesos Raman y directo, excluyendo el proceso Orbach, con un valor U_{eff} de 18.77 K.

Para los compuestos **1** y **5**, a campo cero, se observa una dependencia con la temperatura y frecuencia de las señales fuera de fase (χ''_M) sin máximos definidos por encima de 2 K, lo que sugiere la presencia de QTM en el estado fundamental. Bajo un campo *dc* de 1000 Oe, los complejos **1** y **5** muestran una evidente dependencia con la frecuencia y la temperatura de las señales fuera de fase con máximos bien definidos, lo que indica que estos compuestos presentan relajación

lenta de la magnetización. Para el compuesto **1** (Dy^{III}, D_{5h}), el ajuste de los datos magnéticos sugiere que la relajación magnética ocurre a través de los procesos Orbach y QTM, con un valor de la barrera de energía efectiva U_{eff} de 61.23 K. Para el complejo **5** (Dy^{III}, O_h), esta ocurre a través de una combinación de los procesos Raman y Orbach, con un valor de U_{eff} de 62.41 K. Así pues, estas medidas de susceptibilidad magnética *ac* revelan un comportamiento SMM inducido por el campo para los complejos **1**, **2** y **5**.

Los cálculos *ab initio* están de acuerdo con los resultados magnéticos experimentales y, además, proporcionan información sobre la dinámica de relajación magnética de estos compuestos. Explican la presencia de QTM en ausencia de campo magnético en el caso del compuesto **2** así como que la relajación se produce, predominantemente, a través de los procesos Raman y directo, en lugar de a través del primer estado doblete excitado.

El hecho de que los compuestos **1** y **5** no presenten relajación lenta de la magnetización a campo cero puede deberse a interacciones intermoleculares y/o a interacciones hiperfinas, que facilitan el QTM a campo cero. Sin embargo, nuestro grupo de investigación preparó previamente un compuesto estructuralmente similar a **1**, el cual también presenta una geometría bipirámide pentagonal, distancias de enlace comparables y parámetros estructurales estrechamente relacionados, pero con átomos de bromo en lugar de cloro. Su fórmula es $[Dy(OPAd_2Bz)_2(H_2O)_4Br]Br_2 \cdot 4THF$. Cabe destacar que este compuesto presenta relajación lenta de la magnetización a campo cero, con valores bastante elevados de T_B (14 K) y U_{eff} (428 K) para SMMs mononucleares estables al aire/agua. Por lo tanto, se compararon los resultados *ab initio* de los compuestos **1** y **5** con los del análogo de bromo del compuesto **1**. Los tiempos de relajación QTM se calcularon según un modelo *ab initio* basado en la interacción espín-dipolar y siguen la tendencia: análogo de bromo de **1** < **1** < **5**. Esta tendencia está de acuerdo con los

valores máximos calculados para las componentes transversales del tensor *g* para sus estados fundamentales, que son 0,001 para el análogo de bromo de **1**, 0,01 para **1** y 0,05 para **5**. Estos resultados sugieren que el comportamiento magnético observado en estos compuestos es intrínseco a su estructura molecular. En particular, la presencia de iones haluro más pesados en el plano ecuatorial parece reducir el campo transversal de los ligandos debido, probablemente, a su menor capacidad dadora, suprimiendo así el QTM.

Además, se investigaron a fondo las propiedades fotofísicas del ligando $OPAd_2Bz$ mediante medidas experimentales y cálculos TD-DFT. Estos estudios demostraron que el ligando actúa como una antena para la emisión de los iones lantánidos en todos los compuestos, con diferentes vías de sensibilización implicadas dependiendo del complejo. Los niveles de energía calculados para los estados S_0, S_1 y T_1 del ligando sugieren que la transferencia de energía a los niveles de emisión de los iones Dy^{III}, Tb^{III}, Eu^{III} e Yb^{III} es energéticamente posible, en particular a través del estado triplete del ligando. Los compuestos **2** (Yb, D_{5h}), **5** (Dy, O_h) y **6** (Eu, O_h) experimentan sensibilización, principalmente, a través del mecanismo tradicional de transferencia de energía que implica el estado excitado triplete. Por el contrario, en los complejos **1** (Dy, D_{5h}) y **3** (Tb, D_{5h}), la sensibilización, probablemente, se produce a través de una transferencia de carga ligando-metal (LMCT, del inglés *ligand-to-metal charge transfer*) desde el estado triplete. Además, los compuestos **1, 5** y **6** muestran emisión dual en función de la longitud de onda de excitación, con una banda de emisión también procedente del ligando, probablemente debido a una transferencia parcial de energía desde el estado triplete T_1 del ligando al nivel emisor del ion Ln^{III}. Estos resultados son de gran utilidad para el desarrollo estratégico de sistemas de emisión dual.

En el Capítulo **(4),** se han diseñado los ligandos quirales de tipo base de Mannich, $H_2L_{R,\,R}$ y $H_2L_{S,\,S}$ para preparar complejos heterotrinucleares Zn^{II}-Ln^{III}-

Zn^{II} con interesantes propiedades magnéticas, luminiscentes y quirales. Los complejos heterotrinucleares Zn^{II}-Ln^{III}-Zn^{II} pueden considerarse compuestos mononucleares desde el punto de vista magnético debido a la naturaleza diamagnética del ion Zn^{II}. Además, esta naturaleza diamagnética de los iones Zn^{II} contribuye, por un lado, a reducir el QTM y, por otro, a aumentar la anisotropía magnética que induce un campo de los ligandos axial, lo que, en principio, aumenta la barrera de energía efectiva para la inversión de la magnetización. Los ligandos base de Mannich, en comparación con los ligandos base de Schiff, presentan una mayor flexibilidad y no tienen átomos de hidrógeno unidos a los grupos amino, lo que puede resultar ventajoso para el estudio de las propiedades magnéticas.

La reacción de estos ligandos con $ZnCl_2$ y $Ln(CF_3SO_3)_3$ conduce a la formación de los compuestos deseados de fórmula general $[ZnCl(\mu\text{-}L_{R,R})Ln(\mu\text{-}L_{R,R})ClZn](PF_6)$ y $[ZnCl(\mu\text{-}L_{S,S})Ln(\mu\text{-}L_{S,S})ClZn](PF_6)$ con $Ln^{III} = Dy^{III}$ y Tb^{III}. Por difración de rayos X se confirmó que los complejos $[ZnCl(\mu\text{-}L_{R,R})Dy(\mu\text{-}L_{R,R})ClZn](PF_6)$ **(1)** y $[ZnCl(\mu\text{-}L_{S,S})Tb(\mu\text{-}L_{S,S})ClZn](PF_6)$ **(4)** son isoestructurales. La entidad trinuclear catiónica está formada por dos unidades $[ZnClL_{R,R}]^-$ (o $[ZnClL_{S,S}]^-$) con un ion Dy^{III} o Tb^{III} central unido a los iones Zn^{II} a través de los átomos de oxígeno fenoxo de dos ligandos diferentes, en el que el ion Ln^{III} presenta una esfera de coordinación LnO_8 formada por los átomos de oxígeno de los grupos fenoxo y aldehído de dos ligandos diferentes, dando lugar a una geometría de coordinación intermedia entre antiprisma cuadrado (SAPR-8, del inglés *square antiprism*) y dodecaedro triangular (TDD-8, del inglés *triangular dodecahedron*), pero más próxima a antiprisma cuadrado (SAPR-8). Los átomos de oxígeno fenoxo están en posiciones opuestas al ion Ln^{III}, creando un campo cristalino axial. Mientras que los iones Ln^{III} se sitúan en la cavidad O_2O_2 externa de los ligandos quirales, los iones Zn^{II} ocupan la cavidad N_2O_2 interna. Estos últimos presentan un

entorno de coordinación ZnN_2O_2Cl con una geometría de coordinación pirámide de base cuadrada distorsionada.

Los compuestos **1** y **2** presentan un comportamiento magnético idéntico por lo que solamente se han medido y estudiado por completo las propiedades magnéticas de **1**. Las medidas de susceptibilidad magnética en campo alterno *(ac)* muestran que los complejos que contienen Dy^{III} (**1** y **2**) presentan, a campo cero, una dependencia de las señales fuera de fase (χ''_M) con la temperatura y la frecuencia con un máximo bien definido a alta temperatura y otro menos definido a baja temperatura debido a la existencia de QTM. Este se ve favorecido por interacciones intermoleculares e interacciones hiperfinas. En vista de ello, para eliminar parcial o totalmente el QTM, se puede aplicar un pequeño campo magnético externo.

Así, bajo un campo magnético *(dc)* óptimo de 1000 Oe, el compuesto **1** muestra una dependencia significativa de las señales fuera de fase (χ''_M) con la temperatura y la frecuencia con dos máximos bien definidos, lo que indica la existencia de dos procesos de relajación (uno lento y otro rápido). El compuesto **1**, por tanto, presenta relajación lenta de la magnetización y comportamiento SMM. El ajuste de los tiempos de relajación a la ley de Arrhenius en la región de alta temperatura para un proceso Orbach, que es el activado térmicamente, da lugar a unos valores de las barreras de energía efectivas de U_{eff} = 214.6 K y U_{eff} =157.6 K para los procesos de relajación lento y rápido, respectivamente. La desviación de la linealidad en los tiempos de relajación por debajo de 20 K (proceso lento) y 12 K (proceso rápido) sugiere mecanismos de relajación adicionales más allá del activado térmicamente. Por lo tanto, se realizó un nuevo ajuste en todo el rango de temperatura estudiado (9-24 K y 15-30 K para los procesos rápido y lento, respectivamente). En el caso del proceso de relajación lento, el ajuste de los tiempos de relajación sugiere una relajación magnética a través de una combinación

de los procesos Orbach y Directo, mientras que, para el proceso de relajación rápido, indica una combinación de los procesos Raman y Orbach.

Se han llevado a cabo cálculos *ab initio* para comprender mejor el mecanismo que rige la relajación magnética del complejo **1**. El doblete de Kramer fundamental (KD1) calculado es muy anisotrópico, con componentes transversales muy pequeñas (g_{xx}~g_{yy} < 0.005), lo que está de acuerdo con sus propiedades SMM a campo cero. El eje de anisotropía g_{zz} se encuentra entre los planos formados por los dos conjuntos de átomos Dy-O-Zn-O, cerca de la colinealidad con las dos distancias Dy-O más cortas. Sin embargo, las componentes transversales de las dos primeros KDs excitados (KD2 y KD3) pueden ser lo suficientemente grandes como para promover la relajación magnética a través del primer y segundo estado excitado, dando lugar a las barreras de energía calculadas U_{cal} de 131.0 cm^{-1} (188.48 K) y 267.2 cm^{-1} (384.44 K), que se corresponden con los valores experimentales de las barreras de energía U_{eff} de 109.5 cm^{-1} (157.6 K) y 149.2 cm^{-1} (214.6 K), respectivamente. Los momentos magnéticos transversales calculados concuerdan con los resultados magnéticos experimentales, sugiriendo que ambos procesos de relajación ocurren, principalmente, vía Orbach a través de los dos primeros estados excitados cuando se suprime el QTM al aplicar un campo magnético *dc*, con contribuciones de los procesos de relajación Raman y directo.

Al igual que los compuestos **1** y **2**, los compuestos **3** y **4** presentan un comportamiento magnético idéntico; por lo tanto, sólo se han discutido las propiedades magnéticas del compuesto **4**. El compuesto **4** no presenta señales fuera de fase (χ''_M) a campo cero, lo que indica que, o bien la barrera de energía térmica es muy pequeña incluso a 2 K, o bien existe una relajación rápida de la magnetización originada por QTM. En consecuencia, para eliminar el QTM, se realizaron medidas *ac* en presencia de un campo externo de 1000 Oe. En estas condiciones, el compuesto **4** presenta una clara dependencia de la susceptibilidad

magnética *ac* con la temperatura y la frecuencia, lo que indica que **4** muestra relajación lenta de la magnetización. Del ajuste de los datos magnéticos experimentales se obtiene que la relajación magnética ocurre considerando una combinación de los procesos de relajación Orbach y QTM en todo el rango de temperaturas, obteniéndose un valor de U_{eff} de 11,81 K.

El compuesto **4** no muestra comportamiento SMM porque, en los sistemas que no son tipo Kramers, se produce QTM directo debido a la existencia de un "gap" de túnel inherente que existe sin aplicar campo magnético externo. El comportamiento SMM en complejos de terbio requiere, normalmente, un entorno de coordinación altamente simétrico, cercano a la simetría D_{4d}, para suprimir eficazmente el QTM.

SUMMARY

SUMMARY

In recent decades, a new discipline has emerged: molecular magnetism. This discipline has made numerous contributions to the scientific community, including the discovery of Single Molecule Magnets (SMMs). This research line has experienced remarkable and rapid development over the past three decades. The present doctoral thesis is situated within this context, focusing on the area of molecular magnetism and photochemistry. The main objectives of this doctoral thesis are the design, preparation, and characterisation of multifunctional mononuclear and trinuclear coordination compounds based on lanthanide ions, with phosphine oxide and chiral Mannich base ligands, respectively, as well as the experimental and theoretical study of their magnetic and luminescent properties. All this fundamental research is aimed at generating new knowledge to design multifunctional SMMs with improved properties. At present, we can confirm that this is one of the most active areas within chemistry and materials science because of the potential applications of SMMs in fields as diverse as molecular spintronics, high-density magnetic storage and the generation of qubits to improve the world of molecular computing.

The introduction (**Chapter 1**) deals with aspects of great interest related to Molecular Magnetism and, more specifically, to SMMs, such as: (a) their relationship with coordination chemistry; (b) the evolution that SMMs have undergone; (c) the current state of this discipline, in which both SMMs based on lanthanide ions and those based on transition metal ions stand out; (d) the need to synthesise compounds with not only high effective energy barriers but also stability; (e) the importance of axial symmetry in suppressing QTM (quantum tunnelling of magnetisation). This relaxation mechanism is very fast and, in most cases, reduces the value of the blocking temperature (T_B), *i.e.* the

temperature below which the compound exhibits SMM behaviour; (f) The effect of molecular vibrations on the relaxation of the magnetisation, which limits the blocking temperature, etc; (g) Special emphasis will be given to SMMs based, on the one hand, on mononuclear lanthanide ion complexes with pentagonal bipyramid geometry and, particularly, with phosphine oxide-type ligands and, on the other hand, on hetero-trinuclear Zn^{III}-Ln^{III}-Zn^{II} complexes from chiral Mannich base ligands. Such compounds usually exhibit slow magnetisation relaxation at zero field and are generally stable in air, humidity and light; (h) The final section deals with multifunctional materials and, more specifically, with chiral and/or luminescent SMM based on lanthanide ions.

In chapter **(2),** the general and specific objectives of this doctoral thesis are outlined.

Chapter **(3)**, the first one devoted to the results obtained in this doctoral thesis, describes the design, synthesis, spectroscopic and structural characterisation by single crystal X-ray diffraction, analysis of the magnetic measurements, and *ab initio* theoretical calculations (to support the experimental results) of 7 mononuclear Ln^{III} complexes with pentagonal bipyramidal (D_{5h}) or octahedral (O_h) geometries depending on the synthesis procedure, which was based on solvothermal methods or reflux in inert atmosphere, respectively. These complexes contain Dy^{III} (**1** and **5**), Yb^{III} (**2**), Tb^{III} (**3**), Gd^{III} (**4** and **7**), and Eu^{III} (**6**). In the equatorial plane the pentagonal bipyramidal compounds contain a chloride atom and four water molecules and the octahedral ones a solvent molecule and three chloride ligands, whereas the di(1-adamantyl)benzylphosphine oxide ligand is located in axial positions in all of them. The former compounds are cationic, whose charges are balanced by chloride counteranions, whereas the latter are neutral.

The reason for using this type of ligand is its steric hindrance, which limits the coordination of only two ligands in the *trans* positions, favouring strong axial anisotropy in the ground state and, consequently, SIM behaviour. Additionally, the strong and bulky sigma-giving groups (adamantyls) increase the electron density on the oxygen atom of the phosphine oxide, thus favouring binding to Ln^{III} ions. The phenyl group present in the ligand is intended to sensitize lanthanide luminescence.

Alternating current (*ac*) magnetic susceptibility measurements were performed on complexes **1**, **2**, **3** and **5** as a function of both frequency and temperature. For complexes **2** (Yb^{III}, D_{5h}) and **3** (Tb^{III}, D_{5h}), no slow relaxation of the magnetization was observed above 2 K at zero field, indicating a very low barrier or a fast QTM. Under a *dc* field of 1000 Oe, a weak slow relaxation is observed for **3**, but without clear maxima in the out-of-phase signals up to 10000 Hz. However, complex **2** exhibits slow relaxation of the magnetisation under a *dc* field of 1000 Oe. The fitting of the relaxation times suggests that the dominant relaxation mechanisms are Raman and direct processes, excluding the Orbach process, with an U_{eff} value of 18.77 K.

For compounds **1** and **5**, at zero field, a frequency dependence of the out-of-phase signals (χ''_M) with no clear maxima above 2 K suggests significant quantum tunneling of magnetisation (QTM) in the ground state. Under a *dc* field of 1000 Oe, complexes **1** and **5** show obvious frequency and temperature dependence of the out-of-phase signals with well-defined maxima, indicating slow relaxation of the magnetisation. For compound **1** (Dy^{III}, D_{5h}), the fit of the magnetic data suggests the presence of Orbach and QTM processes, with an effective energy barrier U_{eff} of 61.23 K. For complex **5** (Dy^{III}, O_h), the relaxation times were fitted to the combination of Raman and Orbach processes, leading to an U_{eff} value of 62.41 K. Thus, these *ac* magnetic

susceptibility measurements revealed field-induced SIM behaviour for complexes **1**, **2** and **5**.

Ab initio calculations support the magnetic results and provide further insights into the magnetic dynamics of these compounds. They explain the presence of QTM in the absence of a magnetic field in the case of compound **2** and also indicate that relaxation predominantly proceeds *via* Raman and direct relaxation pathways, rather than through the first excited doublet state.

The lack of slow magnetization relaxation observed in compounds **1** and **5** may be due to intermolecular interactions and/or hyperfine coupling, which can facilitate Quantum Tunneling of Magnetization (QTM) at zero field. However, our research group previously investigated a structurally similar compound to **1**, also featuring a pentagonal bipyramidal geometry, comparable bond distances, and closely related structural parameters, but with bromine atoms in place of chlorine. Its formula is $[Dy(OPAd_2Bz)_2(H_2O)_4Br]Br_2 \cdot 4THF$. Notably, this compound exhibited slow magnetization relaxation at zero field, with quite high T_B (14 K) and U_{eff} (428 K) values for air/water stable SIMs. We therefore compared the *ab initio* results of compounds **1** and **5** with those of the bromine analogue of compound **1**. Tunnelling relaxation times were calculated according to an *ab initio* model based on spin-dipolar interaction and follow the trend: bromine analogue of **1** < **1** < **5**. This trend aligns with the predicted maxima of the transverse *g*-tensor components for their ground states, which are 0.001 for the bromine analogue of **1**, 0.01 for **1**, and 0.05 for **5**. These results suggest that the magnetic behavior observed in these compounds is intrinsic to their molecular structure. In particular, the presence of heavier halide ions in the equatorial plane may reduce the transverse ligand field components, thereby suppressing Quantum Tunneling of Magnetization (QTM), likely due to their weaker donor ability.

Additionally, the photophysical properties of the $OPAd_2Bz$ ligand were thoroughly investigated through both experimental measurements and state-of-the-art TD-DFT calculations. These studies demonstrated that the ligand acts as an antenna for lanthanide emission in all the compounds, with different sensitization pathways involved depending on the specific complex. The calculated energy levels for the S_0, S_1 and T_1 states of the ligand suggest that energy transfer to the emitting levels of the Dy^{III}, Tb^{III}, Eu^{III} and Yb^{III} ions is energetically possible, in particular via the triplet state of the ligand. Compounds **2** (Yb, D_{5h}), **5** (Dy, O_h) and **6** (Eu, O_h) undergo sensitization primarily through the traditional energy transfer mechanism involving the triplet excited state. In contrast, for complexes **1** (Dy, D_{5h}) and **3** (Tb, D_{5h}), sensitization likely proceeds via ligand-to-metal charge transfer (LMCT) from the triplet state. Moreover, compounds **1, 5,** and **6** display dual emission behavior as a function of the excitation wavelength, with an emission band also originating from the ligand, probably due to a partial energy transfer from the T_1 triplet state of the ligand to the emitting level of the Ln^{III} ion. These results offer useful clues for the strategic development of dual-emitting systems.

In Chapter **(4),** the chiral Mannich base ligands, $H_2L_{R,R}$ and $H_2L_{S,S,}$ have been designed to give heterotrinuclear Zn^{II}-Ln^{III}-Zn^{II} complexes with interesting magnetic, luminescent and chiral properties. The heterotrinuclear Zn^{II}-Ln^{III}-Zn^{II} complexes can be considered magnetically as mononuclear entities because the Zn^{II} ion is diamagnetic. This diamagnetic nature of Zn^{II} ions contributes to reducing the fast QTM and increasing the magnetic anisotropy by inducing an axial ligand field, which in principle increases the effective energy barrier for magnetisation reversal. The Mannich base ligands, compared with Schiff base ligands, exhibit greater flexibility and do not have hydrogen atoms attached to amino groups, which may be advantageous for the study of intrinsic magnetic properties.

The reaction of these ligands with $ZnCl_2$ and $Ln(CF_3SO_3)_3$ leads to the formation of the desired compounds of general formula $[ZnCl(\mu\text{-}L_{\mathbf{R,R}})Ln(\mu\text{-}L_{\mathbf{R,R}})ClZn](PF_6)$ and $[ZnCl(\mu\text{-}L_{\mathbf{S,S}})Ln(\mu\text{-}L_{\mathbf{S,S}})ClZn](PF_6)$ with Ln^{III} = Dy^{III} and Tb^{III}. Single crystal X-ray diffraction revealed that complexes $[ZnCl(\mu\text{-}L_{R,R})Dy(\mu\text{-}L_{R,R})ClZn](PF_6)$ **(1)** and $[ZnCl(\mu\text{-}L_{S,S})Tb(\mu\text{-}L_{S,S})ClZn](PF_6)$ **(4)** are isostructural. The trinuclear cationic unit is formed by two $[ZnClL_{R,R}]^-$ (or $[ZnClL_{S,S}]^-$) units with a central Dy^{III} or Tb^{III} ion bridged to the Zn^{II} ions by two phenoxo oxygen atoms from two different chiral ligands, in which the Ln^{III} ion exhibits an LnO_8 coordination sphere formed by the phenoxo and aldehyde oxygen atoms from two different ligands, giving rise to an intermediate geometry between square antiprism (SAPR-8) and triangular dodecahedron (TDD-8), but closer to square antiprism (SAPR-8). The phenoxo oxygen atoms are in opposite positions to the Ln^{III} ion, creating an axial crystal field. While the Ln^{III} ions are located in the outer O_2O_2 cavity of the chiral ligands, the Zn^{II} ions occupy the internal N_2O_2 coordination site. The latter present a ZnN_2O_2Cl coordination environment with a distorted square-pyramid geometry.

Given the identical magnetic behavior of compounds **1** and **2**, only the magnetic properties of **1** have been fully measured and studied. Alternating current (*ac*) susceptibility measurements showed that complexes containing Dy^{III} (**1** and **2**) exhibit, at zero field, a temperature and frequency dependence of out-of-phase signals (χ''_M) with a well-defined maximum at high temperature and a less well-defined one at low temperature due to a significant QTM. This is favored by intermolecular interactions and hyperfine interactions. In view of this, to eliminate partially or completely the QTM, a small external magnetic field can be applied.

Thus, under an optimal *dc* field of 1000 Oe, compound **1** shows a significant temperature and frequency dependence of the out-of-phase signals

(χ''_M) with two well-defined maxima, indicating the existence of two relaxation processes (one slow and one fast). Compound **1**, therefore, exhibits slow relaxation of the magnetization and SIM behaviour. Fitting the relaxation times to the Arrhenius law in the high temperature region for a thermally activated Orbach process yields effective energy barriers of U_{eff} = 214.6 K and U_{eff} = 157.6 K for the slow and fast relaxation processes, respectively. The deviation from linearity in relaxation times below 20 K (slow process) and 12 K (fast process) suggests additional relaxation mechanisms beyond thermal activation. Therefore, a new fit was performed across the full temperature range studied (9–24 K and 15–30 K for fast and slow processes, respectively). In the case of the slow relaxation process, the relaxation times were fitted to a combination of Orbach and Direct processes, whereas for the fast relaxation process, the relaxation times were fitted to the combination of Raman and Orbach processes.

Ab initio calculations were carried out to provide insight into the mechanism that governs the magnetic relaxation of complex **1**. The calculated ground Kramer Doublet (KD1) is highly anisotropic, with very small transverse components ($g_{xx} \sim g_{yy} < 0.005$), in agreement with its zero-field SMM properties. The anisotropy g_{zz} axis lies between the planes formed by the two Dy–O–Zn–O moieties, close to collinearity with the two shortest Dy-O distances. However, the transverse components of the two first excited KDs (KD2 and KD3) can be large enough to promote magnetic relaxation *via* the first and second excited states, giving the calculated magnetisation barriers U_{cal} of 131.0 cm^{-1} (188.48 K) and 267.2 cm^{-1} (384.44 K), which could correspond to the experimental energy barrier values U_{eff} of 109.5 cm^{-1} (157.6 K) and 149.2 cm^{-1} (214.6 K), respectively. The computed transverse magnetic moments support the magnetic results, suggesting that the two relaxation processes mainly proceed *via* Orbach pathways through the two first excited

states when QTM is suppressed by a *dc* field, with contributions from both Raman and direct relaxation processes.

As with compounds **1** and **2**, compounds **3** and **4** exhibit identical magnetic behavior; therefore, only the magnetic properties of compound **4** will be discussed. Compound **4** does not exhibit out-of-phase signals (χ_M'') at zero field, which indicates that either the thermal energy barrier is very small even at 2 K, or there exists a fast relaxation of the magnetization originated by QTM. In consequence, to eliminate the QTM, *ac* measurements were carried out in the presence of an external field of 1000 Oe. Under these conditions, compound **4** presents a clear temperature and frequency dependence of the *ac* magnetic susceptibility, indicating that **4** exhibits slow magnetisation relaxation. A fitting of the experimental data considering the sum of Orbach and QTM relaxation processes was carried out in the whole temperature range, obtaining an U_{eff} value of 11.81 K.

Compound **4** does not show SMM behavior because, in non-Kramers systems, direct QTM occurs due to an inherent tunneling gap that exists without an external magnetic field. SMM behavior in terbium-based complexes typically requires a highly symmetric coordination environment, close to D_{4d} symmetry, to effectively suppress QTM.

CHAPTER 1

INTRODUCTION

1.1 COORDINATION CHEMISTRY AND MOLECULAR MAGNETISM

Molecular Magnetism is a discipline that has emerged and developed over the past few decades.[1] One of the fundamental tools within this field is Coordination Chemistry, which is used to design and synthesize compounds with specific structures and magnetic properties.[2] Throughout the years, this discipline has made significant contributions to the scientific community.[3] In the early stages, researchers focused on preparing dinuclear compounds using different metal ions as a model to understand the factors that govern the magnetic exchange interaction between two metal ions.[4,5] They also used bridging ligands to establish correlations between the magnetic properties and the structure of the compounds. This research has helped advance our understanding of molecular magnetism and its potential applications. Subsequently, emphasis was placed on the design of three-dimensional molecular magnets (MM),[6,7,8] single chain magnets (SCM)[9,10] and spin-transition coordination compounds.[11,12] But the major breakthrough in this field of research came with the discovery of Single Molecule Magnets (SMMs),[13,14] from which point the discipline experienced a colossal development. Currently, this field of research focuses mainly on the design and preparation of mononuclear SMMs, also called Single Ion Magnets (SIMs), as well as multifunctional materials where interesting magnetic properties are combined with other properties such as chirality, luminescence, photomagnetism, electrical conductivity, porosity, etc.[15, 16 ,17, 18, 19, 20, 21, 22]

1.1.1 Single Molecule Magnets (SMMs)

A single molecule magnet is a coordination compound that can be either mononuclear or polynuclear and has the following characteristics:[3]

- Existence of magnetic hysteresis as in classical magnets.

- Slow relaxation of magnetization below the blocking temperature (T_B).
- Their properties are intrinsic to the molecule, unlike classical magnets, where they originate from magnetic exchange interactions between the metal atoms in the three directions of space.
- In certain cases, when the temperature approaches absolute zero, it is possible to observe quantum effects such as quantum tunnelling, quantum coherence and quantum phase interference.

This combination of classical and quantum properties makes SMMs promising candidates for applications in fields such as ultra-high density information storage, molecular spintronics and quantum computing.[23]

In these compounds, below the blocking temperature, the magnetisation can be blocked parallel or antiparallel to the field when the external magnetic field is removed, inducing slow relaxation of the magnetisation, and, as a consequence, magnetic hysteresis. This behaviour is associated with the existence of an energy barrier, which prevents the reversal of the magnetisation in the ground state and depends mainly on the magnetic anisotropy.

The first molecule in which the SMM behaviour was observed is the compound $[Mn_{12}O_{12}(CH_3COO)_{16}(H_2O)_4]\cdot 2CH_3COOH\cdot 4H_2O$, which is commonly known as Mn12-ac.[24] The structure of this compound is shown in figure 1.1, which consists of twelve metal centres, four manganese ions in a 4+ oxidation state (spin of 3/2) and eight manganese ions in a 3+ oxidation state (spin of 2), linked by oxo and acetate bridging ligands. Interactions of antiferromagnetic nature between the metal ions lead to a fundamental state of spin $S = 10$ with a degeneracy 21 $(Ms = 2S + 1)$. This molecule has a high magnetic anisotropy because the Mn^{III} ions have negative axial anisotropy $(D < 0)$ due to the Jahn-Teller distortion.

Moreover, the anisotropy axes of these ions are parallel to each other and to the S_4 axis of the molecule, which favours the total anisotropy of the molecule.

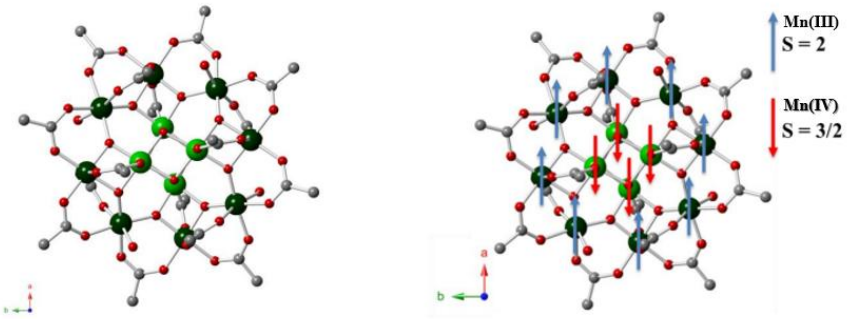

Figure 1.1: (left) Structure of the Mn12-ac molecule. (right) schematic representation of the ground-state spin alignments of the Mn12-ac complex, which gives an *S = 10* ground state. Colour scheme: Mn^{III} dark green, Mn^{IV} light green, O red, C grey. Hydrogens and lattice solvents are omitted for clarity.

Due to zero field splitting (ZFS), which depends mainly on the axial anisotropy of the ground state, the 21 sublevels are separated by an energy which follows the expression: $E(M_s) = M_S^2 D$; where D is the axial anisotropy parameter (see figure 1.2).

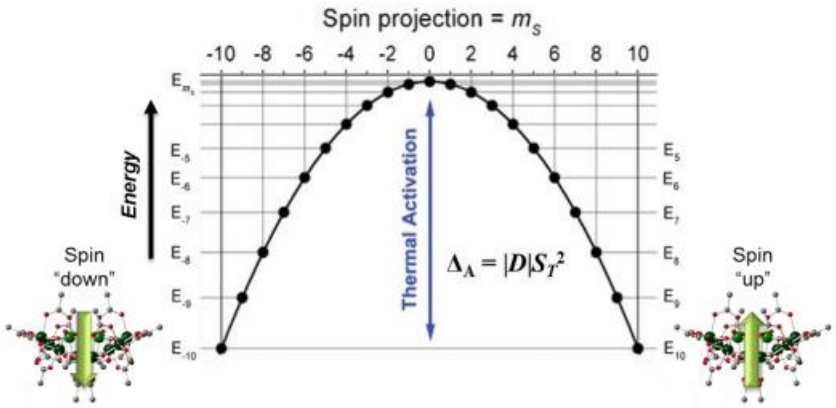

Figure 1.2: Potential-energy diagram for Mn12-ac SMM with a S = 10 ground state experiencing axial zero-field splitting.

When $D < 0$, the lowest energy levels are those with the highest $|Ms|$ value,[25] in this case $Ms = \pm 10$.

The magnetisation associated with each of the $Ms = \pm 10$ sublevels has its particular orientation along the axial anisotropy axis (as for superparamagnetic nanoparticles, see figure 1.3),[26] and, therefore, $Ms = +10$ corresponds to spin up (or 1 in binary language), while $Ms = -10$ corresponds to the spin down (or 0 in binary language). However, when $D > 0$, the sublevels would be inversely oriented, so that the ground state would be $Ms = 0$ (see figure 1.3). In this particular situation, the existence of a bistable ground state is not possible, and, consequently, the system is not valid for information storage. Returning to the first situation, where $D < 0$, for the magnetisation to reverse from $Ms = +10$ to $Ms = -10$ (or vice versa), the system needs to overcome an energy barrier U, as in the case of superparamagnetic materials (figures 1.3 and 1.4). The barrier value is the difference between the highest energy excited state and the ground state. For systems with integer and half-integer spin values this energy barrier, calculated using the Hamiltonian, is $U = S^2 |D|$ and $U = S^2 - 1/4|D|$, respectively (where S is the spin value of the ground state).

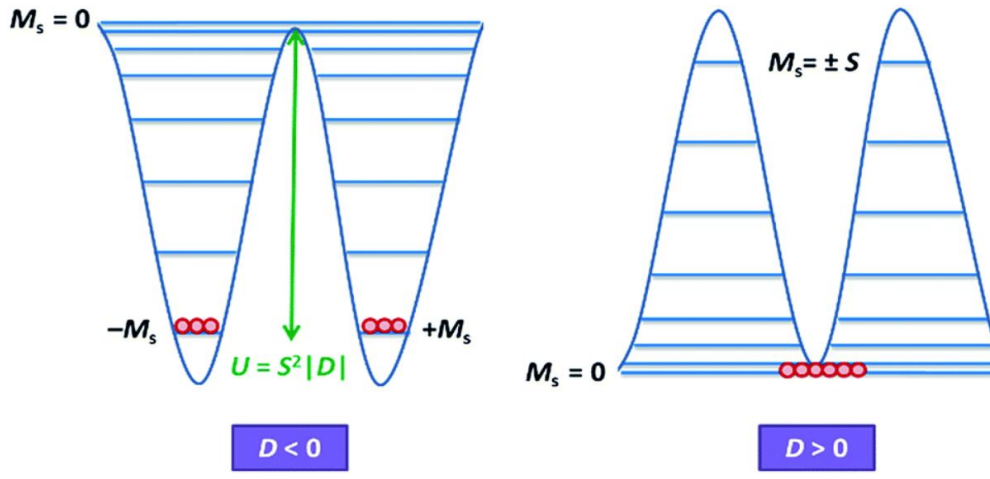

Figure 1.3: Double-well energy diagram for negative (left) and positive (right) D.[25]

Continuing with the example of the Mn12-ac molecule, in the absence of an external magnetic field, the $Ms = \pm 10$ sublevels have the same energy, they are equally populated, and thus the system is not magnetised (figure 1.4, top center). When an external magnetic field of sufficient strength is applied in a given direction, the *Ms* levels on one side of the barrier are stabilised with respect to those on the other side of the barrier, and the material becomes magnetised as a result (figure 1.4, right). When the external magnetic field is removed, if E_T (thermal energy) > U, the material will tend to achieve equilibrium between the two orientations (positive and negative) by losing magnetisation. However, if $E_T < U$, which is the situation when $T < T_B$ (T_B is the blocking temperature), the magnetisation is blocked in one of the orientations and the system is magnetised. The magnetisation can be reversed very slowly over time (slow relaxation of magnetisation), resulting in magnetic hysteresis and, thus, enabling the information storage capacity of SMMs.

In view of the above, it is easy to conclude that the higher the energy barrier, the higher the temperature at which magnetisation and magnetic hysteresis can be maintained. However, this is not always the case, or rather, it is rarely the case.

If magnetisation reorientation or relaxation could occur only by overcoming the energy barrier across all excited states, any material with a value of U = ~298 K (~207 cm^{-1}) would be valid for implementation in an information storage device. Keeping the device temperature below 298 K would ensure no loss of magnetisation, and thus magnetic hysteresis and memory effect. However, as noted above, SMMs with very high activation barriers do not exhibit magnetic hysteresis at such high temperatures.

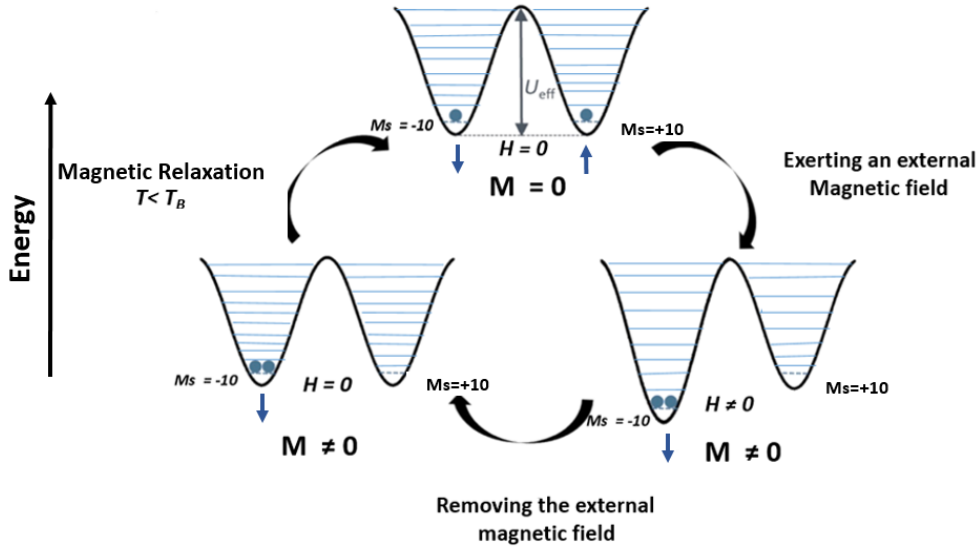

Figure 1.4: Projections of the magnetisation (black arrows) at equilibrium in the absence of an external magnetic field (top center), magnetisation of the material due to the presence of an external field and stabilisation of the sublevels $M_S < 0$ (right) and blocking of the magnetisation in the absence of magnetic field for $T < T_B$ (left). Image modified from reference [26] with Creative Commons license.

This is because the relaxation of the magnetisation, which is facilitated by the absorption and emission of phonons, does not follow over the whole temperature range, the exponential dependence on temperature expected for a relaxation mechanism above the energy barrier (also known as the Orbach process) which occurs as a consequence of the concatenation of a series of simple spin-phonon processes. This is due to the existence of other spin-phonon relaxation mechanisms, such as direct, in which only one phonon is involved, Raman-type processes, which follow a potential law with temperature, where two phonons are involved and, due to the quantum nature of SMMs, the quantum tunnel of magnetisation (QTM), which is independent of temperature, and thermally assisted QTM, TA-QTM.[27] The latter does not occur in the ground state, but between excited states having the same energy.

All these processes allow magnetisation reorientation without having to overcome the thermal energy barrier and are very sensitive to factors such as temperature, magnetic field, transverse anisotropy, hyperfine interactions (interactions between electronic and nuclear spins) and intermolecular magnetic interactions, etc.

An ideal Orbach relaxation would be one in which the system overcomes the complete barrier. The system would absorb phonons from the crystal lattice with an exact energy of $((h/2\pi)\cdot\omega_1)$ to jump from one of the fundamental sublevels *(Ms = ±S)* to the successive excited levels until reaching the highest energy excited sublevel *(Ms = 0).* From this excited state the system would relax towards any of the fundamental *Ms = ±S* states, emitting new phonons ((h/2π)·ω2, figure 1.5, top right). Note that in figure 1.5,[28] the energies of the initial and final states are different due to the existence of internal fields arising from dipole or hyperfine interactions. Consequently, the energy difference between the absorbed and emitted phonon corresponds to the energy difference of the *Ms* sublevels in the ground state. In any case, the Orbach process does not normally occur through the highest energy excited state, but occurs through the first or second excited state (depending on the axiality of the system, figure 1.5, bottom left). The large phonon energy required for this process to occur is the main reason why it normally operates at high temperatures.

The energy constraints related to the Orbach process are not present for the Raman process, as this mechanism operates by inelastic phonon scattering. The molecule absorbs a phonon $(h/2\pi)\cdot\omega_1$, reaches a virtual excited state, and emits another phonon $(h/2\pi)\cdot\omega_2$ (figure 1.5, top left). Again, the energy difference between the two phonons corresponds to the energy difference of the *Ms* sublevels in the ground state.

Meanwhile, the direct process is a magnetisation relaxation process that directly emits a single phonon ($(h/2\pi)\cdot\omega$) corresponding to the energy difference of the *Ms* sublevels in the ground state (figure 1.5, bottom right).

All these mechanisms occurring via spin-phonon interactions require some energy (thermal assistance), but the case of QTM is different. This process occurs between the *Ms* sublevels of the doubly degenerate ground state, and is often the main relaxation pathway at low temperatures, where the ground state is mostly populated (figure 1.5, bottom left). However, the relaxation process could be a combination of different processes, where the excited states are populated by phonon absorption, and then QTM could occur between *Ms* states of the same energy (but different sign), followed by a relaxation to the fundamental sublevel. This combined mechanism is known as thermally assisted quantum tunnelling of magnetization, TA-QTM (figure 1.5, bottom left).

It should be noted that processes such as QTM and direct generally operate at low temperatures, Orbach at the highest temperatures, and TA-QTM in the intermediate range. The Raman process, on the other hand, could operate over the entire temperature range. Among all of them, the QTM and TA-QTM processes are considered as shortcuts to the barrier, as the system relaxes without the need to overcome it. Consequently, QTM, TA-QTM and Raman processes can cause a decrease in the value of the barrier *U*, resulting in an effective energy barrier, U_{eff}, and affecting, at the same time, the value of the blocking temperature and the relaxation time.

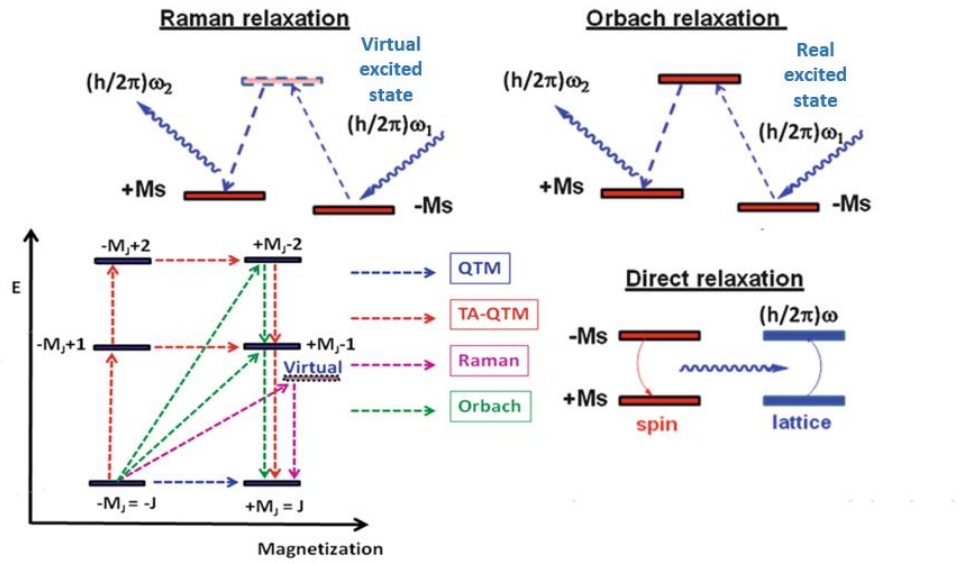

Figure 1.5: Schematic representation of the Orbach (top right), Raman (top left) and Direct (bottom right) relaxation mechanisms. A combination of different relaxation mechanisms, including QTM and TA-QTM, for a part with a double potential energy well (bottom left). Image modified from reference [28] with Creative Commons license.

The most commonly used strategies to suppress undesired QTM are:

I. Design compounds with perfect axial symmetry, since QTM is induced by transverse anisotropy, which is favoured by distortion with respect to the ideal symmetry.

II. Dilution of samples by co-crystallisation of SMM with diamagnetic analogues (usually with Zn^{II} when working with transition metals and Y^{III} or La^{III} when using lanthanides) to avoid intermolecular interactions that promote QTM.

III. Use isotopes with zero nuclear angular momentum to eliminate hyperfine interactions.

IV. Application of an external magnetic field that breaks the degeneracy between the sublevels $Ms = \pm S$ (or $M_J = \pm J$, usually when referring to lanthanides).

V. Design complexes with a more rigid molecular structure that avoid molecular vibrations that favour magnetic relaxation, usually through Raman-type processes.

VI. Design complexes with strong magnetic interactions between neighbouring metal ions.

Some of these strategies will be discussed in more depth below.

It is noteworthy that QTM is usually more important for systems with an integer *S*-value, as they intrinsically possess quantum tunnelling at zero-field. However, for ions with half-integer spin (Kramers-type ions), due to the Van Vleck cancellation principle,[29] phonons emerging from the crystal lattice could not induce QTM and direct-type processes in the absence of a magnetic field. The absence of QTM facilitates magnetic relaxation through thermally assisted Raman and Orbach-type processes. Unfortunately, axial symmetry distortion, hyperfine interactions, and transverse magnetic fields created by intermolecular interactions, unfold the Kramers doublets giving rise to new pathways for magnetisation relaxation by QTM and direct process.

1.1.1.1 Design and synthesis of Single Molecule Magnets (SMMs)

The discovery of the first SMM was a milestone in the field of molecular magnetism. The main challenge associated with this compound for realistic applications was that it needed to be kept at very low temperatures to ensure that the magnetisation remained locked in the absence of the external magnetic field. Since then, numerous efforts have been made to design and synthesise compounds that behave like SMMs at high temperatures. To understand the progress in the design of these systems, we must keep in mind, as previously indicated, that the energy barrier blocking the magnetisation reversal depends simultaneously on the total spin value and the anisotropy:

$$U = S^2|D|;\ \ S = integer\ spin$$

$$U = \left(S^2 - \frac{1}{4}\right) \cdot\ |D|;\ S = non - integer\ spin$$

The first strategy to increase the energy barrier focused on increasing the ground state spin. For this purpose, polynuclear coordination compounds with ferromagnetic exchange interactions between their metal centres were synthesised. Among them, we can highlight those based on Mn^{III}. This ion is a suitable candidate as it generally has a high spin configuration (favoured by its high pairing energy) with four unpaired electrons and Jahn-Teller distortion leading to a zero-field splitting of the ground state and axial anisotropy. Numerous SMMs with Mn^{III} have been synthesised using different synthetic methods.[30, 31, 32] The compound of this type with the highest spin ground state, S = 83/2, is the molecule $Mn^{II}_7Mn^{III}_{12}$, whose structure can be seen in figure 1.6.[32] However, despite the high spin value of the ground state, this compound has almost zero anisotropy and an energy barrier value of 5.8 K.

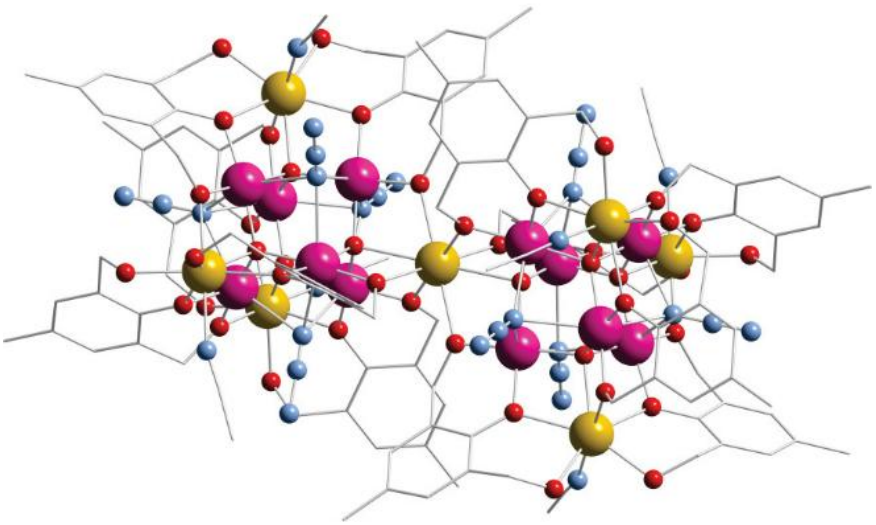

Figure 1.6: Crystal structure of the compound $Mn^{II}_7Mn^{III}_{12}$. Colour code: Mn^{III}, yellow; Mn^{II}, pink; O, red; N, blue; C, grey. Hydrogen atoms and uncoordinated solvent molecules have been omitted for clarity.[32]

The fact that as the spin value of the ground state increased, the anisotropy decreased was observed in a large number of polynuclear compounds with different metal ions. This is because the anisotropy axes of the metal ions in the compound adopted different orientations so that, when added together, the molecule had a lower or even zero total anisotropy *D* in some cases. It should be noted that controlling a collinear arrangement of the anisotropy axes is very difficult and a major synthetic challenge. Moreover, theoretical calculations have shown that the anisotropy *(D)* is inversely proportional to the square of the ground-state spin (S^2), so that the effective activation barrier (U_{eff}) can, to a good approximation, be considered independent of *S*.[33]

In view of the above considerations, increasing the spin of the ground state is not a good strategy to increase the U_{eff} in polynuclear compounds/clusters based on transition metal ions. An alternative strategy to obtain, in principle, higher U_{eff} and T_B values would be to enhance magnetic anisotropy. For this, the most viable options are to use:

I. Mononuclear transition metal coordination compounds with very high magnetic anisotropy.
II. Lanthanide ion coordination compounds, some of which have exceptionally high anisotropy.

To obtain high anisotropies with transition metal coordination compounds, we would have to decrease the field splitting of the ligands, in order to:

- Avoid elimination of first order orbital contribution.
- Increase the second-order spin-orbit (SO) coupling, which is inversely proportional to the separation between the ground state and the excited electronic states.

To decrease the ligand field and, therefore, the splitting of the d-orbitals we should:

i. Prepare compounds with low coordination numbers (fewer ligands, less interaction with metal d-orbitals and less splitting).
ii. Use metal ions with low oxidation states (less polarising, less interaction with the ligands).

Synthetic efforts were therefore directed towards the design of mononuclear coordination compounds with lower nuclearity and highly anisotropic ions, such as lanthanide ions and some transition metal ions.

1.1.2 Transition-metal based Single Ion Magnets (SIMs)

As mentioned above, mononuclear SMMs, also called Single Ion Magnets (SIMs), with highly anisotropic ions are at the forefront of research in this field, as they can exhibit much higher anisotropy, and thus higher energy barriers, than those of a polynuclear nature. This is because, in these simple systems, the anisotropy can be deliberately modulated by controlling the electronic structure of the complex through the properties of the metal ion and its coordination environment.[34, 35]

The concept of significantly improving the total *S* value of the compounds was eventually set aside, and the focus shifted toward increasing the anisotropy value. The transition metal ions do not have buried valence orbitals like the lanthanides (4f), so the electrons present in the 3d-orbitals can interact with the ligands, resulting in quenching of the orbital angular momentum and, therefore, quenching of the first order spin-orbit coupling (SOC). This statement indicates that the SOC causing magnetic anisotropy is typically generated by second-order SOC.[36,37,38] However, first-order SOC can

be maintained through a thoughtful design of the ligand field, which includes low coordination numbers. Thus, the low coordinated transition metal ion-based SIMs are the best candidates to exhibit high magnetic anisotropy due to unrestricted orbital angular momentum and non-integer spin ground state which reduces the probability of QTM.[25, 33, 39] Here we present the transition metal complexes that have the best SIM properties, which have linear geometry and contain Kramers metal ions.

For achieving significant energy barrier for magnetization reversal without an external magnetic field, Long and coworkers studied a linear Fe^{I} coordination compound with S = 3/2 and the formula [K(crypt-222)][Fe(C(SiMe$_3$)$_3$)$_2$] (figure 1.7).[40] They demonstrated that the combination of a low coordination number with a low oxidation state gives rise to a remarkably weak ligand field, which in turn allows the orbital angular momentum to remain unquenched, thereby increasing the total anisotropy of the compound. In this compound, SMM behaviour was observed, with an effective energy barrier (U_{eff}) of 325 K (226(4) cm^{-1}), which is close to the difference between the ground (M_J = ±7/2) and first excited state (M_J = ±5/2), indicating that the relaxation most likely takes place through the first excited state.[40] They observed QTM and attributed its origin to geometric distortions displayed by the C-Fe-C bond, which enhanced transverse components and thus facilitated QTM and to a vibrational effect known as Renner-Teller activity.[41]

Other two-coordinated homoleptic compounds based on iron, cobalt or nickel did not display such a good SMM behaviour due to stronger QTM probably caused by vibronic couplings.[25, 33, 42, 43, 44] This is a direct result of the dynamic distortion of the long metal-ligand bonds observed in the previously mentioned examples. Atanasov, Neese and coworkers carried out a theoretical

study to overcome these limitations and concluded that increasing the covalency of metal-ligand bonds could reduce vibronic coupling while increasing magnetic anisotropy.[41]

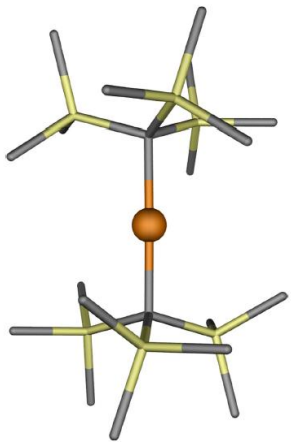

Figure.1.7: Perspective view of the anionic structure of [K(crypt-222)][Fe(C(SiMe$_3$)$_3$)$_2$] compound. Colour code: Fe^{I}, carbon and silicon in orange, grey and yellow, respectively. Hydrogen atoms and counteranion have been omitted for the sake of clarity.[40]

In order to achieve coordination compounds with enhanced covalency Gao et al. synthesized three Co^{II}-based coordination compounds with the general formula [(NHC)CoNDmp] (Dmp = 2,6-dimesitylphenyl and NHC are different N-heterocyclic carbene ligands).[45,46] These compounds exhibited an almost linear arrangement of the ligands, very short Co-N$_{imido}$ bond distances (1.691(6) Å) and high $\chi_M T$ values (3.86, 3.72, and 3.74 emu·K·mol^{-1}) at room temperature, indicating unquenched orbital angular momentum caused by the weak ligand field. The three complexes showed SMM behaviour at zero field and the compound with NHC = sIPr (Figure.1.8 left) displayed a magnetic moment blocking at 3.5 K and a U_{eff} of 594.2 K (413 cm^{-1}), the highest reported until that moment for a 3d-based SMM. Theoretical studies confirmed that the Co=N bond length variations significantly affect magnetic anisotropy. They proposed that the large magnetic anisotropy of the complexes arises from

the $[CoN]^+$ core, which features a ground Kramers doublet (M_J = ±7/2) with strong Co-N exchange coupling, which reduced undesired QTM.

Finally, Long et al. reported the compound $[Co(C(SiMe_2ONaph)_3)_2]$, (Naph = naphthyl) (Figure.1.8 right),[47] with a ground state M_J = ±9/2 and maximal orbital angular momentum L = 3, similar to that observed in lanthanides, leading to very large magnetic anisotropy. They successfully crystallized the desired linear compound with a record U_{eff} of 647.5 K (450 cm^{-1}), the highest reported so far for transition metal-based SMMs.[48]

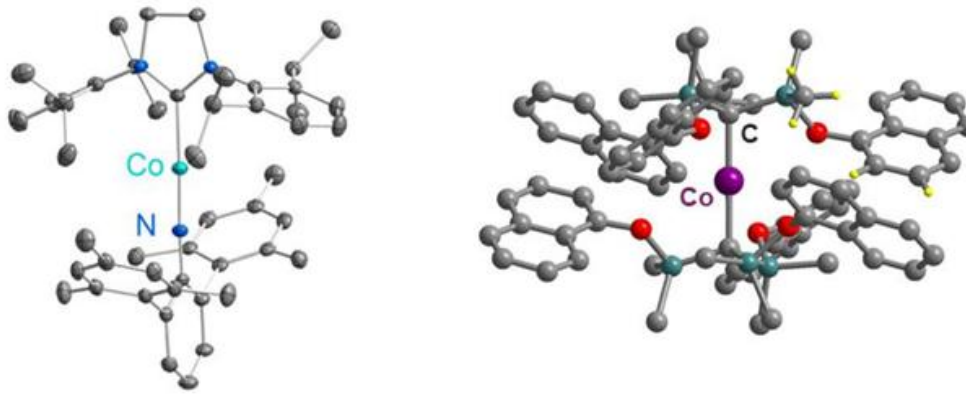

Figure.1.8: (left) Linear Co^{II} compound synthesised by Gao et al.[45] with formula [(NHC)Co(NDMP)]. (right) Linear Co^{II} compound synthesised by Long et al,[47] with formula $Co(C(SiMe_2ONaph)_3)_2$.

It is important to point out that these organometallic compounds, such as lanthanide ion metallocenes, are highly unstable in air and humidity, which considerably limits their direct application in devices. For this reason, research in this area has focused on air-stable Co^{II} complexes in both the solid state and in solution, which will facilitate their future application in electronic, spintronic and photonic devices. The predominance of Co^{II} complexes in the area of transition metal SIMs is largely due to the following reasons:

- High orbital angular momentum and strong spin-orbit coupling: Co^{II} complexes typically exhibit high values of orbital angular momentum ($L \neq 0$) and strong first-order spin-orbit coupling (SOC), leading to high magnetic anisotropy.[33]

  In some cases, the orbital angular momentum can cancel out, generating a degenerate spin ground state. In this situation, second-order spin-orbit coupling (involving excited electronic terms with $L \neq 0$) can exist, also giving rise to very high anisotropy values.
- Kramers-type ion: The Co^{II} ion is a Kramers-type ion (half-integer spin of 3/2). This means that in the absence of a magnetic field, the direct magnetisation relaxation and QTM mechanisms should not be operational.[49] The absence of QTM at zero field facilitates the Orbach and Raman magnetisation relaxation processes, both of which are thermally assisted.

These Co^{II} compounds should have large axial anisotropy (where the axial anisotropy parameter, *D*, is negative) and small transverse anisotropy (where the rhombic anisotropy parameter, *E*, is close to zero), so that the relaxation of the magnetisation by quantum tunnelling of the magnetisation is effectively suppressed, which is of vital importance for observing SIM behaviour at zero field. Similar to lanthanide ion-based SIMs, when the geometry is closer to perfect axial symmetry, the fundamental and excited levels are less mixed, there is reduced transverse anisotropy, and less quantum tunnelling occurs. Indeed, it has been observed that compounds exhibiting large axial anisotropy ($D < 0$) display SIM behavior at zero field or with a small dc magnetic field (to suppress QTM), whereas for Co^{II} complexes with high positive *D* values, the presence of a magnetic field is necessary to observe SIM behavior.

In both scenarios, anisotropy splits the spin quadruplet into two Kramers doublets, with the fundamental doublet being $Ms = \pm 3/2$ and the excited doublet being $Ms = \pm 1/2$ when $D < 0$, whereas in the $D > 0$ case the situation is reversed. The energy difference between these two doublets corresponds to the thermal activation barrier for an Orbach-type magnetisation relaxation process.

In addition to the linear mononuclear Co^{II} compounds, others with high negative D values and SIM behavior at zero field are:

- Planar trigonals (with experimental measured D as low as -85 cm^{-1}).
- Tetrahedral with D_{2d} symmetry (with experimental D values as low as -115 cm^{-1}).
- Hexacoordinate compounds with trigonal prism geometry (with experimental D values as low as -115 cm^{-1}).[50]

1.1.3 Lanthanide-based Single Ion Magnets (SIMs)

As mentioned above, another possibility to increase the value of the U_{eff} is to introduce rare earth ions, in particular lanthanides, into the magnetic cluster. Lanthanide ions possess the two basic ingredients for obtaining SMMs: i) high spin (up to seven unpaired electrons for Gd derivatives) and ii) high magnetic anisotropy due to the strong spin-orbit coupling intrinsic to many of these ions. Thus, in recent years a new generation of SMMs has been prepared based on mixed 3d-4f coordination compounds, in which however the blocking temperature (T_B) does not increase significantly.[51, 52, 53] This is mainly due to the weakness of the magnetic exchange interaction between the 3d and 4f ions, since the latter are internal orbitals, leading to situations where the energy separation between the fundamental spin state and the excited states is very small, limiting the height of the thermal energy barrier U_{eff}.

An alternative approach, which is simpler from a synthetic perspective, has involved the preparation of mononuclear SMMs based on lanthanide ions (lanthanide-based SIMs). The first examples of this kind of compounds were published by the group of Professor Ishikawa in 2002, who prepared mononuclear sandwich-type coordination compounds with bis-phthalocyanine type ligands (Figure 1.9).[54, 55] The compound containing the lanthanide ion Tb^{III} exhibited an effective energy barrier value U_{eff} of 330.9 K and that of Dy^{III} of 40.3 K. This confirmed that a single metal would be sufficient to design compounds with SMM behaviour and high energy barriers. This led the scientific community to preferentially use coordination compounds of lanthanide ions, mainly of a mononuclear nature. However, the origin of this magnetic blocking is distinct from that of SMMs based on d block metal ions. In these nanomagnets, the magnetic anisotropy necessary to observe a slow relaxation of the magnetisation arises from the splitting of the fundamental multiplet, *J*, of the lanthanide ion due to the ligand field. For specific geometries, this splitting stabilises the $\pm M_J$ sublevels with high values of $|M_J|$, which results in the emergence of an easily magnetisable axis. To reverse the orientation of the total angular momentum *J* (from $+J$ to $-J$), it is necessary to overcome an energy barrier.

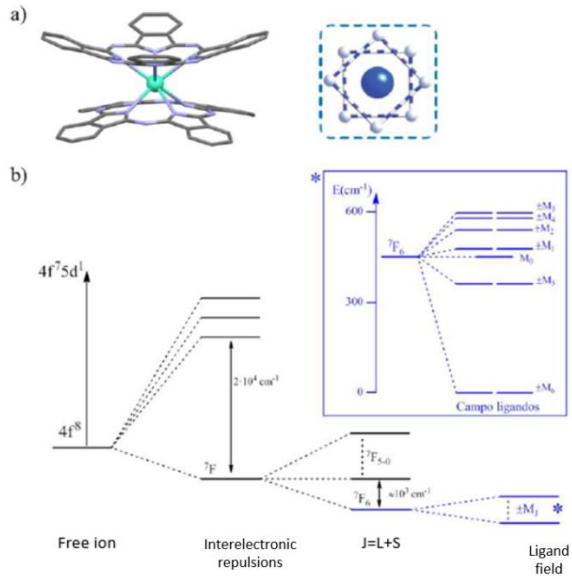

Figure.1.9: a) Structure of the $[Tb(Pc)]^-$ complex (Pc = phthalocyanine) and coordination environment around the Tb^{III} ion (right). b) Energy splitting of the $^7F_6$ ground state for a Tb^{III} ion under the influence of a D_{4d} symmetry ligand field. Colour code in a): Ln^{III} (Tb and Dy), green; C, grey; N, blue. The hydrogen atoms have been omitted for clarity.[54, 55]

In terms of symmetry, what is the geometry that such a complex must have in order to maximise the energy barrier U_{eff} and the blocking temperature T_B? The answer to this question depends on the lanthanide ion under consideration. For the Ln^{III} ions, the electron density cloud resulting from the electron occupation of the different *f* orbitals is spherical. For example, the $4f_{x(x^2-3y^2)}$ orbital has a very pronounced oblate geometry (Figure 1.10). An ion with only one electron in this orbital, such as Ce^{III}, will have an oblate electron density.

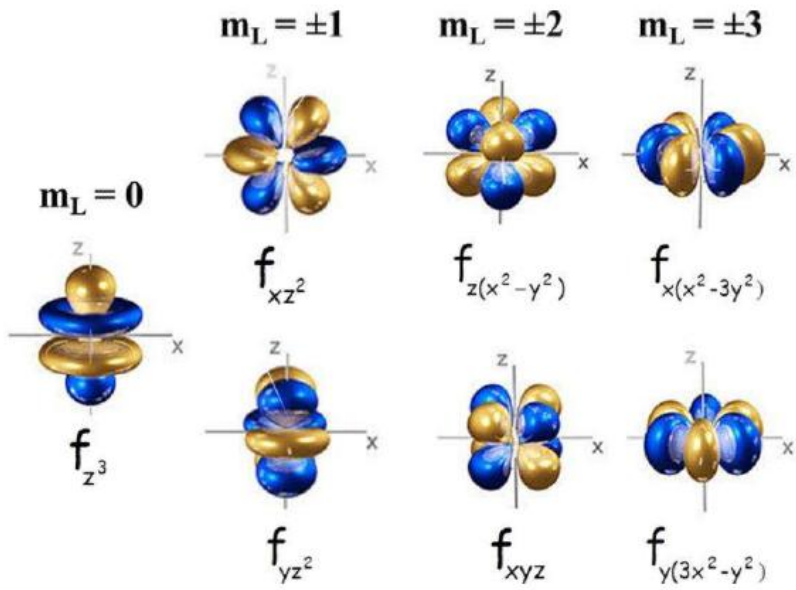

Figure 1.10: Representation of the *f* orbitals in an axial coordination environment with the corresponding m_L values (as the value of m_L increases, the oblate geometry of the orbital becomes more pronounced).

Knowing the shape of the different *f* orbitals and knowing that for the different Ln^{III} ions their electronic occupation is governed by Hund's rules, it is possible to know approximately the geometry of the electron density cloud for each Ln^{III} ion. Thus, the Ce^{III}, Pr^{III}, Nd^{III}, Tb^{III}, Dy^{III} and Ho^{III} ions have electron density clouds of the oblate type, whereas the density of the Pm^{III}, Sm^{III}, Er^{III}, Tm^{III} and Yb^{III} ions is of the prolate type.

To maximise the anisotropy of an oblate ion, the crystal field around it must be such that the electron density of the ligands is confined along the z-axis (above and below the *xy* plane), as is the case for the sandwich-type complexes studied by Ishikawa[54, 55, 56] In this case, the orientation of the magnetic moment in the ground state will be parallel ($+M_J$) or antiparallel ($-M_J$) to the z-axis molecular, since in this situation the electrostatic repulsion between the metal and the ligands is minimal. The reorientation of the

magnetic moment means passing through a situation in which this moment is on the *xy* plane, directly facing the ligands, which is the moment of maximum electrostatic repulsion, creating a high energy state (Figure 1.11). The greater the repulsion, the greater the energy required to reorient the magnetisation. Thus, ligands with very weak interactions must coordinate in the equatorial plane. For a prolate ion, the ideal situation is the opposite; equatorial coordination geometry is preferable as the repulsion with the charge density of the ion located along the z-axis will be minimal. In this case, ligands with low electron density should be located in axial positions.[54, 57, 58]

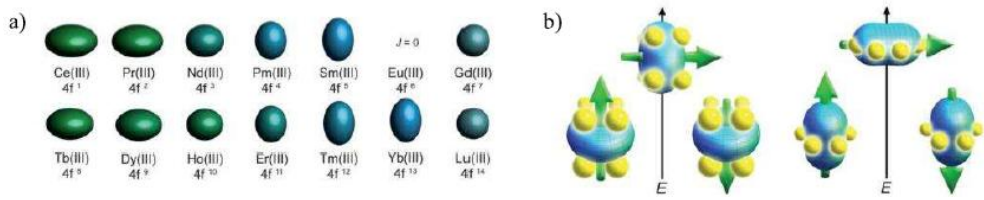

Figure 1.11: a) Electron distribution cloud of electrons located in the 4f shell for Ln^{III} ions (the Eu^{III} ion is not shown because $J = 0$). b) High and low energy configurations of the electron density with respect to the crystal field for an oblate (left) and a prolate (right) lanthanide ion. The green arrow indicates the orientation of the total angular momentum. For an oblate electron density, a sandwich-type crystal field minimises the energy of the $m_J = J$ (maximum) state. For a prolate density, the energy of the $m_J = J$ (maximum) state will be minimal if the ligands adopt an equatorial arrangement.

Therefore, considering all the above, we need a highly symmetric axial coordination. Ishikawa complexes fulfil this condition as they present a highly symmetric $n = 8$ coordination environment (D_{4d}) with a C_4 axial axis. Thus, Tb^{III}, Dy^{III} and Ho^{III} ions, which present ground states with high $|M_J|$ values, are good candidates for obtaining SIMs. However, Tb^{III} and Ho^{III} ions have J = 6 and 8, respectively (non-Kramers type ions, integer spin), and it may happen that the $M_J = 0$ sublevel is the ground state one, so that such behaviour would not be observed. For Dy^{III}, with $J = 15/2$ (Kramers type ion, half-integer spin),

the sublevels with minimum M_J will be $\pm M_J = 1/2$ and will never be zero, making this ion ideal for obtaining mononuclear SMMs.

Numerous works have confirmed the suitability of the conditions just mentioned for obtaining SIMs derived from Dy^{III} ions with high-energy barriers U_{eff} and high blocking temperatures T_B. It has been even possible to synthesise and characterise a SIM derived from Ho^{III}. The Ho^{III} ion is a non-Kramers type ion, and usually has a rapid relaxation of the magnetisation by the QTM effect, making it very difficult to observe a slow relaxation of the magnetisation. In this complex, the highly compressed local environment together with a pseudo-D_{5h} geometry greatly reduces the mixing of the $M_J>$ states caused by the crystalline field, making this compound based on a phosphine oxide a Ho^{III} SIM even at zero field.[59]

All these results mean that, as mentioned above, research in this field is currently focused on the design of mononuclear complexes, also called Single Ion Magnets (SIM)[60] with highly anisotropic ions.

1.1.3.1 Dy^{III} based Single Ion Magnets (SIMs)

Taking into account the above information, the predominance of lanthanide-based SIMs, especially Dy^{III}, is not surprising. This is because Dy^{III} is very anisotropic (the electron density f of the M_J ground state is strongly oblate), with large spin and orbital angular momenta and strong spin-orbit coupling with a ground state spectroscopic term $^6H_{15/2}$. Moreover, as it has an odd number of electrons, it is a Kramers-type ion, for which the double degeneracy at zero field is assured, and, therefore, the magnetic bistability.

It has been possible to obtain metallocene Dy^{III} SIMs with record-breaking blocking temperatures and thermal activation energies. They represent the cutting edge of SMMs with magnetic blocking temperatures

already surpassing that of liquid nitrogen. The absence of equatorial ligands in these compounds leads to a strong axial magnetic anisotropy.[61] This in turn, quenches the transverse components of the crystal field and minimises interactions with the environment. As a result, the quantum-tunneling magnet (QTM) is suppressed, enabling record-breaking blocking temperatures T_B and high energy barriers U_{eff}.

Derivatives of cyclopentadienyl (Cp = cyclopentadienyl anion) have sparked a breakthrough in Dy^{III}-based systems. Building on Rinehart and Long's design strategies, Dy^{III} complexes sandwiched between Cp ligands—lacking equatorial coordination—were identified as promising candidates. However, the considerable ionic radii of lanthanide ions made their synthesis particularly challenging. Nearly concurrently, Mills and Layfield reported the successful creation of a dysprosocenium complex employing bulky Cp^{ttt} ligands (Cp^{ttt} = {$C_5H_2{}^tBu_3$-1,2,4}, where ^tBu = $C(CH_3)_3$) (Figure 1.12, top left).[62, 63] This compound, with the formula $[Dy(Cp^{ttt})_2][B(C_6F_5)_4]$ (**1**), features a notably wide Cp–Dy–Cp angle of 152.56(7)° and short Dy–$Cp_{centroid}$ distances of 2.316(3) Å.[62] These structural attributes hinted at highly favorable slow magnetic relaxation behavior. Indeed, magnetic hysteresis loops were observed up to 60 K (using a sweep rate of 22 Oe/s), although quantum tunneling of magnetization (QTM) effects were evident at 2 K. Field-cooled and zero-field-cooled (FC/ZFC) measurements confirmed a blocking temperature (T_B) of 61 K, as seen by the bifurcation in the curves. To investigate the magnetic relaxation mechanism, *ab initio* calculations were carried out. Notably, the spin–phonon coupling associated with C–H vibrational modes in the Cp^{ttt} ligands emerged as a key factor in facilitating the initial transition from the ground ±15/2 state to the first excited ±13/2 state. This insight suggests that modifying or replacing these groups could further improve the hysteretic properties of dysprosium metallocenes. The exceptional

performance of this compound was also linked to its unique ligand field environment; the bulky and rigid Cp^{ttt} ligands restrict metal–ligand vibrational modes that could otherwise promote quantum tunneling or shortcut relaxation pathways. Remarkably, the compound exhibits an energy barrier of 1760 K (1223 cm^{-1}), comparable to that of other high-performance SMMs like $[Dy(OtBu)_2(py)_5][BPh_4]$.[64] However, despite similar barrier heights, compound $[Dy(Cp^{ttt})_2][B(C_6F_5)_4]$, shows a significantly higher blocking temperature. This contrast is attributed to differences in coordination environments: the complex $[Dy(OtBu)_2(py)_5][BPh_4]$ features monodentate donor atoms and greater metal–ligand flexibility in its first coordination sphere, which likely introduces low-energy vibrational modes that accelerate magnetic relaxation via under-barrier processes.

Building upon these exceptional findings, Layfield and colleagues advanced their work in 2018 by synthesizing a new dysprosocenium compound with even enhanced performance.[65] Insights gained from the study of compound $[Dy(Cp^{ttt})_2][B(C_6F_5)_4]$ helped refine the design strategy for optimizing the ligand field. The key objectives were: (i) to achieve shorter Dy–Cp bond distances, (ii) to increase the Cp–Dy–Cp angle, and (iii) to eliminate C–H bonds near the metal center. However, achieving all three goals required a careful balance—bulky ligands could widen the Cp–Dy–Cp angle and prevent equatorial ligand coordination, but excessive steric bulk might also lead to undesirably long Dy–Cp distances.

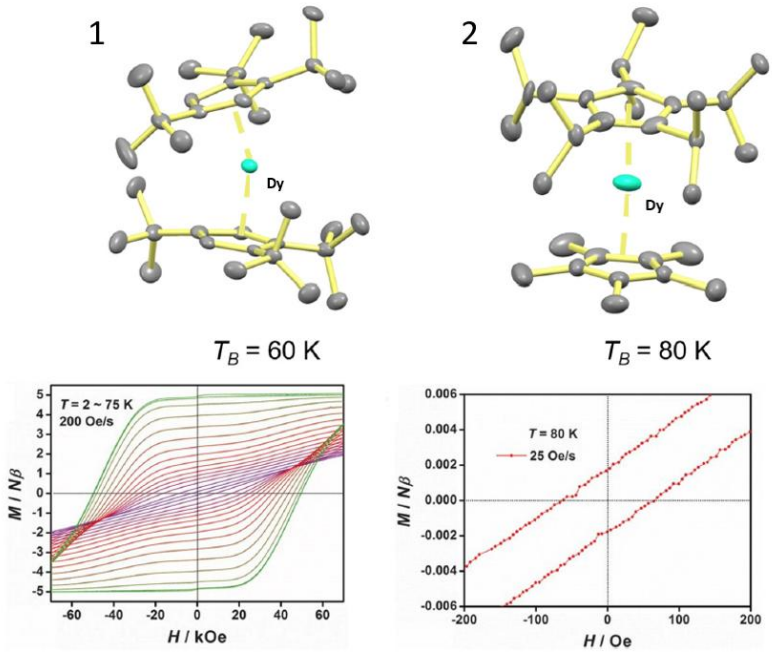

Figure.1.12: Cationic structures of complexes **1** and **2** (top).[62, 65] Hysteresis loops in the 2–75 K temperature range using a sweep rate of 200 Oe/s (bottom left) and hysteresis loops at 80 K using a sweep rate of 25 Oe/s for 2 (bottom right).[65] Color code: Dy^{III} and carbon in turquoise and grey, respectively. Hydrogen atoms and counterions have been omitted for the sake of clarity. Generated from the crystal structures in reference. Copyright 2018. The American Association for the Advancement of Science.

Despite these challenges, the team successfully synthesized a compound with the general formula $[(\eta^5\text{-Cp*})Dy(\eta^5\text{-Cp}^{i\text{Pr5}})][B(C_6F_5)_4]$ (**2**), where Cp* stands for pentamethylcyclopentadienyl and $Cp^{i\text{Pr5}}$ for pentaisopropylcyclopentadienyl (Figure 1.12, top right). X-ray crystallographic analysis confirmed that, on average, the Dy–Cp* and Dy– $Cp^{i\text{Pr5}}$ bond distances were 0.026 Å shorter than those in compound $[Dy(Cp^{ttt})_2][B(C_6F_5)_4]$. Additionally, the Cp*–Dy– $Cp^{i\text{Pr5}}$ angle was significantly wider, with a value of 162.507(1)°, bringing it nearly 10° closer to the ideal linear angle of 180°. These structural refinements pointed toward a stronger axial crystal field, setting the stage for improved magnetic behavior.

At a magnetic field sweep rate of 25 Oe/s, the system displayed open hysteresis loops up to 80 K, which is already above the boiling point of liquid nitrogen (Figure 1.12, bottom). *Ab initio* calculations confirmed the strong axial nature of the complex, indicating a ground state with ideal axial symmetry. In contrast to complex $[Dy(Cp^{ttt})_2][B(C_6F_5)_4]$, no evidence of a zero-field step was detected, implying that quantum tunneling of magnetization (QTM) is entirely suppressed (Figure 1.12, bottom). Furthermore, with the original C–H bonds in the ring substituted by isopropyl or methyl groups, the vibrational mode triggering the first excitation from the ground state was attributed to an out-of-plane vibration of the Cp* ligand.

Around the same time as the discovery of the aforementioned metallocene, Harvey and collaborators reported a series of four related Dy^{III} sandwich complexes (Figure 1.13) with the general formula $[Dy(Cp^{iPr4R})_2][B(C_6F_5)_4]$ (R = H, Me, Et, ^{i}Pr).[66] Inspired by compound $[Dy(Cp^{ttt})_2][B(C_6F_5)_4]$, they employed a set of substituted cyclopentadienyl ligands to fine-tune structural features such as the Dy–Cp distances, Cp–Dy–Cp angles, and the vibrational environment around the metal center. The structural trends observed were consistent with the steric bulk of the substituents: bulkier ligands led to elongated Dy–Cp distances but more open Cp–Dy–Cp angles. This confirmed that even subtle changes within the Cp ring can alter the ligand field, potentially influencing the magnetization relaxation behavior. The first indication of such effects was seen in field-cooled/zero-field-cooled (FC/ZFC) measurements, which showed divergence in the temperature range of 28–65 K. Further *ac* susceptibility measurements revealed effective energy barriers of 1849, 2112, 1986, and 1919 K for these complexes, respectively. These values were successfully explained through magneto-structural correlations.

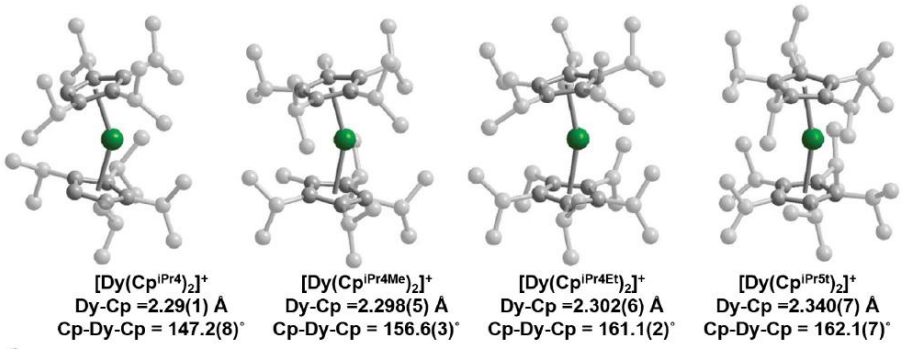

Figure 1.13: Cationic structures of Dy^{III} complexes. Color code: Dy^{III} and carbon in green and grey, respectively. Hydrogen atoms, counterions and positional disorder have been omitted for the sake of clarity.[66] Published by The Royal Society of Chemistry.

Among the four compounds, complex $[Dy(Cp^{iPr4H})_2][B(C_6F_5)_4]$ exhibits the most bent Cp–Dy–Cp angle and, correspondingly, the lowest U_{eff}. Introducing bulkier substituents at the 5-position of the Cp ligand leads to increased linearity. However, the researchers propose that beyond a certain point, the bond angle is no longer the primary factor influencing U_{eff}; instead, the Dy–Cp bond distance becomes more critical. Consistent with this, U_{eff} increases from compound $[Dy(Cp^{iPr4R})_2][B(C_6F_5)_4]$ (R = ^{i}Pr) to $[Dy(Cp^{iPr4R})_2][B(C_6F_5)_4]$ (R = Me) as the Dy–Cp distances decrease. Following this trend, compound $[Dy(Cp^{iPr4R})_2][B(C_6F_5)_4]$ (R = Me) shows open magnetic hysteresis loops at the highest temperatures among the series. Based on these findings, the authors suggest that future ligand designs should aim to strike a balance between wide Cp–Dy–Cp angles and short Dy–Cp bond lengths. Nonetheless, a deeper understanding of spin–phonon coupling is essential, especially since 100-second blocking temperatures are observed in a regime dominated by Raman relaxation processes. While the impact of molecular vibrations on Orbach relaxation can be assessed, predictive models for other under-barrier mechanisms remain necessary.

Building on the remarkable performance of Dy^{III} metallocenes, numerous new structures have been developed in recent years. For example, Mills *et al.* reported a novel sandwich complex in which one carbon atom in the ligand framework was replaced by a phosphorus atom, resulting in a bis-monophospholyl dysprosium compound.[67] This system exhibited magnetic hysteresis up to 48 K. Meng and colleagues explored exchange-coupled dinuclear systems by systematically varying the bridging ligands (CH_3^-, Cl^-, Br^- and I^-).[68] Additionally, isocarbonyl-ligated metallocene coordination polymers have been investigated,[69] along with dinuclear complexes that utilize fulvalene as a scaffold in place of traditional cyclopentadienyl rings.[70] The mixed-valence $Dy^{III}Dy^{II}$ dinuclear $[Dy_2I_3(Cp^{iPr5})_2]$ metallocene[71] compound has achieved a landmark performance with U_{eff} = 2347 K and T_B = 80 K, surpassing the liquid N_2 temperature. The uniaxial local symmetry stabilizes the collinearity of the local anisotropy axes and the strong 4f-radical coupling, resulting in significant separation from the first and higher excited states.[72] All this research highlights how such systems have revolutionized the field of SMMs. However, compounds with such low coordination are unstable and the need for more stable systems with similar magnetic properties arises.

Recognizing the critical role of symmetry in achieving high-performance lanthanide-based single-molecule magnets (SMMs), Tong and co-workers recently conducted a qualitative study using an effective charge model.[73] Their analysis revealed that certain symmetry groups such as C_n (with $n \geq 7$), S_8/D_{4d}, C_{5h}/D_{5h} and S_{12}/D_{6d} can significantly minimize transverse crystal field (CF) components, thereby suppressing QTM. It is important to note that these ideal symmetries are not among the 32 crystallographic point groups, making their perfect realization in crystalline systems unattainable. Nevertheless, molecular designs can strive to approximate these symmetries as closely as possible. Experimental observations, for example, those related to compounds

$[Dy(O^tBu)_2(py)_5][BPh]_4$ (O^tBu = tertbutoxide, py = pyridine),[74] [Dy(bbpen)Br] (H_2bbpen=*N*,*N*'-bis(2hydroxybenzyl)-*N*,*N*-bis(2-methylpyridyl) ethylenediamine))[75] and $[Dy(Cy_3PO)_2(H_2O)_5]Br_3 \cdot 2(Cy_3PO) \cdot 2H_2O \cdot 2EtOH$ (Cy_3PO=tricyclohexyl phosphine oxide),[76] support these theoretical predictions (see below for a detailed description of their properties).

To effectively suppress transverse CF components and QTM, the magnetic anisotropy axis of the $\pm M_J$ ground doublet must align with the principal symmetry axis of the molecule. When this condition is met, the anisotropy axes of the ground and low-lying excited states remain nearly parallel. As a result, magnetic relaxation bypasses the first excited state and proceeds through higher-energy states, contributing to increased U_{eff} values. This behavior is commonly observed in high-performance Dy^{III}-based SMMs. For instance, in compound $[Dy(O^tBu)_2(py)_5][BPh]_4$,[74] the anisotropy axes of the three lowest excited states are nearly collinear with that of the ground state, leading to relaxation through a tightly grouped set of states near the fourth excited level. It is also worth emphasizing that the symmetry of the charge distribution around the trivalent lanthanide ion plays a more crucial role in defining the overall symmetry relevant to magnetic behavior than the molecular geometry itself.

Addressing the requirements of high-temperature performance and thermal air and humidity stability, mononuclear Dy^{III} SMMs with D_{5h} geometry hold a fair position, displaying in many cases stability against these factors with U_{eff} and T_B values as high as 1162 K[77]and 36 K,[78] respectively. Although some recent mononuclear Dy^{III} SMMs with D_{5h} geometry have been shown to be air-sensitive, the majority are stable.[79] These D_{5h} systems typically feature either pentagonal bipyramidal geometries or incorporate strongly electron-donating ligands, such as fluoride ions, which help stabilize an axial

ground state that is well-separated from the excited states.[80] Additionally, the role of the spin-vibrational coupling in designing high-performance pentagonal bipyramidal Dy^{III} SMMs has been recently unravelled using a combination of Density Functional Theory (DFT) and Complete Active Space Self- Consistent Field (CASSCF) calculations.[81]

In general, D_{5h} systems feature strong oxygen-donor ligands at the axial positions, such as phenoxido groups, phosphine oxides, or siloxides. In contrast, the equatorial positions of the pentagonal plane are typically occupied by neutral donor atoms from solvents—like tetrahydrofuran or pyridine—or by weakly coordinating macrocyclic or non-macrocyclic ligands. A fascinating mononuclear Dy^{III} SIMs with D_{5h} symmetry is $[Dy(Cy_3PO)_2(H_2O)_5]Br_3 \cdot 2(Cy_3PO) \cdot 2H_2O \cdot 2EtOH$ (Cy_3PO=tricyclohexyl phosphine oxide) (Figure 1.14, left).[76] The energy barriers can reach to 543(2) K, along with an optimal magnetic hysteresis temperature up to 20 K for its diluted derivative. This provides an illuminating insight into the wide range of possibilities and potential that symmetry rules, which can achieve for molecular magnetism.

Another important Dy^{III} SIMs with D_{5h} symmetry is [Dy(bbpen)Br] (H_2bbpen=*N*,*N*'-bis(2hydroxybenzyl)-*N*,*N*-bis(2-methylpyridyl)ethylenediamine)), which exhibits an U_{eff} value of 1025 K and a hysteresis loop of up to 14 K (Figure 1.14, right).[75] This work demonstrates that the combination of increasing axial field and decreasing transverse field in D_{5h} symmetry are beneficial to obtain high performance SMMs. Within this family, another cutting-edge example is $[Dy(O^tBu)_2(py)_5][BPh]_4$ (O^tBu = tertbutoxide, py = pyridine) (Figure 1.14, center).[74] This complex presents an energy barrier to magnetic relaxation of U_{eff} = 1815(1) K and a blocking temperature of T_B = 14 K. In all these systems, the axiality is provided by

strong oxygen donor atoms in the apical positions while the equatorial planes are occupied by less electron donating atoms with subsequent longer bond distances. Moreover, even though usually Orbach relaxation pathways occur through the first excited state (which could be better described as TA-QTM), the proper ligand field in those compounds provokes relaxation pathways involving higher excited states achieving high effective energy barriers.

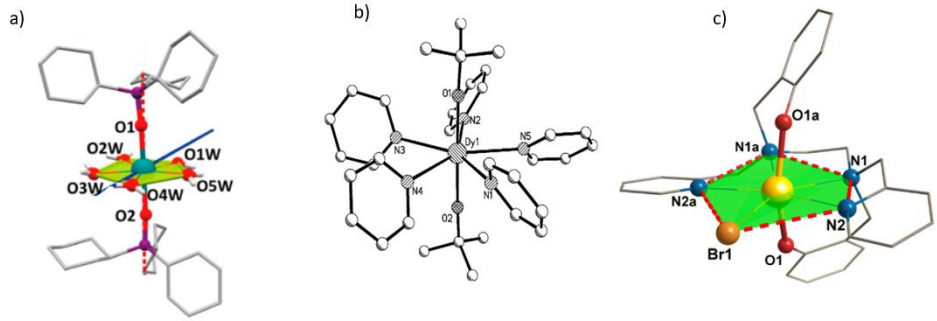

Figure 1.14: Crystal structures of a) $[Dy(Cy_3PO)_2(H_2O)_5]^{3+}$, b) $[Dy(OtBu)_2(py)_5]^{+}$ and c) [Dy(bbpen)Br].[74, 75, 76]

1.1.3.1.1 Phosphine oxide based Dy^{III} SIMs

There are about thirty examples of mononuclear Dy^{III} SMMs with D_{5h} geometry, but those employing axial bulky phosphine oxide type ligands (high electron density) and weak donor equatorial ones (e.g., water),[74, 82-90] are relatively scarce. These D_{5h} based SMMs represent a highly efficient approach to constructing new high-performance SMMs. Apart from the outstanding$[Dy(Cy_3PO)_2(H_2O)_5]Br_3\cdot 2(Cy_3PO)\cdot 2H_2O\cdot 2EtOH$ (Cy_3PO=tricyclohexyl phosphine oxide) compound mentioned before,[74] several phosphine oxide based Dy^{III} complexes have been prepared (Table 1).

Table 1. Pentagonal-bipyramidal Dy^{III} complexes with apical phosphine oxide ligands.

Compound	T_B (K)	U_{eff} (cm^{-1}) (H_{dc})	Ref.
$[Dy(OP^tBu(NH^iPr)_2)_2(H_2O)_5][I_3]\cdot(OP^tBu(NH^iPr)_2)_2\cdot H_2O$	12	651.0 K	[82]
$[Dy(Cy_3PO)_2(H_2O)_5]Cl_3\cdot(Cy_3PO)\cdot H_2O\cdot EtOH$[a]	11	472 K	[74]
$[Dy(Cy_3PO)_2(H_2O)_5]Br_3\cdot 2(Cy_3PO)\cdot 2H_2O\cdot 2EtOH$[a]	11	543 K	[74]
$[Dy(CyPh_2PO)_2(H_2O)_5]Br_3\cdot 2(CyPh_2PO)\cdot EtOH\cdot 3H_2O$[a]	19	508 K	[83]
$[Dy(OPCy_3)_2(H_2O)_5](CF_3SO_3)_3\cdot 2OPCy_3$[a]	8.5	562 K	[84]
[(L)Dy(Cy_3PO)Cl] [a,b]		204 K (1 kOe)	[85]
[(L)Dy(Ph_3PO)Cl] [a,b]		241 K (1.5 kOe)	[86]
[(L)Dy ($Cy_3PO)_2$]$\cdot[BPh_4]$ [a,b]		51 K (0.75 kOe)	[87]
$[Dy(L^{CH_3})(Cy_3PO)_2]ClO_4\cdot CH_3CN$[c]		318	[88]
$[Dy(L^{2(t\text{-}Bu)})(Ph_3PO)_2]ClO_4\cdot 0.63C_2H_5OH$[d]		323	[88]
$[Dy(L^{OCH_3})(Ph_3PO)_2]ClO_4\cdot 2H_2O$[e]		319	[88]
$[Dy(H_2O)_5(HMPA)_2]Cl_3\cdot HMPA\cdot H_2O$[f]	7	460 K	[89]
$[Dy(H_2O)_5(HMPA)_2]I_3\cdot 2HMPA$ [f]	8	600 K	[89]
$[Dy(OPAd_2Bz)_2(H_2O)_4Br]Br_2\cdot 4THF$[g]	14	427.7 K	[90]

[a]Cy:cyclohexyl;[b]H_2L=2,6-diacetylpyridine *bis*-benzoylhydrazone;[c]L^{CH_3} =[2,6-diacetylpyridinebis(acetylhydrazone)]$^{2-}$;[d]$L^{2(t\text{-}Bu)}$ =[2,6-diacetylpyridinebis(3,5di-*tert*-butylbenzoylhydrazone)]$^{2-}$; [e]L^{OCH_3} = [2,6-diacetylpyridine bis(4-methoxybenzoylhydrazone)]$^{2-}$; [f]HMPA = hexamethylphosphoramide; [g]$OPAd_2Bz$: di(1-adamantyl)benzylphosphine oxide

On the one hand, the compound $[Dy(OP^tBu(NH^iPr)_2)_2(H_2O)_5][I_3]$ exhibits the highest U_{eff} = 651 K among these phosphine oxide based Dy^{III} complexes, followed by the $[Dy(H_2O)_5(HMPA)_2]I_3$,

$[Dy(OPCy_3)_2(H_2O)_5](CF_3SO_3)_3$, $[Dy(Cy_3PO)_2(H_2O)_5]Br_3$ and $[Dy(CyPh_2PO)_2(H_2O)_5]Br_3$ compounds, which show U_{eff} values of 600, 562, 543 and 508 K, respectively. On the other hand, the compound $[Dy(CyPh_2PO)_2(H_2O)_5]Br_3$ exhibits the highest T_B value (19 K), followed by $[Dy(OPAd_2Bz)_2(H_2O)_4Br]Br_2$ (14 K) and $[Dy(OP^tBu(NH^iPr)_2)_2(H_2O)_5][I_3]$ (12 K).

The $[Dy(OP^tBu(NH^iPr)_2)_2(H_2O)_5][I_3]$ compound[82] presents the highest U_{eff} value (600 K) and also a considerable T_B (12 K) among the reported phosphine oxide based Dy^{III} compounds. The asymmetric part of the unit cell contains a single Dy^{III} ion in a pseudo-D_{5h} symmetry with the five equatorial coordination sites being occupied by water molecules and the two axial coordination sites being occupied by the phosphonic diamide ligands coordinated to the dysprosium through the phosphoryl oxygen (P=O) (Figure 1.15). The axial Dy–O bond lengths (Dy–O1(P) 2.208(2) Å and Dy–O2(P) 2.203(2) Å) are notably shorter than the five equatorial Dy–O(water) distances, which range from 2.355(3) to 2.375(3) Å. This difference suggests stronger coordination by the phosphonic diamide ligands. Additionally, the nearly linear trans O1–Dy–O2 angle of 175.14(9)° along the axial axis, combined with equatorial O–Dy–O angles ranging from 70.43(9)° to 73.52(10)° (totaling 360.31°), clearly indicates that the metal center adopts a pseudo-D_{5h} geometry. The shortest Dy···Dy distance in the lattice is 10.819 Å, indicating that Dy^{III} ions are well isolated.

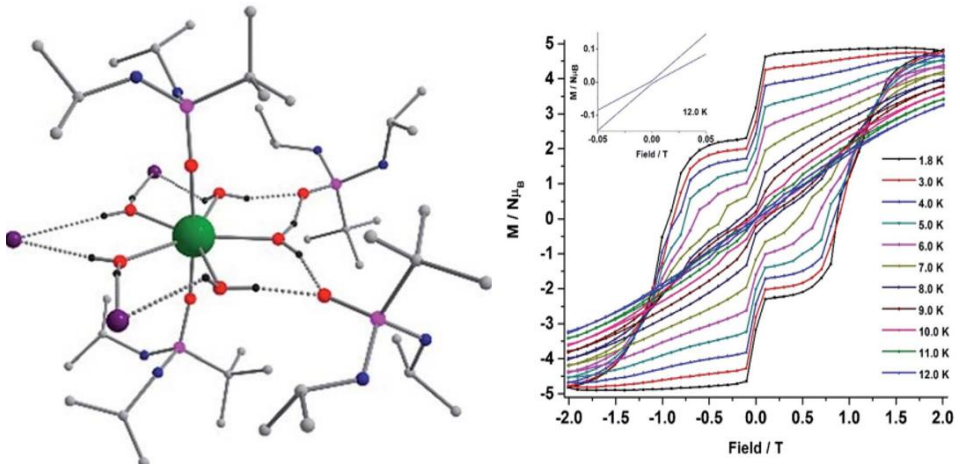

Figure 1.15: (left) Molecular structure of $Dy(OP^tBu(NH^iPr)_2)_2(H_2O)_5][I_3]$. Lattice water molecule and most of the H-atoms have been omitted for clarity. (right) The field-dependent magnetization data were collected at a sweep rate of 0.0018 $T.s^{-1}$ sweeping the field from +2 T to - 2T and back to +2 T in the temperature range 1.8–12.0 K. (Inset; expansion of the M–H curve at 12.0 K.)[82]

Another representative example of this family is the $[Dy(H_2O)_5(HMPA)_2]I_3$ compound, with high U_{eff} and T_B values of 600 K and 8 K, respectively.[89] In this complex, two HMPA ligands occupy the axial positions, while five water molecules coordinate equatorially (Figure1.16). The asymmetric unit comprises one Dy^{III} complex, three iodide anions, and two co-crystallized HMPA molecules. The axial Dy–O bond lengths are 2.202(4) and 2.208(4) Å, whereas the equatorial Dy–O distances range from 2.343(4) to 2.375(4) Å. The nearly linear axial O–Dy–O angle is approximately 178°, and the equatorial O–Dy–O angles span 70.91(14)° to 73.18(14)°. Furthermore, crystal packing analysis shows that the Dy···Dy separation is 11.767 Å and only intramolecular hydrogen bonding is present. In this work, *ab initio* calculations, performed through a stepwise elimination of molecular fragments to create a series of model complexes, demonstrate that the secondary coordination sphere significantly influences the magnetization reversal barrier.

The results also predict that removing outer-sphere molecules and anions would further enhance this barrier.

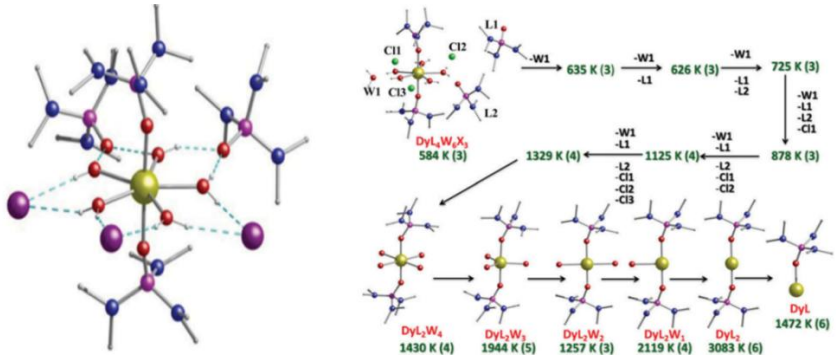

Figure.1.16: (left) Molecular structure of $[Dy(H_2O)_5(HMPA)_2]I_3 \cdot 2HMPA$. Colour code: Dy, gold; O, red; N, blue, P, pink; Cl, green; I, purple. Hydrogen atoms are omitted for clarity, except the H atoms of the equatorial water ligands and only one of the two crystallographically unique Dy units is shown. (right) *Ab initio* SINGLE_ANISO computed U_{cal} values (in K, green text) for all the models created by stepwise removal of fragments for $[Dy(H_2O)_5(HMPA)_2]Cl3 \cdot HMPA \cdot H_2O$. The bold number in brackets for each model gives the Kramers doublet through which relaxation is expected (ground state = KD (1); first excited state = KD (2) etc.) [89]

$[Dy(Cy_3PO)_2(H_2O)_5]Br_3$ and $[Dy(CyPh_2PO)_2(H_2O)_5]Br_3$ also exhibit quite good SIM behaviour, with U_{eff} values of 543 K and 508 K, respectively, and blocking temperatures of 11 K and 19 K, respectively.[74, 83] As mentioned above, the diluted analogue of $[Dy(Cy_3PO)_2(H_2O)_5]Br_3$ exhibited a T_B of 20 K. In these compounds two $OPCy_3$ or $CyPh_2PO$ ligands occupy the axial positions, whereas the five coordinated water molecules are located in the equatorial plane defining an almost regular pentagon. Finally, the $[Dy(OPAd_2Bz)_2(H_2O)_4Br]Br_2$ compound also presents a quite good SIM behaviour, with a T_B value of 14 K and U_{eff} of 427.7 K. Two bulky $OPAd_2Bz$ ligands occupy the axial positions, whereas four water molecules and one bromide ion are in the equatorial plane (Figure 1.17). This compound was recently syntethized in our group.

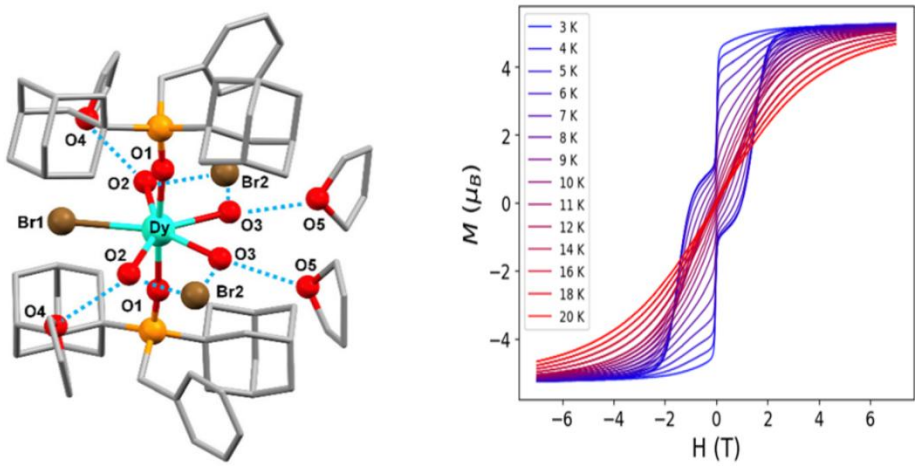

Figure. 1.17: (left) Perspective view of the molecular structure of [Dy(OPAd$_2$Bz)$_2$(H$_2$O)4Br]Br$_2$·4THF. Code colours: dysprosium (cyan), oxygen (red), bromide (brown), phosphorus (orange), and carbon (grey). Hydrogen atoms are omitted for clarity. Blue dashed lines indicate hydrogen bond interactions. (right) Magnetic hysteresis measurements/hysteresis plot at a sweep rate of 20 mT s^{-1}.[90]

Thus, experimental and theoretical studies carried out on this type of compounds have led to the following conclusions on how and why these compounds have these extraordinary properties and what are the guidelines to follow to obtain highly efficient Dy^{III} SIMs:

I. The axial ligand donor atoms must have a high charge density.
II. The absence of ligands in the equatorial plane allows the ligand donor atoms in axial positions to move closer together and generate a larger axial field.
III. Ligands in axial positions must be bulky to avoid coordination of ligands in equatorial positions.

IV. Bulky substituents on ligands and anions give rise to diffuse charges, leading to weak intermolecular interactions and low-energy vibrations (acoustic phonons).

Points I-III lead to a very large M_J level splitting and very high energy barriers, while point IV lead to weak two-phonon couplings, which slows down the relaxation through the Raman mechanism. Thus, two of the most significant areas for the SIMs development are:

a) To reveal the connection between Raman-type relaxation and structure.

b) To understand in depth the factors that generate QTM.

In short, to develop strategies to improve the lifetime of these molecules.

1.1.4. Single-ion magnets based on hetero-trinuclear Zn^{II}-Ln^{III}-Zn^{II} complexes

Another type of coordination compounds that can present SIM behaviour are the hetero-trinuclear Zn^{II}-Ln^{III}-Zn^{II} complexes.[91] These kinds of complexes, from the point of view of molecular magnetism, can be considered as mononuclear compounds because of the diamagnetic nature of the Zn^{II} ions. In addition, the diamagnetic nature of Zn^{III} ion presents other advantages in the preparation of these SIM because; (i) it contributes to reduce the fast QTM as decrease the intermolecular interactions (stabilisation sublevels); (ii) it lead to an axial ligand field that increases the magnetic anisotropy and, in principle, the effective energy barrier for magnetisation reversal.[92] Moreover, the presence of Zn^{II} metal ions in these complexes can give rise to others interesting chemical and physical properties, such as luminescence, obtaining multifunctional SIMs with potential applications in diverse fields such as high-

density data storage, quantum computing, sensors, imaging, batteries and so on.[93]

The most common ligands used for the preparation of these complexes are the Schiff-Base type ligands.[94] Schiff bases ligands possess two different metal-binding sites in accordance with the soft-hard acid-base principle, one being specific for d-metal ions and the other for f-metal ions. Usually, they have two N_2O_2 cavities or one N_2O_2 and one O_4 cavity. The Zn^{II} metal ions exhibit the capacity to bond both oxygen and nitrogen atoms from the Schiff base ligands and occupy the internal cavity N_2O_2. The Zn^{II} ions typically exhibit distorted octahedral or pentacoordinate geometries where the fifth and sixth position can be occupied by water molecules or halide ions (bromide or chloride) which helps to stabilize the overall structure of the complex. In the case of Ln^{III} ions, generally, coordinate to the oxygen atoms, that is, the external O_4 cavity and can display more complex coordination environment with higher coordination numbers. With this arrangement, the complex often features a central Ln^{III} ion bridged by two Zn^{II} ions through the oxygen atoms belonging to the Schiff-Base ligands creating a stable structure that incorporates both types of metal ions in a single complex.

It is well known that the SIM behaviour depends on the character and strength of magnetic anisotropy which, at the same time, depends on the coordination geometry and negative charge distribution around Ln^{III} ions. Therefore, the design of the Schiff-base ligands is crucial for the arrangement of the Zn^{II} and Ln^{II} ions which is determining for the electronic distribution of the Ln^{III} ions. In this sense, the electron density and spatial arrangement of the oxygen donor atoms coordinated to the Ln^{III} play a decisive role in determining the SIM behaviour of these complexes.[95] The phenoxyl oxygen donor atoms possess larger negative charges than aldehyde-oxygen and methoxyl-oxygen

donor atoms within the ligand so, the strong easy-axis anisotropy could be achieved by placing the phenoxo oxygen atoms in positions opposite of the Ln^{III} ion.[96] Thus, this disposition for oblate lanthanide ions would create an axial crystal field with negatively charged oxygen atoms favouring the stabilization of the electronic density of lanthanide ions. Therefore, the lanthanide ions, ligands and coordination geometry are all crucial factors in determining the SIM behaviour in these trinuclear complexes.

Although the Ln^{III} ion par excellence to exhibit SIM behaviour is Dy^{III} ion (see next section), there are some examples of trinuclear Zn^{II}-Ln^{III}-Zn^{II} containing other Ln^{III} ions that present SIM behaviour. Kajiwara and co-workers synthesised, with a Schiff-base ligand formed by a condensation reaction between ethylenediamine and o-vanillin, several linear Zn^{II}-Ln^{III}-Zn^{II} complexes (figure 1.18) exhibiting field-induced SIM behaviour (Ln^{III} = Tb^{III}, Er^{III}, Yb^{III}, Ce^{III}, Nd^{III}).[97] Within the complexes, the Ln^{III} ions are deca-coordinated and the coordination environment is formed by four equatorial oxygen donors atoms from the methoxy groups and four axial oxygen donors atoms from the phenoxo groups belonging to the Schiff-base ligands and, two oxygen atoms from the acetate or nitrate anions. The SIM behaviour of these complexes is related with the connection between the ligand field anisotropy and the shape of the electronic distribution of the ground sublevels. In these complexes, the negative charge of the phenoxo oxygen atoms is the largest among the oxygen donors atoms and they are located at the axial positions of the Ln^{III} ions. In the case of oblate-type ions, this disposition stabilises the sublevels with a maximum |Jz| value, thus leading to axial anisotropic ground states that favours the SIM behaviour.

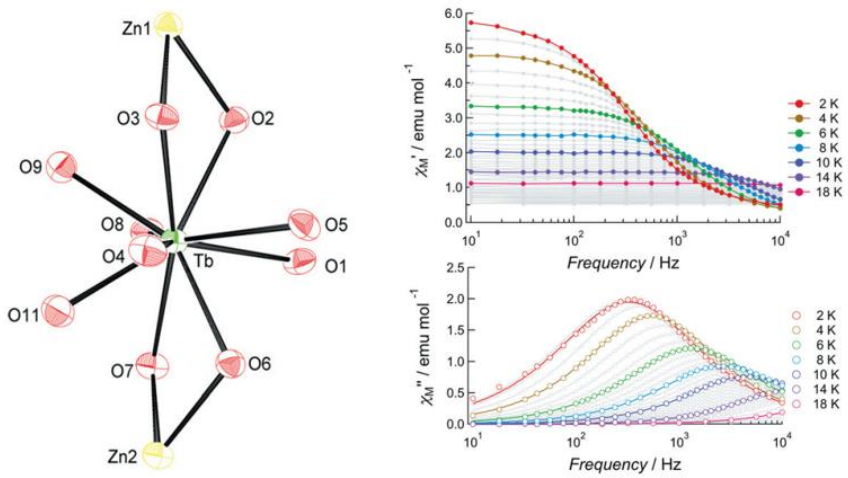

Figure 1.18: (left) ORTEP representation of the coordination environment around the Tb^{III} ion. Colour code: green Tb, yellow Zn, red O. (right) Frequency dependence of the *ac* susceptibility data for Tb^{III} complex measured under a 1000 Oe *dc* field. The closed circles and open circles represent the in-phase (χ_M') and out-of-phase (χ_M'') components of the molar *ac* susceptibilities, the solid lines for the χ_M'' data is the fitting to the generalized Debye equation.[97a]

1.1.4.1 Hetero-trinuclear Zn^{II}-Dy^{III}-Zn^{II} single-ion magnets

In general, the magnetic anisotropy, also depends on the specific lanthanide ion belonging to the coordination compound. Among Ln^{III} ions, the Dy^{III} ion plays a crucial role in achieving strong anisotropy due to its large angular momentum and strong spin-orbit coupling. In addition, the Zn^{II} ions and the rational ligand design can improve the SIM properties by modifying the coordination around the Dy^{III} ions, thus modulating the magnetic anisotropy and, therefore, the energy barrier. Accordingly, several studies report Zn^{II}-Dy^{III}-Zn^{II} complexes that exhibit SIM behaviour and good effective energy barrier values.[98]

Colacio and collaborators synthesised three Zn^{II}-Dy^{III}-Zn^{II} complexes from a Schiff-base ligand (figure 1.19).[95a] Within the complexes, the Dy^{III} ions

are nonacoordinate to eight oxygen atoms from the two ligands and to a water molecule while the Zn^{II} ions are pentacoordinate, linked to the N_2O_2 cavity from the ligand, and the apical position of the coordination sphere occupied by a water molecule (**Zn-OH$_2$**) or bromide (**Zn-Br**) or chloride (**Zn-Cl**) ions. These three complexes behave as SIM in absence of *dc* field with a significant QTM. With an external field of 1000 Oe to eliminate fully or partially the QTM, the energy barrier values are 128.6 K for **Zn-OH$_2$**, 214.7 K for **Zn-Br** and 202.4 K for **Zn-Cl**. In these complexes, the two pairs of largely negatively charged phenoxido groups with short Dy-O bonds are disposed on opposed sides of the Dy^{III} ion, which creates a strong crystal field that leads to these large energy barriers. The small value of the U_{eff} value in **Zn-OH$_2$** compared with **Zn-Cl** and **Zn-Br** could be explain because Dy^{III} atom in **Zn-OH$_2$** presents a larger deviation from the ideal geometries than complexes **Zn-Cl** and **Zn-Br** which are more symmetric. Moreover, the experimental results and the DFT calculations support that the electronic effects of the halide co-ligands coordinated to the Zn^{II} ions increase the energy barrier with respect to the coordinated water co-ligand.

In line with this, Panja and collaborators prepared also three Zn^{II}-Dy^{III}-Zn^{II} complexes from a Schiff-base ligand.[95b] In the complexes, the coordination environment of Dy^{III} ions is identical. The DyO_8 coordination sphere is formed by the outer O_2O donor sites from two ligands, leaving one methoxy-oxygen atom non-coordinated from each ligand, and two water molecules. However, there exist two important differences in these complexes: (i) the Zn^{II} coordination sphere which is formed, in all cases, by the inner N_2O_2 cavity, but the apical position is occupied by different halide ions (Cl (**Cl**), Br (**Br**) and I (**I**)); (ii) the counteranions in the structure (Cl^- (**Cl**) or NO_3^- (**Br, I**)). The crystal packing reveals that there are hydrogen bonds between the coordinated water molecules and solvent water molecules (**Cl**) or nitrate anions (**Br, I**).

These two differences cause important differences in the magnetic behaviour.

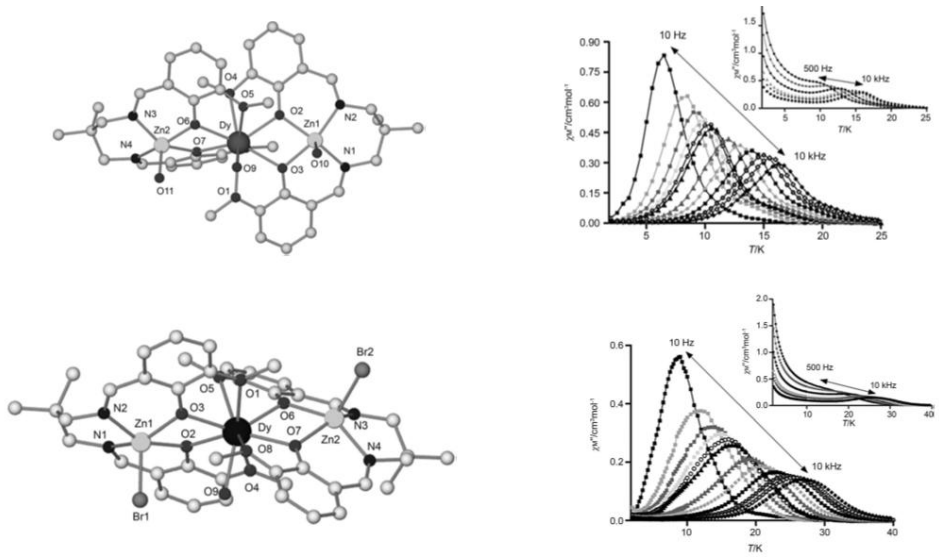

Figure 1.19: (left) Molecular structure of compounds **Zn-OH$_2$** (top) and **Zn-Cl** (bottom). (right) Temperature dependence of out-of-phase χ_M'' component of the *ac* susceptibility for complexes **Zn-OH$_2$** (top) and **Zn-Cl** (bottom) measured under zero (insets) and 1000 Oe applied *dc* fields.[95a]

In fact, the complex **Cl** present slow relaxation of the magnetisation with well-defined maxima in the χ_M'' signals while in complexes **Br** and **I** only the tails are observed. Therefore, only the complex containing Cl in the coordination sphere of the Zn^{II} ions and as a counteranion in the structure exhibit SIM behaviour above 2 K. This is due, in one hand, to the significant influence of the Zn^{II} coordination environment on the magnetic anisotropy and, on the other hand, to the intermolecular interactions involving the counterions which are responsible for the fast relaxation of magnetization in these compounds.

Ultimately, in these two examples is highlighted the impact of peripheral ligands coordinated to the Zn^{II} ions for the design of efficient Zn^{II}-Dy^{III}-Zn^{II} SIMs, which imply a modification of the coordination environment around the

Dy^{III} ion leading to a significant increase in the energy barrier for magnetisation reversal and, also the influence of the counteranions on the intermolecular interactions which cause a fast relaxation of the magnetization and, consequently, no observation of the SIM behaviour.

On the other hand, the Dy^{III} ions in these hetero-trinuclear complexes are, usually, between octa- and deca-coordinated. However, Tong and collaborators have published one Zn^{II}-Dy^{III}-Zn^{II} complex in which the Dy^{III} ion is hexa-coordinated with a distorted octahedral coordination geometry (S Shape values of 1.91 and 1.29).[94b] This complex exhibit slow relaxation of the magnetisation at both 0 and 1000 Oe external fields with effective energy barriers (U_{eff}) of 324 K and 565 K, respectively. These U_{eff} values are larger than those observed for other Zn^{II}-Dy^{III}-Zn^{II} complexes in which the Dy^{III} ion is octa- nona- or deca-coordinated. Again, it is proved the importance of the coordination geometry around the Dy^{III} ion in the crystal field splitting and, therefore, in the SIM behaviour for oblate Ln^{III} ions.

Moreover, these energy barriers are also larger compared with another hexa-coordinated Dy^{III} ion in a Zn^{II}-Dy^{III}-Zn^{II} complex published also by these authors (U_{eff} = 64 K).[98a] The improvement in the U_{eff} could be come from the designing of a ligand with a rigid functional group that reinforce the structural rigidity of the whole molecule which has influence on the molecular vibrational modes and, consequently, in the SIM properties.

1.1.4.1.1. Hetero-trinuclear Zn^{II}-Dy^{III}-Zn^{II} single-ion magnets with Mannich bases ligands

As mentioned above, the ligand design is crucial to obtain Zn^{II}-Dy^{III}-Zn^{II} complexes with SIMs behaviour and large energy barrier values. The most commons ligands used to obtain this type of complexes are the Schiff-base ligands, however, the Mannich base ligands could also be good candidates to

prepare heteronuclear Zn^{II}-Dy^{III}-Zn^{II} SIMs with large energy barrier values. The Mannich base ligands also possess an inner cavity N_2O_2 and an outer cavity O_2O_2 which facilitate complexation with the Zn^{II} ion and Ln^{III} ion, respectively and, in addition, present two important advantages with respect to the Schiff base ligands. The first is that these ligands show greater flexibility and, therefore, greater ability in coordinating metals with different ionic radii. The second one is that they do not contain hydrogen atoms bonded to amino groups, which could eventually form intermolecular hydrogen bonds and mask magnetic properties coming from the isolated complexes (fast relaxation of the magnetization).

In view of these considerations, Colacio and co-workers synthesized a Mannich base ligand containing bridging phenoxido groups and prepared Zn^{II}-Dy^{III}-Zn^{II} coordination compounds.[92, 96a, 99] The first complex synthesised was $[ZnCl(\mu\text{-}L)Dy(\mu\text{-}L)ClZn][ZnCl_3(CH_3OH)]\cdot 3CH_3OH$ (**1**).[96a] Within the cationic unit, the Zn^{II} ions exhibit a distorted square-pyramid coordination geometry with the apical position occupied by a chloride atom while the Dy^{III} ion exhibits a DyO_8 coordination sphere, which is formed by four phenoxo and four aldehyde oxygen atoms from the ligand, leading to a compressed square-antiprism geometry (figure 1.20). The complex exhibits, in a zero *dc* field, slow relaxation of the magnetization with a significant QTM and, SIM behaviour with a large effective energy barrier value of 140 K. These good SIM properties are due to an almost pure $M_J = \pm 15/2$ ground state with a marked axiality and with negligible transverse components which is caused by the arrangement of the four phenoxido oxygen atoms (those having the highest electron density and the shortest Dy–O distances) placed by couples in opposite sides of the Dy^{III} ion. Moreover, the QTM is suppressed with the application of a small external *dc* field and the energy barrier increases until a value of 150 K.

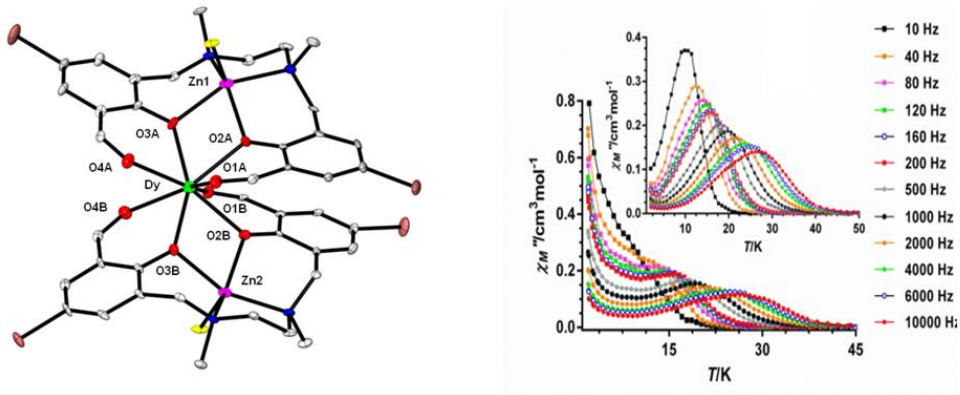

Figure 1.20: (left) Molecular structure of $[ZnCl(\mu\text{-}L)Dy(\mu\text{-}L)ClZn]^{+}$. Hydrogen atoms, the $[ZnCl_3(CH_3OH)]^{-}$ counteranion, and solvent methanol molecules have been omitted for the sake of clarity. (right) Temperature dependence of out-of-phase χ_M'' component of the *ac* susceptibility measured under zero and 1000 Oe (inset) applied *dc* fields. [96a]

After, they replaced the counteranion of this complex changing the $[ZnCl_3(CH_3OH)]$ by PF_6, then obtaining the compound $[ZnCl(\mu\text{-}L)Dy(\mu\text{-}L)ClZn]$ PF_6 (**2**).[92] In this compound exists a very important difference with respect to **1**, the DyO_8 coordination geometry that, in this case, is closer to the square antiprism and presents a different distribution of the phenoxide oxygen atoms around the Dy^{III} ion. At zero *dc* field, the complex exhibits slow relaxation of the magnetization and SIM behaviour with an effective energy barrier for the reversal of the magnetization of 268 K. However, there exists fast relaxation of the magnetization via a QTM mechanism. Then, when the *ac* measurements were performed in the presence of a small external *dc* field, as expected, the energy barrier increases until a value of 320 K.

As it can be seen, the energy barrier for **2** is approximately twice that of **1**. The increase of the energy barrier is due to the different distribution of the phenoxide oxygen atoms around the Dy^{III} ion (in **2** the phenoxide oxygen atoms are closer to each other and the Zn–Dy–Zn angle is much smaller) caused by an C_2 axis. The presence of the C_2 axis imposes collinearity of the

anisotropic axes of the two lowest KDs, so that the thermal activated relaxation is suppressed via the first excited KD and takes place via the second excited state, giving rise to a dramatic increase in the effective energy barrier.

Finally, Colacio and collaborators change, in this type of complexes, the coordination sphere of the Zn^{II} ions, obtaining six new compounds of general formula of [ZnX(μ-L)Dy(μ-L)XZn]Y·nS (X = Cl, Br, I and N_3, Y = counteranion, S = crystallization solvent molecules).[99] The structures of the complexes are very similar but differ in the coligands coordinated to the Zn^{II} ions and/or the counteranions (figure 1.21). The change of the coligand and counteranions leads to different dispositions of the phenoxo and aldehyde oxygen atoms around Dy^{III} ion in the DyO_8 coordination environment (figure 1.21, right). These complexes, under a zero-external dc field exhibit SIM behaviour with the existence of fast QTM that give rise to effective energy barriers that are in the 144–170 K range. The application of a small external field leads to slightly higher U_{eff} values (in the 147–178 K range). Once again, the disposition of the oxygen atoms (phenoxo and aldehyde) around the Dy^{III} ions, affected by the coligands and counteranions that are present in the Zn–Dy–Zn complex, is the responsible of the large energy barrier for magnetization reversal. When the atoms with the largest negative charges (shortest Dy–O distances) exhibit very close Dy–O distances and are located at the same side of the upper and lower planes, the SIM magnetic properties of these complexes seem to improve.

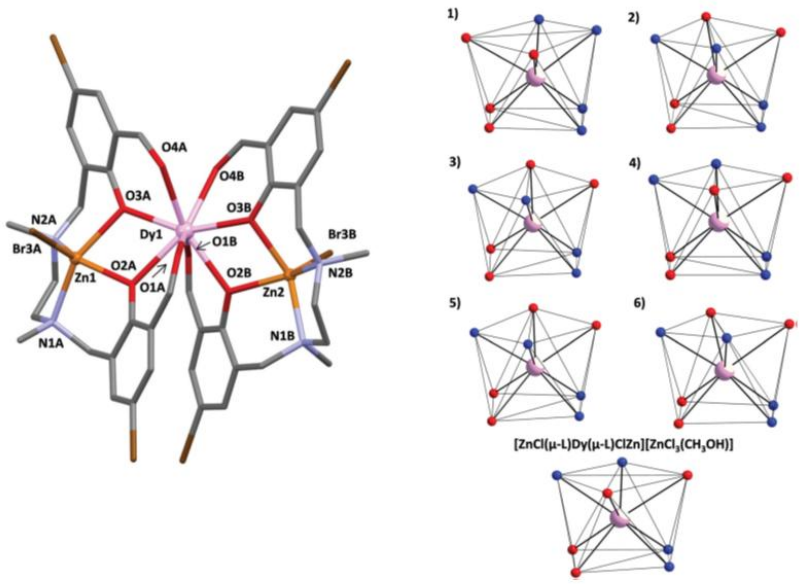

Figure 1.21: (left) Perspective view of the structure. Colour code: N = blue, O = red, C = grey, Br = brown, Zn = orange, Dy = pink. H atoms, counteranions and crystallization molecules have been omitted for the sake of clarity. (right) Square antiprism DyO_8 coordination sphere in the sis complexes and in **1**. Colour code: Dy = pink, $O_{aldehyde}$ = red, $O_{phenoxo}$ = blue.[99]

1.1.5 Multifunctional materials

Multifunctional materials are defined by the combination of various distinct physical properties within a single material, which offers significant benefits for a range of advanced applications in various fields.[100] Lanthanide complexes are at the heart of research into multifunctional materials due to their potential to combine different physical properties within a single material, such as magnetic, optical, chirality, electrical and mechanical properties,[101] resulting in the creation of materials with advanced functionalities that have numerous potential applications, including sensitive luminescent thermometers, data storage devices, solid electrolytes for fuel cells, multifunctional sensors, optomagnetic devices, optoelectronic devices, and smart devices capable of

performing multiple tasks simultaneously. The following section will discuss key types of multifunctional materials that involve lanthanide ions.[28, 102, 103]

1.1.5.1 Multifunctional Single-Molecule Magnets (SMMs)

1.1.5.1.1 Luminescent SMMs

The combination of magnetic and luminescent properties is the most common synergy for lanthanide single molecule magnets (SMMs). As previously noted, the unquenched spin-orbit coupling in Ln^{III} ions originates from their deeply embedded 4f valence electrons. The shielding of 4f electrons by the filled 5s and 5p orbitals makes the luminescence and magnetic properties intrinsic to the lanthanide ions. These 4f electrons are relatively insensitive to their surrounding coordination environment, resulting in only slight changes to the energy level spectrum of each Ln^{III} ion.

Consequently, the absorption and emission bands are very narrow, producing exceptionally pure colors.[104] They also exhibit long-lived excited states, and/or pronounced pseudo-Stokes shifts. This property makes luminescent lanthanides suitable for time-gated or time-resolved live-cell and in vivo imaging.[104] Each emission band serves as a distinct fingerprint for the specific ion. Across the lanthanide series, these emission bands appear either in the visible spectrum (e.g., Tm^{III}, Tb^{III}, Dy^{III}, Eu^{III}, and Sm^{III}; Figure 1.22a) or in the near-infrared range (e.g., Yb^{III}, Nd^{III}, and Er^{III}; Figure 1.22a).

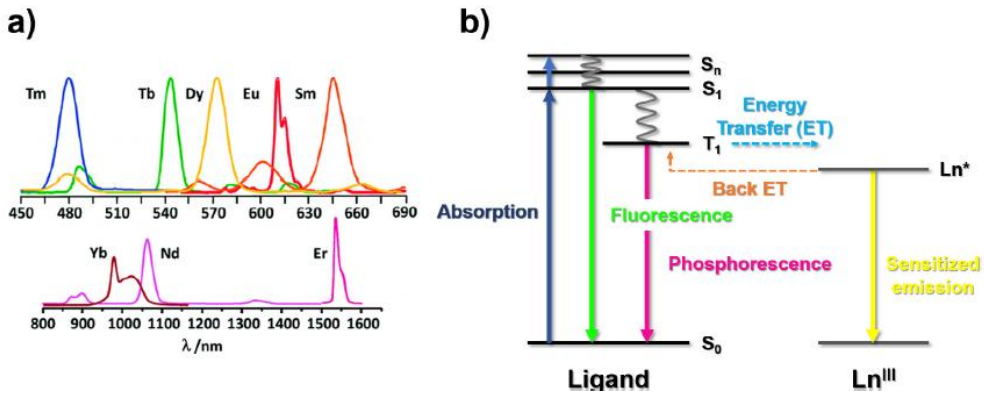

Figure. 1.22: a) Emission spectra of tris-β-diketonate compounds. b) Simplified Jablonsky diagram. [28]

A key challenge for 4f-4f transitions is their classification as parity forbidden according to the Laporte rule. This leads to low intensity emissions and a low radiative transition probability. Moreover, directly exciting Ln^{III} ions is generally inefficient because of their low absorption coefficients (ε). This means that only a small fraction of the incident photons are actually captured by the Ln^{III} ion to initiate the transition to an excited state. One strategy to overcome the limitations of 4f-4f transitions is the so-called antenna effect.

This is necessary to significantly enhance their luminescent properties by using ligands with broad, intense absorption bands (organic ligands with strong absorbing chromophores) that act as antennas to trap light and transfer energy to the central metal ion, achieving intramolecular energy transfer in the lanthanide system.[105] This process is mainly based on energy transfer from the excited state of the ligand (T_1) to the emitting level of the Ln^{III} ion, which is usually its lowest excited state. Antenna effect, among other factors, depends on the energy difference between the lowest triplet state of the ligand (T_1) and the excited state of the lanthanide ion, which must be in the optimal range.[102] Upon exposure to excitation light, the ligand is excited to a singlet excited state (S_n), from which it may either relax back to the ground state, resulting in

fluorescence, or undergo intersystem crossing to the triplet state (T_1). From the triplet state (T_1), two possible pathways can occur: (i) the ligand may relax back to the ground state, emitting phosphorescence, or (ii) if the energy gap between the ligand's T_1 state and the emitting level of the Ln^{III} ion falls within an optimal range, energy transfer can take place, effectively sensitizing the lanthanide's emission (Figure. 1.22b). For each trivalent lanthanide ion, the optimum energy difference required for this transfer has been previously established.[102]

After the sensitization process, deactivation may occur via non-radiative pathways, which reduces the quantum yield (Φ) of the emission. It is important to note that the occurrence of these non-radiative mechanisms depends both on the specific Ln^{III} ion involved (intrinsic to the metal ion) and on external factors that may enhance them. Generally, the smaller the energy gap between the emitting state and the nearest lower-lying energy level, the higher the probability of non-radiative deactivation. This explains, for instance, why compounds based on Tb^{III} typically exhibit brighter emission compared to those based on Dy^{III}.[103]

In this regard, magneto-luminescent materials are crucial for potential applications in optoelectronics, sensors and various biological fields which include luminescent markers, neurobiology, cancer, stem cell biology and infectious diseases.[102, 106] Moreover, these systems offer a valuable platform for experimentally correlating emission properties with electronic structure and magnetic relaxation dynamics.[107] Specifically, luminescent properties allow obtaining information about the crystal-field energy splitting of the ground multiplet.

As an example, W.-B. Sun *et al.* prepared a series of mononuclear and binuclear Dy^{III} complexes with mono- and bi-phosphine oxide and β-diketonate

ligands, each with different steric hindrance effects, which were structurally, optically and magnetically characterized.[108] Their formulae were $[Dy(Cy_3PO)(tmhd)_3]$, $[Dy_2(dppeO_2)(tmhd)_6]$ and $[Ln_2(dppeO_2)(acac)_6(H_2O)_2]$ (Ln = Dy^{III}, Gd^{III}, Eu^{III}, Tb^{III}) (Cy_3PO = tricyclohexyl phosphine oxide, tmhd = 2,2,6,6-tetramethyl-3,5-heptane dionate, acac = acetylacetone, $dppeO_2$ = 1,2-bis(diphenylphosphino)ethane dioxide). By managing the steric hindrance, complexes with a high axial symmetry and a D_{4d} configuration were successfully prepared, showing impressive SMM behavior with a hysteresis temperature as high as 3 K (Figure 1.23). Notably, the Gd^{III} variant demonstrated not only remarkable magnetocaloric effect (MCE) properties but also field-induced SMM characteristics, while the Dy^{III}, Eu^{III}, and Tb^{III} analogues exhibited their distinct metal-centered luminescence. This research demonstrates an effective strategy for designing multifunctional materials that incorporate SMM, luminescence, and MCE properties, achieved by selecting organic ligands with adjustable molecular structures and considering both electronic and steric hindrance effects.

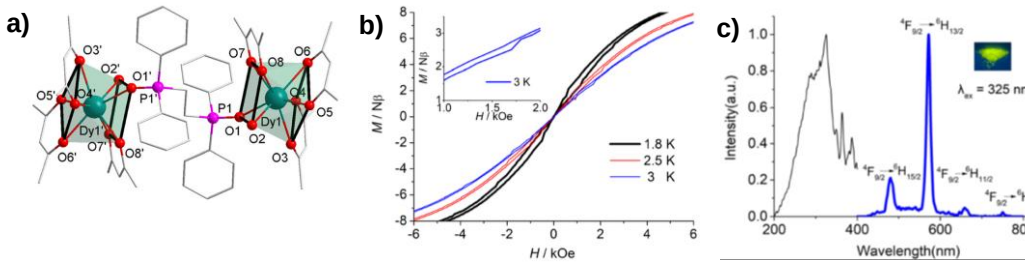

Figure. 1.23: a) Partially labeled molecular structure of complex $Dy_2(dppeO_2)(acac)_6(H_2O)_2$. b) Field dependence of the magnetization of the complex. c) Emission spectra of the complex (λ_{exc} = 325 nm). Color code: Dy (teal), P (pink), O(red), and C (grey).[108]

F. Pointillart and co-workers[109] have also designed multifunctional materials that combine magnetic and optical properties. They synthetized new

mononuclear Ln^{III} complexes involving effective organic chromophores, with the formula $[Ln(hfac)_3(L)]$ ($hfac^-$ = 1,1,1,5,5,5-hexafluoroacetylacetonate) (Ln = Dy^{III} and Yb^{III}) and $[Ln(tta)_3(L)]$ (tta^- = 2-tenoyl-trifluoroacetylacetonate) (Ln = Dy^{III} and Yb^{III}) and one dinuclear complex $[Na(Dy_2(hfac)_6(L)_2)](BArF)$ ($BArF^-$ = tetrakis[3,5-bis(trifluoromethyl)phenyl]borate). The ligand L is 1,4(1,4)-dibenzenacyclohexaphane-1^2,4^3-diylbis(diphenylphosphine oxide). In the $[Yb(tta)_3(L)]$ complex, the coordination geometry around the Yb^{III} ion is described as a dodecahedron prism (D_{2d} symmetry). The Yb^{III} ion is coordinated by two phosphine oxide groups (P=O) of the ligand L and six oxygen atoms from three $hfac^-$ anions. The average Yb-$O_{P=O}$ and Yb-O_{hfac} bond distances are 2.188 Å and 2.336 Å, respectively. The present complex showed slow magnetic relaxation when exposed to an external magnetic field, thus exhibiting SIM behaviour (Figure 1.24a).

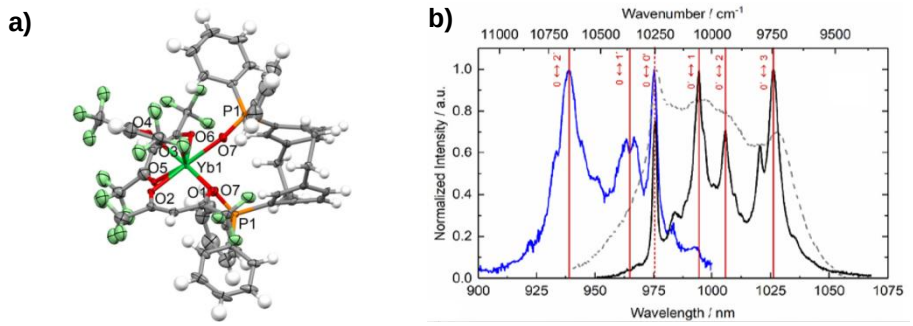

Figure 1.24: a) Ortep view of the molecular structure for the $[Yb(tta)_3(L)]$ complex. Thermal ellipsoids are drawn at 30% probability. b) Room (dashed grey line) and low (full black line) temperature (77 K) solid-state emission spectra for the $[Yb(tta)_3(L)]$ complex under irradiation at λ_{exc} = 340 nm and their corresponding excitation spectra (full blue line) obtained by detection at 1025 nm.[109]

The Yb complex exhibited Yb^{III} centred emission in the near infrared (NIR) region due to the $^2F_{5/2} \rightarrow {}^2F_{7/2}$ transitions because the ligand acts as an

efficient organic antenna for Yb^{III} sensitization (Figure 1.24b). At 77 K, its emission spectra showed the four well-resolved main signals expected for the $^2F_{5/2} \rightarrow {}^2F_{7/2}$ transition. The energy difference between the experimentally observed m_J doublets reflect the crystal field splitting of the $^2F_{7/2}$ ground state and the excitation spectra measurements enabled the determination of the energy splitting of the $^2F_{5/2}$ excited state and the identification of the zero-phonon line.

Furthermore, the total energy splitting for the ground state is 492 cm^{-1} for the Yb^{III} complex, indicating low-symmetry coordination environments around the metal ion, which is generally desirable to obtain more intense luminescence.

The emission decay curves for Yb^{III} complex can be fitted by mono-exponential functions (lifetime of 21.0 μs), which confirms the presence of a single Yb^{III} spectroscopic site and suggests the existence of monomeric species in solution. Thus, this Yb^{III} complex combines luminescence properties and SMM behaviour induced by the application of an external magnetic field. These properties are advantageous for a range of applications, including bioimaging and optical telecommunications devices.

1.1.5.1.2 Chiral SMMs

In multifunctional materials based on coordination compounds, chirality can be spawn by using enantiomerically pure ligands. In other cases, the coordination of polydentate achiral ligands around the metal ion gives rise to chiral complexes. The strategy of rationally inducing chirality in molecular materials can indeed be used in various fields of science and technology. For example, conduction physics such as electric magnetochiral anisotropy

(eMChA),[110] spintronics, superconductivity, materials science (optimisation of conductive properties by controlling structural disorder)[111] and optics and spectroscopy, and all of these are achieved by combining or interacting more than two properties such as chirality, magnetism and luminescence.[112]

Taniguchi and his co-workers have carried out significant research on magneto-chiral dichroism (MChD) by visible light emission in chiral lanthanide complexes with two different coordination geometries (nona- and octa-coordinated complexes) and investigated their magneto-chiral properties, opening new avenues for understanding MChD and its potential applications in molecular chemistry (Figure 1.25).[113] These compounds were formulated as $[Ln(L^{SS/RR})_3]X_3$ and $[Ln((d/l)\text{-tfc})_3(phen)]$, where Ln represents the lanthanide ion (Tb^{III} or Eu^{III}), $L^{SS/RR}$ is a chiral ligand with the formula *N,N'-(X,X)*-bis(1-phenylethyl)-2,6-pyridine carboxamide, X = $CF_3SO_3^-$, ClO_4^-, and phen = phenantroline. By comparing the intensity of MChD, the results showed that the intensity of MChD signals was stronger for the Tb^{III} complexes compared to Eu^{III} ones, and for the nona-coordinated complexes when compared to the octa-coordinated ones. They attribute the former observation to the larger magnetic moment of Tb^{III} (ground state with $J = 6$) and the latter with the smaller inversion symmetry breaking at the lanthanide center. This results in more intense MChD signals, which is important for optimising the MChD effect for technological applications such as optical magnetic data reading, smart windows, light filters, valves and also for the emergence of homochirality of life on Earth. In this respect, magneto-chiral dichroism offers a promising opportunity to replace electronics with photonics.[112]

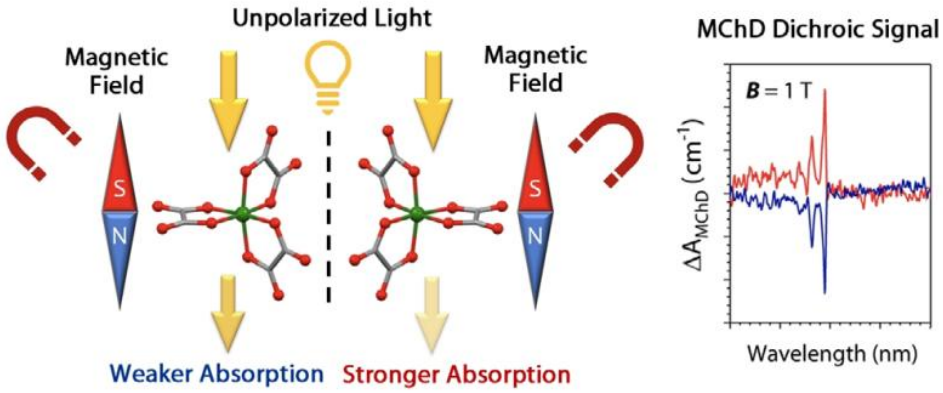

Figure 1.25: Schematic representation of the conditions needed to observe a MChD signal on a chiral molecule. Ln complex (left) and generic MChD dichroic signal resulting from the weaker and stronger absorption of light for a series of electronic transitions as a function of the enantiomer (right).[113]

1.1.5.1.3 Luminescent and chiral SMMs: Circularly Polarized Luminescence (CPL)

Circularly Polarized Luminescence (CPL) is an interesting property in the field of luminescent single-molecule magnets (SMMs). CPL is manifested by a difference in intensity between left- and right-circularly polarized emitted light by chiral luminescence systems. Achiral components such as solvent or counterions can also make an influence. Lanthanide ions are ideal candidates to present CPL, because they show high dissymmetry factors g_{lum} as high as 1.45 due to the nature of f-f transitions.[114] However, organic molecules or coordination compounds based on transition metals generally exhibit low g_{lum} values (≤ 0.2).[102, 115] This value of 1.45 is therefore considered relatively high in comparison with other types of compounds. CPL is important as a chiroptical property that can be combined with SMM behavior for advanced applications in spintronics and information storage, among others.

As an example, S. Gao et al. rationally designed and successfully prepared a new pair of multifunctional Zn^{II}–Dy^{III} enantiomeric complexes, namely [*R*,*R*-ZnLDy(H_2O)(NO_3)$_3$] (1*R*2*R*-ZnDy) and [*S*,*S*-ZnLDy(H_2O)(NO_3)$_3$] (1*S*2*S*-ZnDy) (Figure 1.26a), based on the chiral Schiff-base ligands (H_2L = phenol, 2,2'-[[(1*R*,2*R*/1*S*,2*S*)-1,2-diphenyl-1,2-ethanediyl]bis[(*E*)-nitrilomethylidyne]]bis[6-methoxy]).[116] The complex 1*R*2*R*-ZnDy exhibited typical SMM behaviour. Additionally, both 1*R*2*R*-ZnDy and 1*S*2*S*-ZnDy complexes showed circularly polarized luminescence (CPL, Figure 1.26b) as well as magneto-optical effects. This study showed that chiral Schiff base ligands are a practical source for creating unichiral SMMs, while also enabling circularly polarized luminescence and magneto-optical Faraday effects. It provides a valuable approach for the development of chiral SMMs and multifunctional molecular materials with magneto-optical properties.

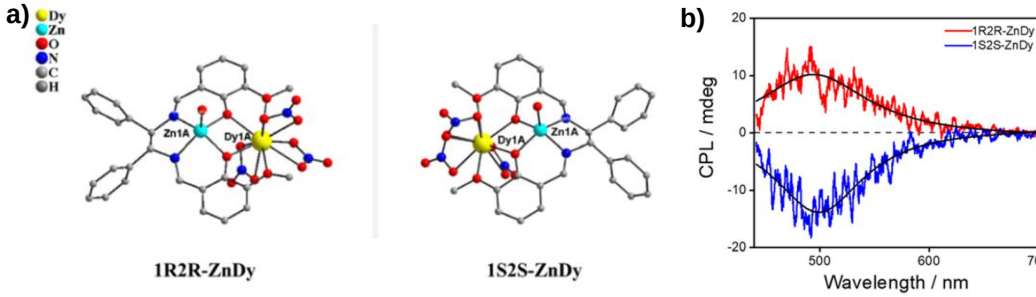

Figure 1.26: a) Molecular structures of the dinuclear complexes 1*R*2*R*-ZnDy and 1*S*2*S*-ZnDy. The H atoms are omitted for clarity. b) Circularly polarized luminescence emission spectra measured in N,N-dimethylformamide (DMF) solution at room temperature.[116]

Additionally, figure 1.27[117] presents the findings for two chiral $Zn^{II}Dy^{III}$-based coordination compounds reported by Sutter et al.[117] These compounds showed slow magnetic relaxation below 12 K, with g_{lum} values ranging from 0.04 to 0.18 for the Λ complex and from 0.04 to 0.16 for the Δ complex. These values gradually decreased and eventually disappeared at 25 K.

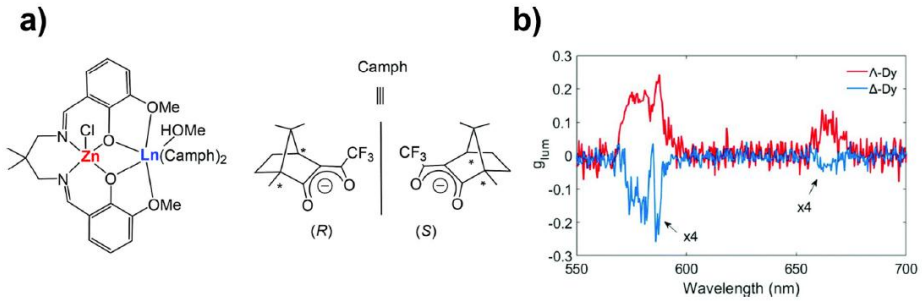

Figure 1.27: a) Scheme of the $Zn^{II}Ln^{III}$ based compounds. b) CPL dissymmetry factor g_{lum} as a function of the wavelength at 5 K for the Λ and Δ complexes, respectively.[117]

Since CPL can arise not only from chiral environments but also from magnetic fields, either externally applied or inherent to the material[118] the CPL behaviour of $Zn^{II}Eu^{III}$ analogues was also examined to better understand the origin of the optical activity. Notably, the emission intensities of left- and right-circularly polarized light remained equal down to 5 K, resulting in g_{lum} values near zero. This indicates that the contribution of the chiral structure to CPL in these compounds was quite low.

As a last example, C. M. Liu and co-workers[119] synthesised a family of chiral 3d–4f trinuclear and tetranuclear heterometallic complexes with magnetic and luminescent properties. The trinuclear Zn^{II}-Ln^{III}-Zn^{II} complexes are based on a Schiff base ligand (the chiral amine−phenol ligand) with the formula $[Zn_2Ln(R,R\text{-L})_2(H_2O)_4](ClO_4)_3$ and $[Zn_2Ln(S,S\text{-L})_2(H_2O)_4](ClO_4)_3$ [Ln = Dy^{III}, Tb^{III}], H_2L = cyclohexane-1,2-diylbis(azanediyl)bis-(methylene)bis(2-methoxyphenol) (figure 1.28, top). These four trinuclear compounds are isostructural. In them, the two Zn^{II} ions and the Ln^{III} ion (Dy^{III} or Tb^{III}) are coordinated by four oxygen atoms from the phenoxo groups of the ligand L^{2-} to form a $[ZnO_2LnO_2Zn]$ unit, the Ln^{III} ion being surrounded by eight oxygen atoms.

Of these eight oxygen atoms, two come from terminal water molecules. The coordination geometry around the Ln^{III} ion is described as a square-based antiprism. Each Zn^{II} ion is penta-coordinated (N_2O_3), completed by a water molecule. The coordination geometry around each Zn^{II} ion is of the trigonal bipyramid type, in which the Zn-O bond lengths range from 1.979 to 2.137 Å, while the Zn-N bond lengths range from 2.065 to 2.160 Å. As all the four complexes are chiral enantiomers, the focus of the study was exclusively on the magnetic and luminescent properties of the $[Zn_2Ln(R,R\text{-}L)_2(H_2O)_4](ClO_4)_3$ compounds.

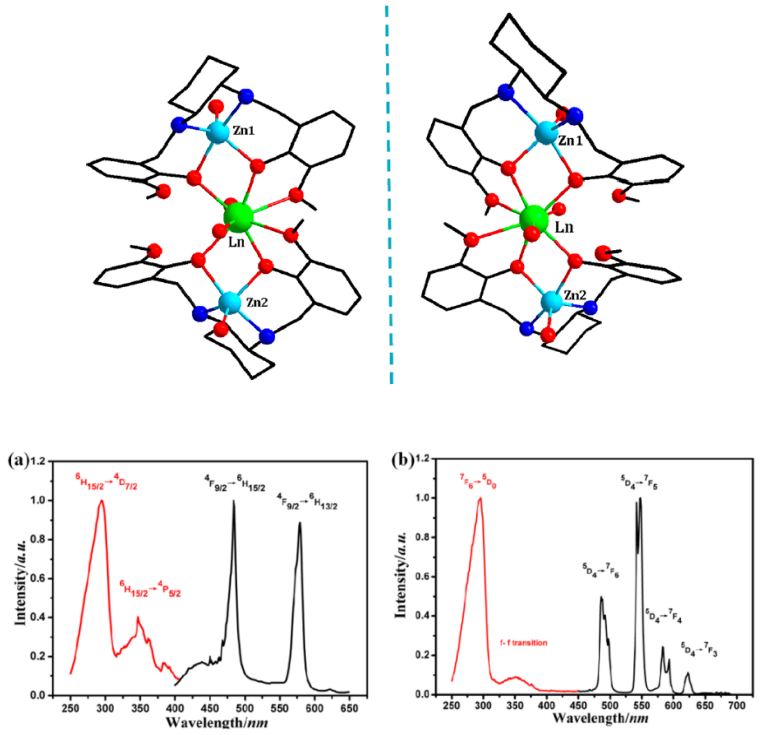

Figure 1.28: (top) Cationic structures of $[Zn_2Ln(R,R\text{-}L)_2(H_2O)_4](ClO_4)_3$ and $[Zn_2Ln(S,S\text{-}L)_2(H_2O)_4](ClO_4)_3$ complexes, with Ln = Dy^{III}, Tb^{III}. All hydrogen atoms and solvent molecules are omitted for clarity. (bottom) Fluorescent excitations (red) and emissions (black) spectra of $[Zn_2Ln(R,R\text{-}L)_2(H_2O)_4](ClO_4)_3$ complexes with Ln = Dy^{III} (a) and Tb^{III} (b).[119]

The complexes exhibit field-induced SIM behaviour characterised by effective energy barriers of 22.46 K for the Dy^{III} complex and 38.70 K or 41.87 K for the Tb^{III} complexes. The solid-state luminescence was also studied in these compounds. Their chromophore ligands were able to efficiently absorb light at certain wavelengths and, through an energy transfer process, sensitize lanthanide ions and act as antennas. The emission spectrum of the Dy^{III} complex, using λ_{exc} = 295 nm, showed a characteristic peak at 484 nm, corresponding to a magnetic dipole transition of the line $^4F_{9/2} \rightarrow {}^6H_{15/2}$ (blue), which is more intense than the emission $^4F_{9/2} \rightarrow {}^6H_{13/2}$ (yellow). This relative intensity is due to the fact that the Dy^{III} ion is surrounded by eight oxygen atoms in a D_{4d} point group with an inversion centre, which makes the effect of the electric dipole transition relatively weak and favours blue emission. The emission spectrum of Tb^{III} complex exhibits four emission peaks characteristic of the Tb^{III} ion at 494, 549, 588 and 622 nm excited at λ_{exc} = 296 nm, which are attributed to the transitions $^5D_4 \rightarrow {}^7F_6$, $^5D_4 \rightarrow {}^7F_5$, $^5D_4 \rightarrow {}^7F_4$ and $^5D_4 \rightarrow {}^7F_3$, respectively. The $^5D_4 \rightarrow {}^7F_5$ transition at 549 nm (green) is more intense than the others (Figure 1.28, bottom). All the emission peaks are narrow, which indicates that the green light is emitted with high colour purity.

Furthermore, the decay curves are of fundamental importance in understanding the luminescent properties of the complexes. They provide insights into emission dynamics, quenching effects, and potential applications in material science. Consequently, they can guide the selection of complexes for specific applications.The Dy^{III} complex can be fitted with a biexponential model, indicating the presence of two components in its fluorescence decay. The average fluorescence lifetime is measured at 0.020 milliseconds. The relatively short lifetime of the Dy^{III} ion suggests that it experiences significant quenching effects, likely due to the surrounding coordination environment and the presence of water molecules (quenching agents on fluorescence). These

factors can affect the emission efficiency. In contrast, the Tb^{III} complex exhibits a longer average fluorescence lifetime of 0.905 ms. This finding suggests that the Tb^{III} ion is situated within a more favourable environment, thereby facilitating enhanced emission efficiency. The reduced quenching effects extend the lifetime of Tb^{III}, making it a more effective luminescent centre. This makes the Tb^{III} complex a good candidate for multifunctional materials.

Although these Dy^{III} and Tb^{III} compounds show potential CPL properties because they exhibit interesting chiral and luminescent properties, their CPL properties were not measured.

1.2 REFERENCES

[1] O. Kahn, *Molecular Magnetism*, VCH Publishers, Inc., New York, 1993.

[2] J. S. Miller and M. Drillon, *Magnetism: Molecules to Materials*, WILEY-VCH, 2005.

[3] D. Gatteschi, R. Sessoli and J. Villain, *Molecular Nanomagnets*, Oxford University Press Inc, New York, 2006.

[4] O. Kahn and B. Briat, *J. Chem. Soc.*,1976, **72**, 268-281.

[5] A. Jordan, D. Gayner, I. R. Jeon and T. David Harr, *Chem. Science.*, 2015, **6**, 6639-6648.

[6] O. Kahn, *Adv. Inorg. Chem.*, 1993, **43**, 179-259.

[7] O. Kahn, *Acc. Chem. Res.*, 2000, **33**, 647–657.

[8] M. Sorai, M. Nakano and Y. Miyazaki, *Chem. Rev.*, 2006, **106**, 976–1031.

[9] C. Coulon, H. Miyasaka and R. Clérac, *Struct. Bond*, 2006, **122**, 163–206.

[10] R. Clérac, H. Miyasaka, M. Yamashita and C. Coulon, *J. Am. Chem. Soc.*, 2002, **124**, 12837-12844.

[11] O. G. Shakirova and L.G. Lavrenova, *Crystals.*, 2020, **10**, 843.

[12] J. A. Real, A. B. Gaspar, V. Niel and M. C. Muñoz, *Coord. Chem. Rev.*, 2003, **236**, 121-141.

[13] X. Yin, L. Deng, L. Ruan, Y. Wu, F. Luo, G. Qin, X. Han and X. Zhang, *materials.*, 2023, **16**, 3568.

[14] D. Shao and X.-Y. Wang, *Chin. J. Chem.*, 2020, **38**, 1005-1018.

[15] J.-H. Jia, Q.-W. Li, Y.-C. Chen, J.-L. Liu and M.-L. Tong, *Coord. Chem. Rev.*, 2019, **378**, 365-381.

[16] A. K. Singh, *Coord. Chem. Rev.*, 2022, **455**, 214365.

[17] M.-M. Wang , X.-Q. Wei, J.-L. Zhu, J. Wang, M. Wang, L.-Z. Liou, T.-M. Sun and Y.-F. Tang, *J. Solid State Chem.*, 2020, **283**, 121172.

[18] P.-P. Ferreira da Rosa, Y. Kitagawa and Y. Hasegawa *Coord. Chem. Rev.*, 2020, **406**, 213153.

[19] E.-A. Mikhalyova, M. Zeller, J.-P. Jasinski, R.-J. Butcher, L.-M. Carrella, A. -E. Sedykh, K.-S. Gavrilenko, S.-S. Smola, M. Frasso, S.-C. Cazorla, K. Perera, A. Shi, H.-G. Ranjbar, C. Smith, A. Deac, Y. Liu, S.-M. McGee, V.-P. Dotsenko, M.-U. Kumke, K.-M. Buschbaum, E. Rentschler, A.-W. Addison and V.-V. Pavlishchuk, *Dalton Trans.*, 2020, **49**, 7774–7789.

[20] H. Huang, R. Sun, X.-F. Wu, Y. Liu, J.-Z. Zhan, B.-W. Wang and S. Gao, *Dalton Trans.*, 2023, **52**, 7646–7651.

[21] J.-T. Chen, T.-D. Zhou and W.-B. Sun, *Dalton Trans.*, 2023, **52**, 4643–4657.

[22] G. Peng, Q. Yang, Y. Chen, X.-T. Dong, Z. Zhang and X.-M. Ren, *Dalton Trans.*,2022, **51**, 12484–12493.

[23] E. Moreno-Pineda and W. Wernsdorfer, *Nat. Rev. Phys.*, 2021, **3**, 645–659.

[24] R. Sessoli, D. Gatteschi, A. Caneschi and M. A. Novak, *Nature*, 1993, **365**, 141–143.

[25] J.-M. Frost, K.-L. M. Harriman and M. Murugesu, *Chem. Sci.*, 2016, **7**, 2470–2491.

[26] Q.-C. Luo and Y.-Z. Zheng, *Trends Chem.*,2023 ,**5**, 869-872.

[27] J.-G. C. Kragskow, A. Mattioni, J.-K. Staab, D. Reta, J.-M. Skelton and N.-F. Chilton, *Chem. Soc. Rev.*, 2023, **52**, 4567–4585.

[28] A. Zabala-Lekuona, J. M. Seco and E. Colacio, *Coord. Chem. Rev.*, 2021, **441**, 213984.

[29] J. H.Van Vleck, *Phys. Rev.*, 1932, **57**, 426-447.

[30] M. Murugesu, M. Habrych, W. Wernsdorfer, K. A. Abboud and G. Christou, *J. Am. Chem. Soc.*, 2004, **126**, 4766–4767.

[31] E. Ruiz, T. Cauchy, J. Cano, R. Costa, J. Tercero and S. Alvarez, *J. Am. Chem. Soc.*, 2008, **130**, 7420–7426.

[32] A. M. Ako, I. J. Hewitt, V. Mereacre, R. Clerac, W. Wernsdorfer, C. E. Anson and A.-K. Powell, *Angew. Chem. Int. ed.*, 2006, **45**, 4926 –4929.

[33] S.-G.Coca, D. Aravena and R. Morales, *Coord. Chem. Rev.*, **2015**, 379–392.

[34] S. G. McAdams, A. M. Ariciu, A. K. Kostopoulos, J. P.S. Walsh and F. Tuna, *Coord. Chem. Rev.*, 2017, **346**, 216–239.

[35] J. L. Liu, Y. C. Chen, and M. L. Tong, *Chem. Soc. Rev.*, 2018, **47**, 2431–2453.

[36] P.-P. Power, *Chem. Rev.*,2012, **112**, 3482–3507.

[37] R. Ruamps, L. Batchelor, R. Maurice, N. Gogoi, P.-J. Lozano, N. Guihéry, C. Degraaf, A. Barra, J. Sutter and T. Mallah, *Chem. Eur. J.*, 2013, **19**, 950–956.

[38] Y. Rechkemmer, F. Breitgoff, M. Van Der Meer, M. Atanasov, M. Hakl, M. Orlita, P. Neugebauer, F. Neese, B. Sarkar and J. Van Slageren, *Nat. Commun.*, 2016, **7**, 10467.

[39] M.-T. M. Feng, *Chem. Eur. J.*, 2018, **24**, 7574–7594.

[40] J.-M. Zadrozny, D.-J. Xiao, M. Atanasov, G.-J. Long, F. Grandjean, F. Neese and J.-R. Long , *Nat. Chem.*, 2013, **5**, 577–581.

[41] M. Atanasov, J. Zadrozny, J. Long and F. Neese *Chem. Sci.*, 2013, **4**, 139–156.

[42] G. Craig and M. Murrie, *Chem. Soc. Rev.*, 2015, **44**, 2135–2147.

[43] Y. Meng , Z. Mo, B. Wang, Y. Zhang, L. Deng and S. Gao, *Chem. Sci.*, 2015, **6**, 7156–7162.

[44] M. Dey and N. Gogoi, *Angew. Chem. Int. Ed.*, 2013, **52**, 12780–12782.

[45] X.-N. Yao, J.-Z. Du, Y.-Q. Zhang, X.-B. Leng, M.-W. Yang, S.-D. Jiang, Z.-X. Wang, Z.-W. Ouyang, L. Deng, B.-W. Wang and S. Gao, *J. Am. Chem. Soc.*, 2017, **139**, 373−380.

[46] J.-D. Wang, M. Xie and L. Deng, *Angew. Chem. Int. Ed.*, 2015, **54**, 12640–12644.

[47] P. Bunting, M. Atanasov, E. Damgaard-Møller, M. Perfetti, I. Crassee, M. Orlita, J. Overgaard, J. Van Slageren, F. Neese and J. Long, *Science.,* 2018, **362**, 3719.

[48] M. Atanasov, D. Aravena, E. Suturina, E. Bill, D. Maganas and F. Neese, *Coord. Chem. Rev.,* 2014, **289–290**, 177–214.

[49] J. E. Wertz and J. R. Bolton, *Electron Spin Resonance. Elementary Theory and Practical Applications*, Springer Dordrecht, 1986.

[50] a) A. Landart-Gereka, M. -M Quesada-Moreno, I.-F. Díaz-Ortega, H. Nojiri, M. Ozerov, J. Krzystek, M.-A. Palacios and E. Colacio, *Inorg. Chem. Front.*, 2022, **9**, 2810; b) A. Landart-Gereka, I.-F. Dıaz-Ortega, M.-M Quesada-Moreno, H. Nojiri, M.-A. Palacios, M. Ozerov, J. Krzystek and E. Colacio, *Chem. Commun.,* 2023, **59**, 952-954; c) A. Landart, M.-M Quesada-Moreno, M.-A. Palacios, Y. Li, M. Ozerov, J. Krzystekd and E Colacio, Dalton Trans., 2024, **53**, 12876.

[51] P. Zhang, Y.-N. Guo and J. Tang, *Coord. Chem. Rev*., 2013, **257**, 1728–1763.

[52] H.-L. C. Feltham and S. Brooker, *Coord. Chem. Rev*., 2014, **276**, 1–33.

[53] Y.-S. Meng, S -D. Jiang, B -W. Wang and S. Gao, *Acc. Chem. Res*., 2016, **49**, 2381–2389.

[54] N. Ishikawa, M. Sugita, T. Ishikawa, S.-Y. Koshihara and Y. Kaizu, *J. Am. Chem. Soc.,* 2003, **125**, 8694-8695.

[55] N. Koike, H. Uekusa, Y. Ohashi, C. Harnoode, F. Kitamura, T. Ohsaka, K. Tokuda, *Inorg. Chem.,* 1996, **35**, 5798–5804.

[56] L. Zhu, B. Yin, P. Ma and D. Li, *Inorg. Chem.,* 2020, **59**, 16117-16121.

[57] E. Damgaard-Møller, L. Krause, K. Tolborg, G. Macetti, A. Genoni and J. Overgaard, *Angew. Chem. Int. Ed.,* 2020, **59**, 21203– 21209.

[58] C. Gao, A.Genoni, J.Overgaard, S. Gao, S. Jiang and A. Soncini, *Nat. Chem.,* 2020, 213–219.

[59] Y.-C. Chen, J.-L. Liu, W. Wernsdorfer, D. Liu, L.-F. Chibotaru, X.-M. Chen and M.-L. Tong, *Angew. Chem. Int. Ed.*, 2017, **56**, 4996-5000.

[60] D. Atanu , K. Pankaj and C. Vadapalli, *ACS Omega*, 2018, **3**, 9462-9475.

[61] M.-S. Norre, C. Gao, S. Dey, S.-K. Gupta, A. Borah, R. Murugavel, G. Rajaraman and J. Overgaard, *Inorg. Chem.*, 2020, **59**, 717−729.

[62] C.-A. P. Goodwin, F. Ortu, D. Reta, N.-F. Chilton and D.-P. Mills, *Nature*, 2017, **548**, 439–442.

[63] F.-S. Guo, B.M. Day, Y.-C. Chen, M.-L. Tong, A. Mansikkamäki and R.-A. Layfield, *Angew. Chem. Int. Ed.*, 2017, **56**, 11445–11449.

[64] Y.-S. Ding, N.-F. Chilton, R.-E. P. Winpenny and Y.-Z. Zheng, *Angew. Chem. Int. Ed.*, 2016, **55**, 16071–16074.

[65] F.-S. Guo, B.M. Day, Y.-C. Chen, M.-L. Tong, A. Mansikkamäki and R.-A, Laifield, *Science*, 2018, **362**, 1400–1403.

[66] K.-R. McClain, C.-A. Gould, K. Chakarawet, S.-J. Teat, T.-J. Groshens, J.-R. Long and B.-G. Harvey, *Chem. Sci.*, 2018, **9**, 8492–8503.

[67] P. Evans, D. Reta, G.-F.S. Whitehead, N.-F. Chilton and D.-P. Mills, *J. Am. Chem. Soc.*, 2020, **141**, 19935–19940.

[68] Y. Meng, J. Xiong, M. Yang, Y. Qiao, Z. Zhong, H. Sun, J. Han, T. Liu, B. Wang and S. Gao, *Angew. Chem. Int. Ed.*, 2020, **59**, 13037–13043,

[69] R. Collins, M.-J. Heras Ojea, A. Mansikkamäki, J. Tang and R.-A. Layfield, *Inorg. Chem.*, 2020, **59**, 642–647.

[70] M. He, F.-S. Guo, J. Tang, A. Mansikkamäki and R.-A. Layfield, *Chem. Sci.*, 2020, **11**, 5745–5752.

[71] C.-A. Gould, K.-R. McClain, D. Reta, J.-G. C. Kragskow, D.-A. Marchiori, E. Lachman, E.-S. Choi, J.-G. Analytis, R.-D. Britt, N.-F. Chilton, B.-G. Harvey and J.-R. Long, *Science.*, 2022, **375**, 198-202.

[72] a) M. Gregson, N.-F. Chilton, A.-M. Ariciu, F. Tuna, I.-F. Crowe, W. Lewis, A.-J. Blake, D. Collison, E.-J. L. McInnes, R.-E. P. Winpenny and S.-T. Liddle, *Chem. Sci.*, 2016, **7**, 155-165; b) S.-T. Liddle and J. van Slageren, *Chem. Soc. Rev.*, 2015, **44**, 6655-6669.

[73] J.-L. Liu, Y.-C. Chen and M.-L. Tong, *Chem. Soc. Rev.*, 2018, **47**, 2431–2453.

[74] Y.-S. Ding, N.-F. Chilton, R.-E.P. Winpenny, Y.-Z. Zheng, *Angew. Chem. Int. Ed.*, 2016, **55**, 16071–16074.

[75] J. Liu, Y.-C. Chen, J.-L. Liu, V. Vieru, L. Ungur, J.-H. Jia, L.-F. Chibotaru, Y. Lan, W.Wernsdorfer, S. Gao, X.-M. Chen and M.-L. Tong, *J. Am. Chem. Soc.*, 2016, **138**, 5441–5450.

[76] Y.-C. Chen, J.-L. Liu, L. Ungur, J. Liu, Q.-W. Li, L.-F. Wang, Z.-P. Ni, L.-F. Chibotaru, X.-M. Chen and M.-L. Tong, *J. Am. Chem. Soc.*, 2016, **138**, 2829–2837.

[77] Z. Jiang, L. Sun, Q. Yang, B. Yin, H. Ke, J. Han, Q. Wei, G. Xie and S. Chen, *J. Mater. Chem. C*, 2018, **6**, 4273-4280.

[78] L. Zhu, Y. Dong, B. Yin, P. Ma and D. Li, Dalton Trans., 2021, **50**, 12607–12618.

[79] a) Y.-S. Ding, T. Han, Y.-Q. Zhai, D. Reta, N.-F. Chilton, R.-E. P. Winpenny and Y.-Z. Zheng, *Chem. Eur. J.*, 2020, **26**, 5893-5902; b) Y.-S. Ding, K.-X. Yu, D. Reta, F. Ortu, R.-E. P. Winpenny, Y.-Z. Zheng and N.-F. Chilton, *Nat. Commun.*, 2018, **9**, 3134; c) K.-X. Yu, Y.-S. Ding, Y.-Q. Zhai, T. Han and Y.-Z. Zheng, *Dalton Trans.*, 2020, **49**, 3222-3227.

[80] a) S.-K. Gupta, T. Rajeshkumar, G. Rajaraman and R. Murugavel, *Chem. Sci.*, 2016, **7**, 5181–5191; d) L. Norel, L.-E. Darago, B.-Le Guennic, K. Chakarawet, M.-I. Gonzalez, J.-H. Olshansky, S. Rigaut and J.-R. Long, *Angew. Chem. Int. Ed.*, 2018, **57**, 1933–1938.

[81] S. Dey, T. Sharma and G. Rajaraman, *Chem. Sci.*, 2024, **15**, 6465-6477

[82] S. Gupta, T. Rajeshkumar, G. Rajaraman and R. Murugavel, *Chem.Sci.*, 2016, **7**, 5181-5191.

[83] Y.-C. Chen, J.-L. Liu, Y. Lan, Z.-Q. Zhong, A. Mansikkamäki, L. Ungur, Q.-W. Li, J.-H. Jia, L. F. Chibotaru, J.-B. Han, W. Wernsdorfer, X.-M. Chen and M.-L. Tong, *Chem. Eur. J.*, 2017, **23**, 5708-5715.

[84] I.-F. Díaz-Ortega, J.-M. Herrera, S. Dey, H. Nojiri, G. Rajaraman and E. Colacio, *Inorg. Chem. Front.*, 2020, **7**, 689-699.

[85] P. Kalita, N. Ahmed, A. Bar, S. Dey, A. Jana, G. Rajaraman, J.-P. Sutter and V. Chandrasekhar, *Inorg. Chem.*,2020, **59**, 6603-6612.

[86] A.-B. Canaj, S. Dey, C. Wilson, O. Céspedes, G. Rajaraman and M. Murrie, *Chem. Commun.*, 2020, **56**, 12037-12040.

[87] P. Kalita, A. Kumar Bar, N. Ahmed, S. Moorthy, V. Béreau, P. Kumar, P. Nayak, J.-P Sutter and S.-K Singh, *Dalton Trans.*, 2023, **52**, 2804-2815.

[88] T.-A. Bazhenova, V.-A. Kopotkov, D.-V. Korchagin, E.-A. Yureva, M.-V. Zhidkov, A.-I. Dmitriev, I.-A. Yakushev, N.-N. Efimov, K.-A. Babeshkin, V.-S. Mironov and E.-B. Yagubskii, *Inorg. Chem. Front.*, 2025, **12**, 231-252.

[89] A.-B. Canaj, M.-K Singh, C. Wilson, G. Rajaraman and M. Murrie, *Chem. Commun.*, 2018, **54**, 8273-8276.

[90] Y. Gil, M.-M. Quesada-Moreno, M.-A. Palacios, S. Gómez-Coca, E. Colacio, E. Ruiz and Daniel Aravena, *Inorg. Chem. Front.*, 2025, **12**, 2856-2871.

[91] N. Ahmed and K. U. Ansari, *Dalton Trans.*, 2022, **51**, 8766–8776.

[92] I. Oyarzabal, J. Ruiz, E. Ruiz, D. Aravena, J. M. Seco and E. Colacio, *Chem. Commun.*, 2015, **51**, 12353-12356.

[93] a) H.-R. Wen, P.-P. Dong, S.-J. Liu, J.-S. Liao, F.-Y. Liang and C.-M. Liu, *Dalton Trans.*, 2017, **46**, 1153–1162; b) H.-R. Wen, J.-L. Zhang, F.-Y. Liang, K. Yang, S.-J. Liu, J.-S. Liao and C.-M. Liu, *New J. Chem.*, 2019, **43**, 4067-

4074; c) X.-N. Zhang, J.-J. Hu, J.-L. Zhang, S.-J. Liu, J.-S. Liao and H.-R. Wen, *New J. Chem.*, 2021, **45**, 3392-3399;

d) F.-Z. C. Fellah, F. Pointillart, T. Guizouarn, T. Roisnel, N. Dege, A.-C. Fellah and R. Hassaine, *Eur. J. Inorg. Chem.*, 2022, e202200349.

[94] a) P. Ling Then, C. Takehara, Y. Kataoka, M. Nakano, T. Yamamurac and T. Kajiwara *Dalton Trans.*, 2015, **44**, 18038–18048; b) J. J. Lai, Z. Y. Ruan, G. Z. Huang , J. L. Liu, M. L. Tong, *Inorg. Chem. Commun.*, 2021, **132**, 108807.

[95] a) J. P. Costes, S. Titos-Padilla, I. Oyarzabal,T. Gupta, C. Duhayon, G. Rajaraman and E. Colacio, *Chem. Eur. J.*, 2015, **21**, 15785 – 15796; b) A. Panja, Z. Jaglicic, R. Herchel, P. Brandao, K. Pramanik and N. Ch. Jana, *New J. Chem.*, 2022, **46**, 13546–13557

[96] a) I. Oyarzabal, J. Ruiz, J.-M. Seco, M. Evangelisti, A. Camón, E. Ruiz, D. Aravena and E. Colacio, *Chem. Eur. J.*, 2014, **20**, 14262 – 14269; b) P.-Y. Shan, H.-F. Li, P. Chen, Y.-M. Tian, W.-B. Sun and P.-F. Yan, *Z. Anorg. Allg. Chem.*, 2015, **641**, 1119–1124.

[97] a) M. Maeda, S. Hino, K. Yamashita, Y. Kataoka, M. Nakano, T. Yamamurac and T. Kajiwara, *Dalton Trans.*, 2012, **41**, 13640–13648; b) C. Takehara, P. Ling Then, Y. Kataoka, M. Nakano, T. Yamamurac and T. Kajiwara, *Dalton Trans.*, 2015, **44**, 18276–18283.

[98] a) J. L. Liu, Y. C. Chen, Y. Z. Zheng, W. Q. Lin, L. Ungur, W. Wernsdorfer, L. F. Chibotaru and M. L. Tong, *Chem. Sci.*, 2013, **4**, 3310–3316; b) S. Das, K. S. Bejoymohandas, A. Dey, S. Biswas, M. L. P. Reddy, R. Morales, E. Ruiz, S. Titos-Padilla, E. Colacio and V. Chandrasekhar, *Chem. Eur. J.*, 2015, **21**, 6449 – 6464; c) J. P. Costes, S. Titos-Padilla, I. Oyarzabal, T. Gupta, C. Duhayon, G. Rajaraman and E. Colacio, *Inorg. Chem.*, 2016, **55**, 4428−4440; d) A. L. Boulkedid, J. Long, C. Beghidja, Y. Guari, A. Beghidja and J. Larionova, *Dalton Trans.*, 2018, **47**, 1402–1406.

[99] I. Oyarzabal, A. Rodríguez-Diéguez, M. Barquín, J. M. Seco and E. Colacio, *Dalton Trans.,* 2017, **46**, 4278–4286.

[100] a) L.Ouahab, *Multifunctional Molecular Material*, Pan Stanford Publishing, Singapore, 2013; b) M.Clemente-Leon, E. Coronado, C. Marti-Gastaldo and F. M. Romero, *Chem. Soc. Rev*., 2011, **40**, 473-497.

[101] a) J. Tang and P. Zhang, *Lanthanide Single Molecule Magnets*, Springer, 2015; b) J.-H. Jia, Q.-W. Li, Y.-C. Chen, J.-L. Liu, M.-L. Tong, *Coord. Chem. Rev.,* 2019, **378**, 365-381; c) C. Train, M. Gruselle and M. Verdaguer, *Chem. Soc. Rev.,* 2011, **40**, 3297-3312; d) J. Long, J. Rouquette, J.-M. Thibaud, Rute A. S. Ferreira, L. D. Carlos, B. Donnadieu, V. Vieru, L. F. Chibotaru, L. Konczewicz, J. Haines, Y. Guari and J. Larionova, *Angew. Chem. Int. Ed.*, 2014, **53**, 1-6.

[102] R. Marin, G. Brunet, and M. Murugesu, *Angew. Chem. Int. Ed.,* 2021, **60**, 1728– 1746.

[103] J.-T. Chen, T.-D. Zhou, and W.-B. Sun, *Dalton Trans.,* 2023, **52**, 4643–4657.

[104] Y. Yang, X. Hu, Z. Yang and W. Huang, *Adv. Funct. Mater.,* 2024, 2412970.

[105] M.-C. Heffern, L.-M. Matosziuk and T.-J. Meade, *Chem. Rev.,* 2014, **114**, 4496−4539.

[106] S.-V. Eliseeva, M. Ryazanov, F. Gumy, S.-I. Troyanov, L.-S. Lepnev, J.-C.G. Bünzli, and N.-P. Kuzmina, *Eur. J. Inorg. Chem.,* 2006, 4809–4820.

[107] G. Cucinotta, M. Perfetti , J. Luzon , M. Etienne , P.-E. Car, A. Caneschi, G. Calvez, K. Bernot and R. Sessoli. *Angew. Chem. Int. Ed.,* 2012, **51**, 1606-1610.

[108] H. Yan, Z.-W. Che, W.-B. Sun, *New J. Chem.,* 2023, **47**, 140–146.

[109] H. Flichot, A. Sickinger, J. Brom, B. Lefeuvre, V. Dorcet, T. Guizouarn, O. Cador, B. Le Guennic, L. Micouin, O. Maury, E. Benedetti, and F. Pointillart, *Dalton Trans.,* 2024, **53**, 8191-8201.

[110] F. Pop, P. Auban-Senzier, E. Canadell, G.-L. J. A. Rikken, N. Avarvari, *Nat. Commun*. 2014, **5**, 3757.

[111] C. Rethore, M. Fourmigue, N. Avarvari, *Tetrahedron*., 2005, **61**, 10935 – 10942.

[112] M. Atzori, G.-L. J. A. Rikken, and C. Train., *Chem. Eur. J*. 2020, **26**, 9784-9791.

[113] K. Taniguchi, M. Nishio, S. Kishiue, P.-J. Huang, S. Kimura, H. Miyasaka, *Phys. Rev. Mater.* 2019, **3**, 045202.

[114] J. Kumar, B. Marydasan, T. Nakashima, T. Kawai, J. Yuasa, *Chem. Commun.*, 2016, **52**, 9885–9888.

[115] E.-M.Sanchez-Carnerero, *J. Am. Chem. Soc*., 2014, **136**, 3346-3349.

[116] H. Huang, R. Sun, X.-F. Wu, Y. Liu, J.-Z. Zhan, B.-W. Wang, S. Gao, *Dalton Trans.*, 2023, **52**, 7646–7651.

[117] B. El Rez, J. Liu, V. Béreau, C. Duhayon, Y. Horino, T. Suzuki, L. Coolen, J.P.Sutter, *Inorg.Chem. Front*. 2020, **7**, 4527–4534.

[118] J. P. Riehl, F.S. Richardson, 1986, *Chem*, **86**, 1–16.

[119] R. Wen, J.-J Hu, K Yang, J.-L Zhang, S.-J Liu, J.-S Liao, and C.-M Liu., *Inorg. Chem*., 2020, **59**, 2811−2824.

CHAPTER 2

OBJECTIVES

2. OBJECTIVES

The main objectives of this doctoral thesis are the design, preparation, and characterisation of multifunctional mononuclear and trinuclear coordination compounds based on lanthanide ions, with phosphine oxide and chiral Mannich base ligands, respectively, as well as the experimental and theoretical study of their magnetic and luminescent properties.

The specific objectives of this work, taking into account the background presented in the introduction, are as follows:

1. Synthesis of different mononuclear Ln^{III} complexes (Dy^{III}, Eu^{III}, Tb^{III}, Yb^{III}, Gd^{III}) with pentagonal bipyramid geometries or other geometries that also give rise to strong axial anisotropy, such as octahedral geometry. These complexes will be prepared from the di(1-adamantyl)benzylphosphine oxide ligand (scheme 2.1) and anhydrous Ln^{III} chloride salts.

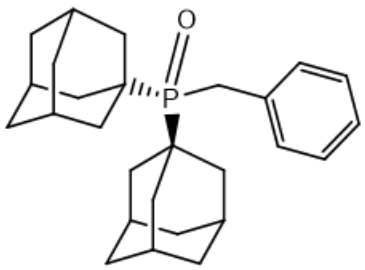

Scheme 2.1: Structure of the di(1-adamantyl)benzylphosphine oxide ligand.

This ligand, having strong and bulky sigma-giving groups (adamantyls), increases the electron density of the oxygen atom of the phosphine oxide, thus favouring its coordination to the central lanthanide ion (Dy^{III}, Eu^{III}, Tb^{III}, Yb^{III} or Gd^{III}). Due to their steric hindrance, only two of these alkyl ligands will occupy *trans* positions, creating a considerably strong axial crystal-field. The

equatorial positions will be occupied by auxiliary ligands such as water, tetrahydrofuran, and/or halide atoms, which will lead to weak fields.

2. These compounds will be chemically and structurally characterised using the usual spectroscopic, analytical and X-ray diffraction techniques. Once their structures have been confirmed, their magnetic properties will be investigated, from an experimental point of view, through direct current (*dc*) and alternating current (*ac*) magnetic measurements and, from a theoretical point of view, using *ab initio* calculations. This approach aims to determine if the compounds exhibit slow magnetic relaxation and single-ion magnet (SIM) behavior. If such behavior is observed, it will be determined whether other magnetisation relaxation mechanisms occur besides the thermally activated one (Raman, QTM, direct process) and the thermal activation barrier will be calculated. The electronic structure of the Dy^{III} ion and the relative orientation of the main anisotropy axes will be analyzed through a detailed study by *ab initio* calculations.

3. To analyse if there is a change in the magnetic properties when changing the geometry of the lanthanide ion coordination sphere from pentagonal bipyramid to octahedral and the causes of this change. For this purpose, the same lanthanide ion salt, namely anhydrous $DyCl_3$, will be used and the experimental conditions will be modified to try to obtain both geometries.

4. To study, for the same coordination geometry, if the change of coordinated halogen in equatorial position affects the magnetic properties. For this purpose, the magnetic properties of the compounds obtained in this

doctoral thesis will be compared with others obtained previously by our research group.

5. To determine if the mentioned phosphine oxide ligand can act as an antenna to sensitize lanthanide luminescence and, in this way, know if any of these complexes exhibit luminescent properties that can give rise to bifunctional magneto-luminescent materials. If luminescence is observed in the compounds, TD-DFT calculations will be carried out to reveal the different pathways that take part in the lanthanide sensitization.

6. Synthesis of chiral and luminescent Zn^{III}-Ln^{III}-Zn^{II} complexes (Ln^{III} = Dy^{III}, Tb^{III}) from the chiral Mannich base ligands ($H_2L_{R,\,R}$ and $H_2L_{S,\,S}$) shown in Scheme 2.2 and Ln $(CF_3SO_3)_3$ salts.

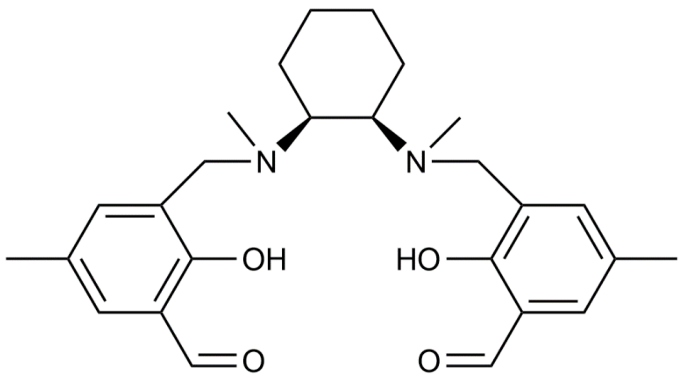

Scheme 2.2: Structure of the designed chiral Mannich base ligand.

These Mannich base ligands have two different cavities, the inner N_2O_2 and the outer O_2O_2, through which the Zn^{II} and Ln^{III} ions can coordinate and give rise to hetero-trinuclear complexes. The Ln^{III} ion will exhibits an axially

distorted square antiprism LnO_8 coordination sphere with a disposition of the phenoxo bridging oxygen atoms (shortest Ln–O distances) and the aldehyde oxygen atoms (larger Ln–O distances) that will give rise to high effective energy barriers.

7. These trinuclear compounds will be chemically and structurally characterised using the usual spectroscopic, analytical and X-ray diffraction techniques. Once their structures have been confirmed, their magnetic properties will be investigated, from an experimental point of view, through direct current (*dc*) and alternating current (*ac*) magnetic measurements and, from a theoretical point of view, using *ab initio* calculations. This approach aims to determine if the compounds exhibit slow magnetic relaxation and single-ion magnet (SIM) behavior. If such behavior is observed, it will be determined whether other magnetisation relaxation mechanisms occur besides the thermally activated one (Raman, QTM, direct process) and the thermal activation barrier will be calculated. The electronic structure of the Dy^{III} ion and the relative orientation of the main anisotropy axes will be analyzed through a detailed study by *ab initio* calculations.

CHAPTER 3

MONONUCLEAR Ln^{III} COMPLEXES WITH PHOSPHINE OXIDE LIGANDS

3.1 INTRODUCTION

Ln-based complexes have made significant advancements in SMM field, owing to their inherent large magnetic moments and magnetic anisotropy, which are further enhanced by the surrounding ligand field. This includes complexes such as Dy^{III},[1] Tb^{III},[2] Ho^{III},[3] and Er^{III},[4] which have all contributed to notable progress in this research field.

The Dy^{III} mononuclear $[Dy(C_5Me_5(Cp^{iPr5})][B(C_6F_5)_4]$[1d] and the mixed-valence $Dy^{III}Dy^{II}$ dinuclear $[Dy_2I_3(Cp^{iPr5})_2]$ metallocene[1f] compounds have achieved remarkable performance with U_{eff} values of 2217 K and 2347 K, respectively, and a T_B of 80 K in both cases, surpassing the temperature of liquid nitrogen. This breakthrough paves the way for potential commercial applications of these molecules in technology. However, their major limitation is their extreme instability. Mononuclear SMMs with bipyramid pentagonal geometry occupy a relevant place because they display in most of the cases (there are some exceptions[5]) thermal air and humidity stability, with U_{eff} and T_B value as high as 1162 K[6] and 36 K[7] in Dy^{III} SIMs, respectively.

Furthermore, the combination of SMM and luminescence in the same compound leads to magneto-luminescent multifunctional materials that can display a synergistic effect due to the interaction of both properties.[8] Moreover, these systems are useful to establish an experimental correlation experimental between the emissions, the electronic structure and the relaxation dynamics.[9]

In view of the previous considerations, in this chapter we present a series of multifunctional mononuclear lanthanide complexes with bipyramid pentagonal geometry, luminescent properties and field-induced SMM behaviour.

3.2 SYNTHESIS OF LIGAND

In a round-bottom flask, the di(1-adamantyl)benzylphosphine (0.5 g, 1.274 mmol) was dissolved in the minimum amount of dichloromethane and reacted with an excess of 30 % hydrogen peroxide in water (10 mL/g of di(1-adamantyl)benzylphosphine) and allowed to stir under ambient conditions for 12 hours, during which time the solution changed from clear to light yellow in color. Upon completion, the reaction mixture was washed three times with water, then three times with brine solution, dried with sodium sulphate and filtered. Finally, the solvent was removed under reduced pressure. Yield: 85%. IR (cm^{-1}): 3000-2800, ν(C-H, alkyl and aromatic); 1601, ν(C=C); 1500-1300, ν(C-H, alkyl and aromatic); 1200-1100, ν(P=O); 700, ν(P-C). Anal. Calc. for $C_{27}H_{37}OP$, C: 79.37%, H: 9.13%. Found C: 79.38%, H: 8.92% ^{1}H NMR ($CDCl_3$, ppm): 7.47-7.18 (m, H_{Ar}), 3.15 (d, $H_{methylene}$), 2.17-1.70 (m, H_{Ad}). ^{31}P NMR ($CDCl_3$, ppm): 48.45 (s).

3.3 SYNTHESIS OF COMPLEXES

3.3.1 Synthesis of complex [Dy(OPAd$_2$Bz)$_2$(H$_2$O)$_4$Cl]Cl$_2$·2THF (1)

Solid anhydrous $DyCl_3$ (22.85 mg, 0.085 mmol) in dry THF (7 mL) was heated at 80 ºC in aerobic conditions until $DyCl_3$ was dissolved and a clear solution was obtained. Additional dry THF was added when necessary while heating. After that, the ligand di(1-adamantyl)benzylphosphine oxide (70 mg, 0.17 mmol) was added and next, dry THF until reaching a final volume of 10 mL. The resulting mixture was sealed in a 25 mL teflon-lined stainless container and kept at 100 ºC for three days. The solution obtained was filtered and after several days, X-ray quality colourless crystals were obtained from slow evaporation of the mother solution. Yield: 27%. Anal. Calc. for $C_{62}H_{98}Cl_3DyO_8P_2$, C: 57.18%, H: 7.59%. Found C: 57.17%, H: 7.48%. IR (cm^{-1}): 2900-2800, ν(C-H alkyl and aromatic); 1600-1500, ν(C=C); 1500-1300 δ(C-H alkyl and aromatic); 1200-1100, ν(P=O); 700, ν(P-C).

3.3.2 Synthesis of complex [Yb(OPAd$_2$Bz)$_2$(H$_2$O)$_4$Cl]Cl$_2$·2THF (2)

This complex was synthesised following the same procedure as for **1** but using anhydrous $YbCl_3$ (23.75 mg, 0.085 mmol) instead of $DyCl_3$. After several days, X-ray quality pale yellow crystals were obtained by slow evaporation of hexane into the mother solution. Yield: 31%. Anal. Calc. for $C_{62}H_{98}Cl_3YbO_8P_2$, C: 57.72%, H: 7.52%. Found C: 57.72%, H: 7.75%. IR (cm^{-1}): 2900-2800, ν(C-H alkyl and aromatic); 1600-1500, ν(C=C); 1500-1300 δ(C-H alkyl and aromatic); 1200-1100, ν(P=O); 700, ν(P-C).

3.3.3 Synthesis of complex [Tb (OPAd$_2$Bz)$_2$(H$_2$O)$_4$Cl]Cl$_2$·3THF·1.5H$_2$O (3)

This complex was synthesised following the same procedure as for **1** but using anhydrous $TbCl_3$ instead of $DyCl_3$ and different quantity of reagents ($TbCl_3$ (32.46 mg, 0.125 mmol); ligand (100 mg, 0.25 mmol)). After several

days, suitable colourless crystals for X-ray diffraction were obtained from slow evaporation of the mother solution. Yield: 29%. Anal. Calc. for $C_{66}H_{109}Cl_3TbO_{10.5}P_2$, C: 56.71%, H: 7.86%. Found C: 56.61%, H: 8.02%. IR (cm^{-1}): 2900-2800, ν(C-H alkyl and aromatic); 1600-1500, ν(C=C); 1500-1300 δ(C-H alkyl and aromatic); 1200-1100, ν(P=O); 700, ν(P-C).

3.3.4 Synthesis of complex $[Gd(OPAd_2Bz)_2(H_2O)_4Cl]Cl_2 \cdot 1.8THF$ (4)

This complex was synthesised following the same procedure as for **1** but using anhydrous $GdCl_3$ instead of $DyCl_3$ and double quantity of reagents ($GdCl_3$ (44.82 g, 0.17 mmol); ligand (140 mg. 0.34 mmol)). Crystallization from slow diffusion of hexane into the THF solution produces quality colourless single crystals for X-ray diffraction. Yield: 14%. Anal. Calc. for $C_{61.2}H_{96.4}Cl_3GdO_{7.8}P_2$, C: 57.31%, H: 7.58%. Found C: 57.29%, H: 7.73%. IR (cm^{-1}): 2900-2800, ν(C-H alkyl and aromatic); 1600-1500, ν(C=C); 1500-1300 ν(C-H alkyl and aromatic); 1200-1100, ν(P=O); 700, ν(P-C).

3.3.5 Synthesis of complex $[Dy(OPAd_2Bz)_2(THF)Cl_3]$ (5)

In a two-neck round-bottom flask, anhydrous $DyCl_3$ (32.90 mg, 0.12 mmol) in THF (8 mL) under inert atmosphere was refluxed until the metal salt was completely dissolved. Next, a solution of the ligand di(1-adamantyl)benzylphosphine oxide (100 mg, 0.25 mmol) in dry THF (8 mL) was added drop by drop using a syringe and, the resulting solution was refluxed for one hour. Then, the solution was filtered and suitable colourless crystals were obtained from slow diffusion of hexane into the mother solution. Yield: 71%. Anal. Calc. for $C_{58}H_{82}Cl_3DyO_3P_2$, C: 60.15%, H: 7.14%. Found C: 60.18%, H: 7.14%. IR (cm^{-1}): 2900-2800, ν(C-H alkyl and aromatic); 1600-1500, ν(C=C); 1500-1300 δ(C-H alkyl and aromatic); 1200-1100, ν(P=O); 700, ν(P-C).

3.3.6 Synthesis of complex [Eu(OPAd$_2$Bz)$_2$(H$_2$O)Cl$_3$]·1.4 THF (6)

This complex was synthesised following the same procedure as for **5** but using anhydrous $EuCl_3$ instead of $DyCl_3$ and different quantities ($EuCl_3$ ((21.96 mg, 0.085 mmol); ligand (70 mg, 0.17 mmol)). After few days, pale pink single crystals for X-ray diffraction were obtained from slow diffusion of hexane into the mother solution. Yield: 18%. Anal. Calc. for $C_{59.4}H_{86.8}Cl_3EuO_{4.4}P_2$, C: 59.95%, H: 7.21%. Found C: 59.94%, H: 7.21%. IR (cm^{-1}): 2900-2800, ν(C-H alkyl and aromatic); 1600-1500, ν(C=C); 1500-1300 δ(C-H alkyl and aromatic); 1200-1100, ν(P=O); 700, ν(P-C).

3.3.7 Synthesis of complex [Gd(OPAd$_2$Bz)$_2$(THF)Cl$_3$] (7)

This complex was synthesised following the same procedure as for **6** but using anhydrous $GdCl_3$ (22.41 mg, 0.085 mmol) instead of $EuCl_3$. Crystallization from slow diffusion of hexane into the mother solution produces suitable colorless single crystals for X-ray diffraction. Yield: 25%. Anal. Calc. for $C_{58}H_{82}Cl_3GdO_3P_2$, C: 60.43%, H: 7.17%. Found C: 60.37%, H: 7.16%. IR (cm^{-1}): 2900-2800, ν (C-H alkyl and aromatic); 1600-1500, ν (C=C); 1500-1300 δ(C-H alkyl and aromatic); 1200-1100, ν (P=O); 700, ν (P-C).

3.4 RESULTS AND DISCUSSION

With the purpose of obtaining complexes with bipyramid pentagonal coordination geometry and good SMM properties, we have designed and prepared a phosphine oxide ligand (figure 3.1), concretely, the ligand di(1-adamantyl)benzylphosphine oxide. In this ligand, the inductive effects from diadamantyl groups will increase the electronic density at the phosphine oxide oxygen atom which will have a high tendency to bind Ln^{III} ions and, then, form coordination complexes. Due to their steric hindrance, only two of these ligands will occupy *trans* positions, creating a considerably strong axial crystal-field. Additionally, the ligand contains a phenyl group for lanthanide emission. The equatorial positions will be occupied by auxiliary ligands such as H_2O or THF as they will lead to weak fields.

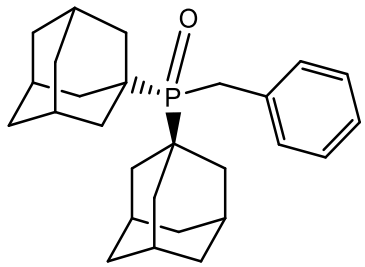

Figure 3.1: Scheme of the designed phosphine oxide ligand

The reaction in solvothermal conditions of anhydrous $LnCl_3$ (Ln = Dy^{III}, Yb^{III}, Tb^{III}, Gd^{III}) with the ligand di(1-adamantyl)benzylphosphine oxide in a 1:2 molar ratio using THF as solvent and further slow evaporation of the resulting solution or slow diffusion of hexane into the mother solution, results in the formation of complexes of formula $[Ln(OPAd_2Bz)_2(H_2O)_4Cl]Cl_2 \cdot xTHF \cdot zH_2O$ (Ln = Dy^{III}, x = 2, z = 0 (**1**); Ln = Yb^{III}, x = 2, z = 0 (**2**); Ln = Tb^{III}, x = 3, z = 1.5 (**3**); Ln = Gd^{III}, x = 1.8, z = 0 (**4**)), where the lanthanide ion exhibit a pentagonal bipyramidal coordination geometry. However, if the synthetic conditions are changed, a series of

complexes of formula $[Ln(OPAd_2Bz)_2(z)Cl_3]\cdot xTHF$ ($Ln = Dy^{III}$, z = THF, x = 0 (**5**); $Ln = Eu^{III}$, z = H_2O, x = 1.4 (**6**); $Ln = Gd^{III}$, z = THF, x = 0 (**7**)) are obtained by refluxing, in inert atmosphere, the ligand with anhydrous $LnCl_3$ in a 2:1 molar ratio using THF as solvent and further slow evaporation of hexane into the mother solution. In these cases, the Ln^{III} ions present a distorted octahedral coordination environment.

In view of these results, it seems that the coordination geometry adopted by the metal ion depends, to a greater extent, on the synthetic methodology employed in each case (solvothermal methods or reflux) than on the nature of the lanthanide ion.

3.4.1 Crystal structures of complexes 1-4

The structures of compounds **1-4** are very similar, so that only the structure of **1** will be described as a representative example, indicating, in any case, the differences between them. The complexes **1** and **2** crystallize in the tetragonal I_4 space group while compounds **3** and **4** crystallize in the $P4_3$ space group. Crystallographic data and structural refinement details for compounds **1-4** are shown in Table 3.1.

The structure of **1** consists of distorted pentagonal bipyramidal mononuclear $[Dy(OPAd_2Bz)_2(H_2O)_4Cl]^{2+}$ cationic units together with two chloride counteranions and two THF solvent molecules (the same for **2)**, while in compound **4** there are 1.8 THF molecules (figure 3.2). Compound **3** crystallizes with two chloride anions, three THF and one and a half water solvent molecules.

Table 3.1: Crystallographic data and structural refinement details for complexes **1-4**

Compound	**1**	**2**	**3**	**4**
Formula	$C_{31}H_{49}Cl_{1.5}Dy_{0.5}O_4P$	$C_{31}H_{49}Cl_{1.5}Yb_{0.5}O_4P$	$C_{66}H_{109}Cl_3TbO_{10.5}P_2$	$C_{61.2}H_{96.4}Cl_3GdO_{7.8}P_2$
M_r	651.09	656.36	1397.80	1282.49
Crystal System	Tetragonal	Tetragonal	Tetragonal	Tetragonal
Space Group	$I\bar{4}$	$I\bar{4}$	$P4_3$	$P4_3$
a (Å)	24.3000(13)	24.1565(11)	24.1557(6)	24.2107(8)
b (Å)	24.3000(13)	24.1565(11)	24.1557(6)	24.2107(8)
c (Å)	12.2067(10)	12.1744(8)	12.2000(4)	12.1822(6)
α (°)	90	90	90	90
β (°)	90	90	90	90
γ (°)	90	90	90	90
V (Å^3)	7207.9(10)	7104.2(8)	7118.7(4)	7140.7(6)
Z	8	8	4	4
Dc (g cm^{-1})	1.200	1.227	1.304	1.190
μ(MoK$_\alpha$) (mm^{-1})	1.237	1.520	1.204	1.130
T (K)	150	100	100	100
Observed reflections[a]	8198 (7639)	10751 (9282)	21231 (20992)	21479 (20458)
R_{int}[a]	0.0320	0.0630	0.0266	0.0359
Parameters	354	348	766	749
GOF	1.177	1.113	1.185	1.081
R_1[b,a]	0.0620 (0.0568)	0.0531 (0.0386)	0.0300 (0.0297)	0.0474 (0.0445)
wR_2[c,a]	0.1570 (0.1528)	0.1109 (0.1046)	0.0775 (0.0773)	0.1142 (0.1212)

[a] Values in parentheses for reflections with I > 2s(I)
[b] $R1 = \sum||Fo| - |Fc||/\sum|Fo|$
[c] $wR2 = \{\sum [w(F_o^2 - F_c^2)^2] / \sum [w(F_o^2)^2]\}^{½}$

Within the mononuclear unit, two phosphine oxide ligands coordinate to the Dy^{III} atom in axial positions through the oxygen atom with a bond distance of 2.223 (5) Å. In the equatorial position, one chloride atom (2.708 (4) Å) and

four water molecules (average distance of 2.359 (9) Å) are coordinated to the Dy^{III}, leading to a DyO_6Cl coordination sphere. The Ln–O and Ln–Cl distances decrease from Gd^{III} ion to Yb^{III} due to the lanthanide contraction. The most significant bond lengths and angles are listed in Tables 3.2-3.5.

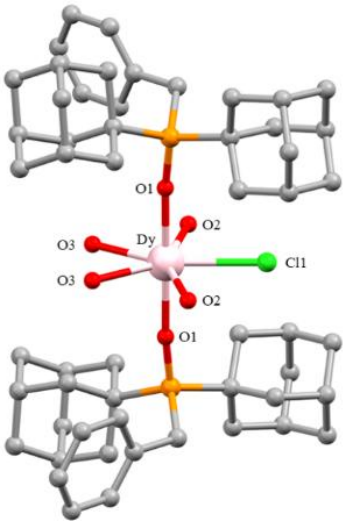

Figure 3.2: Crystal structure of **1**. Hydrogen atoms, anions and solvent molecules are omitted for clarity. Color code: Dy pink, C grey, O red, P orange, Cl green.

Table 3.2: Selected bond distances (Å) and angles (º) for complex **1**.

Selected bond distances (Å)			
Dy1-O1	2.223 (5)	Dy1-Cl1	2.708 (4)
Dy1-O2	2.350 (9)	O1-P1	1.513 (5)
Dy1-O3	2.367 (8)		
Selected bond angles (º)			
O1-Dy1-O2	87.6 (3)	O2-Dy1-O3	72.8 (4)
O1-Dy1-O2	92.7 (3)	O2-Dy1-Cl1	74.1 (3)
O1-Dy1-O3	88.0 (3)	O3-Dy1-O3	66.5 (7)
O1-Dy1-O3	90.9 (3)	O1-Dy1-O1	178.8 (3)
O1-Dy1-Cl1	90.62 (18)	Dy1-O1-P1	172.6 (4)

Table 3.3: Selected bond distances (Å) and angles (º) for complex **2**.

Selected bond distances (Å)			
Yb1-O1	2.163 (4)	Yb1-Cl1	2.673 (2)
Yb1-O2	2.313 (5)	O1-P1	1.524 (4)
Yb1-O3	2.328 (5)		
Selected bond angles (º)			
O1-Yb1-O2	92.44 (19)	O2-Yb1-O3	71.3 (3)
O1-Yb1-O2	87.68 (19)	O2-Yb1-Cl1	75.1 (2)
O1-Yb1-O3	88.43 (17)	O3-Yb1-O3	67.3 (4)
O1-Yb1-O3	91.18 (17)	O1-Yb1-O1	179.5 (2)
O1-Yb1-Cl1	90.24 (11)	Yb1-O1-P1	173.5 (3)

Table 3.4: Selected bond distances (Å) and angles (º) for complex **3**.

Selected bond distances (Å)			
Tb1-O1	2.234 (3)	Tb1-O6	2.367 (3)
Tb1-O2	2.243 (3)	Tb1-Cl1	2.720 (11)
Tb1-O3	2.3781 (3)	O1-P1	1.520 (3)
Tb1-O4	2.393 (3)	O2-P2	1.509 (3)
Tb1-O5	2.396 (3)		
Selected bond angles (º)			
O1-Tb1-O3	85.96 (12)	O2-Tb1-Cl1	88.21 (10)
O1-Tb1-O4	92.48 (13)	O3-Tb1-O4	70.53 (13)
O1-Tb1-O5	88.51 (13)	O3-Tb1-Cl1	73.94 (9)
O1-Tb1-O6	89.64 (12)	O4-Tb1-O5	67.78 (13)
O1-Tb1-Cl1	92.79 (10)	O5-Tb1-O6	71.17 (13)
O2-Tb1-O3	96.90 (12)	O6-Tb1-Cl1	77.24 (10)
O2-Tb1-O4	88.30 (13)	O1-Tb1-O2	177.14 (12)
O2-Tb1-O5	89.24 (13)	Tb1-O1-P1	171.5 (2)
O2-Tb1-O6	87.96 (12)	Tb1-O2-P2	172.0 (2)

Table 3.5: Selected bond distances (Å) and angles (º) for complex **4**.

Selected bond distances (Å)			
Gd1-O1	2.256 (3)	Gd1-O6	2.368 (5)
Gd1-O2	2.250 (3)	Gd1-Cl1	2.714 (2)
Gd1-O3	2.388 (5)	O1-P1	1.513 (3)
Gd1-O4	2.408 (5)	O2-P2	1.520 (4)
Gd1-O5	2.390 (5)		
Selected bond angles (º)			
O1-Gd1-O3	85.93 (16)	O2-Gd1-Cl1	90.29 (11)
O1-Gd1-O4	91.38 (16)	O3-Gd1-O4	71.1 (3)
O1-Gd1-O5	87.42 (16)	O3-Gd1-Cl1	73.85 (18)
O1-Gd1-O6	91.42 (19)	O4-Gd1-O5	67.5 (3)
O1-Gd1-Cl1	92.25 (11)	O5-Gd1-O6	71.5 (3)
O2-Gd1-O3	96.14 (17)	O6-Gd1-Cl1	76.6 (2)
O2-Gd1-O4	87.37 (16)	O1-Gd1-O2	177.09 (16)
O2-Gd1-O5	89.67 (17)	Gd1-O1-P1	171.0 (3)
O2-Gd1-O6	87.79 (17)	Gd1-O2-P2	171.1 (3)

Continuous shape measurements using SHAPE software[10] (see Table 3.6) indicate that the DyO_6Cl coordination geometry is very close to the ideal pentagonal bipyramid polyhedron (PBPY-7 = 0.574). The apical distances are shorter than the equatorial ones, just indicating that the cationic unit shows a compressed PBPY-7 geometry with an almost linear axial O1–Dy1–O1 angle (178.8 (3)°) and equatorial Cl1–Dy–O2, O2–Dy–O3 and O3–Dy–O3 angles of 74.1 (3)°, 72.8 (4)° and 66.5 (7)°, respectively, close to the ideal angle of 72°. It seems that the coordinated chloride atom causes certain steric repulsion with the water molecules close to it, which is reflected in a Cl1–Dy–O2 angle greater than 72° for an ideal pentagon. Consequently, this implies a nearness between these two water molecules with the other two, leading to O3–Dy–O3 angle smaller than 72°. The P–O1–Dy angle is also very close to linearity

(172.6 (4)°) and the angles between the equatorial and axial atoms are around 90° (Table 3.2). The shortest Dy···Dy intermolecular distance of 12.527 Å indicates that the mononuclear $[Dy(OPAd_2Bz)_2(H_2O)_4Cl]^{2+}$ units are well isolated in the structure.

Table 3.6: Obtained S values with the SHAPE software for complexes **1-4**.

Complex		**JETPY-7**	**JPBPY-7**	**CTPR-7**	**COC-7**	**PBPY-7**	**HPY-7**	**HP-7**
1	Dy	23.659	2.720	6.055	7.740	0.574	25.557	33.805
2	Yb	24.036	2.612	6.026	7.717	0.648	25.096	33.744
3	Tb	23.139	2.834	5.204	7.015	0.716	24.351	33.548
4	Gd	23.673	2.845	5.456	7.165	0.635	25.000	33.612

JETPY-7 = Johnson elongated triangular pyramid J7; JPBPY-7 = Johnson pentagonal bipyramid J13; CTPR-7 = Capped trigonal prism; COC-7 = Capped octahedron; PBPY-7 = Pentagonal bipyramid; HPY-7 = Hexagonal pyramid; HP-7 = Heptagon

In compounds **1-4**, there are hydrogen bond interactions between the coordinated water molecules and THF solvent molecules with donor-acceptor distances of 2.725 Å for **1**, 2.717 Å for **2**, 2.747 Å and 2.756 Å for **3** and 2.782 Å and 2.926 Å for **4**. In addition, there exist intermolecular interactions between the coordinated water molecules and the non-coordinated chloride anions with O···Cl distances of 2.799 and 3.224 Å for **1**, 2.786 and 2.819 Å for **2**, 2.973 Å and 3.044 Å for **3** and average distances of 2.562 Å and 2.887 Å for **4**. Moreover, in **3** there are also hydrogen bond interactions between the water molecules (coordinated and non-coordinated), as well as between the coordinated chloride atom and non-coordinated water molecules with average O···O distances of 2.554 Å and Cl···O distances of 3.087 Å, respectively. There are no π···π stacking interactions in **1-4** between the aromatic benzene rings of different units.

3.4.2 Magnetic properties of complex 1

The *dc* magnetic properties of **1** were collected in the 2-300 K temperature range under an applied magnetic field of 1000 Oe and they are shown in the form of the temperature dependence of $\chi_M T$ (χ_M is the molar magnetic susceptibility) in Figure 3.3.

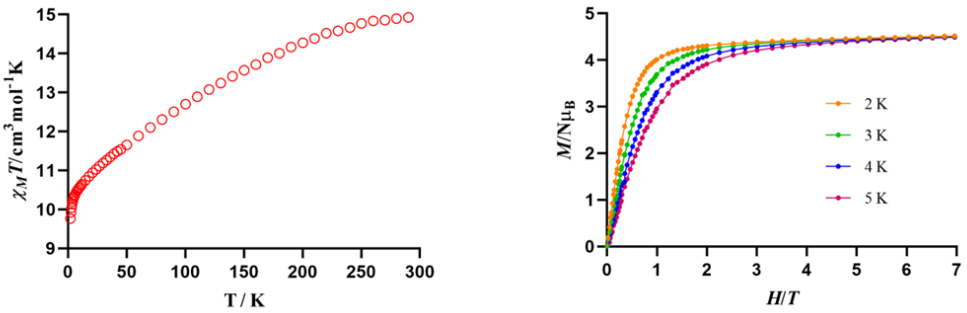

Figure 3.3: Temperature dependence of $\chi_M T$ (left) and field dependence of the magnetization (right) at the indicted temperatures for **1**.

At room temperature, the $\chi_M T$ value of 15.02 cm^3 mol^{-1} K is higher but still in accordance to the expected value for an isolated Dy^{III} ion (14.17 cm^3 K mol^{-1} with S = 5/2, g_J = 4/3). When lowering the temperature, the $\chi_M T$ value gradually decreases until approximately 10 K, below which it decreases abruptly until 9.77 cm^3 K mol^{-1}. This decrease is due to the depopulation of the m_j levels of the Dy^{III} ions generated from the splitting of the spin-orbit coupling ground level by the ligands crystal field. It is discarded that this decrease is due to the existence of weak intermolecular interactions between the Dy^{III} ions since the molecular units are well isolated in the crystal structure.

The field dependence of the magnetization for **1** (figure 3.3, right) indicates that the magnetization, in the low field region, increases rapidly with the increase of the external magnetic field and slightly from 1 T to 7 T,

reaching the saturation. The M value at the higher applied field of 7 T (4.52 Nβ at 2 K) significantly deviates from the expected 10 *N*β saturation value, proving the existence of a significant magnetic anisotropy which is caused by the ligands' crystal field.

To explore if **1** present slow relaxation of the magnetisation, temperature and frequency dependent measurements of the *ac* magnetic susceptibility have been carried out, under an alternating field of 3 Oe on a polycrystalline sample. Under zero *dc* field, there is a frequency dependent of the out-of-phase signals (χ_M'') but without maxima (figure 3.4, left) due to the existence of a significant QTM which is generated from dipolar and/or hyperfine interactions that allow the mixture of the degenerated $+m_j$ and $-m_j$ levels at both sides of the barrier.

In order to eliminate the QTM effect, temperature and frequency dependence of the *ac* susceptibility under an external *dc* field of 1000 Oe was measured. In these conditions, complex **1** shows obvious frequency and temperature dependence of the out-of-phase signals with well-defined maxima between 6 K (100 Hz) and 16 K (10000 Hz) (figure 3.4, right) indicating that complex **1** exhibit slow relaxation of the magnetisation and field-induced SIM behaviour. Moreover, the out-of-phase susceptibility signals at temperatures below the maximum indicates that the QTM has been significantly but not totally eliminated, allowing the observation of slow magnetization relaxation (figure 3.4, right).

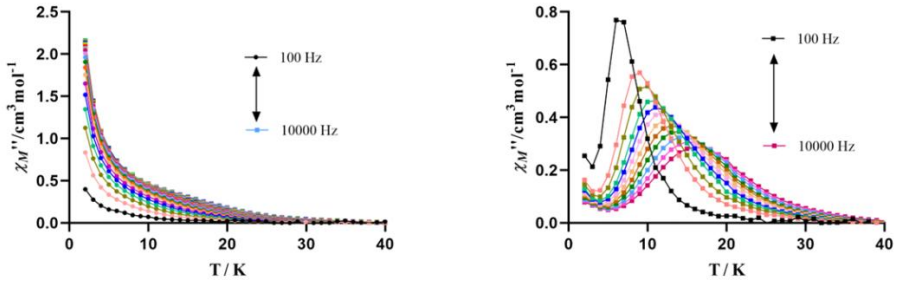

Figure 3.4: Temperature dependence of the out-of-phase *ac* susceptibility signals (χ_M'') for **1** at 0 Oe (left) and at 1000 Oe (right)

The relaxation times for **1** have been determined from the fitting of the frequency dependence of the χ_M'' signals to the generalized Debye model (figure 3.5, left). As shown in figure 3.5 right, at high temperatures, the representation of Ln τ vs 1/T presents a linear region which correspond to the thermally activated process (Orbach process). The fitting of this linear region to the Arrhenius law leads to an effective energy barrier of U_{eff} = 57.91 K and τ_0 = 9.86 x 10^{-7} s. Although there exist other pentagonal bipyramidal field-induced Dy^{III} SIMs with similar U_{eff} values,[11] this value is rather small taking into account the pentagonal bipyramidal geometry of the Dy^{III} ion and the quasi-linearity of the axial O–Dy–O sequence. The reason for this behavior is explored in detail in Subsection 3.4.3 through quantum-chemical calculations.

The Cole−Cole plot (Figure 3.6) shows, in the 7 K-15 K temperature region, relatively semicircular shapes with α values in the range of 0.20−0.28. The observed α values for **1** and the deviation from linearity of the Ln τ vs 1/T representation at low temperatures (figure 3.5, right), suggest the existence of other competitive relaxation processes.

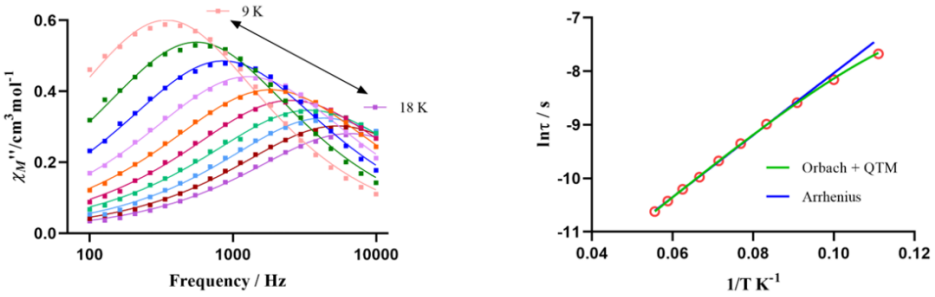

Figure 3.5: (left) Frequency dependence of the χ_M" signals at different temperatures for **1** under a field of 0.1 T. The solid lines represent the best fitting to the Debye model. (Right) Representation of Ln t vs 1/T for **1** at 0.1 T. The solid lines represent the best fit of the experimental data to the Arrhenius equation for a thermally activated process (blue) or for a combination of Orbach and QTM relaxation processes (green).

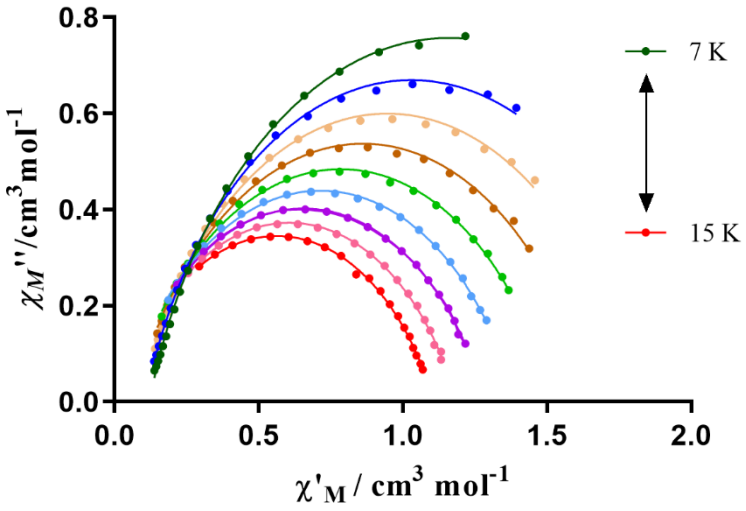

Figure 3.6: Cole-Cole plot for **1**

In view of this, new fittings have been carried out in the entire studied temperature range (9 K – 18 K) using the equation 1

$$\tau^{-1} = AT + \frac{B_1}{1+B_2H^2} + CT^n + \tau_0 \exp^{(-\frac{Ueff}{k_BT})} \quad \text{Equation 1}$$

where the first two terms represent the field-dependent direct and QTM processes, respectively, while the third and fourth terms represent the field-independent Raman and Orbach relaxation processes.

The efforts to fit using the sum of Orbach and Raman processes, or the sum of Orbach and Direct processes, were unsuccessful, suggesting that the QTM process was reduced greatly but not completely eliminated (as observed in figure 3.4, right). Then, the fit of the magnetic data to the combination of Orbach and QTM processes was excellent, leading to the following parameters: U_{eff} = 61.23 K, τ_0 = 8.28 x 10^{-7} s and τ_{QTM} = 1.4 x 10^{-3} s.

3.4.3 Computational calculations of complex 1

Ab initio calculations based on the experimental X-ray structural data of complex **1** were performed in order to confirm that the target molecule possesses the expected energetic scheme and to provide insight into the mechanism that governs the magnetic relaxation of complex **1**. In particular, multiconfigurational CASSCF[12] calculations with the SINGLE_ANISO[13] code implemented in ORCA 5.0.4 program package[14-16] were carried out. These methodologies are quite helpful to elucidate and predict the electronic structure and relaxation mechanism of SIM complexes. The computed eight Kramers' doublets (KDs) for **1**, corresponding to the $^6H_{15/2}$ ground state of the Dy^{III} ion, span an energy range of about 616 cm^{-1} (Table 3.7). The ground KD (KD1) is a pure $m_J = |\pm 15/2\rangle$ state that is highly anisotropic (g_{zz} = 19.83) with very small transverse components ($g_{xx} \sim g_{yy} < 0.01$), establishing thus a strong magnetic anisotropy axis. The anisotropy g_{zz} axis is almost collinear with the pseudo-C_5

axis lying along the axial O–Dy–O bonds (the deviation between the g_{zz} axis and O–Dy–O direction is 2.1°, see Figure 3.7, left).

Table 3.7: CASSCF computed relative energies (in cm^{-1}) of the eight low-lying Kramers' doublets, g tensors for **1** and tilting angle (θ) of the main anisotropy axes of the corresponding excited (ES1, ES2, etc.) KD with respect to the ground state (GS) KD for **1**.

Energy (cm^{-1})	**g_{xx}**	**g_{yy}**	**g_{zz}**	**θ (°)**
0.0	0.004622	0.006815	19.831053	
265.27	11.195089	7.833638	1.215217	85.6
290.68	8.812928	7.449865	2.008383	84.2
384.27	10.426206	7.301708	2.585772	6.4
432.41	7.514461	5.154203	0.198311	84.7
455.84	0.737887	4.701380	11.563421	30.2
497.85	9.239861	6.047917	2.121482	90.0
616.36	0.033854	0.102655	18.853655	58.0

The first excited state (KD2) lies at 265.3 cm^{-1} above the ground state. This KD2 shows large transverse components of g (g_{xx} = 11.20 and g_{yy} = 7.83). In this case, the g_z tensor is perpendicular to the O–Dy–O direction and so to the g_{zz} anisotropy axis of the ground state (85.6º, Figure 3.7, right, and Table 3.7). The transverse components of KD2 can be large enough to promote magnetic relaxation *via* the first excited state. However, the absence of slow relaxation of magnetization at zero field suggests that magnetic relaxation likely occurs via other relaxation pathways (see below). The next excited state (KD3) is close in energy (290.7 cm^{-1}) and also shows large transverse components of g (g_{xx} = 8.81 and g_{yy} = 7.45).

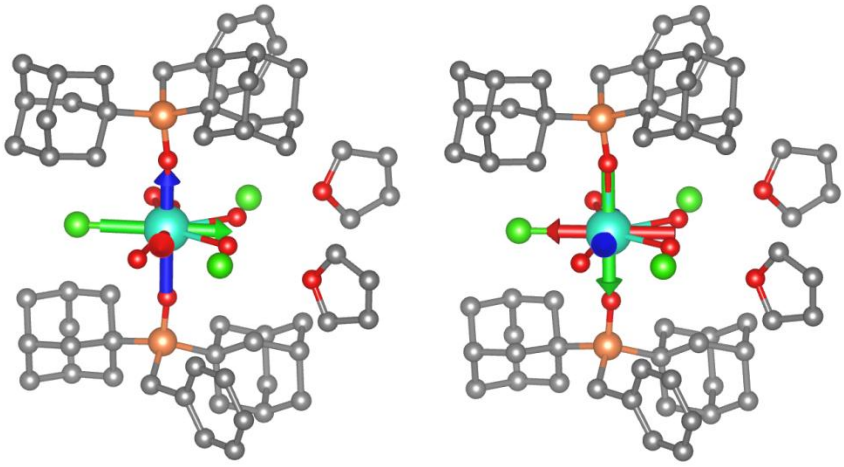

Ground KD (KD1) **First excited KD (KD2)**

Figure 3.7: Orientation of the *g*-tensor components obtained from CASSCF calculations for the ground Kramers' doublet (left) and first excited KD (right) of complex **1** using ORCA. The reference axis *x*, *y* and *z* of the *g*-tensor are displayed in red, green and blue, respectively. Code colours: dysprosium (cyan), oxygen (red), chloride (green), phosphorus (orange), and carbon (grey). Hydrogen atoms have been omitted for clarity.

The computed transverse magnetic moments help to shed light on the relaxation mechanism of **1** (Figure 3.8). The ground state exhibits a transverse magnetic moment of 0.19×10^{-2} μ_B, which is small enough to allow for slow relaxation of the magnetization, as the threshold value of 0.1 μ_B is commonly considered the limit for this behavior.[17] The absence of this experimental slow relaxation of the magnetization could be attributed to intermolecular interactions (although the molecules are sufficiently spaced, as noted earlier) and/or hyperfine interactions that may induce Quantum Tunneling of Magnetization (QTM) at zero field. Hyperfine interactions, through the coupling of nuclear and electron spins, could introduce additional relaxation pathways.

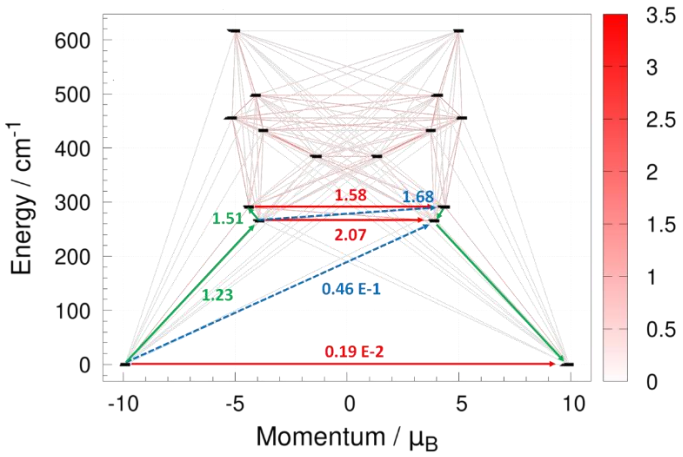

Figure 3.8. *Ab initio* calculated relaxation pathways in compound **1**. The black lines indicate the KDs as a function of the magnetic moments. Red lines denote QTM in the ground state and TA/QTM through the first and second excited states. Blue dashed lines represent possible Orbach processes.

However, in our group we studied a compound very similar to **1**, with bromine atoms instead of chlorine, and also having pentagonal bipyramid geometry. Its formula is $[Dy(OPAd_2Bz)_2(H_2O)_4Br]Br_2 \cdot 4THF$. It is striking that this compound with bromine atoms showed slow relaxation of magnetization at zero field, with quite high T_B (14 K) and U_{eff} (428 K) values for air/water stable SIMs.[18] The fact that this bromine compound, with similar distances and close structural parameters to **1,** exhibits slow magnetization relaxation leads us to think that this value of 0.19×10^{-2} μ_B, as proposed by some authors,[17] may not be enough to prevent QTM. To confirm this, tunnelling relaxation times were calculated according to an *ab initio* model based on spin-dipolar interaction in collaboration with Dr. Daniel Aravena (Universidad de Santiago de Chile).[19] The obtained preliminary results agree with this statement. For the ground state (KD1) of compound **1** the calculated tunnelling demagnetization is 50 times faster than for its bromine analogue. These results suggest that the issue is

intrinsic to the system, and it seems that replacing bromine with chlorine atoms may induce QTM in the ground state.

3.4.4 Magnetic properties of complex 2

The *dc* magnetic properties of **2** were collected in the 2-300 K temperature range under an applied magnetic field of 1000 Oe and they are shown in the form of the temperature dependence of $\chi_M T$ (χ_M is the molar magnetic susceptibility) in Figure 3.9

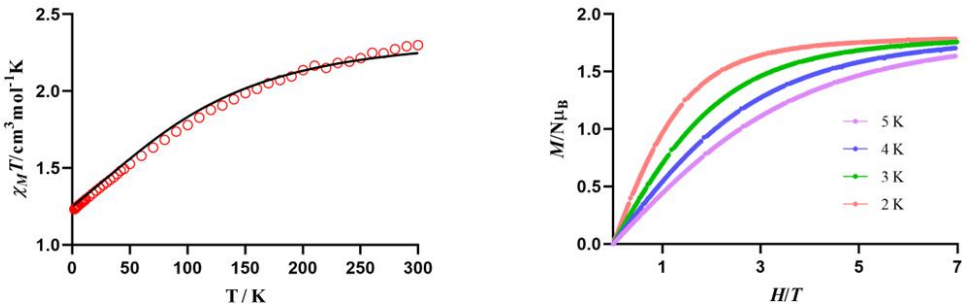

Figure 3.9: Temperature dependence of $\chi_M T$ (left) and field dependence of the magnetization (right) at the indicted temperatures for **2**. The solid black line represents the *ab initio* calculated $\chi_M T$ curve (scaled by 0.92).

At room temperature, the $\chi_M T$ value of 2.30 cm^3 K mol^{-1} for **2** matches well with the expected value for one free Yb^{III} ion (2.57 cm^3 K mol^{-1} with S = ½, g_J = 8/7). Upon cooling, the $\chi_M T$ value of **2** steadily decreases until reach a value of 1.23 cm^3 K mol^{-1} at 2 K. This decrease is due to the depopulation of the m_j levels of the Yb^{III} ions generated from the splitting of the spin-orbit coupling ground level by the ligands crystal field. It is discarded that this decrease is due to the existence of weak intermolecular interactions between the Yb^{III} ions since the molecular units are well isolated in the crystal structure.

The field dependence of the magnetization for **2** (figure 3.9, right) indicates that the magnetization increases rapidly at low fields and slightly from 1 T to H = 7 T, reaching the saturation. The M value at the higher applied field of 7 T (1.79 Nβ at 2 K) is significantly lower than the expected saturation value for the Yb^{III} ion (4 Nβ), probably due to the existence of a significant magnetic anisotropy caused by the splitting of the m_j levels by the crystal field created by the ligands.

In order to know if **2** presents slow relaxation of the magnetization, temperature and frequency dependent measurements of the *ac* magnetic susceptibility have been carried out, under an alternating field of 3 Oe on a polycrystalline sample. In absence of external field (H_{dc} = 0 Oe), this complex does not present out-of-phase signals (χ_M") above 2 K, indicating that either the thermal activation barrier is very small or there exists fast magnetization relaxation by QTM, which is generated from dipolar and/or hyperfine interactions that allow the mixture of the degenerated $+m_j$ and $-m_j$ levels at both sides of the barrier. In view of this, to eliminate partially or completely the QTM, a small external magnetic field can be applied to break off the degeneracy of the levels with the same m_j value at both sides of the energy barrier. To determinate the optimal magnetic field, *ac* measurements in the presence of different magnetic fields at 3 K have been performed for **2**. In this case, the field of 1000 Oe was chosen due to the maximum intensity in the χ_M" signal, and also because, above this field, the maxima of χ_M" signals are superimposed (figure 3.10).

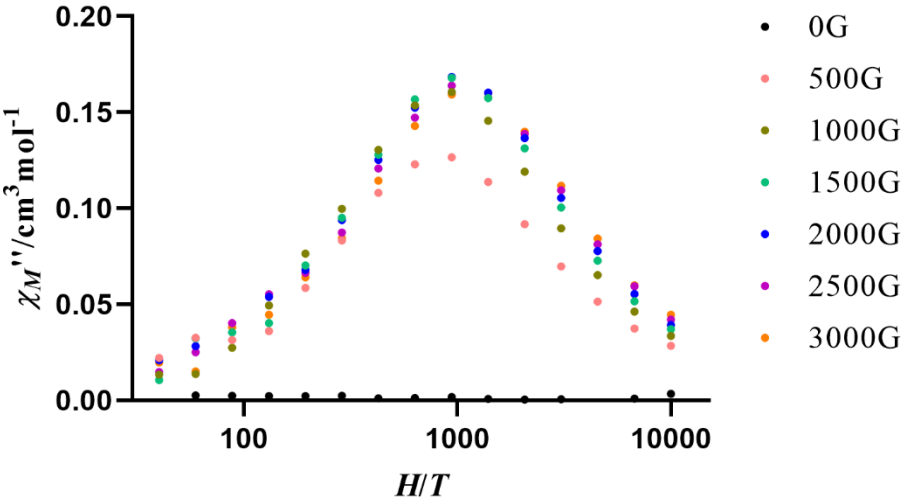

Figure 3.10: Field dependence of the out-of-phase signals (χ_M'') at different frequencies and 3 K for **2**.

Under an external field of 0.1 T, complex **2** shows a clear temperature and frequency dependence of the out-of-phase signals with maxima between 3 K (800 Hz) and 5.5 K (10000 Hz). Moreover, the out-of-phase susceptibility signals approach to zero at temperatures below the maximum, indicating that the QTM has been significantly eliminated, allowing the observation of slow magnetization relaxation (figure 3.11).

The relaxation times for **2** have been determined from the fitting of the frequency dependence of the χ_M'' signals to the generalized Debye model (figure 3.12, left). The fitting of the high temperature extracted relaxation times to an Arrhenius law, for a thermally activated process (Orbach process), leads to an effective energy barrier of U_{eff} = 18.77 K and τ_0 = 6.74 x 10^{-7} s (figure 3.12, right). These parameters are similar to those previously published for other pentagonal bipyramidal field-induced Yb^{III} SIMs.[20, 21]

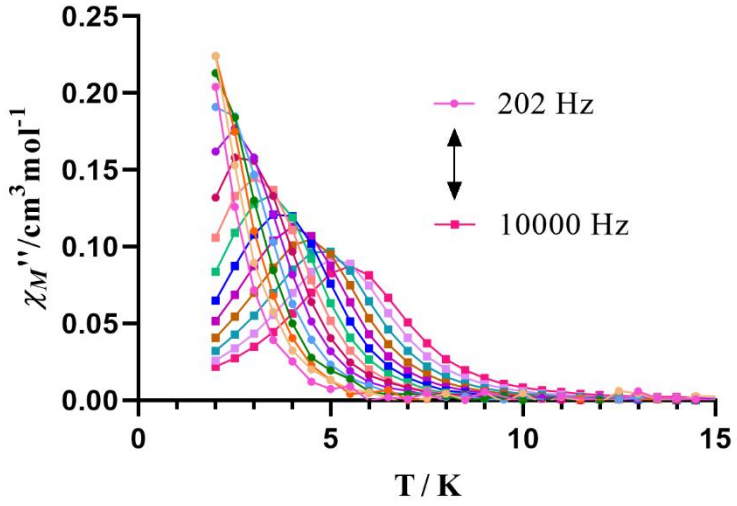

Figure 3.11: Temperature dependence of the out-of-phase ac susceptibility signals (χ_M") at 1000 Oe for **2**

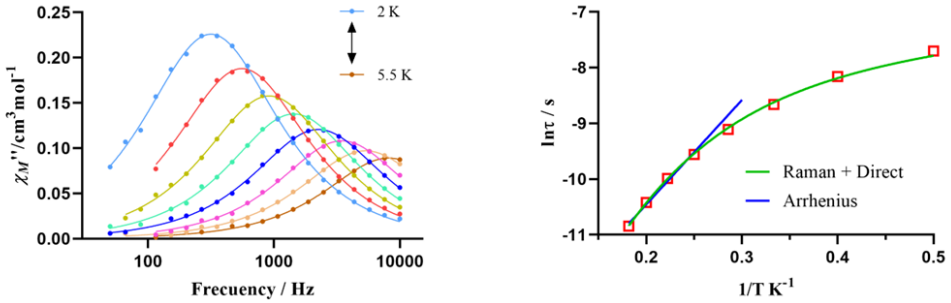

Figure 3.12: (left) Frequency dependence of the χ_M" signals at different temperatures for **2** under a field of 0.1 T. The solid lines represent the best fitting to the Debye model. (Right) Representation of Ln t vs 1/T for **2** at 0.1 T. The solid lines represent the best fit of the experimental data to the Arrhenius equation for a thermally activated process (blue) or for a combination of Raman and Direct relaxation processes (green).

The Cole–Cole plot (Figure 3.13) shows, in the 2 K-5 K temperature region, semicircular shapes with α values in the range of 0.06–0.1. Considering that α values close to zero indicate a single relaxation process, whereas α = 1 corresponds to an infinitely wide distribution of relaxation times, the α values observed for **2** at low temperature suggested the existence of several competitive relaxation processes.

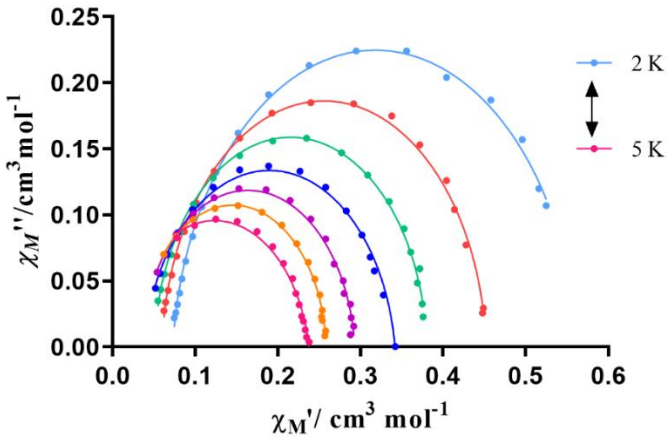

Figure 3.13: Cole-Cole plot for **2**

In view of this, new fittings have been carried out in the entire studied temperature range (2 K – 5.5 K) using the equation 1

$$\tau^{-1} = AT + \frac{B_1}{1+B_2H^2} + CT^n + \tau_0 \exp^{(-\frac{Ueff}{k_BT})} \quad \text{Equation 1}$$

where the first two terms represent the field-dependent direct and QTM processes, respectively, while the third and fourth terms represent the field-independent Raman and Orbach relaxation processes.

However, if the Orbach and/or QTM processes are considered in the equation 1, the fitting does not reproduce the experimental relaxation times. In fact, it is well known that the magnetic relaxation in Yb^{III} complexes generally takes place through a Raman process.[20, 22] In the case of **2**, the theoretically calculated energy gap between the ground a first excited Kramers doublets of 244.5 cm^{-1} is much larger than the effective energy barrier, U_{eff} = 18.77 K extracted from the Arrhenius plot thus supporting that the Orbach process, which takes place through real states, could be discarded for **2**. Therefore, the extracted τ vs T data were fitted to equation 1, but considering only that both direct and Raman processes contribute to the magnetic relaxation. The fit of the magnetic data to this combination of processes was excellent, leading to the following parameters: A = 1027 s^{-1} K^{-1}, C = 12.65 s^{-1} K^{-n} and n = 4.80. Although for Kramer ions as Yb^{III} ion the n value should be theoretically 9, *n* can also have values between 1 and 6 depending on the structure of the energy levels.[23] These parameters are similar to others Yb^{III} SIMs with the same relaxation mechanisms.[20, 21, 24]

3.4.5 Computational calculations of complex 2

Ab initio calculations, based on the experimental X-ray structural data of complex **2**, were carried out to verify that the molecule exhibits the anticipated electronic structure and to gain insight into the mechanism underlying its magnetic relaxation. As in compound **1**, multiconfigurational CASSCF[12] calculations with the SINGLE_ANISO[13] code implemented in ORCA 5.0.4 program package[14-16] were carried out. The computed seven Kramers Doublets (KDs) for **2**, corresponding to the four KDs of $^2F_{7/2}$ and three KDs of $^2F_{5/2}$, span an energy range of about 490 cm^{-1} and 10565 cm^{-1}, respectively (Table 3.8). The computed temperature dependence of $\chi_M T$ reproduces rather well the experimental temperature dependence of $\chi_M T$ (Figure 3.9, left). The ground

KD1 is an almost pure $m_J = |\pm 1/2\rangle$ state that shows large g_{xx} / g_{yy} values (g_{xx} = 5.12, g_{yy} = 3.97 and g_{zz} = 1.17, figure 3.14), which could promote QTM within the ground state.

Table 3.8: CASSCF computed relative energies (in cm^{-1}) of the seven Kramers Doublets and *g* tensors for **2**.

Energy (cm^{-1})	**g_{xx}**	**g_{yy}**	**g_{zz}**	**Wavefunction composition**
0.0	5.123933	3.966495	1.168982	99.0 |± 1/2 >
244.48	0.016056	1.167941	3.440506	97.4 |± 3/2 >
373.72	0.356761	1.231451	7.069514	62.0 |± 7/2 > + 36.5 |± 5/2 >
489.84	0.179423	0.854961	6.937494	61.9 |± 5/2 > + 36.8 |± 7/2 >
10173.86	2.807313	2.316409	0.815353	
10459.05	0.195214	0.467792	3.308989	
10565.41	0.293360	0.482721	4.070826	

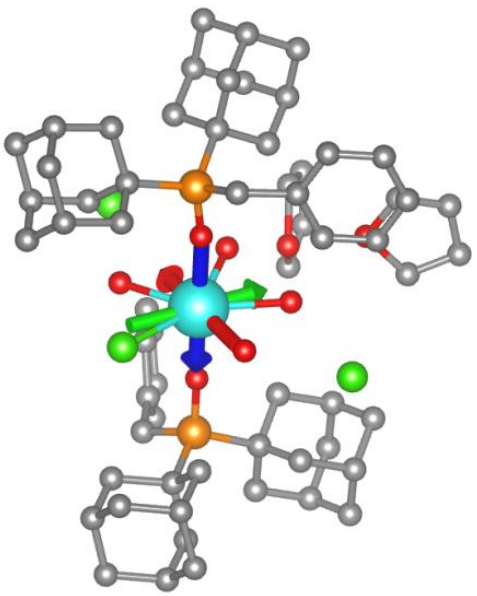

Figure 3.14: Orientation of the *g*-tensor components obtained from CASSCF calculations for **2**. The reference axis *x*, *y* and *z* of the *g*-tensor are displayed in red, green and blue, respectively. Code colours: yterbium (cyan), oxygen (red), chloride (green), phosphorus (orange), and carbon (grey). Hydrogen atoms have been omitted for clarity.

In order to better understand the relaxation mechanism, we have attempted to use computed crystal field parameters (Table 3.9). The corresponding crystal field Hamiltonian is given as $H_{CF} = B_k^q O_k^q$, where B_k^q is the crystal field parameter while O_k^q is the Steven's operator. The QTM contributions are negligible where the non-axial B_k^q (where q ≠ 0, and k=2, 4, 6) terms are smaller than the axial B_k^q (where q = 0, and k=2, 4, 6) terms. In the case of **2**, axial and non-axial terms are of similar magnitude and therefore a significant contribution of the QTM to the magnetic relaxation is expected. The large positive axial terms compared to non-axial terms stabilizes the ground KD with the smaller *mj* value in **2** (easy-plane magnetic anisotropy), which is in agreement with the calculated *g*-values.

The anisotropy g_{zz} axis is almost collinear with the pseudo-C_5 axis lying along the axial O–Yb–O bonds, but, as commented, its value is quite low. However, the three first excited states (KD2-KD4) lie at 244.5 cm^{-1}, 373.7 cm^{-1} and 489.9 cm^{-1} above the ground state, respectively, and present respective large g_{zz} values of 3.44, 7.07 and 6.94, passing also through the O–Yb–O direction and almost coincident with the g_{zz} anisotropy axis of the ground state. They correspond to an almost pure $m_J = |\pm 3/2\rangle$ state (KD2) and a mixture of $m_J = |\pm 5/2\rangle$ and $m_J = |\pm 7/2\rangle$ (KD3 and KD4).

These statements are supported by the computed transverse magnetic moments (Figure 3.15). Thus, the ground state shows a substantial transverse magnetic moment (1.52 μ_B) that could indicate a large operative QTM relaxation, whereas its values are smaller for the first excited state (0.27 μ_B). This is consistent with the absence of slow magnetization relaxation at zero-field. Experimentally, this QTM is quenched when a *dc* field is applied, leading to the observed slow relaxation of the magnetization.

Table 3.9: Computed B_k^q parameters from CASSCF calculations for **2**.

k	q	B(k,q)
2	-2	-0.30
2	-1	-8.53
2	0	10.24
2	1	-1.44
2	2	-2.17

k	q	B(k,q)
4	-4	0.16
4	-3	0.19
4	-2	-0.25E-01
4	-1	-0.20
4	0	-0.19
4	1	-0.75E-01
4	2	-0.94E-03
4	3	-0.45
4	4	0.25E-01

k	q	B(k,q)
6	-6	-0.21E-01
6	-5	0.31E-01
6	-4	0.26E-02
6	-3	0.91E-02
6	-2	-0.28E-02
6	-1	-0.14E-02
6	0	0.24E-02
6	1	-0.10E-02
6	2	0.53E-03
6	3	-0.12E-01
6	4	-0.15E-02
6	5	0.75E-02
6	6	0.61E-02

Moreover, the transverse moment for the Orbach process connecting the ground and KD1 of opposite magnetization is also predicted to be smaller (0.64 $\times 10^{-1}$ μ_B), which could point out that this relaxation pathway is not operative, in agreement with the experimental results. Accordingly, the *ab initio* studies support the magnetic findings: the QTM prevents the observation of slow

magnetic relaxation and possible SIM behaviour at zero field, and the calculations also indicate that the Orbach process can be ruled out in favor of a combination of Raman and direct processes.

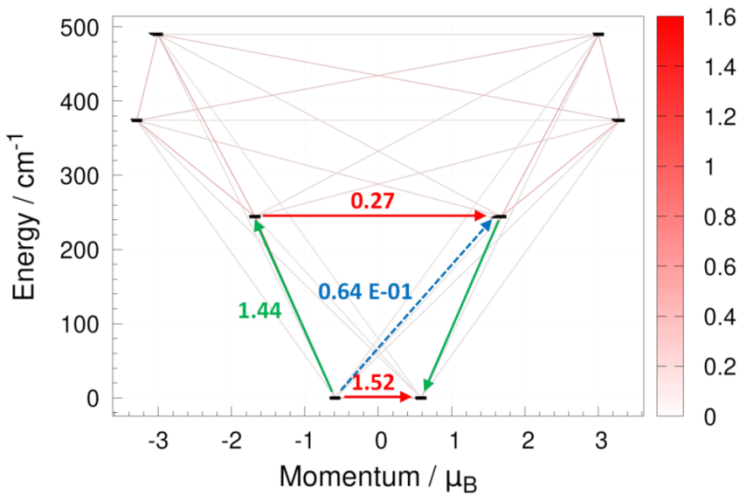

Figure 3.15: *Ab initio* calculated relaxation pathways in compound **2**. The black lines indicate the KDs as a function of the magnetic moments. Red lines denote QTM in the ground state and TA/QTM through the first and second excited states. Blue dashed lines represent possible Orbach processes.

3.4.6 Magnetic properties of complex 3

The *dc* magnetic properties of **3** were collected in the 2-300 K temperature range under an applied magnetic field of 1000 Oe and they are shown in the form of the temperature dependence of $\chi_M T$ (χ_M is the molar magnetic susceptibility) in Figure 3.16, left.

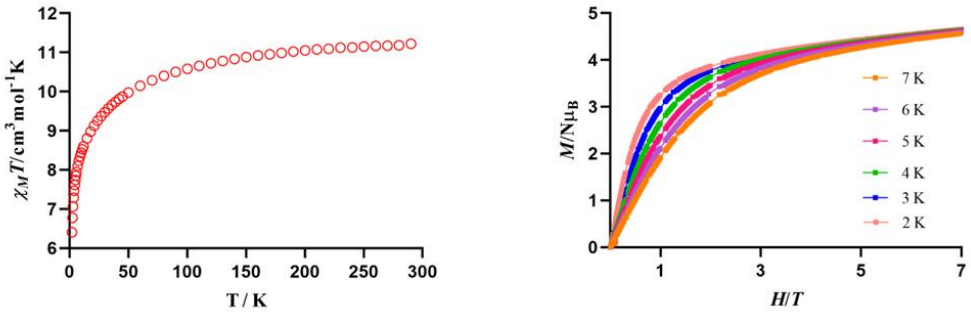

Figure 3.16: Temperature dependence of $\chi_M T$ (left) and field dependence of the magnetization (right) at the indicted temperatures for **3**.

At room temperature, the $\chi_M T$ value of 11.22 cm^3 K mol^{-1} for **3** is close to the expected value for one free Tb^{III} ion (11.82 cm^3 K mol^{-1} with S = 3, g_J = 3/2). Upon cooling, the $\chi_M T$ value slightly decreases until 50 K and then abruptly to reach a minimum of 6.41 cm^3 K mol^{-1} at 2 K. This decrease is due to the depopulation of the m_j levels of the Tb^{III} ions generated from the splitting of the spin-orbit coupling ground level by the ligands crystal field. It is discarded that this decrease is due to the existence of weak intermolecular interactions between the Tb^{III} ions since the molecular units are well isolated in the crystal structure.

The field dependence of the magnetization for **3** (figure 3.16, right) indicates that the magnetization increases rapidly at low fields and slightly from 1 T to H = 7 T, without reaching the saturation. The M value at the higher applied field of 7 T (4.66 Nβ at 2 K) is significantly lower than the expected saturation value for this Ln^{III} ion (9 Nβ), probably due to the existence of a significant magnetic anisotropy caused by the splitting of the m_j levels by the crystal field created by the ligands.

In order to know if **3** present slow relaxation of the magnetization, temperature and frequency dependent measurements of the *ac* magnetic susceptibility have been carried out, under an alternating field of 3 Oe on a polycrystalline sample. In absence of external field (H_{dc} = 0 Oe), the complex does not present out-of-phase signals (χ_M'') above 2 K, indicating that either the thermal activation barrier is very small or there exists fast magnetization relaxation by QTM. In view of this, to eliminate partially or completely the QTM, a small external magnetic field of 0.1 T has been applied. However, compound **3** shows out-of-phase signals but without reaching a maximum, even at the maximum frequency used of 10000 Hz (figure 3.17), just indicating that this compound presents a weak slow relaxation of the magnetization above 2 K.

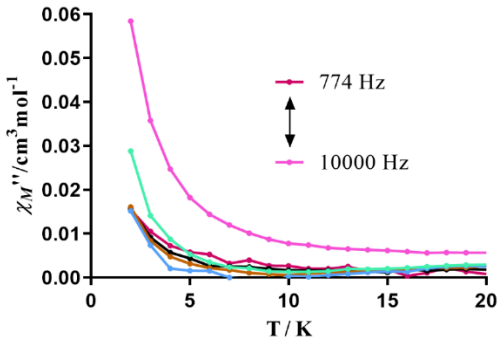

Figure 3.17: Temperature dependence of the out-of-phase ac susceptibility signals (χ_M'') at 1000 Oe for **3**

3.4.7 Crystal structures of complexes 5-7

The structures of complexes **5-7** are similar, so only the structure of **5** will be described, indicating in any case the differences existing between them. The compounds **5** and **7** crystallize in the C2/c monoclinic space group while

compound **6** crystallize in the P-1 triclinic space group. Crystallographic data and structural refinement details for compounds **5-7** are shown in Table 3.10.

Table 3.10: Crystallographic data and structural refinement details for complexes **5-7**.

Compound	**5**	**6**	**7**
Formula	$C_{58}H_{82}Cl_3DyO_3P_2$	$C_{59.4}H_{86.8}Cl_3EuO_{4.4}P_2$	$C_{58}H_{82}Cl_3GdO_3P_2$
M_r	1158.08	1191.50	1152.77
Crystal System	Monoclinic	Triclinic	Monoclinic
Space Group	C2/c	P-1	C2/c
a (Å)	17.2673(7)	12.2190(5)	17.3000(12)
b (Å)	11.6997(5)	15.2856(5)	11.6907(7)
c (Å)	25.5877(10)	15.8953(5)	25.6789(18)
α (°)	90	99.2160(10)	90
β (°)	93.6980(10)	101.3970(10)	93.668(2)
γ (°)	90	101.4720(10)	90
V (Å^3)	5158.5(4)	2790.01(17)	5182.9(6)
Z	4	2	4
Dc (g cm^{-1})	1.479	1.401	1.477
μ(MoK$_\alpha$) (mm^{-1})	1.711	1.371	1.541
T (K)	100	100	100
Observed reflections[a]	7941 (7782)	13941 (11306)	6431 (5958)
R_{int}[a]	0.0354	0.1295	0.0479
Parameters	305	774	314
GOF	0.949	1.054	1.113
R_1[b,a]	0.0235 (0.0231)	0.0750 (0.0415)	0.0234 (0.0181)
wR_2[c,a]	0.0995 (0.0988)	0.1090 (0.0993)	0.0440 (0.0431)

[a] Values in parentheses for reflections with I > 2s(I)

[b] $R1 = \sum||Fo| - |Fc||/\sum|Fo|$

[c] $wR2 = \{\sum [w(F_o^2 - F_c^2)^2] / \sum [w(F_o^2)^2]\}^{½}$

The structure of **5** is made of mononuclear neutral $[Dy(OPAd_2Bz)_2(THF)Cl_3]$ units (figure 3.18) without solvent molecules in the crystal structure (the same for **7**) while compound **6** consist of mononuclear neutral $[Eu(OPAd_2Bz)_2(H_2O)Cl_3]$ units together with 1.4 THF solvent molecules.

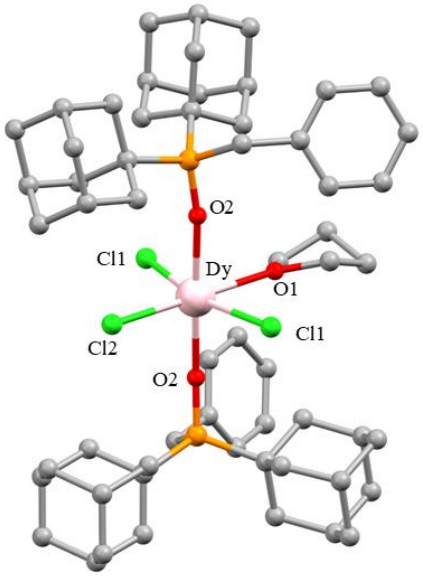

Figure 3.18: Molecular structure of **5**. Hydrogen atoms are omitted for clarity. Colour code: Dy pink, C grey, O red, P orange, Cl green.

Within the octahedral unit, the Dy^{III} ion is coordinated to two di(1-adamantyl)benzylphosphine oxide ligands with a Dy-O bond distance of 2.422 (15) Å, which is slightly longer than that found in compound **1**. These ligands occupy the axial positions with a nearly linear O2-Dy-O2 angle of 178.04 (5)º. The Dy^{III} atom is also coordinated in the equatorial plane by three chloride atoms in a T-type disposition, with an average Dy-Cl bond distance of 2.605 (5) Å, and by a THF molecule with a Dy-O bond distance of 2.468 (2) Å.

In the case of **6**, this equatorial position is occupied by a coordinated water molecule with a Eu-O bond distance of 2.437 (5) Å. It should be noted that Cl2 presents a shorter Cl-O bond distance than the other two chloride ligands in the equatorial plane. Selected bond distances and bond angles are shown in Tables 3.11-3.13.

Table 3.11: Selected bond distances (Å) and angles (º) for complex **5**.

Selected bond distances (Å)			
Dy1-O1	2.468 (2)	Dy1-Cl2	2.593 (6)
Dy1-O2	2.422 (15)	O1-P1	1.514 (15)
Dy1-Cl1	2.611 (4)		
Selected bond angles (º)			
O2-Dy1-O1	89.02 (3)	Cl1-Dy1-Cl2	98.94 (11)
O2-Dy1-Cl2	90.98 (3)	O2-Dy1-O2	178.04 (5)
O2-Dy1-Cl1	91.74 (4)	O1-Dy1-Cl2	180.00 (9)
O2-Dy1-Cl1	87.96 (4)	Cl1-Dy1-Cl1	162.11 (2)
O1-Dy1-Cl1	81.06 (11)	Dy1-O2-P1	170.38 (9)

Table 3.12: Selected bond distances (Å) and angles (º) for complex **7**.

Selected bond distances (Å)			
Gd1-O1	2.287 (2)	Gd1-Cl2	2.632 (4)
Gd1-O2	2.501 (15)	O1-P1	1.513 (10)
Gd1-Cl1	2.620 (5)		
Selected bond angles (º)			
O1-Gd1-O2	89.16 (3)	O1-Gd1-O1	178.31 (5)
O1-Gd1-Cl1	90.84 (3)	O2-Gd1-Cl1	180.00 (5)
O1-Gd1-Cl2	92.18 (3)	Cl2-Gd1-Cl2	164.30 (16)
O2-Gd1-Cl2	82.15 (8)	Gd1-O1-P1	168.53 (7)
Cl2-Gd1-Cl1	97.85 (8)		

Table 3.13: Selected bond distances (Å) and angles (º) for complex **6**.

Selected bond distances (Å)			
Eu1-O1	2.289 (2)	Eu1-Cl2	2.648 (10)
Eu1-O2	2.312 (2)	Eu1-Cl3	2.652 (15)
Eu1-O3	2.437 (5)	O1-P1	1.516 (3)
Eu1-Cl1	2.656 (8)	O2-P2	1.513 (3)
Selected bond angles (º)			
O1-Eu1-O3	93.64 (14)	Cl1-Eu1-Cl2	107.57 (3)
O1-Eu1-Cl1	87.79 (7)	Cl2-Eu1-Cl3	91.95 (5)
O1-Eu1-Cl2	90.28 (7)	Cl3-Eu1-O3	76.43 (16)
O1-Eu1-Cl3	89.96 (8)	O1-Eu1-O2	175.37 (8)
O2-Eu1-O3	87.30 (14)	Cl2-Eu1-O3	167.71 (16)
O2-Eu1-Cl1	87.79 (6)	Cl3-Eu1-Cl1	160.36 (5)
O2-Eu1-Cl2	89.73 (7)	Eu1-O1-P1	177.68 (15)
O2-Eu1-Cl3	94.67 (7)	Eu1-O2-P2	172.94 (15)
O3-Eu1-Cl1	84.24 (16)		

In this arrangement, the Dy^{III} metal ion presents a distorted octahedral coordination environment. This coordination geometry adopted by the Dy^{III} ion has been evaluated using the Shape software,[10] confirming that it is closer to the ideal octahedron (OC-6) polyhedron than the other possible ideal polyhedrons with a value of 1.059 (table 3.14).

Table 3.14: S-parameter values calculated with the Shape software for compounds **5-7**.

Complex		**JPPY-6**	**TPR-6**	**OC-6**	**PPY-6**	**HP-6**
5	Dy	29.610	14.877	1.059	26.904	33.125
6	Eu	26.621	11.310	1.605	23.708	33.265
7	Gd	29.862	15.058	0.896	27.105	32.920

JPPY-6 = Johnson pentagonal pyramid J2; TPR-6 = Trigonal prism; OC-6 = Octahedron; PPY-6 = Pentagonal pyramid; HP-6 = Hexagon

As in compound **1**, the axial Dy-O distances are shorter than the Dy-Cl and Dy-O bond distances in the equatorial plane, thus indicating that the Dy^{III} atom presents a compressed octahedral coordination geometry. The O1-Dy-Cl2 bond angle has a value of 180.00 (9)º, while the Cl1-Dy-Cl1 bond angle is 162.11 (2)º. Within the equatorial plane, the bond angles are: Cl2-Dy-Cl1 of 98.94 (11)º and O1-Dy-Cl1 81.06 (11)º. These parameters again indicate that the DyO_3Cl_3 coordination geometry is very close to the ideal octahedron polyhedron (180º for axial angles and 90º for equatorial angles). Moreover, the coordinated chloride atoms, as in the case of **1**, undergo some repulsion from each other and this causes that the bond angle between them acquires a value greater than 90º, and consequently, the angle between the Cl1 and the oxygen atom of the coordinated THF molecule is less than 90º. The angles between the axial and equatorial atoms are close to 90º. Finally, the angle Dy1-O2-P1 is 170.38 (9)º. The shortest intermolecular Dy···Dy distance is 10.429 Å, less than that of compound **1**.

In **6**, there exist hydrogen bond interactions between the coordinated water molecule and the THF solvent molecules with a O···O distance of 2.697 Å, while the packing of **5** and **7** reveals the absence of hydrogen bond interactions. There are weak π···π stacking interactions in **5-7** between the aromatic benzene rings of different units with a centroid-centroid distance of 4.587, 4.824 and 4.528 Å for **5-7**, respectively.

3.4.8 Magnetic properties of complex 5

The temperature dependence of the $\chi_M T$ product (where χ_M is the molar susceptibility) was measured for **5** under a *dc* field of 0.5 T (Figure 3.19, left). At 300 K, the value of $\chi_M T$ product is 14.21 cm^3 K mol^{-1}, which is in good agreement with the expected value for an isolated Dy^{III} ion (14.17 cm^3 K mol^{-1} with S = 5/2, g = 4/3).

On cooling, the $\chi_M T$ product remains constant to approximately 130 K and, from this temperature, decreases smoothly until 2 K to reach a value of 11.74 cm^3 K mol^{-1}. This decrease is due to the depopulation of the excited ± m_j sublevels originated from the splitting of the spin-orbit coupling $^6H_{15/2}$ term by the ligands crystal field.

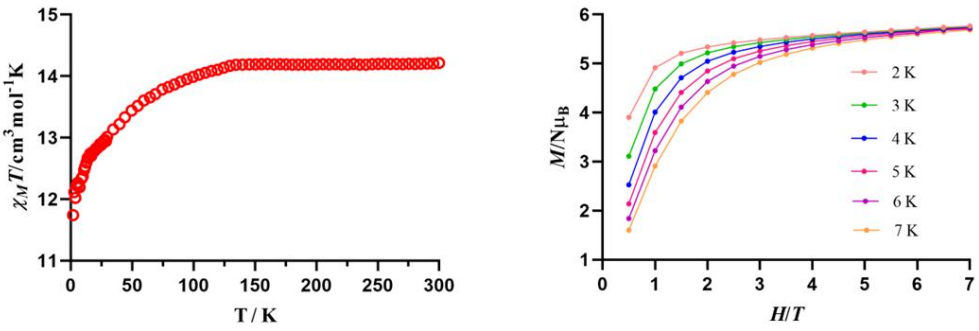

Figure 3.19: Temperature dependence of $\chi_M T$ (left) and field dependence of the magnetization (right) at the indicted temperatures for **5**.

The field dependence of the magnetization in the 2-7 K temperature range shows a fast increase at low fields and from 1 T to H = 7 T, the magnetization increases slightly reaching the saturation with a value of 5.77 Nβ at 7 T and 2 K (Figure 3.19, right). This saturation value is lower than that expected saturation value for a free Dy^{III} ion (M_{sat} = 10.00 Nβ), confirming the existence of magnetic anisotropy caused by the splitting of the m_j levels by the crystal field created by the ligands.

To reveal if **5** present slow relaxation of the magnetization, temperature and frequency dependence of *ac* magnetic susceptibility were measured on a polycrystalline sample of **5**. At zero field, compound **5** presents slow relaxation of the magnetization but without maxima above 2K in the out-of-phase signals (χ_M'') (figure 3.20, left) due to the existence of QTM in the

ground state that induces a very fast magnetization relaxation. This QTM is caused by the transverse anisotropy (g_x and g_y different from zero), dipole interactions and hyperfine interactions between the nuclear and the electronic spin.

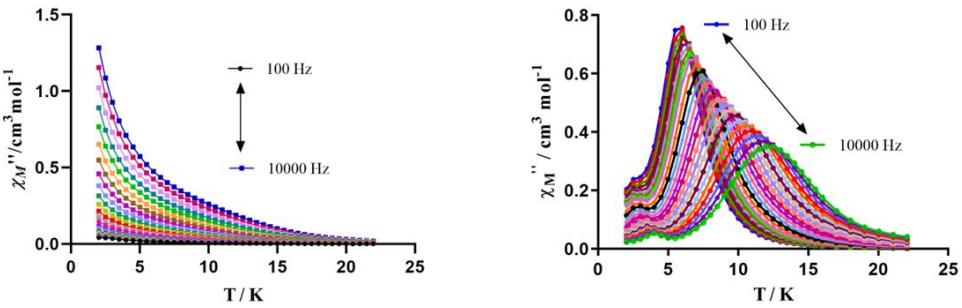

Figure 3.20: Temperature dependence of the out-of-phase *ac* susceptibility signals (χ_M'') for **5** at 0 Oe (left) and at 1000 Oe (right)

To eliminate, at least partially, the QTM, a small *dc* field is applied. In the presence of a 0.1 T field, compound **5** exhibits strong temperature and frequency dependence of the *ac* magnetic susceptibility (Figure 3.20, right) with maxima in the range from 5.5 K (100 Hz) to 12 K (10000 Hz), which indicates that **5** presents slow relaxation of the magnetization and field-induced SIM behavior.

The relaxation times, in the 6.5 K-12 K temperature range, were obtained from the fitting of the frequency dependence of the out-of-phase *ac* susceptibility data (χ_M'') (Figure 3.21, left) to the generalized Debye model.

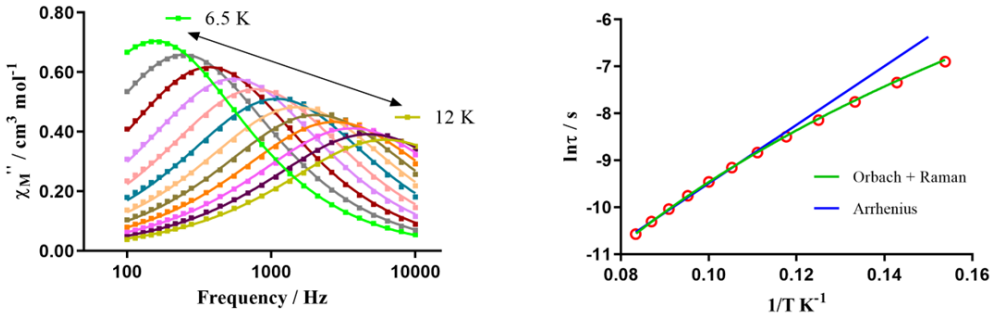

Figure 3.21: (Left) Frequency dependence of the χ_M'' signals at different temperatures for **5** under a field of 0.1 T. The solid lines represent the best fitting to the Debye model. (Right) Representation of Ln t vs 1/T for **5** at 0.1 T. The solid lines represent the best fit of the experimental data to the Arrhenius equation for a thermally activated process (blue) or for a combination of Raman and Orbach relaxation processes (green).

The linear region of the temperature dependence of the relaxation times at high temperatures (Figure 3.21, right), which corresponds to the thermally activated process (Orbach process), was fitted to the Arrhenius law leading to the following parameters: U_{eff} = 62.41 K and τ_0 = 1.47 x 10^{-7} s. These parameters are similar to those previously published for other octahedral field-induced Dy^{III} SIMs.[25]

The Cole−Cole plot (Figure 3.22) shows, in the 7 K-13 K temperature region, semicircular shapes with α values in the range of 0.15−0.26. Considering that α values close to zero indicate a single relaxation process, whereas α = 1 corresponds to an infinitely wide distribution of relaxation times, the α values observed for **5** at low temperature suggested the existence of several competitive relaxation processes. Moreover, the relaxation times deviate from linearity below 9 K (Figure 3.21, right), which is due to the contribution, in addition to the Orbach process, of other relaxation mechanisms.

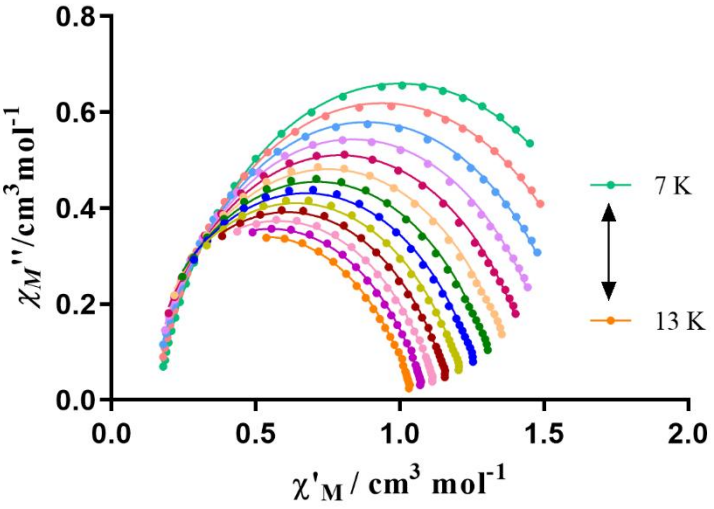

Figure 3.22: Cole-Cole plot for **5**

In view of this, a new fitting has been carried out in the entire studied temperature range (6.5 K – 12 K) using the equation 1

$$\tau^{-1} = AT + \frac{B_1}{1+B_2H^2} + CT^n + \tau_0 \exp^{(-\frac{Ueff}{k_BT})} \quad \text{Equation 1}$$

The QTM process has not been included as the out-of-phase susceptibility signals approach to zero at temperatures below the maximum, indicating that the QTM has been significantly eliminated (figure 3.20, right). Therefore, the relaxation times were fitted to the combination of Raman and Orbach processes. To avoid over parameterization, the parameters U_{eff} and τ_0 were fixed to those obtained with the Arrhenius law in the high temperature region. From the best fitting (Figure 3.21, right), the Raman parameters obtained are: C = 0.0115 s^{-1} K^{-n} and n = 6.05. Although for compounds with Kramer ions *n* should be 9, when acoustic and optical phonons are involved, it is normal to observe smaller *n* values.[23]

3.4.9 Computational calculations of complex 5

Ab initio calculations based on the experimental X-ray crystal structure of complex **5** were carried out to gain insight into its magnetic relaxation mechanism. Specifically, multiconfigurational CASSCF[12] calculations were performed using the SINGLE_ANISO[13] module in the ORCA 5.0.4[14-16] software package. For complex **5**, the eight computed Kramers doublets (KDs), corresponding to the $^6H_{15/2}$ ground term of the Dy^{III} ion, span an energy range of approximately 537 cm^{-1} (Table 3.15). The ground state (KD1) is a nearly pure $m_J = |\pm 15/2\rangle$ state, exhibiting axial anisotropy with $g_{zz} = 19.76$ and low transverse components of $g_{xx} \sim g_{yy} < 0.05$, defining a well-oriented magnetic anisotropy axis (Figure 3.23, left). The magnetic anisotropy axis (g_{zz}) aligns with the pseudo-C_5 axis along the axial O–Dy–O bonds, deviating by 7.7° (Figure 3.23, left).

Table 3.15: CASSCF computed relative energies (in cm^{-1}) of the eight low-lying Kramers' doublets, *g* tensors for **5** and tilting angle (θ) of the main anisotropy axes of the corresponding excited (ES1, ES2, etc.) KD with respect to the ground state (GS) KD for **5**.

Energy (cm^{-1})	**g_{xx}**	**g_{yy}**	**g_{zz}**	**θ (°)**
0.0	0.025621	0.045775	19.755699	
211.64	1.893761	6.537793	12.521114	44.6
262.16	3.599974	3.648370	9.421879	55.4
352.75	3.994829	4.659097	13.560008	90.0
441.83	0.675929	2.247000	10.681190	90.0
483.72	1.906329	5.080410	9.968343	90.0
510.86	1.538830	4.083763	11.976517	90.0
536.77	10.088348	8.702495	1.859251	37.4

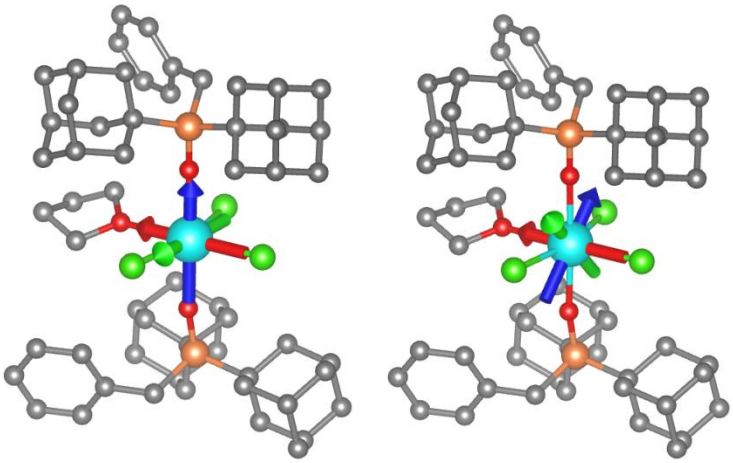

Ground KD (KD1) **First excited KD (KD2)**

Figure 3.23: Orientation of the *g*-tensor components obtained from CASSCF calculations for the ground Kramers' doublet (left) and first excited KD (right) of complex **5** using ORCA. The reference axis *x*, *y* and *z* of the *g*-tensor are displayed in red, green and blue, respectively. Code colours: dysprosium (cyan), oxygen (red), chloride (green), phosphorus (orange), and carbon (grey). Hydrogen atoms have been omitted for clarity.

The first excited state (KD2), located 211.6 cm^{-1} above the ground state, shows significant transverse anisotropy (g_{xx} = 1.89 and g_{yy} = 6.54), with its g_{zz} tensor at 44.6º with respect to the ground state's g_{zz} axis (Figure 3.23, right; Table 3.15). The third excited state (KD3), at 262.2 cm^{-1}, also exhibits considerable transverse components (g_{xx} = 3.60 and g_{yy} = 3.65).

Calculated transverse magnetic moments (Figure 3.24) offer insight into the relaxation mechanism of compound **5**. The ground state shows a small transverse magnetic moment of 0.12×10^{-1} μ_B, which is typically low enough for slow magnetization relaxation, as 0.1 μB is generally considered the threshold for this behavior.[17] However, the absence of slow relaxation of magnetization at zero field may be due to intermolecular and/or hyperfine interactions, potentially inducing Quantum Tunneling of Magnetization

(QTM). As mentioned before in section 3.4.3., the bromine analogue of **1** displayed slow magnetization relaxation, with high T_B and U_{eff} values. This observation leads us to think that the 0.19×10^{-2} μ_B value in the case of **1** and, in this case, 0.12×10^{-1} μ_B for **5** may not be sufficient to prevent QTM.

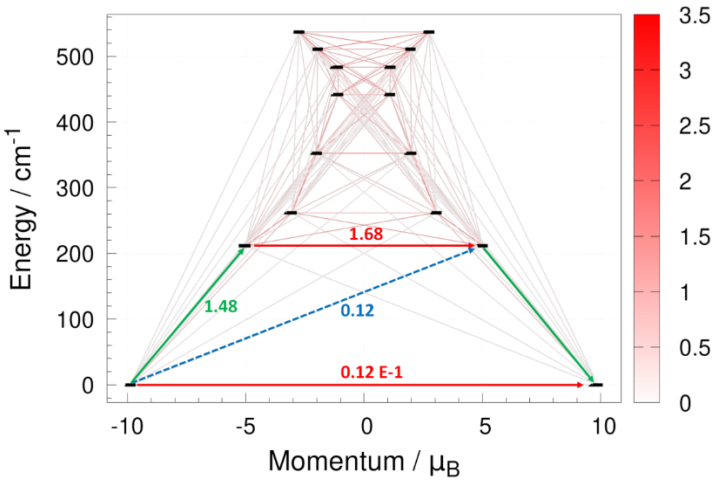

Figure 3.24: *Ab initio* calculated relaxation pathways in compound **5**. The black lines indicate the KDs as a function of the magnetic moments. Red lines denote QTM in the ground state and TA/QTM through the first and second excited states. Blue dashed lines represent possible Orbach processes.

We calculated again the tunneling relaxation times using an *ab initio* model incorporating spin-dipolar interactions.[19] The ground-state tunneling demagnetization rate in complex **5** is approximately $4 \cdot 10^3$ times faster than in the bromine analogue of complex **1**. As mentioned above, for **1** it was 50 times faster than for the bromine analogue (section 3.4.3). Thus, these rates follow the trend: (bromine analogue of **1**) < (**1**) < (**5**). These computational results are in agreement with the experimental ones. The transverse *g*-tensor components support this result. Their maxima values are around 0.001 (bromine analogue of **1**) < 0.01 (**1**) < 0.05 (**5**). These results lead us to think again that their different magnetic behavior is intrinsic to the molecular system and probably

due to the donor ability of the halides involved in the equatorial plane. This ability is weaker in heavier halides, which reduces the transverse ligand field components and thus suppresses QTM.

Interestingly, two similar compounds with O_h geometry,[26] $[Dy(Cy_3PO)_2I_3(CH_3CN)]$ and $[Dy(Cy_3PO)_2(I)_3THF]$ equatorially coordinated by I^- ions instead of Cl^- ions, exhibited SIM behavior at zero field with quite high energy barriers over 1000 K. This work also confirms the influence of the halogen atoms on the magnetic anisotropy, and consequently, on the slow relaxation of magnetization. The calculated transverse magnetic moments for these compounds are on the order of 10^{-4}.

3.4.10 Photophysical properties and TD-DFT calculations of the di(1-adamantyl)benzylphosphine oxide ligand

An in-depth photophysical study has been carried out for the ligand di(1-adamantyl)benzylphosphine oxide. First, in the absorption and luminescence spectra (Figure 3.25), the ligand exhibits one sharp and one broad absorption maxima at 235 nm and 261 nm in solution, respectively, while it shows two broad bands at 234 nm and 265 nm in the solid phase. Following that, its emission spectrum in solution displays two bands at 409 nm and 431 nm (Figure 3.25, right).

DFT and TD-DFT methodologies were employed to assign the electronic transitions that give rise to the photophysical properties. First, a conformational search with the MMFF force field found a total of three conformers of the antenna ligand. Their geometries only differed in the orientation of the benzene group (Figure 3.26).

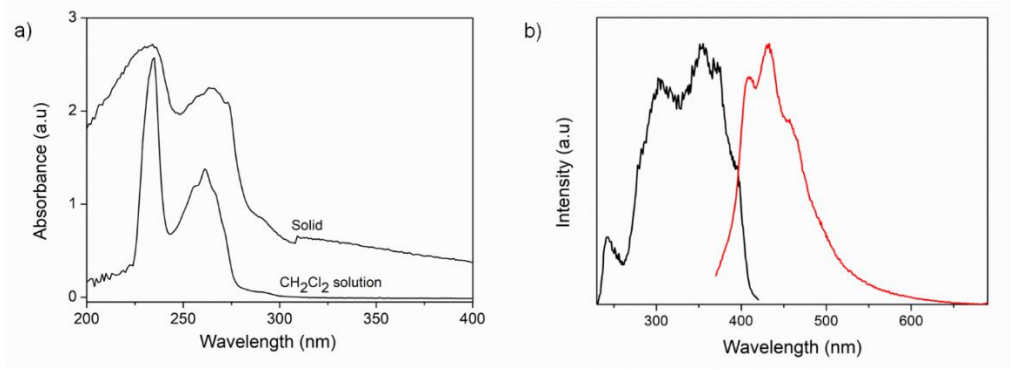

Figure 3.25: a) Experimental absorption spectra of the ligand in CH_2Cl_2 solution and solid phase and b) excitation (in black) and emission (in red) spectra in CH_2Cl_2 solution with λ_{exc} = 350 nm.

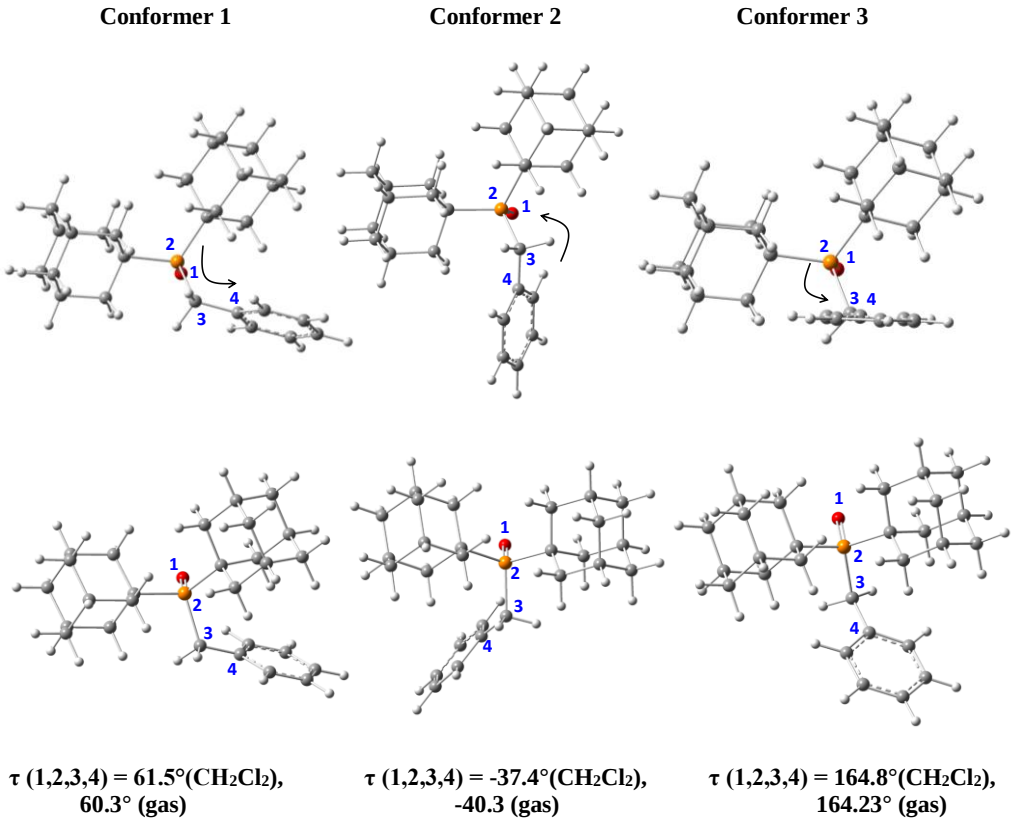

Figure 3.26: Two different views of the three optimized conformations of the di(1-adamantyl)benzylphosphine oxide ligand) in its ground state (S_0) at the CAM-B3LYP-D3/6-31+G** level of theory in dichloromethane solution and in the gas phase.

They were optimized in the ground state at the CAM-B3LYP-D3 (BJ)/6-31+G(d,p) level of theory in CH_2Cl_2 solution and in the gas phase. Table 3.16 lists the relative energies for the three conformers, showing that conformer 1 is the most stable in the two phases. Thus, only the vertical electronic transitions for conformer 1 were computed.

Table 3.16: Energy (in Hartrees) of the ligand conformers, energy difference (AE, kcal/mol) and kJ/mol with respect to the most stable conformer and dipole moment (μ, in Deybe), calculated at the CAM-B3LYP-D3(BJ)/6-31+G** level of theory in the gas phase and dichloromethane solution.

Phase	Conformer	Energy	ΔE (kcal/mol)	ΔE (kJ/mol)	μ (D)
Gas	1	-1.466.69957	0.00	0.00	3.69
	2	-1.466.698756	0.51	2.14	3.80
	3	-1.466.69434	3.28	13.73	3.99
CH_2Cl_2	1	-1.466.71027	0.00	0.00	5.58
	2	-1.466.709422	0.53	2.23	5.69
	3	-1.466.705861	2.77	11.58	5.69

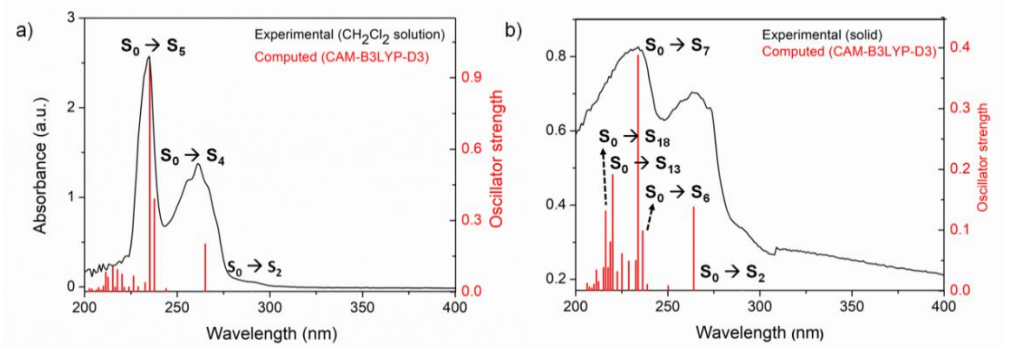

Figure 3.27: Experimental absorption spectra of the ligand in CH_2Cl_2 solution (left) and in the solid phase (right) (black colour) along with the oscillator strength of the vertical electronic transitions calculated at the TD-CAM-B3LYP-D3/6-31+G** level of theory in CH_2Cl_2 solution (left) and in the gas phase (rihgt) (red colour). The theoretical energies were scaled by a factor of 1.25.

To aid in assigning the electronic transitions, figure 3.27 displays the experimental absorption spectra of the ligand in CH_2Cl_2 solution and solid phase along with the vertical electronic transitions calculated at the TD-CAM-B3LYP-D3/6-31G** level of theory. Table 3.17 provides a list of some calculated CAM-B3LYP-D3 vertical electronic transitions with notable oscillator strengths and their assignments.

In solution, the weaker experimental band at 261 nm could be assigned to the $S_0 \rightarrow S_2$ electronic transition (calculated at 212 nm), in agreement with the lower oscillator strength predicted for it (f = 0.16), with 69% contribution of HOMO → LUMO+1. The strong and sharp absorption band observed at 235 nm was attributed to the $S_0 \rightarrow S_4$ and $S_0 \rightarrow S_5$ electronic transitions, which were predicted at 190 nm (f = 0.31) and 188 nm (f = 0.77), corresponding mainly to HOMO−2 → LUMO+2 with 44% and 62% and contributions, respectively (Figure 3.28). Figure 3.28 displays the frontier molecular orbitals involved in the most intense $S_0 \rightarrow S_5$ transition, whereas Figure 3.29 shows those involved in the dominant transitions described in Table 3.17. The HOMO-2, LUMO+1 and LUMO+2 are mainly localized on the benzene ring, whereas the HOMO resides in the benzene and one of the adamantyl moieties. This indicates, as expected, that the benzene ring is the main responsible for the absorption properties of the ligand, with minor participation of one of the adamantyl moieties.

Table 3.17: Experimental absorption wavelength (λ_{ab}^{exp}), theoretical vertical electronic transitions ($\lambda_{vert-ab}^{calc}$), oscillator strength (*f*), and the main molecular orbital contributions (≥ 10%) calculated at the CAM-B3LYP-D3 (BJ)/6-31+G** levels of theory in dichloromethane solution and in the solid phase for the conformer 1 of the ligand.

Phase	λ_{ab}^{exp} **nm (eV)**	$\lambda_{vert-ab}^{calc}$ **nm (eV)**	**Transition**	***f***	**Contribution (%)**
Solution	261 (4.75)	231 (5.35)	$S_0 \rightarrow S_1$	0.0018	HOMO → LUMO+2 (49%) HOMO-2 → LUMO+1 (28%)
		212 (5.85)	$S_0 \rightarrow S_2$	0.16	HOMO → LUMO+1 (69%) HOMO-2 → LUMO+2 (14%)
	235 (5.28)	190 (6.53)	$S_0 \rightarrow S_4$	0.31	HOMO-2 → LUMO+2 (44%) HOMO → LUMO+2 (37%)
		188 (6.58)	$S_0 \rightarrow S_5$	0.77	HOMO-2 → LUMO+2 (62%) HOMO → LUMO+1 (16%)
Solid	265 (4.68)	232 (5.35)	$S_0 \rightarrow S_1$	0.0008	HOMO → LUMO+3 (36%) HOMO-2 → LUMO+1 (15%) HOMO → LUMO+3 (12%)
		211 (5.87)	$S_0 \rightarrow S_2$	0.11	HOMO → LUMO+1 (38%) HOMO→ LUMO+4 (15%) HOMO-2 → LUMO+3 (14%) HOMO→ LUMO+3 (11%)
	234 (5.30)	187 (6.62)	$S_0 \rightarrow S_6$	0.20	HOMO-2 → LUMO+1 (15%) HOMO-2 → LUMO+2 (14%) HOMO → LUMO+2 (14%)
		187 (6.63)	$S_0 \rightarrow S_7$	0.31	HOMO-2 → LUMO+3 (29%) HOMO → LUMO+1 (18%) HOMO-2 → LUMO+4 (10%)
		176 (7.06)	$S_0 \rightarrow S_{13}$	0.15	HOMO-3 → LUMO+1 (17%)
		173 (7.18)	$S_0 \rightarrow S_{18}$	0.11	HOMO-3 → LUMO+4 (9%) HOMO-3 → LUMO+1 (8%) HOMO-2 → LUMO (7%)

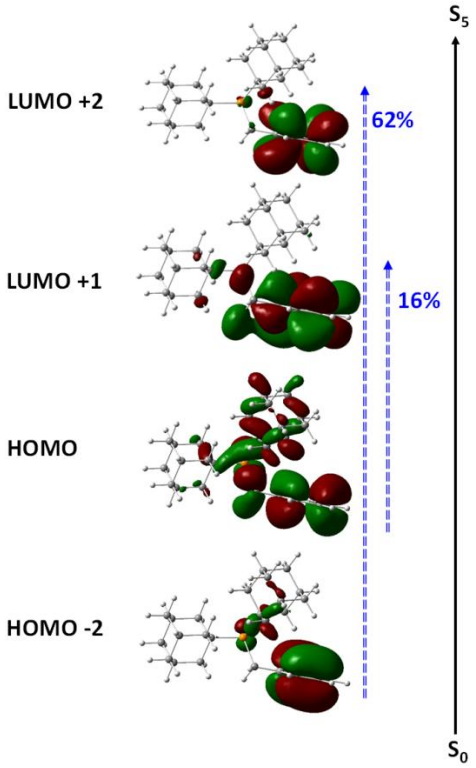

Figure 3.28: Schematic representation of the $S_0 \rightarrow S_5$ electronic transition in dichloromethane solution for the ligand (isocontour plots 0.02 a.u.).

a) Dichloromethane solution

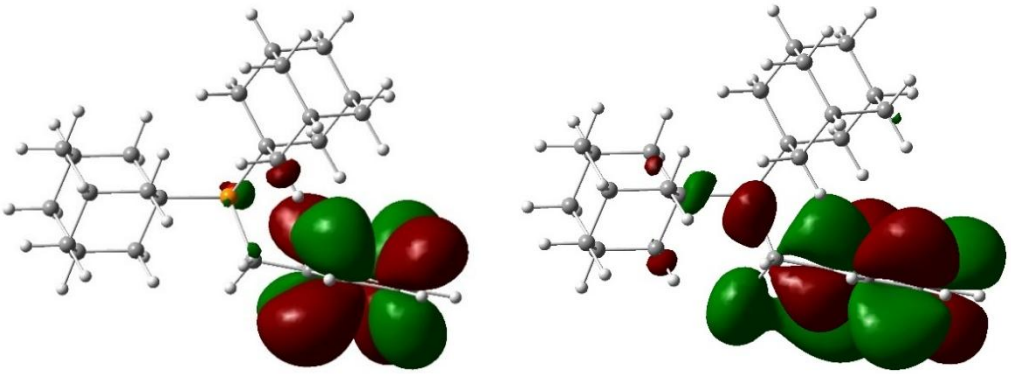

LUMO +2 **LUMO +1**

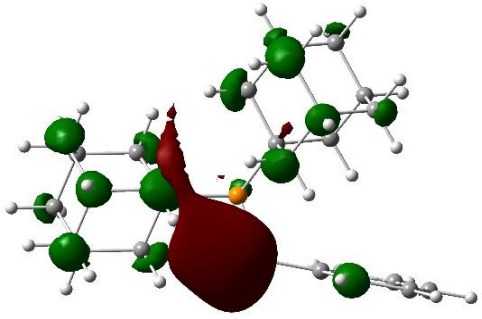

LUMO

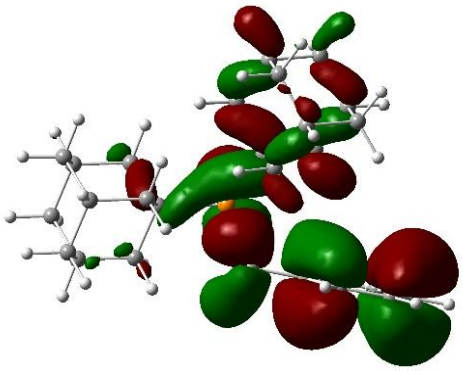

HOMO

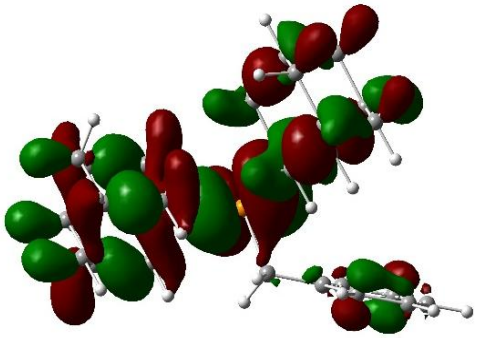

HOMO -1

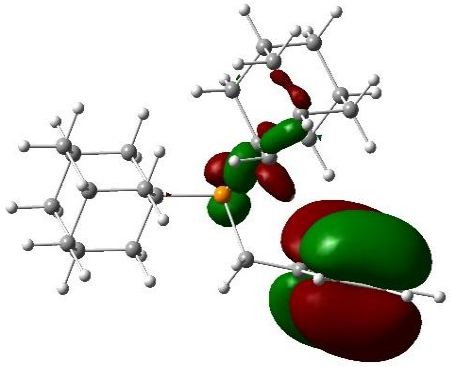

HOMO -2

b) Gas phase

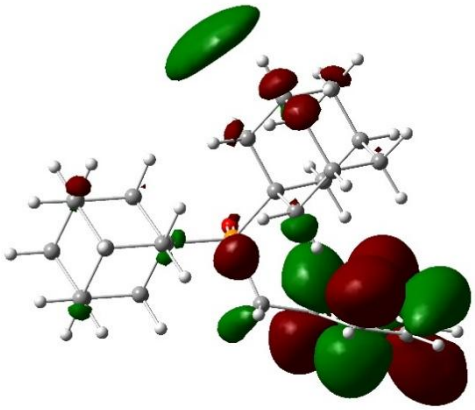

LUMO +4

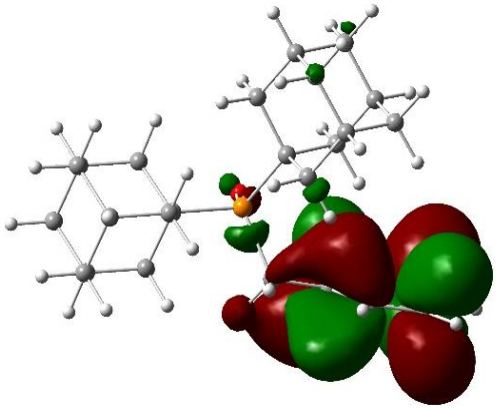

LUMO +3

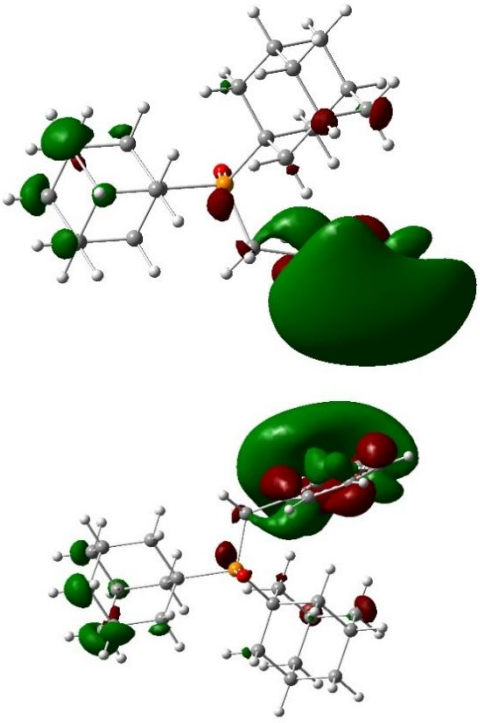

LUMO +2

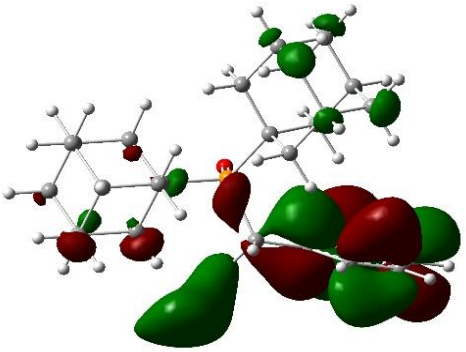

LUMO +1

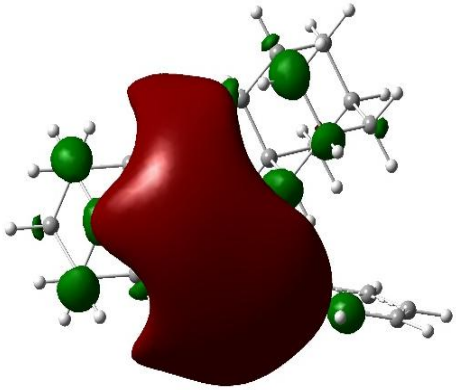

LUMO

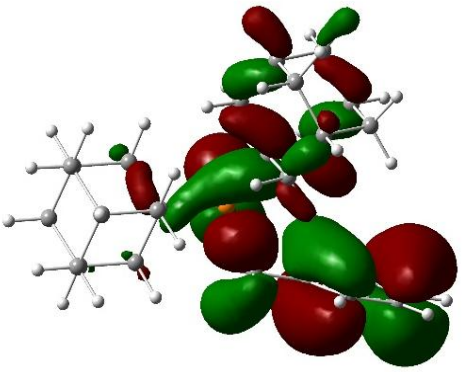

HOMO

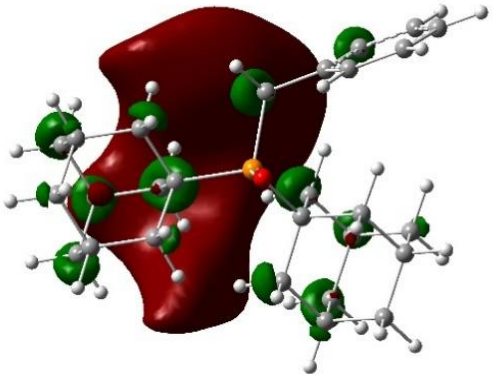

HOMO -1

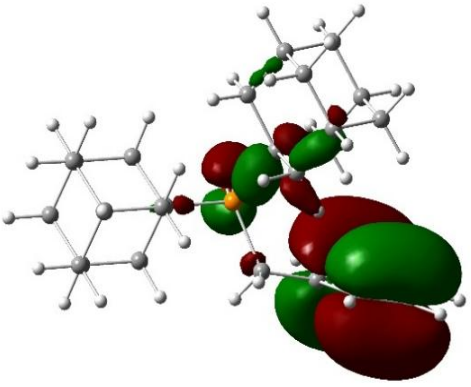

HOMO -2

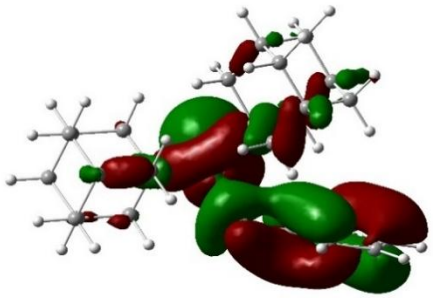

HOMO -3

Figure 3.29: Localization of the HOMO, LUMO, HOMO-1, HOMO-2, LUMO+1 and LUMO+2 orbitals for the ground state S_0 of the $OPAd_2Bz$ ligand at the CAM-B3LYP-D3/6-31+G** level of theory in dichloromethane solution and, additionally, HOMO-3, LUMO+3 and LUMO+4 in the gas phase.

In the absorption spectrum of the solid, the second lowest energy transition observed at 265 nm could be assigned to the $S_0 \rightarrow S_2$ transition predicted at 211 nm with f = 0.11 and 38% contribution of HOMO → LUMO+1. The absorption band at 234 nm could be assigned mainly to the $S_0 \rightarrow S_6$ and $S_0 \rightarrow S_7$ electronic transitions, which were calculated both at 187 nm. The $S_0 \rightarrow S_7$ transition is predicted to be the most intense one with f = 0.31 and contributions of HOMO−2 → LUMO+3 (29%), HOMO → LUMO+1 (18%) and HOMO−2 → LUMO+4 (10 %) (Figures 3.29 and 3.30).

With respect to the emission, the first excited state was optimized in CH_2Cl_2 solution and the $S_1 \rightarrow S_0$ transition was predicted at 387 nm with the CAM-B3LYP-D3 method (Table 3.18), in agreement with the experimental value. Despite the fact that the excited states S_2, S_6, and S_7 were predicted to be the most populated during the absorption process, the molecule relaxes to the S_1 excited state and a Kasha-type emission occurs from it.

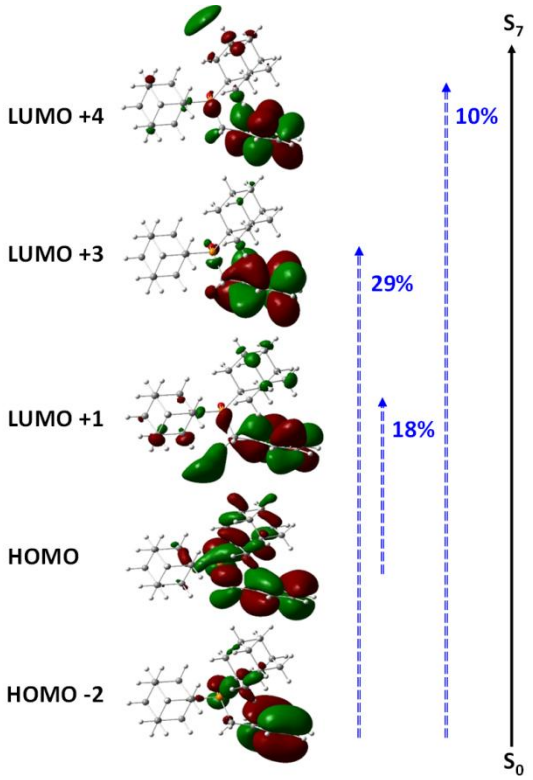

Figure 3.30: Schematic representation of the $S_0 \rightarrow S_7$ electronic transition in the gas phase for the ligand (isocontour plots 0.02 a.u.).

Table 3.18: Experimental emission (λ_{emis}^{exp}), theoretical transition ($\lambda_{vert-emis}^{calc}$), and oscillator strength (*f*) for the $S_1 \rightarrow S_0$ transition calculated at the CAM-B3LYP-D3 (BJ)/6-31+G** level of theory in dichloromethane solution for the conformer 1 of the ligand.

Phase	$\boldsymbol{\lambda_{emis}^{exp}}$ **nm (eV)**	$\boldsymbol{\lambda_{vert-emis}^{calc}}$ **nm (eV)**	**Transition**	***f***
Solution	431 (2.88) 409 (3.03)	387 (3.21)	$S_1 \rightarrow S_0$	0.01

3.4.11 Photophysical properties and TD-DFT calculations of complexes 1-7

The photophysical properties in the solid phase of the compounds **1-7** have been investigated. The energy ranges of the absorption and emission spectra of the ligand make it suitable for use as an antenna for lanthanide ions.[27-29] This would enable efficient energy transfer and enhanced emission sensitization, as it has been demonstrated in previous studies.[30-31]

The experimental absorption spectra recorded in the solid phase for compounds **1-7** are shown in figure 3.31. All of them exhibit two intense bands in the 200-280 nm range. The emission spectra of compounds **1-3** and **5-6** and the appearance of the well-defined, narrow Dy^{III}, Yb^{III}, Tb^{III}, and Eu^{III} luminescence emission bands confirm the antenna performance of the ligand (Figures 3.32 and 3.33).

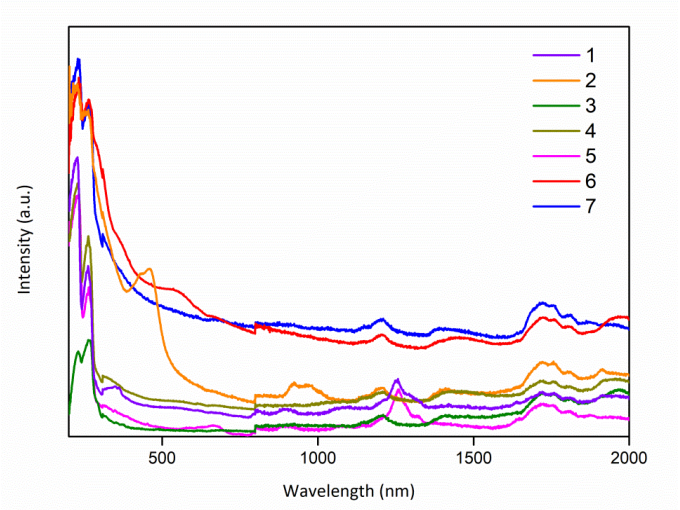

Figure 3.31: Experimental absorption spectra of compounds **1-7** in the solid phase.

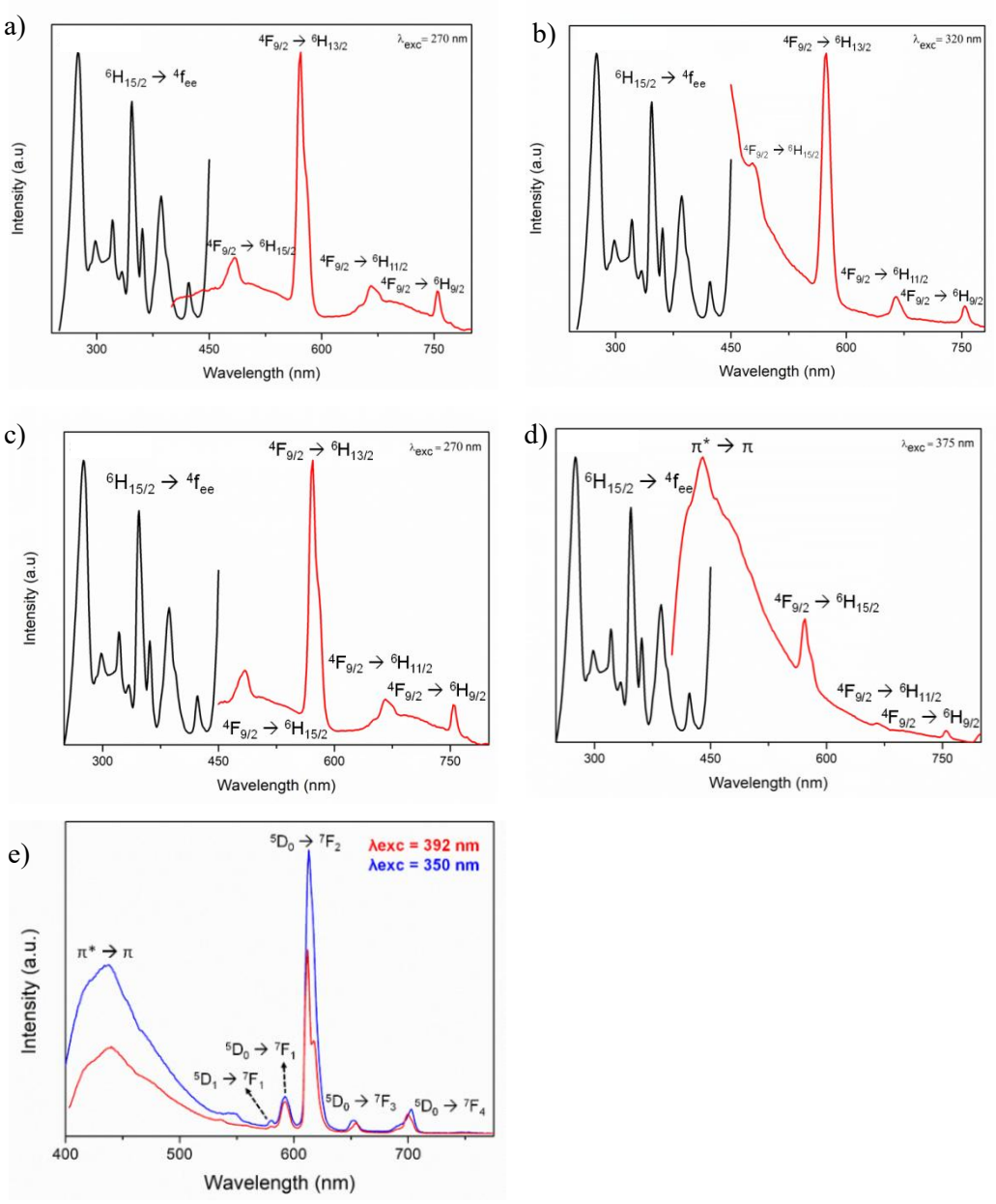

Figure 3.32: Emission spectra of compounds **1** (a and b), **5** (c and d) and **6** (e) at the indicated λ_{exc} in solid state at room temperature.

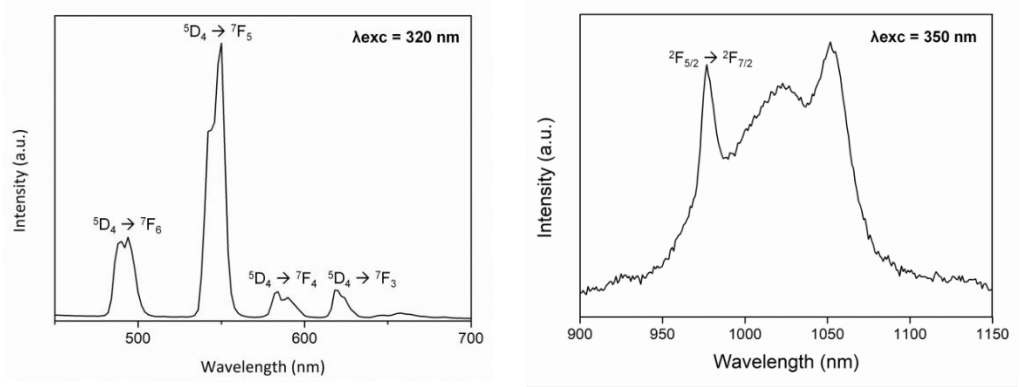

Figure 3.33: Emission spectra of **3** (left) and **2** (right) at the indicated λ_{exc} in solid state at room temperature.

It is striking that in compounds **1, 5,** and **6**, the emission band from the ligand is also visible depending on the λ_{exc}, presenting thus dual emission properties (Figure 3.32). This is probably due to partial energy transfer from the ligand T_1 state to the emitting level of the Ln^{III}.[32] The design and synthesis of dual-emission systems are at the forefront in the research development of advanced luminescent materials and sensors.[33]

The emission spectra of Gd^{III} compounds only show two emission bands at 457 nm and 485 nm in the case of **4** and one band at 501 nm in the emission spectrum of **7**, indicative of ligand-based emission (Figure. 3.34).

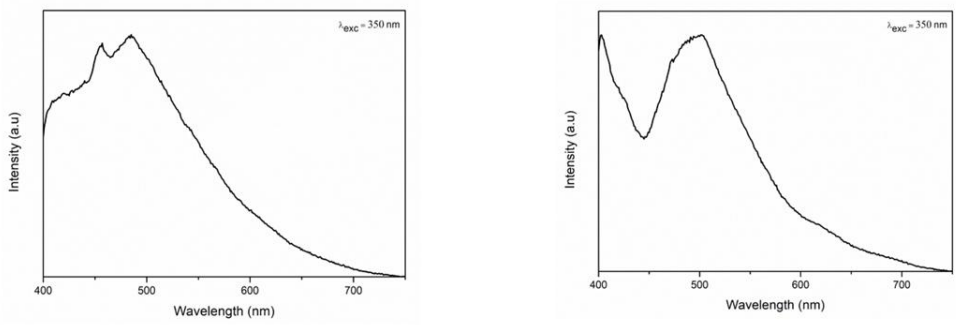

Figure 3.34: Emission spectra of **4** (left) and **7** (right) at λ_{exc} = 350 nm in solid state at room temperature.

Figure 3.32 shows the dual emission behavior in Dy^{III} complexes (**1** and **5,** panels a-d), particularly at λ_{exc}= 270, 320 and 375 nm. In the emission spectrum at λ_{exc}= 270 nm several narrow transitions were detected in the visible to near-infrared region (Figure 3.32, panels a and c). These bands are ascribed to the dysprosium centered f-f transitions and can be assigned to the $^4F_{9/2} \rightarrow {}^6H_{15/2}$ (482 nm), $^4F_{9/2} \rightarrow {}^6H_{13/2}$ (576 nm), $^4F_{9/2} \rightarrow {}^6H_{11/2}$ (665 nm), and $^4F_{9/2} \rightarrow {}^6H_{9/2}$ (755 nm) electronic transitions. The excitation spectrum was monitored at λ_{em} of 575 nm and it displays a series of sharp lines in the 230-490 nm region, which are ascribed to the transitions from the ground state, $^6H_{15/2}$, to the excited states in the $4f^9$ configuration of Dy^{III} (Figure 3.32, panels a-d). The emission spectrum of **5** upon excitation at 375 nm, *i.e.* upon ligand-centered excitation, displays $\pi^* \rightarrow \pi$ ligand-centered fluorescence at 440 nm together with visible to NIR dysprosium-centered radiative relaxations (Figure 3.32, panel d). As indicated above, the observation of ligand centered residual emission is probably due to partial energy transfer from the ligand T_1 to the $^4F_{9/2}$ emitting level of Dy^{III} at this λ_{exc}= 375 nm.

The same effect is observed in the emission spectra recorded for compound **6**. In this case, the emission spectra upon excitation at 350 nm and 392 nm show $\pi^* \rightarrow \pi$ ligand-centered fluorescence at 440 nm together with the characteristic europium centered f-f transitions (Figure 3.32, panel e). These last bands can be attributed to the $^5D_1 \rightarrow {}^7F_1$ (580 nm), $^5D_0 \rightarrow {}^7F_1$ (592 nm), $^5D_0 \rightarrow {}^7F_2$ (613 nm), $^5D_0 \rightarrow {}^7F_3$ (652 nm), and $^5D_0 \rightarrow {}^7F_4$ (703 nm) electronic transitions. The antenna effect is more efficient at λ_{exc}= 392 nm than at λ_{exc}= 350 nm, since the relative intensity of the emission band of the ligand is weaker at λ_{exc}= 392 nm.

However, compound **3** (Tb) does not present dual emission properties, since its emission spectrum only shows the characteristic terbium centered f-f transitions, that is, the $^5D_4 \rightarrow {}^7F_6$ (492 nm), $^5D_4 \rightarrow {}^7F_5$ (550 nm), $^5D_4 \rightarrow {}^7F_4$ (586 nm) and $^5D_4 \rightarrow {}^7F_3$ (618 nm) transitions (Figure 3.33, left). This indicates an efficient ligand to metal energy transfer mechanism. In the case of compound **2** (Yb), the ytterbium $^2F_{5/2} \rightarrow {}^2F_{7/2}$ transition is observed at 978 nm (Figure 3.33, right), proving again that antenna effect takes place.

Time-resolved experiments were carried out in solid state with excitation and emission wavelengths of 320 nm and 575 nm for **1**, 375 nm and 978 nm for **2**, 350 nm and 500 nm for **3**, 250 nm and 575 nm for **5** and 350 nm and 620 nm for **6**, respectively. The experiments reveal a mono-exponential (**2**, **6**), bi-exponential (**5**) or tri-exponential (**1**, **3**) decay of the luminescence signal with lifetimes (τ) of 26.1 μs (50%) 8.6 μs (49%) and 131.9 μs (1%) for **1**, 30.3 μs for **2**, 878.1 μs (59%), 2869 μs (5%) and 328.8 μs (36%) for **3**, 127.5 μs (0.1%), 18.7 μs (99.9%) for **5** and 454.4 μs for **6** (figures 3.35). These lifetimes are in concordance with other observed for recent lanthanides complexes.[34]

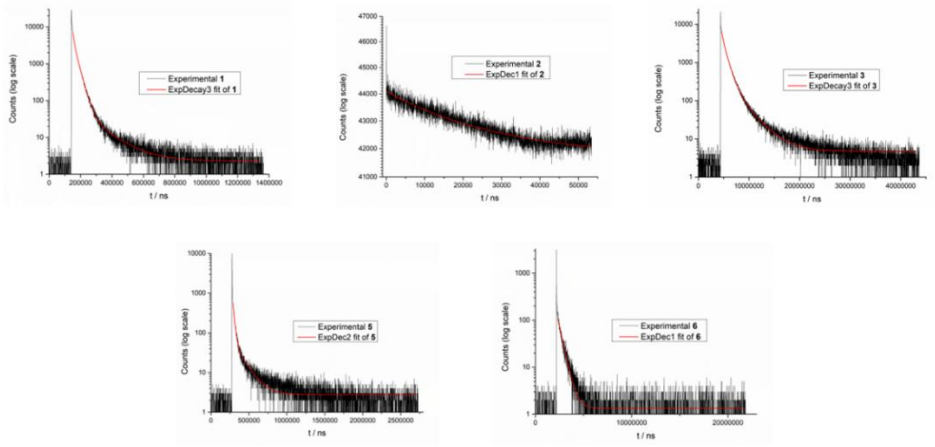

Figure 3.35: Experimental exponential fitting of the excited state lifetime of **1-3** and **5-6** using a flash lamp light source (1 μs pulse, HORIBA Scientific).

After proving the ligand's capability to sensitize luminescence, the photophysics behind the antenna effect has been explored and analyzed by using TD–DFT calculations. It is generally accepted that the energy transfer from the antenna follows the sensitization pathway from singlet (S_1) → triplet (T_1) → Ln^{III} (Figure 3.36).[35-38] Upon absorption of energy, the ligand is excited from the ground state (S_0) to the excited state (S_1), after which it quickly relaxes to the triplet state (T_1) via intersystem crossing. After that, energy can be transferred to the lanthanide ion through a Förster energy transfer mechanism.[27] Although intersystem crossing (ISC) from S_1 to T_1 is spin-forbidden to first order, the interaction between singlet and triplet states is promoted by the presence of a nearby heavy atom.[39] In our compounds **1-3** and **5-6**, it can be induced by spin–orbit coupling enhanced through the presence of the heavy lanthanides. While compounds **2** (Yb, D_{5h}), **5** (Dy, O_h) and **6** (Eu, O_h) were sensitized through the conventional triplet-state-fostered energy transfer, the sensitization of complexes **1** (Dy, D_{5h}) and **3** (Tb, D_{5h}) likely occurred via ligand-to-metal charge transfer (LMCT), also from the excited triplet state.

The position of the antenna triplet energy level is critical for the sensitization of the lanthanide, with a lower limit of at least 2500 cm^{-1} above the main luminescent state of the lanthanide ion to make energy transfer fast and irreversible.[31, 38, 40, 41] TD-DFT, along with the CAM-B3LYP-D3 functional, has been proved to be very efficient in predicting electronic vertical transitions in similar chemical systems.[31, 42, 43] Thus, we used this functional to confirm this by comparing the emitting levels of the lanthanides with the T_1 level of the antenna ligand. A list of the energy levels for the S_0, S_1 and T_1 states of the ligand and the energy gaps with respect to the emitting levels of Dy^{III}, Yb^{III}, Tb^{III} and Eu^{III} is provided in Table 3.19.

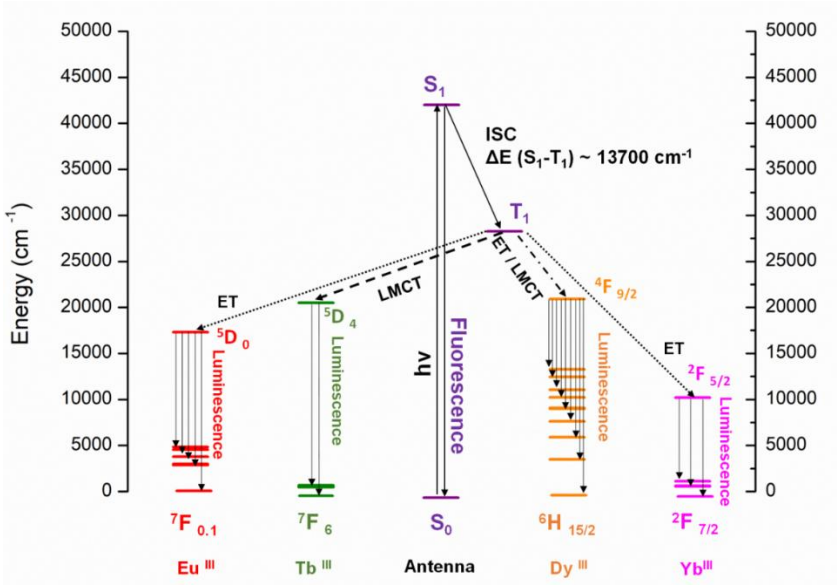

Figure 3.36: A schematic representation of the antenna ligand's energy levels, calculated at the CAM-B3LYP-D3(BJ)/6-31+G(d, p) level of theory, along with the corresponding processes for sensitizing **2** (Yb, D_{5h}), **5** (Dy, O_h) and **6** (Eu, O_h) through inter-system crossing (ISC) to the first triplet state, T_1, and subsequent energy transfer (ET), and for sensitizing **1** (Dy D_{5h}) and **3** (Tb, D_{5h}) through ligand-to-metal charge transfer (LMCT) also via T_1.

The energy gaps between the T_1 level of the ligand $\Delta E(T_1\text{-}S_0)$ and the corresponding $^4F_{9/2}$, $^2F_{5/2}$, $^5D_4$ and $^5D_0$ levels of Dy^{III}, Yb^{III}, Tb^{III} and Eu^{III} were 7388 cm^{-1}, 18081 cm^{-1}, 7785 cm^{-1} and 10985 cm^{-1}, respectively. The energies of the triplet levels are situated at the specified wavenumbers above the lanthanide energy levels. These energy differences are so large that backward energy transfer from the lanthanide to the ligand is highly unlikely.[27] These energy gaps in compounds **1-3**, and **5-6** are much higher than the established 2500 cm^{-1} value, which could indicate that energy transfer occurs via their long-lived triplet states. It has also been reported that intersystem crossing ($S_1 \rightarrow T_1$) in the antenna ligand is maximized when the $\Delta E(S_1\text{-}T_1)$ energy difference amounts to about 5000 cm^{-1},[40, 44] as is the case of our lanthanide

compounds, with $\Delta E(S_1\text{-}T_1)$ values ranging from ~ 8000 cm^{-1} to ~ 14000 cm^{-1}, depending on the level of theory.

Table 3.19: Energy levels for the S_0, S_1 and T_1 states (in Hartrees) calculated at the CAM-B3LYP-D3(BJ)/6-31+G** levels in dichloromethane along with the energy gaps between levels (in cm^{-1}), $\Delta(S_1\text{-}S_0)$, $\Delta(T_1\text{-}T_0)$, and $\Delta(S_1\text{-}T_1)$ (in cm^{-1}); and the difference with the emissive levels of Dy^{III}, Tb^{III}, Eu^{III} and Yb^{III} (in cm^{-1}).

State	CAM-B3LYP-D3
S_0	-1467.300127
S_1	-1467.108687
T_1	-1467.171249
$\Delta(S_1\text{-}T_1)$	13,730.5
$\Delta(S_1\text{-}S_0)$	42,015.3
ΔDy^a	21,118.3
ΔTb^b	21,515.3
ΔEu^c	24,715.3
ΔYb^d	31,811.3
$\Delta(T_1\text{-}S_0)$	28,284.9
ΔDy^a	7,387.9
ΔTb^b	7,784.9
ΔEu^c	10,984.9
ΔYb^d	18,080.9

[a] Difference with the Dy^{III} $^4F_{9/2}$ level at 20897 cm^{-1}.
[b] Difference with the Tb^{III} $^5D_4$ level at 20500 cm^{-1}.
[c] Difference with the Eu^{III} $^5D_0$ level at 17300 cm^{-1}.
[c] Difference with the Yb^{III} $^2F_{5/2}$ level at 10204 cm^{-1}.

Depicting frontier molecular orbitals is an essential method for understanding the distribution of electron density and the characteristics of orbital transitions during photoexcitation in the formation of ligand–lanthanide complexes. The HOMO, LUMO and LUMO+1 of complexes **3** and **6** computed at the ground state at the PBE0/(6–31+G** + SARC-ZORA) level of theory are displayed in Figure 3.37, which are involved in the main electronic transitions, whereas those for the rest of the complexes are gathered in Figure 3.38 for molecular orbitals from HOMO–1 to LUMO+1.

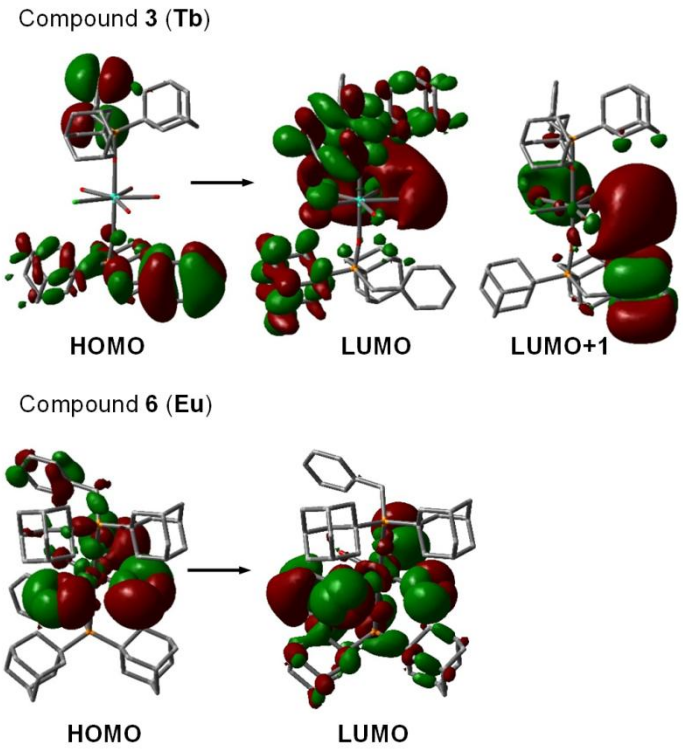

Figure 3.37: Frontier molecular orbitals for compounds **3** and **6** in the gas phase calculated for the ground state at the PBE0/(6–31+G** + SARC-ZORA) level of theory (isocontour plots 0.02 a.u).

Compound **1** (Dy)

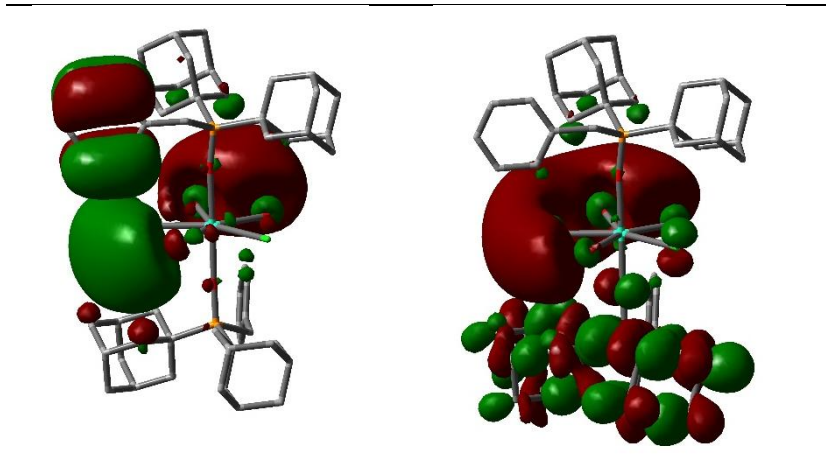

LUMO +1	LUMO

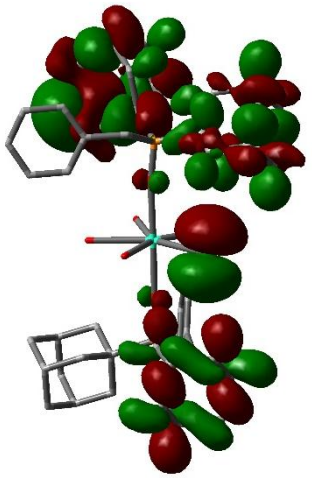

HOMO

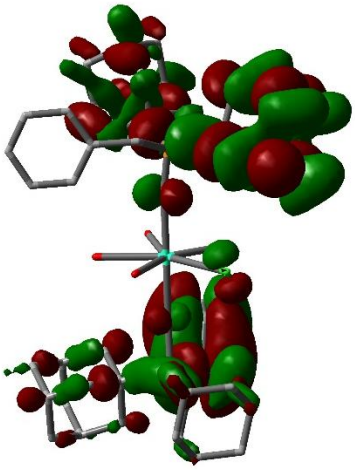

HOMO -1

Compound **2** (Yb)

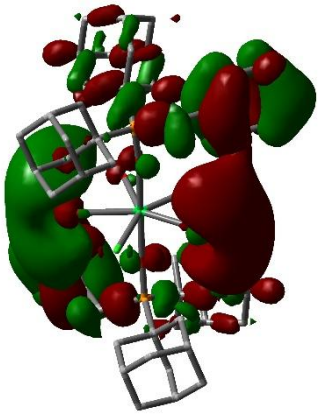

LUMO +1

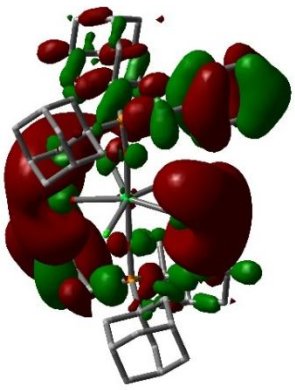

LUMO

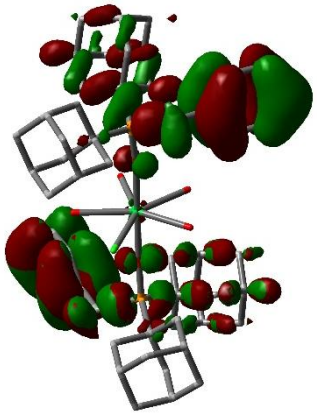

HOMO

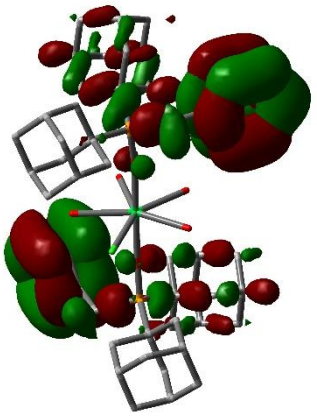

HOMO -1

Compound **3** (Tb)

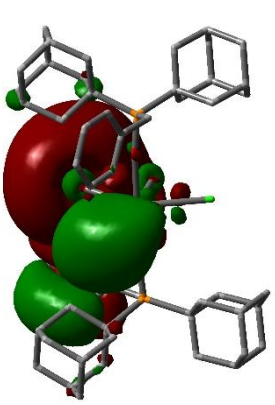

LUMO +1

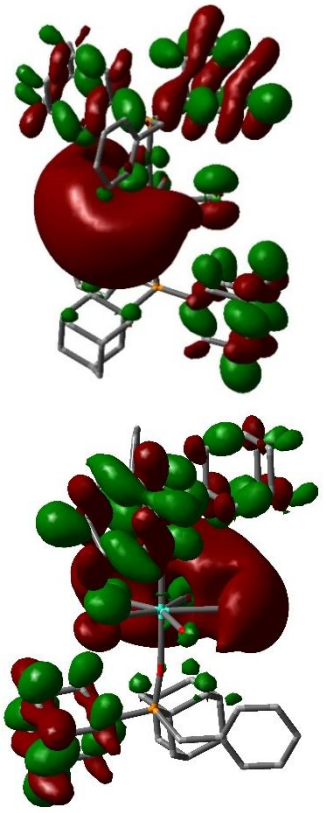

LUMO

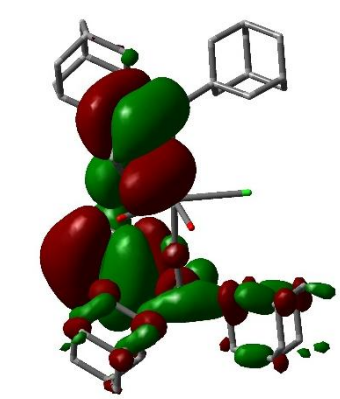

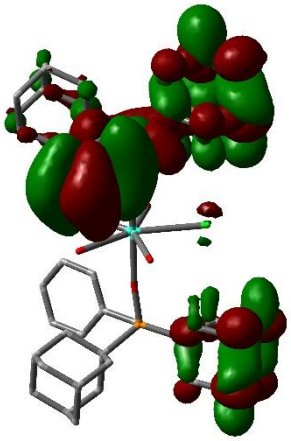

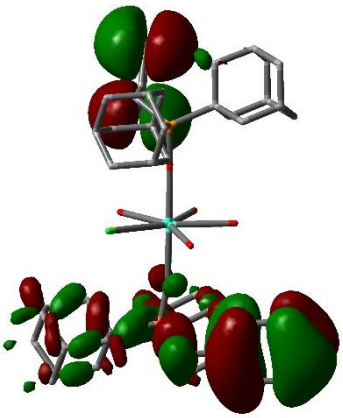

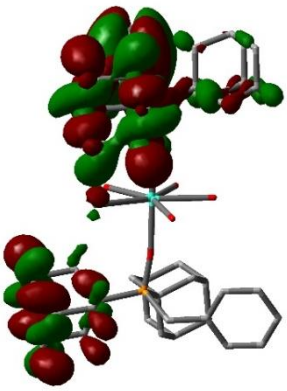

HOMO	HOMO -1

Compound **5** (Dy)

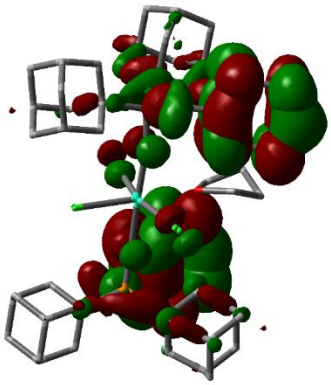

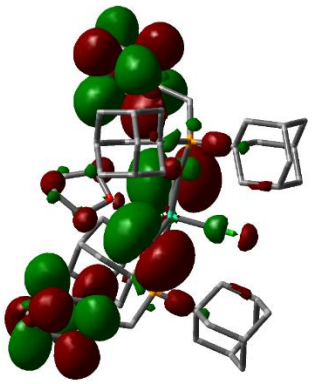

LUMO +1	LUMO

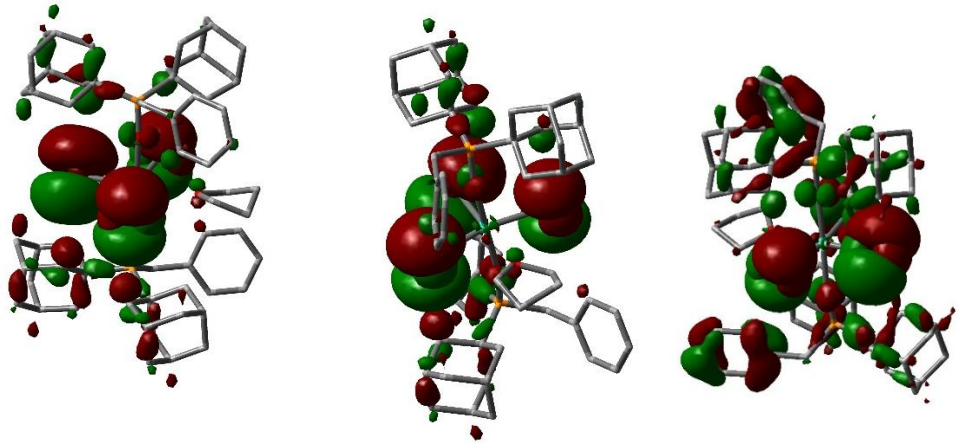

HOMO	HOMO -1

Compound **6** (**Eu**)

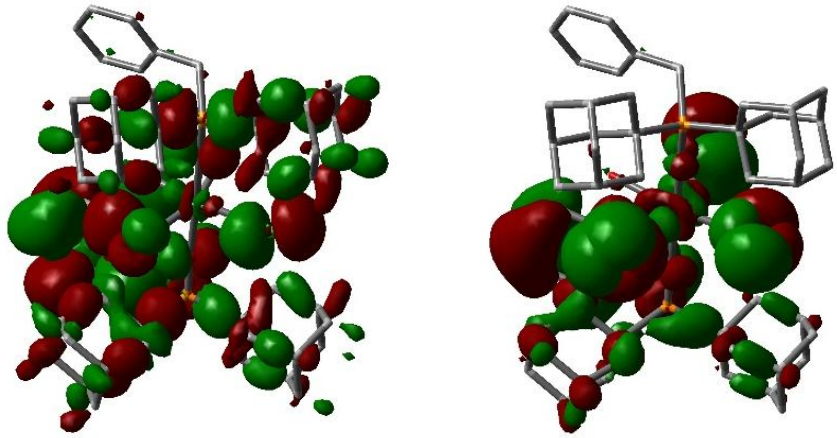

LUMO +1	LUMO

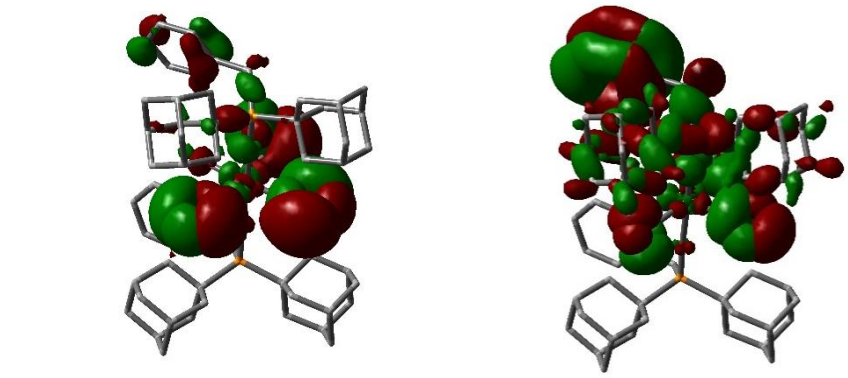

Figure 3.38: Molecular orbitals in the gas phase calculated for the ground state at the PBE0/(6–31+G** + SARC-ZORA) level of theory (isocontour plots 0.02 a.u.). Hydrogen atoms and counterions have been omitted for clarity.

For compound **3** (Tb), the HOMO is localized over the benzene groups of the two ligands and one adamantly moiety, and the LUMO is mainly localized on one benzene, the equatorial plane and three adamantyl groups, whereas the electronic density of the LUMO+1 moves to the Tb^{III} center, the coordinated water molecules and one benzene, suggesting a clear ligand-to-metal (LMCT) charge transfer. This transfer of excited electrons from HOMO to LUMO+1 could occur via a Dexter energy transfer mechanism. Additionally, donor and acceptor must be "in contact" and typically at a distance less than 10 Å, which is our case.[45] Something similar occurs in compound **1** (Dy). In compound **1**, the electron density is localized in the coordinated chloride atom and three adamantyl groups in the HOMO, whereas it resides in the Dy^{III} center, the equatorial plane and two adamantyl rings in the LUMO. In contrast, for compounds **5** (Dy) and **6** (Eu) both HOMO and LUMO are localized on Dy^{III} or Eu^{III} as well as mainly on the benzene rings and the equatorial plane. This result supports the idea that charge transfer to the lanthanide ion was not essential for Dy^{III} and Eu^{III} sensitization in compounds **5** and **6**; thus, this

sensitization could take place via intersystem crossing to the antenna triplet state. This is the case also for compound **2** (Yb), where little electron density is located on the Yb^{III} center in HOMO and LUMO, as well as mainly on the benzene rings of the two ligands, and the coordinated water molecules in the LUMO.

In a recent work of Carneiro Neto et al.[46] it was reported that the energy transfer occurred from the triplet state of the antenna to the nearest energy state of Eu^{III} in a series of Eu^{III} complexes, rather than directly to the luminescent state of the Ln^{III}, as conventionally posited. Actually, they reported large gaps, as in our case, between the T_1 state of their group I ligands and the Eu^{III} emitting level, concluding that the forward intramolecular energy transfer mechanism mainly involved the pathway from T_1 to $^7F_1 \rightarrow {}^5G_2$. In particular, their group I antenna ligands have $\Delta E(S_1\text{-}S_0)$ around 38,900 cm^{-1} and $\Delta E(T_1\text{-}S_0)$ around 31,400 cm^{-1}, which are large as our respective values of ~42,000 cm^{-1} and ~ 26,700 cm^{-1}. Thus, the emission pathway in our compound **6** could also happen via the $^7F_1 \rightarrow {}^5G_2$ pathway or through a closer pathway to our difference energy gaps.

3.5 CONCLUSIONS

Seven lanthanide complexes with two different geometries depending on the synthesis method, pentagonal bipyramidal (D_{5h}) and octahedral (O_h), which contain Dy^{III} (**1** and **5**), Yb^{III} (**2**), Tb^{III} (**3**), Gd^{III} (**4** and **7**) and Eu^{III} (**6**) have been prepared. In all of them, the di(1-adamantyl)benzylphosphine oxide ligand occupy axial positions, whereas chloride atoms and water or THF molecules are located in the equatorial plane. Magnetic measurements carried out on compounds **1-3** and **5** reveal that complexes **1-2** and **5** shows field-induced slow relaxation of the magnetisation and Ln^{III}-centred fluorescence, acting as bifunctional compounds. *Ab initio* calculations support the magnetic findings and provide further insights into the magnetic dynamics of the compounds **1** (Dy^{III} D_{5h}), **2** (Yb^{III} D_{5h}) and **5** (Dy^{III} O_h). They explain the presence of quantum tunneling of magnetization (QTM) in the absence of a magnetic field in the case of compound **2** and they also confirm that the relaxation process occurs primarily through Raman and direct relaxation pathways, rather than through the first excited doublet state.

The absence of slow relaxation of the magnetization for compounds **1** and **5** could be attributed to intermolecular interactions and/or hyperfine interactions that may induce Quantum Tunneling of Magnetization (QTM) at zero field. However, in our group we studied a compound very similar to **1**, with also bipyramidal pentagonal geometry, similar distances, close structural parameters and bromine atoms instead of chlorine, which showed slow relaxation of magnetization at zero field. We thus compared the *ab initio* results for **1** and **5** with those of bromine analogue of **1**. The *ab initio* calculated ground-state tunneling demagnetization rate followed the trend (bromine analogue of **1**) < (**1**) < (**5**). This is in agreement with the maxima values predicted for the transverse *g*-tensor components 0.001 (bromine analogue of

1) < 0.01 (**1**) < 0.05 (**5**). Thus, these results lead us to believe that the observed magnetic behavior of these compounds is intrinsic to the molecular system. Specifically, the presence of heavier halides in the equatorial plane may reduce the transverse ligand field components, thereby suppressing QTM. This is probably due to their weaker donor ability.

Their photophysical properties and the ligand were investigated in detail experimentally and computationally using state-of-the-art TD–DFT calculations, which revealed that the selected ligand acts as an antenna for lanthanide emission in all of them, and also that different pathways take part in the lanthanide sensitization depending on the compound. While compounds **2** (Yb, D_{5h}), **5** (Dy, O_h) and **6** (Eu, O_h) were sensitized through the conventional triplet-state-fostered energy transfer, the sensitization of complexes **1** (Dy D_{5h}) and **3** (Tb, D_{5h}), likely occurred via ligand-to-metal charge transfer (LMCT), also from the excited triplet state. In addition, compounds **1, 5,** and **6** present dual emission properties, which adds a piece to the rational design puzzle of dual emitters.

3.6 REFERENCES

[1] a) F.-S. Guo, B.-M. Day, Y.-C. Chen, M.-L. Tong, A. Mansikkamäki and R. A. Layfield, *Angew. Chem. Int. Ed.*, 2017, **56**, 11445–11449; b) J. Liu, Y.-C. Chen, J.-L. Liu, V. Vieru, L. Ungur, J.-H. Jia, L.-F. Chibotaru, Y. Lan, W. Wernsdorfer, S. Gao, X.-M. Chen and M.-L. Tong, *J. Am. Chem. Soc.*, 2016, **138**, 5441–5450; c) C.-A. P. Goodwin, F. Ortu, D. Reta, N.-F. Chilton and D. P. Mills, *Nature*, 2017, **548**, 439–442; d) F.-S. Guo, B.-M. Day, Y.-C. Chen, M.-L. Tong, A. Mansikkamäki and R.-A. Layfield, *Science*, 2018, **362**, 1400–1403; e) J. Wang, Q.-W. Li, S.-G. Wu, Y.-C. Chen, R.-C. Wan, G.-Z. Huang, Y. Liu, J. L. Liu, D. Reta, M. J. Giansiracusa, Z.-X. Wang, N. F. Chilton and M.-L. Tong, *Angew. Chem. Int. Ed.*, 2021, **60**, 5299–5306; f) C.-A. Gould, K. R. McClain, D. Reta, J. G. C. Kragskow, D.-A. Marchiori, E. Lachman, E.-S. Choi, J.-G. Analytis, R.-D. Britt, N. F. Chilton, B.-G. Harvey and J.-R. Long, *Science*, 2022, **375**, 198-202.

[2] a) S. Sakaue, A. Fuyuhiro, T. Fukuda and N. Ishikawa, *Chem. Commun.*, 2012, **48**, 5337–5339; b) T. Morita, M. Damjanović, K. Katoh, Y. Kitagawa, N. Yasuda, Y. Lan, W. Wernsdorfer, B.-K. Breedlove, M. Enders and M. Yamashita, *J. Am. Chem. Soc.*, 2018, **140**, 2995–3007.

[3] a) R.-J. Blagg, L. Ungur, F. Tuna, J. Speak, P. Comar, D. Collison, W. Wernsdorfer, E.-J. McInnes, L.-F. Chibotaru and R.-E. Winpenny, *Nat. Chem.*, 2013, **5**, 673–678; b) Y.-C. Chen, J.-L. Liu, W. Wernsdorfer, D. Liu, L. F. Chibotaru, X.-M. Chen and M.-L. Tong, *Angew. Chem. Int. Ed.*, 2017, **56**, 4996–5000.

[4] a) L. Ungur, J.-J. Le Roy, I. Korobkov, M. Murugesu and L.-F. Chibotaru, *Angew. Chem. Int. Ed.*, 2014, **53**, 4413–4417; b) K. R. Meihaus and J. R. Long, *J. Am. Chem. Soc.*, 2013, **135**, 17952–17957; c) M.-A. AlDamen, J.-M.

Clemente-Juan, E. Coronado, C. Marti-Gastaldo and A. Gaita-Arino, *J. Am. Chem. Soc.*, 2008, **130**, 8874–8875.

[5] a) Y.-S. Ding, N.-F. Chilton, R.-E. Winpenny and Y.-Z. Zheng, *Angew. Chem. Int. Ed.*, 2016, **55**, 16071-16074; b) Y.-S. Ding, T. Han, Y.-Q. Zhai, D. Reta, N.-F. Chilton, R. E. Winpenny and Y.-Z. Zheng, *Chem. Eur. J.*, 2020, **26**, 5893-5902; c) K.-X. Yu, J.-G. Kragskow, Y.-S. Ding, Y.-Q. Zhai, D. Reta, N. F. Chilton and Y.-Z. Zheng, *Chem*, 2020, **6**, 1777-1793; d) Y.-S. Ding, K.-X. Yu, D. Reta, F. Ortu, R. E. Winpenny, Y.-Z. Zheng and N.-F. Chilton, *Nat. Commun.*, 2018, **9**, 3134.

[6] Z. Jiang, L. Sun, Q. Yang, B. Yin, H. Ke, J. Han, Q. Wei, G. Xie and S. Chen, *J. Mater. Chem. C*, 2018, **6**, 4273-4280.

[7] L. Zhu, Y. Dong, B. Yin, P. Ma and D. Li, *Dalton* Trans., 2021, **50**, 12607-12618.

[8] a) J. Larionova, Y. Guari, S. Sene and G. Félix, *Handbook on the Physics and Chemistry of Rare Earths*, 2023, **64**, 93-173; b) R. Marin, G. Brunet and M. Murugesu, *Angew. Chem. Int. Ed.*, 2021, **60**, 1728-1746; c) J.-T. Chen, T.-D. Zhou and W.-B. Sun, *Dalton Trans.*, 2023, **52**, 4643-4657.

[9] G. Cucinotta, M. Perfetti, J. Luzon, M. Etienne, P.-E. Car, A. Caneschi, G. Calvez, K. Bernot and R. Sessoli *Angew. Chem., Int. Ed.*, 2012, **51**, 1606-1610.

[10] M. Llunell, D. Casanova, J. Cirera, P. Alemany and S. Alvarez, SHAPE, v2.1; Universitat de Barcelona: Barcelona, Spain, 2013.

[11] a) J. Long, A.-N. Selikhov, E. Mamontova, K.-A. Lyssenko, Y. Guari, J. Larionova and A.-A. Trifonov, *Dalton Trans.*, 2019, **48**, 35-39; b) P. Kalita, N. Ahmed, S. Moorthy, V. Béreau, A. Kumar Bar, P. Kumar, P. Nayak, J.-P. Sutter, S. Kumar Singh and V. Chandrasekhar, *Dalton trans.*, 2019, **48**, 2804-2815.

[12] P.-A. Malmqvist and B.-O. Roos, *Chem. Phys. Lett.*, 1989, **155**, 189.

[13] L.-F. Chibotaru and L. Ungur, *J. Chem. Phys.*, 2012, **137**, 064112.

[14] F. Neese, *WIREs Comput. Mol. Sci.*, **2012**, ***2***, 73–78.

[15] F. Neese, U.-B. Wennmohs and C. Riplinger, *J. Chem. Phys.*, 2020, **152**, 224108.

[16] F. Neese, *WIREs Comput. Mol. Sci.*, 2022, **12**, e1606.

[17] S. Gómez-Coca, D. Aravena, R. Morales, E. Ruiz, *Coord. Chem. Rev.*, 2015, **289–290**, 379-392.

[18] Y. Gil, M.-M. Quesada-Moreno, M.-A. Palacios, S. Gómez-Coca, E. Colacio, E. Ruiz, D. Aravena, *Inorg. Chem. Front.*, 2025, **12**, 2856-2871.

[19] D. Aravena, *J. Phys. Chem. Lett.,* 2018, **9**, 5327-5333.

[20] M. Fondo, J. Corredoira-Vázquez, A.-M. García-Deybe, J. Sanmartín-Matalobos, M. Amoza, A.-M. P. Botas, R.-A. S. Ferreira, E.-D. Carlos and E. Colacio, *Inorg. Chem. Front.,* 2020, **7**, 3019-3029.

[21] A.-V. Gavrikov, N.-N. Efimov, Z.-V. Dobrokhotova, A.-B. Ilyukhin, P.-N. Vasilyev and V.-M. Novotortsev, *Dalton Trans.,* 2017, **46**, 11806–11816.

[22] a) J. Ruiz, G. Lorusso, M. Evangelisti, E.-K. Brechin, S.-J. A. Pope and E. Colacio, *Inorg. Chem.* 2014, **53**, 3586-3594; b) J.-L. Liu, K. Yuan, J.-D. Leng, L. Ungur, W. Wernsdorfer, F.-S. Guo, L.-F. Chibotaru and M.-L. Tong, *Inorg. Chem.,* 2012, **51**, 8538-8544; F. Guégan, J. Jung, B. Le Guennic, F. Riobé, O. Maury, B. Gillon, J.-F. Jacquot, Y. Guyot, C. Morell and D. Luneau, *Inorg. Chem. Front.,* 2019, **6**, 3152-3157.

[23] a) A. Singh and K.-N. Shrivastava, *Phys. Status Solidi B,* 1979, **95**, 273–277; b) K.-N. Shrivastava, *Phys. Status Solidi B,* 1983, **117**, 437–458.

[24] a) A Borah, S. Dey, S.-K. Gupta, M.-G. Walawalkar, G. Rajaraman and R. Murugavel, *Chem. Commun.,* 2020, **56**, 11879-11892; b) A. Borah, S. Dey, K. Siddiqui, S.-K. Gupta, G. Rajaraman and R. Murugavel, *Dalton Trans.,* 2024, **53**, 7263-7267.

[25] a) J. Long, A.-N. Selikhov, E. Mamontova, K.-A. Lyssenko, Y. Guari, J. Larionova and A.-A. Trifonov, *Dalton Trans.,* 2020, **49**, 4039–4043; b) X. Yina, S. Lia and B. Liaoa, *Inorg. Chim. Acta,* 2020, **504**, 119451; c) K. R.

Vignesh, D.-I. Alexandropoulos, H. Xie and K.-R. Dunbar, *Dalton Trans.*, 2020, **49**, 4694-4698; d) X. Sun, R. Ding, P. Cen, X. Wang, X. Qin, D. Tian and X. Liu, *Inorg. Chem. Commun.*, 2024, **169**, 113064.

[26] M. Li, H. Wu, Z. Xia, L. Ungur, D. Liu, L.F. Chibotaru, H. Ke, S. Chen, S. Gao. *Inorg. Chem.,* 2020, 59, 7158.

[27] J.-C.-G. Bünzli and S.V. Eliseeva, Springer, Berlin Heidelberg, Berlin, Heidelberg, 2011, 1–45.

[28] D. Parker, J.D. Fradgley and K. L. Wong, *Chem. Soc. Rev.,* 2021, **50**, 8193–8213.

[29] E.-G. Moore, A.P.S. Samuel and K.-N. Raymond, *Acc. Chem. Res.,* 2009, **42**, 542–552.

[30] a) Y. Yang, X. Hu, Z. Yang and W. Huang, *Adv. Funct. Mater.,* 2024, 2412970; b) P. Li and H. Li, *Coord. Chem. Rev.,* 2021, **441**, 213988; c) M. C. Heffern, L. M. Matosziuk and T. J. Meade, *Chem. Rev.,* 2014, **114**, 4496−4539.

[31] A. Navarro, A. Ruiz-Arias, F. Fueyo-González, C. Izquierdo-García, T. Peña-Ruiz, M. Gutiérrez-Rodríguez, R. Herranz, J. M. Cuerva, J. A. González-Vera and A. Orte, *Spectrochim. Acta A: Mol. Biomol. Spectrosc.,* 2024, **323**, 124926.

[32] Y. Ma, M. Zhu, Y. Zhang, E. Gao and S. Wu, *Inorg. Chim. Acta,* 2022, **537**, 120928.

[33] K. Yuhara, K. Tanaka and Y. Chujo, *Mater. Chem. Front.,* 2022, **6**, 1414–1420.

[34] a) B. Ay, R. Takano and T. Ishida, *Solid State Sci.,* 2024, **157**, 107723; b) X. Liu, R. Yang, L. Zhang, J. Zhou, C. Huang, H. Zou and Z. Xiao, *J. Rare Earths.,* 2024, **42**, 1101-1109; c) L. N. Puntus, D. A. Bardonov, E. A. Varaksina, I. V. Taydakov, D. M. Roitershtein, I. E. Nifanteva and K. A. Lyssenkof, *Mendeleev Commun.,* 2024, **34**, 325-328; d) N. M. Moraes Fernandes, G. Barbosa-Reis, D. Oliveira Silva and I. A. Bagatin, *ChemistrySelect,* 2023, **8**, e202302321; e) D. M. Lyubov, T. V. Mahrova, A. V.

Cherkasov, G. K. Fukin, Y. V. Fedorov and A. A. Trifonov, *Eur. J. Inorg. Chem.,* 2023, **26**, e202300292; f) I. N. Hegarty, C. S. Hawes and T. Gunnlaugsson, *Org. Chem. Front.,* 2023, **10**, 1915-1926;

g) V. M. Korshunov, A. V. Tsorieva, V. E. Gontcharenko, S. R. Zanizdra, M. T. Metlin, T. A. Polikovskiy and I. V. Taydakov, *Inorganics,* 2023, **11**, 15; h) Sushila, R. Siddiqui, S. Patra, K. Shivam, A. Sil, B. Guchhait, H. Tian, R. Kataria, S. Goswami, P. Venugopalan and R. Patra, *Inorg. Chem.,* 2022, **61**, 11484-11496.

[35] C. P. Montgomery, B. S. Murray, E. J. New, R. Pal and D. Parker, *Acc. Chem. Res.,* 2009, **42**, 925-937.

[36] M. H. V. Werts, *Sci. Prog.,* 2005, **88**, 101-131.

[37] E. G. Moore, A. P. S. Samuel and K. N. Raymond, *Acc. Chem. Res.,* 2009, **42**, 542-552.

[38] W. Thor, H. Y. Kai, Y. H. Yeung, Y. Wu, T. L. Cheung, L. K. B. Tam, Y. Zhang, L. J. Charbonniere, P. A. Tanner and K. L. Wong, *J. Am. Chem. Soc.,* 2024, **4**, 3813−3822.

[39] A. Balamurugan, A. K. Gupta, R. Boomishankar, M. Lakshmipathi Reddy and M. Jayakannan, *ChemPlusChem*, 2013, **78**, 737–745.

[40] F. J. Steemers, W. Verboom, D. N. Reinhoudt, E. B. van der Tol and J. W. Verhoeven, *J. Am. Chem. Soc.,* 1995, **117**, 9408-9414.

[41] W. Liu, G. Liu, G. Gao, Z. Gao, Y. Zhang, S. Wu, E. Gao and M. Zhu, *Inorg. Chem. Commun.,* 2021, **133**, 10895.

[42] J. Hanuza, P. Godlewska, R. Lisiecki, W. Ryba-Romanowski, P. Kadłubanski, J. Lorenc, A. Łukowiak, L. Macalik, Y. Gerasymchuk and J. Legendziewicz*, Spectrochim. Acta A,* 2018, **196**, 202–208.

[43] Y. Okayasu and J. Yuasa, *J. Phys. Chem. Lett.,* 2021, **12**, 6867–6874.

[44] E. Kasprzycka, V. A. Trush, V. M. Amirkhanov, L. Jerzykiewicz, O. L. Malta, J. Legendziewicz and P. Gawryszewska, *Chem. Eur. J.,* 2017, **23**, 1318 – 1330.

[45] L. Singh, R. Dubey and R. N. Rai, Reino Unido: CRC Press, 2023.

[46] A. N. Carneiro Neto, R. T. Moura Jr, L. D. Carlos, O. L. Malta, M. Sanadar, A. Melchior, E. Kraka, S. Ruggieri, M. Bettinelli and F. Piccinelli, *Inorg. Chem.,* 2022, **61**, 16333-16346.

CHAPTER 4

HETERO-TRINUCLEAR Zn^{II}-Ln^{III}-Zn^{II} COMPLEXES WITH CHIRAL MANNICH BASE LIGANDS

4.1 INTRODUCTION

For the past few decades, lanthanide complexes have been of great interest for researchers as they exhibit interesting physico-chemical properties, in particular, magnetic and luminescent properties which lead to potential applications in areas such as molecular spintronics, ultrahigh density magnetic storage, sensors, display technologies, optical storage and so on.[1] In the field of Molecular Magnetism and Coordination Chemistry, hetero-trinuclear Zn^{II}-Ln^{III}-Zn^{II} complexes with Schiff-base ligands are of particular interest for achieving magneto-luminescent coordination compounds, that is, molecules that combine luminescence and SIM behavior.[2]

Moreover, the use of chiral Schiff base ligands could lead to the formation of enantiomeric pairs that exhibit circularly polarised luminescence (CPL), resulting in lanthanide complexes with a combination of chiral, luminescent and magnetic properties, providing a rich platform for multifunctional materials with applications ranging from data storage to advanced optical devices.[3] Some examples of Zn^{II}-Ln^{III}-Zn^{II} complexes from chiral Schiff base ligands have been reported.[4] In these examples, the complexes containing Dy^{III} ion exhibit field-induced single-molecule magnet behaviour and, all of them display the characteristic emission of lanthanide ions originated by the energy transfer from the ligand to the metal ion center. Therefore, complexes containing Dy^{III} ions might be good candidates for chiral magneto-luminescent molecular materials. However, the CPL properties have not measured even though the Kurtz−Perry measurements reveal that these complexes are potential nonlinear optical materials.

In view of the above considerations, this chapter focuses on the design and preparation of the chiral Mannich base ligands $\mathbf{H_2L_{R,\,R}}$ and $\mathbf{H_2L_{S,\,S}}$ (see figure 4.1) and the study of their reactivity towards Ln^{III} and Zn^{II} metal ions.

The Mannich base ligands, which also have two distinct cavities for the complexation with the Zn^{II} and Ln^{III} ions, show some advantages with respect to the Schiff base ligands as they possess greater flexibility and do not contain hydrogen atoms bonded to amino groups. In fact, some Zn^{II}-Ln^{III}-Zn^{II} complexes have been prepared with good SIM behaviour and large energy barriers.[5] Therefore, the aim of this chapter is to synthesize lanthanide trinuclear Zn^{II}-Ln^{III}-Zn^{II} complexes that exhibit good magnetic and luminescent properties and the possibility of showing CPL due to the presence of chiral ligands.

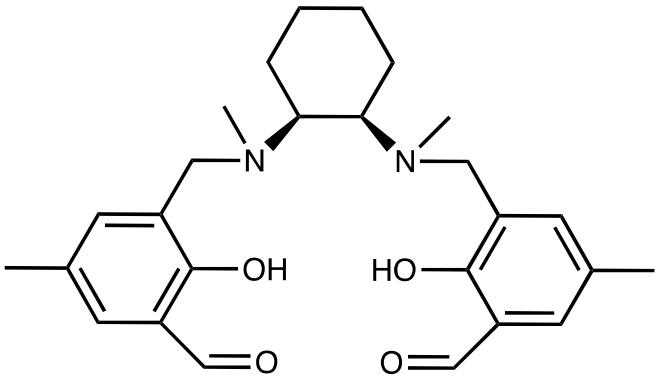

Figure 4.1: Proposed chiral ligand to obtain Zn^{II}-Ln^{III}-Zn^{II} complexes

4.2 SYNTHESIS OF PRECURSOR AND CHIRAL LIGANDS

4.2.1 Synthesis of 3-(chloromethyl)-2-hydroxy-5-methylbenzylaldehyde

Formaldehyde (1.963 g, 65.4 mmol) and 5-methylsalicyaldehyde (3.002 g, 22 mmol) were added to 40 mL of concentrated hydrochloric acid in a 250-mL round flask. The mixture was refluxed at 60°C for 4 hours. After, the pink solution was extracted three times with dichloromethane, dried with sodium sulphate, filtered, and concentrated under vacuum to give a white-grey powder. Yield: 66%. IR (KBr, cm^{-1}): 3100, ν(OH); 3000, 2889 ν(CH); 1665, ν(C=O), 764, ν (C−Cl). ^{1}H NMR ($CDCl_3$, ppm): 11.21 (s, $H_{hydroxy}$), 9.85 (s, $H_{Aldehyde}$), 7.44 (s, H_{Ar}), 7.33 (s, H_{Ar}), 4.66 (s, $H_{methylene}$), 2.35 (s, H_{methyl}).

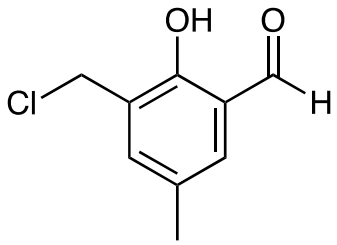

4.2.2 Synthesis of R,R'-dimethyl-N,N'-bis(2-hydroxy-3-formyl-5-methyl -benzyl)cyclohexanediamine ($H_2L_{R,R}$)

Sodium hydride 60% (1.16 g, 29.02 mmol) was added to (1*R*, 2*R*)-dimethyl cyclohexane diamine (1.03 g, 7.25 mmol) in 12 ml of dry THF. After stirring under nitrogen atmosphere for 20 minutes, 3-(chloromethyl)-2-hydroxy-5-methylbenzylaldehyde (2.68 g, 14.51 mmol) was added in a portion, and the mixture was heated to 50 °C. After 18 h, the reaction mixture was extracted three times with dichloromethane and the organic layer was dried with sodium sulphate. Finally, the solvent was removed under vacuum to yield the product as a brown solid. Yield: 63%. IR (KBr, cm^{-1}): 2925, ν(CH); 1679, ν(C=O); 1662, 1447, ν (C=C and C–N). Anal. Calc. for $C_{26}H_{34}N_2O_4$: C, 71.21; H, 7.81; N, 6.39. found:

C, 71.56; H, 7.69; N,6.49. ^{1}H NMR ($CDCl_3$, ppm): 10.8 (s, $H_{aldehyde}$), 7.38 (s, H_{Ar}), 7.26 (s, H_{Ar}), 3.68 (s, $H_{methylene}$), 2.68 (dt, $H_{cyclohexane}$), 2.24 (s, H_{methyl}), 2.19 (s, H_{methyl}), 1.87 (m, $H_{cyclohenane}$), 1.28 (m, $H_{cyclohenane}$).

4.2.3 Synthesis of S,S'-dimethyl-N,N'-bis(2-hydroxy-3-formyl-5-methyl -benzyl)cyclohexanediamine ($H_2L_{S,S}$)

This ligand was prepared following the same procedure of $\mathbf{H_2L_{R,R}}$ but using (1*S*, 2*S*)-dimethyl cyclohexane diamine instead of (1*R*, 2*R*)-dimethyl cyclohexane diamine. Yield: 60%. IR (KBr, cm^{-1}): 2925, ν(CH); 1680, ν(C=O); 1661, 1445 ν(C=C and C-N). Anal. Calc. for $C_{26}H_{34}N_2O_4$: C, 71.21; H, 7.81; N, 6.39. found: C, 71.00; H, 7.69; N, 6.19. ^{1}H NMR ($CDCl_3$, ppm): 10.11 (s, $H_{aldehyde}$), 7.36 (s, H_{Ar}), 7.26 (s, H_{Ar}), 3.68 (s, $H_{methylene}$), 2.62 (dt, $H_{cyclohexane}$), 2.24 (s, H_{methyl}), 2.19 (s, H_{methyl}), 1.87 (m, $H_{cyclohexane}$), 1.25 (m, $H_{cyclohexane}$).

4.3. SYNTHESIS OF CHIRAL COMPLEXES

4.3.1. Synthesis of chiral complex [ZnCl(μ-$L_{R,R}$)Dy(μ-$L_{R,R}$)ClZn]PF_6 (1)

$H_2L_{R,R}$ (20.00 mg, 0.046 mmol), triethylamine (25μL, 0.182 mmol), and $ZnCl_2$ (6.27 mg, 0.046 mmol) were dissolved in 8 mL of methanol. Then, a water solution (1 mL) of potassium hexafluorophosphate KPF_6 (4.23 mg, 0.023 mmol) was added. After stirring for 10 min, $Dy(CF_3SO_3)_3$ (14.02 mg, 0.023 mmol) was added. The reaction mixture was stirred at room temperature for 30 minutes. Crystallization from slow diffusion of isopropanol into the MeOH solution produced colourless single-crystals for X-ray diffraction. Yield: 10%. Anal. Calc for. $C_{52}H_{64}N_4O_8DyZn_2Cl_2PF_6$: C, 45.18; H, 4.67; N, 4.05. Found: C, 45.09; H, 4.01; N, 3.97. IR (cm^{-1}): 1622, 1560 ν(C=C and C-N); 835, ν(C–O).

4.3.2. Synthesis of chiral complex [ZnCl(μ-$L_{S,S}$)Dy(μ-$L_{S,S}$)ClZn]PF_6 (2)

This compound was obtained following the same methodology as for **1** but using $H_2L_{S,S}$ instead of $H_2L_{R,R}$. After several days, a microcrystalline yellow powder was obtained from slow diffusion of isopropanol into the MeOH solution. Yield:10%. Anal. Calc for. $C_{52}H_{64}N_4O_8DyZn_2Cl_2PF_6$: C, 45.18; H, 4.67; N, 4.05. Found: C, 45.21; H, 4.83; N, 3.91. IR (KBr, cm^{-1}): 1620, 1561 ν(C=C and C–N); 835, ν(C–O).

4.3.3. Synthesis of chiral complex [ZnCl(μ-$L_{R,R}$)Tb(μ-$L_{R,R}$)ClZn] (PF_6) (3)

This compound was obtained following the same procedure as for **1** but using $Tb(CF_3SO_3)_3$ (13.94 mg, 0.023 mmol) instead of $Dy(CF_3SO_3)_3$. After several days, a microcrystalline yellow powder was obtained from slow diffusion of isopropanol into the MeOH solution. Yield: 10%. Anal. Calc for. $C_{52}H_{64}N_4O_8TbZn_2Cl_2PF_6$: C 45.30; H 4.68; N 4.06. Found: C 44.96; H 4.94; N 4.03. IR (KBr, cm^{-1}): 1623, 1562 ν(C=C and C–N); 835, ν(C–O).

4.3.4. Synthesis of chiral complex [ZnCl(μ-$L_{S,S}$)Tb(μ-$L_{S,S}$)ClZn] (PF_6) (4)

This compound was obtained following the same procedure as for **3** but using $H_2L_{S,S}$ instead of $H_2L_{R,R}$. Crystallization from slow diffusion of isopropanol into the MeOH solution produced colourless single-crystals for X-ray diffraction. Yield: 63%. Anal. Calc for. $C_{52}H_{64}N_4O_8TbZn_2Cl_2PF_6$: C 45.30; H 4.68; N 4.06. Found: C 45.20; H 4.46; N 3.97. IR (cm^{-1}): 1625, 1565 ν(C=C and C–N); 835, ν(C–O).

4.4. RESULTS AND DISCUSSION

The chiral Mannich base ligands, $H_2L_{R,R}$ and $H_2L_{S,S}$, have been designed to obtain hetero-trinuclear Zn^{II}-Ln^{III}-Zn^{II} complexes with interesting magnetic, luminescent and chiral properties. The reaction of these ligands with $ZnCl_2$ and $Ln(CF_3SO_3)_3$ in 2:2:1 molar ratio in methanol and further diffusion of isopropanol into the mother solution give rise to the desired compounds of general formula [ZnCl(μ-L)Ln(μ-L)ClZn] (PF_6) with Ln^{III} = Dy^{III} and Tb^{III}.

4.4.1. Crystal structure of compounds 1 and 4

The molecular structures of **1** and **4** were determined by single X-ray diffraction, revealing that they crystalize in the triclinic space group, P-1. The crystallographic data and structural refinement details are shown in table 4.1. Since complexes **1** and **4** are isostructural, only the structure of **1** is described as a representative example.

Compound **1** consists of cationic trinuclear units $[ZnCl(\mu\text{-}L_{R.R})Dy(\mu\text{-}L_{R,R})ClZn]^+$ and one hexafluorophosphate counteranion (Figure 4.2). The cationic unit $[ZnCl(\mu\text{-}L_{R.R})Dy(\mu\text{-}L_{R,R})ClZn]^+$ is constructed by two $[ZnClL_{R,R}]^-$ units with a central Dy^{III} ion bridged to the Zn^{II} ions through two phenoxo oxygen atoms from two different chiral ligands. The Zn1-Dy and Zn_2-Dy bond distances are 3.592 (5) Å and 3.579 (6) Å, respectively. The main N_2O_2 basal planes are not parallel but making an angle of 25.74°, so that the Zn1−Dy−Zn_2 ions are not aligned and they form and angle of 142.38º. The most important bond distances and angles for **1** and **4** are listed in tables 4.2, 4.3, 4.4 and 4.5.

Table 4.1: Crystallographic data and structural refinement details for complexes **1** and **4**.

Compound	**1**	**4**
Formula	$C_{52}H_{64}N_4O_8$ $DyZn_2Cl_2PF_6$	$C_{52}H_{64}N_4O_8TbZn_2Cl_2P$ F_6
M_r	1382.18	1376.58
Crystal System	triclinic	triclinic
Space Group	P-1	P-1
a (Å)	13.3528(3)	13.3708(4)
b (Å)	14.3326(4)	14.3148(4)
c (Å)	16.0053(5)	15.9891(5)
α (°)	81.4050(10)	81.2630(10)
β (°)	66.6600(10)	66.5670(10)
γ (°)	84.7720(10)	84.7300(10)
V (Å^3)	2779.14(13)	2773.67(14)
Z	2	4
Dc (g cm^{-1})	1.652	1.648
μ(MoK$_\alpha$) (mm^{-1})	2.387	2.320
T (K)	100	100
Observed reflections[a]	13778 (12.492)	13780 (11828)
R_{int}[a]	0.0351	0.0471
Parameters	765	763
GOF	1.300	1.216
R_1[b,a]	0.0471(0.0398)	0.0579 (0.0451)
wR_2[c,a]	0.0939 (0.1038)	0.1013 (0.1138)

[a] Values in parentheses for reflections with I > 2s(I)
[b] $R1 = \sum||Fo| - |Fc||/\sum|Fo|$
[c] $wR2 = \{\sum [w(F_o^2 - F_c^2)^2] / \sum [w(F_o^2)^2]\}^{½}$

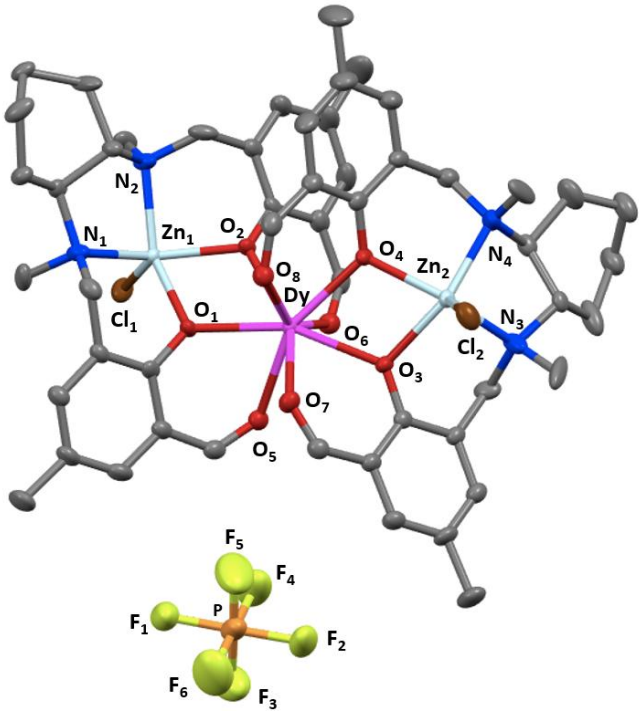

Figure 4.2: Perspective view of the structure of complex **1**. The hydrogen atoms are omitted for clarity. Code colors: Dy (purple), O (red), Zn (light blue), N (blue), Cl (brown), P (orange) and S (yellow).

Table 4.2: Selected bond distances (Å) for complex **1**.

Selected bond distances (Å)			
Dy – O1	2.263 (3)	Zn1 – O2	2.080 (3)
Dy – O2	2.305 (3)	Zn1 – N1	2.125 (4)
Dy – O3	2.263 (3)	Zn1 – N2	2.159 (4)
Dy – O4	2.310 (3)	Zn1 – Cl1	2.247 (11)
Dy – O5	2.433 (3)	Zn2 – O3	2.094 (3)
Dy – O6	2.388 (3)	Zn2 – O4	2.076 (3)
Dy – O7	2.433 (3)	Zn2 – N3	2.127 (4)
Dy – O8	2.382 (3)	Zn2 – N4	2.148 (4)
Zn1 – O1	2.089 (3)	Zn2 – Cl2	2.222 (12)

Table 4.3: Selected bond angles (º) for complex **1**.

Selected bond angles (º)					
O1– Dy – O2	65.8 (10)	O1– Dy – O3	156.2 (10)	O1 – Dy – O4	136.2 (10)
O1– Dy – O5	71.6 (11)	O1– Dy – O6	110.1(11)	O1 – Dy – O7	89.4 (10)
O1– Dy – O8	76.9 (11)	O2– Dy – O3	135.4 (11)	O2 – Dy – O4	81.0 (10)
O2– Dy – O5	112.6 (10)	O2– Dy – O6	72.3 (11)	O2 – Dy – O7	151.3 (11)
O2 –Dy – O8	84.6 (11)	O3– Dy – O4	66.4 (10)	O3 – Dy – O5	87.6 (10)
O3 –Dy – O6	74.7 (11)	O3– Dy – O7	72.2 (11)	O3 – Dy – O8	111.5 (10)
O4 – Dy– O5	150.9 (11)	O4 –Dy – O6	83.9 (11)	O4 – Dy – O7	111.7 (11)
O4 –Dy – O8	72.4 (11)	O5 –Dy – O6	76.7 (11)	O5 – Dy – O7	69.7 (11)
O5 –Dy – O8	132.3 (11)	O6 –Dy – O7	133.06 (11)	O6 – Dy – O8	149.3 (11)
O7 – Dy– O8	75.2 (11)	O1–Zn1– O2	73.06 (11)	Cl1–Zn1 – O1	106.68 (9)
Cl1–Zn1-O2	110.34 (9)	Cl1–Zn1–N1	108.57(12)	Cl1– Zn1– N2	107.2 (13)
N1–Zn1– O2	140.67(15)	O2–Zn1– N2	89.37 (14)	N2 –Zn1 – N1	84.57 (14)
N1–Zn1– O1	90.61 (13)	O1–Zn1– N2	143.23 (15)	O3 –Zn2 – O4	73.79 (11)
Cl2–Zn2-O3	103.55 (9)	Cl2–Zn2–O4	111.51(10)	Cl2–Zn2 – N3	104.74(15)
Cl2–Zn2-N4	110.48 (13)	N3–Zn2– O3	90.46 (14)	O4 –Zn2 – N4	84.91 (14)
N4–Zn2– N3	84.57 (14)	O4–Zn2– N3	142.87(17)	O3 –Zn2 – N4	90.48(14)

Table 4.4: Selected bond distances (Å) for complex **4**.

Selected bond distances (Å)			
Tb – O1	2.321(2)	Zn1 – O2	2.092 (3)
Tb – O2	2.277 (4)	Zn1 – N1	2.150 (4)
Tb – O3	2.314 (3)	Zn1 – N2	2.128 (4)
Tb – O4	2.280 (3)	Zn1 – Cl1	2.222 (14)
Tb – O5	2.396 (4)	Zn2 – O3	2.082 (3)
Tb – O6	2.446 (3)	Zn2 – O4	2.086 (3)
Tb – O7	2.402 (3)	Zn2 – N3	2.160 (4)
Tb – O8	2.447 (3)	Zn2 – N4	2.128 (4)
Zn1 – O1	2.081 (3)	Zn2 – Cl2	2.245 (12)

Table 4.5: Selected bond angles (º) for complex **4**.

Selected bond angles (º)					
O1 – Tb – O2	66.2 (11)	O1 – Tb – O3	81.44 (11)	O1 – Tb – O4	136.4 (11)
O1 – Tb – O5	72.1 (12)	O1 – Tb – O6	110.8 (12)	O1 – Tb – O7	84.01 (12)
O1 – Tb – O8	151.35 (11)	O2 – Tb – O3	135.3 (11)	O2 – Tb – O4	156.5 (11)
O2 – Tb – O5	111.4 (12)	O2 – Tb – O6	71.8 (12)	O2 – Tb – O7	74.6 (12)
O2 – Tb – O8	88.0 (11)	O3 – Tb – O4	65.5 (11)	O3 – Tb – O5	84.9 (12)
O3 – Tb – O6	151.8 (11)	O3 – Tb – O7	72.0 (12)	O3 – Tb – O8	112.1 (11)
O4 – Tb – O5	76.9 (12)	O4 – Tb – O6	90.1 (11)	O4 – Tb – O7	110.1 (12)
O4 – Tb – O8	71.4 (11)	O5 – Tb – O6	75.7 (12)	O5 – Tb – O7	149.0 (12)
O5 – Tb – O8	132.1 (12)	O6 – Tb – O7	132.8 (12)	O6 – Tb – O8	69.5 (12)
O7 – Tb – O8	77.1 (12)	O1 – Zn1 – O2	73.06 (12)	Cl1– Zn1 – O1	111.41 (10)
Cl1– Zn1 – O2	103.56 (10)	Cl1– Zn1 – N2	104.48 (16)	Cl1– Zn1 – N1	110.60 (15)
O2 – Zn1 – N2	90.47 (15)	N2 – Zn1 – N1	85.04 (17)	N1 – Zn1 – O1	89.60 (14)
O1 – Zn1 – N2	143.23 (18)	N1 – Zn1 – O2	145.61 (17)	O3 – Zn2 – O4	73.23 (12)
Cl2– Zn2 – O3	110.15 (10)	Cl2– Zn2 – O4	106.93 (10)	Cl2– Zn2 – N3	107.24 (13)
Cl2– Zn2 – N4	108.50 (14)	O4 – Zn2 – N4	90.51 (15)	N4 – Zn2 – N3	84.57 (15)
N3 – Zn2 –N4	89.25 (14)	O3 – Zn2 – N4	140.93 (16)	O4 –Zn2 –N3	145.27 (16)

In the structure, the Zn^{II} ions occupy the inner N_2O_2 coordination site and the Dy^{III} ion the outer O_2O_2 cavity of the chiral ligands. In this disposition, the Zn^{II} ions present a ZnN_2O_2Cl coordination environment with a distorted square-pyramid geometry, in which the two nitrogen atoms and the two oxygen atoms are located in the equatorial plane, while the chloride atom is located in the apical position. The Zn–O bond distances are in the 2.076 (3) – 2.094 (3) Å range, whereas the Zn-N bond distances are larger and in the 2.125 (4) –2.159 (4) Å range. The Zn1– Cl1 and Zn2-Cl2 bond lengths are 2.247 (11) Å and 2.222 (12) Å, respectively. All these bond distances are comparable to those reported previously for other complexes containing similar ligands.[5] The coordination geometry of Zn^{II} ions has been confirmed by the SHAPE software[6] indicating that it is very close to the ideal square-pyramid (SPY-5) with S values of 0.724 and 0.656 for Zn1 and 0.642 and 0.703 for Zn2 (see table 4.6).

Table 4.6: Obtained S values with the SHAPE software for the geometries of Zn^{II} atoms in **1** and **4**

	JTBPY-5	**SPY-5**	**TBPY-5**	**OC-5**	**PP-5**
Zn1 (**1**)	8.557	0.724	5.032	3.752	32.313
Zn2 (**1**)	8.796	0.656	5.398	3.469	30.465
Zn1 (**4**)	8.882	0.642	5.470	3.437	30.397
Zn2 (**4**)	8.640	0.703	5.098	3.725	32.369

JTBPY-5: 5(D_{3h}) Johnson trigonal bipyramid J12, SPY-5: 4(C_{4v}) Spherical square pyramid, TBPY-5:3(D_{3h}) Trigonal bipyramid, vOC-5:2 (C_{4v}) Vacant octahedron, PP-5:1(D_{5h}) Pentagon

The Dy^{III} ion is coordinated to eight oxygen atoms belonging to phenoxo and aldehyde oxygen atoms from two different chiral ligands with Dy–O bond distances in the 2.263 (3)–2.433 (3) Å range. The Dy-$O_{phenoxo}$ bond distances are shorter than those of Dy-$O_{aldehyde}$. The degree of distortion of the DyO_8 coordination polyhedron with respect to an ideal eight-vertex polyhedral using the SHAPE software,[6] indicates a geometry intermediate between square antiprism (SAPR-8) and triangular dodecahedron (TDD-8) but closer to square antiprism with values of 1.320 and 2.174, respectively. As it can be observed in table 4.5, the shape measures are significantly larger for other reference polyhedral (see table 4.7).

Table 4.7: Obtained S values with the SHAPE software for the geometries of Dy^{III} atom in **1** and Tb^{III} in **4**.

Complex	**ETBPY-8**	**TT-8**	**JSD-8**	**BTPR-8**	**JBTPR-8**	**JETBPY-8**	**JGBF-8**
Dy (**1**)	24.634	6.966	6.037	3.336	3.807	28.431	15.318
Tb (**4**)	24.690	6.869	6.107	3.457	3.933	28.086	15.450
	TDD-8	**SAPR-8**	**CU-8**	**HBPY-8**	**HPY-8**	**OP-8**	
Dy (**1**)	2.174	1.320	6.078	12.822	21.926	32.468	
Tb (**4**)	2.206	1.407	5.983	12.713	21.730	32.724	

ETBPY-8: 13(D_{3h}) Elongated trigonal bipyramid, TT-8: 12 (T_d) Triakis tetrahedron, JSD-8: 11(D_{2d}) Snub diphenoid J84, BTPR-8: 10(C_{2v}) Biaugmented trigonal prism, JBTPR-8:9(C_{2v}) Biaugmented trigonal prism J50, JETBPY-8: 8(D_{3h}) Johnson elongated triangular bipyramid J14, JGBF-8: 7(D_{2d}) Johnson gyrobifastigium J26, TDD-8: 6(D_{2d}) Triangular dodecahedron, SAPR-8:5(D_{4d}) Square antiprism, CU-8: 4(O_h) Cube, HBPY-8:3(D_{6h}) Hexagonal bipyramid, HPY-8: 2(C_{7v}) Heptagonal pyramid,OP-8: 1(D_{8h}) Octagon.

Compound **1** shows absence of hydrogen bonds but presents intermolecular interactions between the chloride atoms and the hydrogen atoms of the methylene (2.653 and 2.902 Å), benzene (2.710-2.741 Å) and methyl (2.828 Å) groups as well as with the carbon atom of the methyl groups with a distance of 3.381 Å. Additionally, the fluorine atoms exhibit intermolecular interactions with the hydrogen atoms of benzene (average distance of 2.554 Å) and methyl (average distance of 2.570 Å) groups as well as with the hydrogen atoms of aldehyde and cyclohexane groups with distances of 2.445 Å and 2.634 Å, respectively.

4.4.2 X- ray powder diffraction of compounds 1- 4

The simulated and experimental x-ray powder spectra of **1** and **4** are coincident, just indicating that the samples are pure and homogeneous (figure 4.3). On other hand, the crystals of compounds **2** and **3** were not of sufficient quality to obtain the structure by single X-ray diffraction. However, the IR spectra and elemental analysis suggest that compounds **2** and **3** should be isostructural to compound **4** and **1**, respectively. This fact indicates that the experimental powder X-ray diffractogram of **2** and **3** and the simulated of **4** and **1** should be identical. Therefore, if both spectra are compared and they were superimposable, we could affirm that **2** and **3** have the same structure as **4** and **1**, respectively. In figure 4.4 it can be seen that the diffractograms present the same diffraction peaks, thus confirming that **2** and **3** (and **4** and **1**) are isostructural.

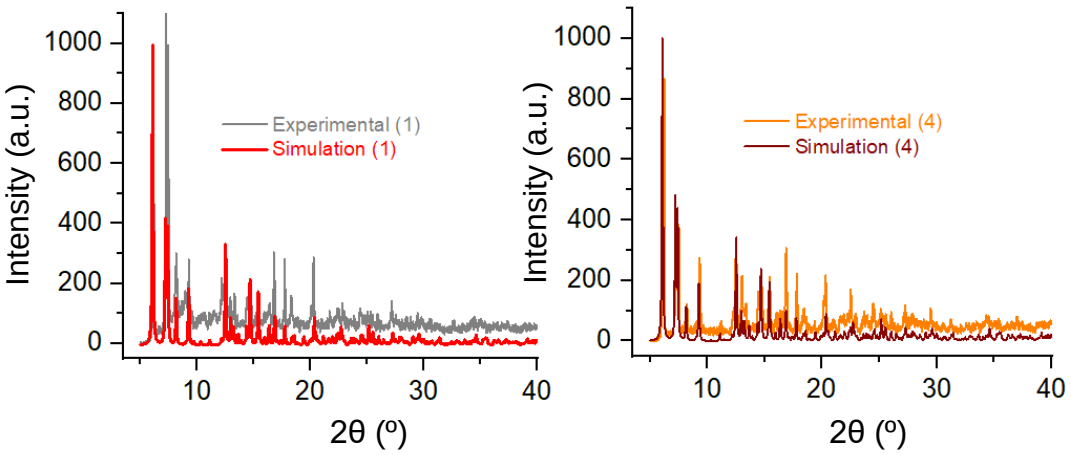

Figure 4.3: Experimental x- ray powder diffractograms for **1** (grey) and **4** (orange) and the calculated from the single X-ray crystal structures of **1** (red) and **4** (brown).

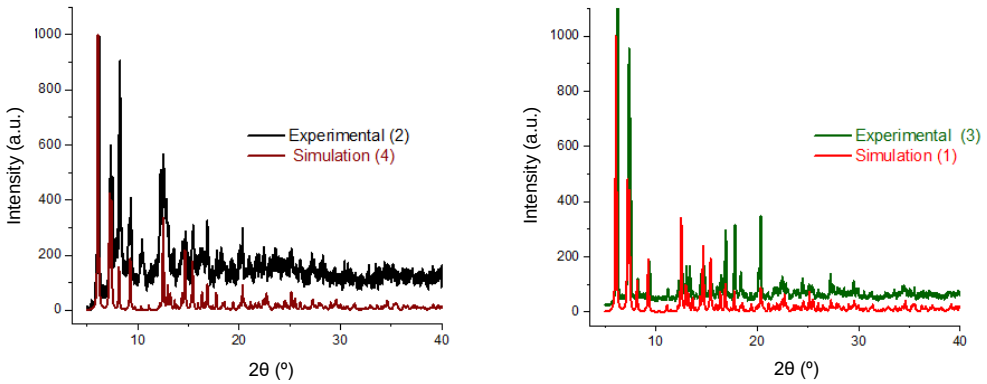

Figure 4.4: Experimental x- ray powder diffractograms for **2** (black) and **3** (green) and the calculated from the single X-ray crystal structure of **1** (red) and **4** (brown).

4.4.3 Magnetic properties of compounds 1 and 2

Since the magnetic behaviour of **1** and **2** is identical, only the magnetic properties of **1** have been fully measured and studied. They were measured on a polycrystalline sample, in the temperature range 2-300 K and using a magnetic

field of 0.1 T. The temperature dependence of $\chi_M T$ (where χ_M is the magnetic susceptibility per mole of compound) is shown in figure 4.5 left. At room temperature, the $\chi_M T$ value is 13.81 cm^3 K mol^{-1} which is in accordance with the expected value (14.17 cm^3 K mol^{-1}) for one independent Dy^{III} ion with S = 5/2 and g = 4/3. As the temperature decreases, the $\chi_M T$ value also decreases, first slightly to 90 K and then sharply, to reach a value of 10.11 cm^3 K mol^{-1} at 2 K. This decrease is due to the depopulation of the m_j sublevels of the Dy^{III} ion, which are generated by the splitting of the spin-orbit coupling levels by the ligand crystal field.

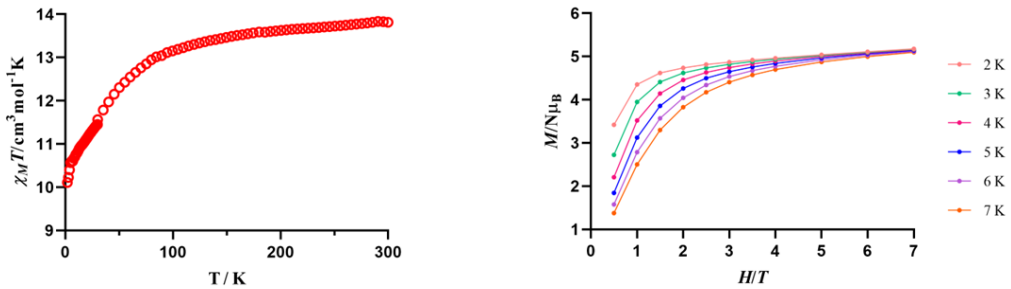

Figure 4.5: Temperature dependence of $\chi_M T$ (left) and field dependence of the magnetization (right) at the indicted temperatures for **1**.

The field dependence of the magnetization for **1** (figure 4.5, right) shows a relatively rapid increase of the magnetization at low fields and then an almost linear increase without reaching complete saturation at 7 T. It should be noted that the magnetisation value for the complex at 7 T and 2 K (5.18 Nβ) significantly deviates from the expected 10 *N*β saturation value suggesting the presence of significant magnetic anisotropy which is caused by the ligands crystal field.

In order to explore the SIM behavior of **1**, temperature and frequency dependent measurements of the *ac* magnetic susceptibility have been carried out under an alternating field of 4 Oe on a polycrystalline sample. Under zero static

field (dc), there exists a temperature and frequency dependence of the out-of-phase signals (χ''_M) with a well-defined maximum at high temperature and, another at low temperature which is not well-defined due to the significant presence of QTM, which is favored by the intermolecular interactions and the hyperfine interactions between the nuclear and the electron spin (figure 4.6).

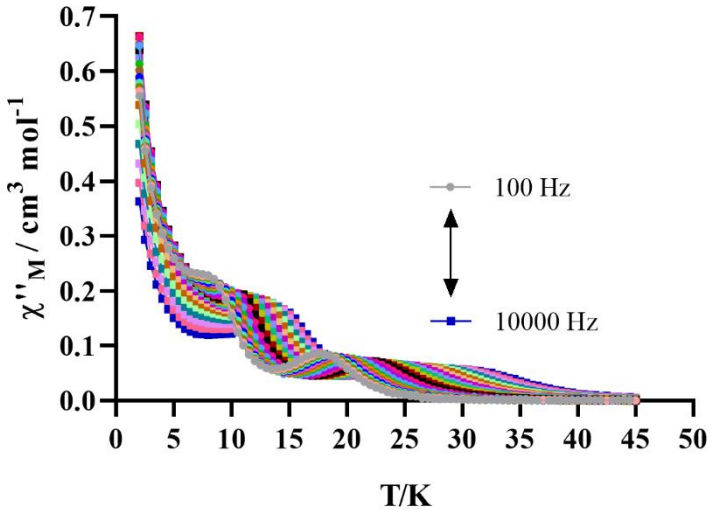

Figure 4.6: Temperature dependence of the out-of-phase ac susceptibility signals (χ_M'') at 0 Oe for **1**.

In view of this, to eliminate partially or completely the QTM, a small external magnetic field can be applied. To determinate the optimal magnetic field, *ac* measurements in the presence of different magnetic fields at 11 K have been performed for **1** (figure 4.7). As it can be observed in figure 4.7 (left), when the magnetic field increase, the out-of-phase signals shifts towards lower frequency values until a field of around 1000 Oe. The relaxation times have obtained by fitting the frequency dependence of the out-of-phase signals to the generalized Debye model. The magnetic field dependence of the relaxation times in the form of τ^{-1} vs H (figure 4.7, right) indicates that the relaxation slows down until reaching a field of 0.1 T (optimal field), which is due to the decrease of QTM. By

increasing the field from 0.12 T, the relaxation slowly accelerates due to the existence of a direct relaxation process.

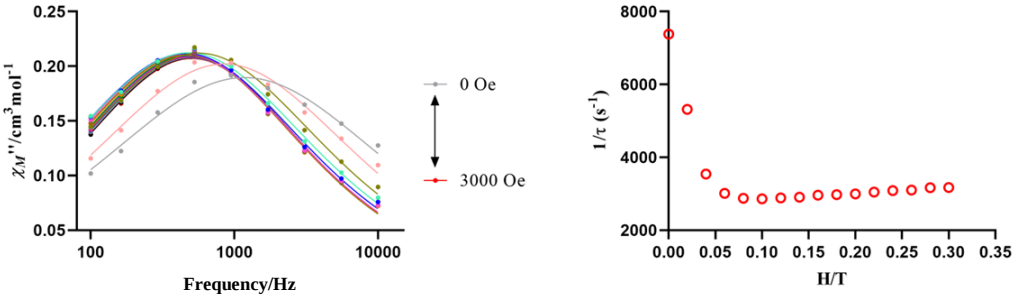

Figure 4.7: (left) Field dependence of the out-of-phase signals (χ_M'') at different frequencies and 11 K for **1**. The solid lines represent the best fitting to the Debye model. (right) Field dependence of the relaxation times at 11 K for **1**.

Under the optimal dc field of 0.1 T, compound **1** shows an important temperature and frequency dependence of the out-of-phase signals (χ''$_M$), with two well-defined maxima in the range of 8.5 K (100 Hz)-14.5 K (10000 Hz) and 17 K (100 Hz)-30 K (10000 Hz), thus indicating the existence of two relaxation processes, one at low temperature and one at high temperature (figure 4.8). Therefore, compound **1** presents slow magnetisation relaxation and SIM behaviour.

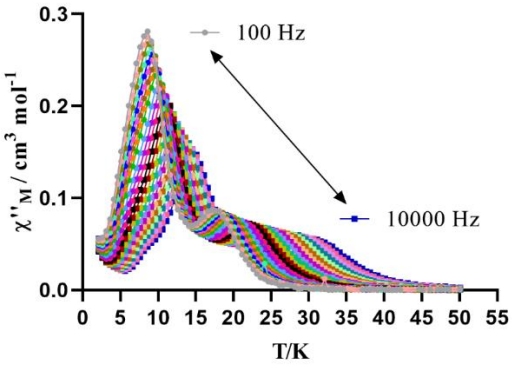

Figure 4.8: Temperature dependence of the out-of-phase ac susceptibility signals (χ_M'') at 1000 Oe for **1.**

From the Cole-Cole plot (χ''_M vs χ''_M at different temperatures, figure 4.9), we can obtain information about the existence of different relaxation processes. The shape of the cole-cole curves, clearly confirms the existence of two different relaxation processes for Dy^{III} ion (slow relaxation and fast relaxation magnetisation processes).

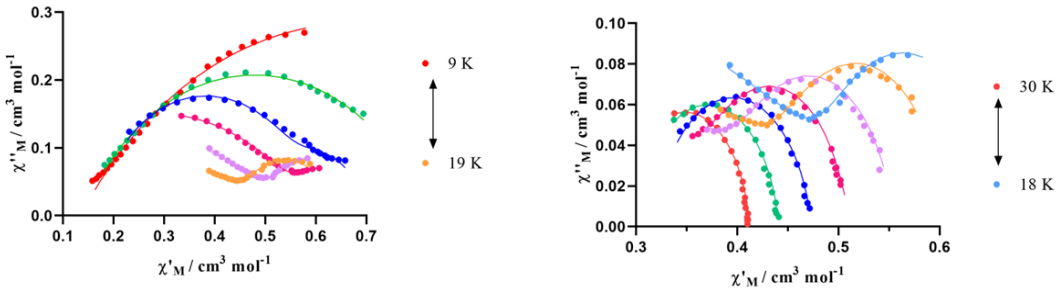

Figure 4.9: Cole-Cole for compound **1** at the indicated temperatures. The solid lines represent the best fitting to the generalised Debye model.

The relaxation times, in the 9 K-24 K (fast relaxation process) and 15 K-30 K (slow relaxation process) temperature ranges, were obtained from the fitting of the cole-cole curves to the generalized Debye model using the CCFit software.[7] The fitting of the relaxation times to the Arrhenius law in the high temperature region (20-30 K for the slow relaxation process and 12-24 K for the fast one) for a thermally activated relaxation mechanism (Orbach process) gives rise to effective energy barrier values of U_{eff} = 214.6 K and $\tau_0 = 1.57 \cdot 10^{-8}$ s and, U_{eff} = 157.6 K and $\tau_0 = 3.05 \cdot 10^{-10}$ s for the slow and fast relaxation processes, respectively (figure 4.10).

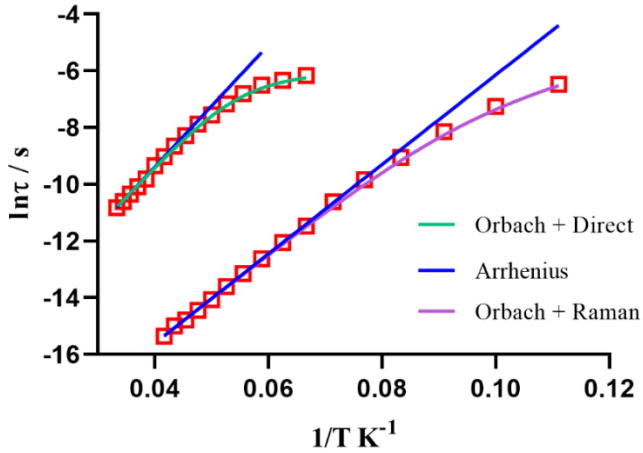

Figure 4.10: Representation of Ln τ vs 1/T for **1** at 0.1 T. The solid lines represent the best fit of the experimental data to the Arrhenius equation for a thermally activated process (blue) or for a combination of Orbach and Direct (green) or Orbach and Raman (purple) relaxation processes.

The deviation from the linearity of the relaxation times at temperatures below 20 K for the slow and 12 K for the fast processes indicate the existence of other additional magnetization relaxation mechanisms which compete with the thermally activated one. In view of this, a new fitting has been carried out in the entire studied temperature range (9 K – 24 K and 15 K – 30 K) using the equation 1

$$\tau^{-1} = AT + \frac{B_1}{1+B_2H^2} + CT^n + \tau_0 \exp^{\left(-\frac{Ueff}{k_BT}\right)} \quad \text{Equation 1}$$

The QTM process has not been included as the out-of-phase susceptibility signals approach to zero at temperatures below the maximum, indicating that the QTM has been significantly eliminated (figure 4.8). To avoid overparameterization, the parameter U_{eff} was fixed to that obtained with the Arrhenius law in the high temperature region. In the case of the slow relaxation process, the relaxation times were fitted to a combination of Orbach and Direct

processes giving rise to the parameters of: A = 31.73 and $\tau_0 = 1.61 \cdot 10^{-8}$ s. For the fast relaxation process, the relaxation times were fitted to the combination of Raman and Orbach processes. From the best fitting, the parameters obtained are C = 0.00103 $s^{-1}K^{-n}$, n = 6.04 and, $\tau_0 = 3.22 \cdot 10^{-10}$ s. Although for compounds with Kramer ions n should be 9, when acoustic and optical phonons are involved, it is normal to observe smaller n values.[8]

The effective energy barrier values for compound **1** (157.6 K and 214.6 K) are in the range of those observed for Zn^{II}-Dy^{III}-Zn^{II} complexes with analogous Mannich base ligands (150-320 K)[5] because all of them exhibit similar coordination geometry (distorted square antiprism) as well as similar disposition of the phenoxo bridging oxygen atoms (shortest average Dy–O distances) and the aldehyde oxygen atoms (larger average Dy–O distances).

However, compound **1**, possesses two different relaxation mechanisms (fast and slow relaxation processes) which are not observed in any of the similar Zn^{II}-Dy^{III}-Zn^{II} complexes with analogous Mannich or Schiff base ligands. Therefore, theoretical calculations will be carried out to try to disclose the origin of this relaxation pathway.

4.4.4 Computational calculations of compound 1

Ab initio calculations, based on the experimental X-ray structural data of complex **1**, were carried out to provide insight into the mechanism that governs its magnetic relaxation. In particular, multiconfigurational CASSCF[9] calculations were performed using the SINGLE_ANISO[10] module implemented in the ORCA 5.0.4 program package[11-13]. The computed eight Kramers' doublets (KDs) for **1**, corresponding to the $^6H_{15/2}$ ground state of the Dy^{III} ion, span an energy range of about 563 cm^{-1} (Table 4.8). The energy gap between the ground and first excited state is 131 cm^{-1}, which are rather normal values for Dy^{III} complexes. The ground KD (KD1) is an almost pure $m_J = |\pm 15/2\rangle$ state (90.6 %) that is highly anisotropic

(g_{zz} = 19.32) with very small transverse components (g_{xx} ~ g_{yy} < 0.005), thereby defining a well-oriented magnetic anisotropy axis. Its *g*-tensor values are in agreement with its zero-field SMM properties. The anisotropy g_{zz} axis lies between the planes formed by the two Dy–O–Zn–O moieties, close to collinearity with the two shortest Dy-O distances (Figure 4.11, both 2.263 Å, with 16.99º and 18.11º deviations between g_{zz} and the Dy-O bond vectors, respectively).

Table 4.8: CASSCF computed relative energies (in cm^{-1}) of the eight low-lying Kramers' doublets, g tensors for **1** and tilting angle (θ) of the main anisotropy axes of the corresponding excited (ES1, ES2, etc.) KD with respect to the ground state (GS) KD for **1**.

Energy (cm^{-1})	**g_{xx}**	**g_{yy}**	**g_{zz}**	**θ (°)**
0.00	0.002283	0.004789	19.315757	
130.99	0.090529	0.107908	16.351145	4.3
267.20	0.209858	0.242628	12.738997	4.5
339.01	8.443929	6.162470	3.234692	125.4
384.76	2.328471	4.183446	10.760304	96.8
490.73	0.301572	1.446664	13.053274	94.6
533.38	0.225839	1.819738	14.433170	83.6
562.56	1.016020	1.451114	16.547589	92.5

The two first excited states (KD2 and KD3) lie at 131.0 cm^{-1} and 267.2 cm^{-1} above the ground state, respectively. These KD2 and KD3 are also axial in nature, with g_{zz} = 16.35, g_{xx} = 0.09, and g_{yy} = 0.11 for KD2 and g_{zz} = 12.74, g_{xx} = 0.21, and g_{yy} = 0.24 for KD3. In both cases, the g_z tensors pass close to the shortest Dy-O distances as in KD1 and present respective deviations of 4.3° and 4.5º with respect to the g_{zz} anisotropy axis of the ground state. The transverse components of KD2 and KD3 can be large enough to promote magnetic relaxation via the first and second excited states giving the corresponding calculated magnetisation barrier U_{cal} values of 131.0 cm^{-1} (188.48 K) and 267.2 cm^{-1} (384.44 K), which

could correspond to the experimental energy barrier values U_{eff} of 109.5 cm^{-1} (157.6 K) and 149.2 cm^{-1} (214.6 K), respectively. The calculated energy barrier values are overestimated, which is normal for this type of calculation.[14]

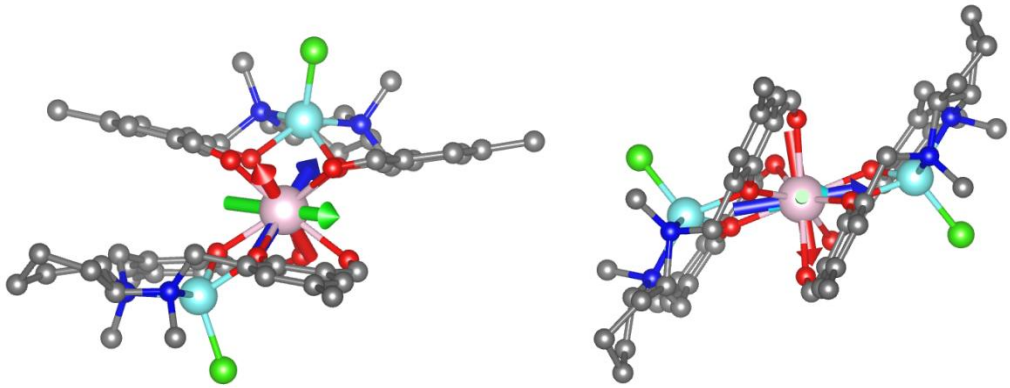

Figure 4.11: Two different views of the orientation of the *g*-tensor components obtained from CASSCF calculations for the ground Kramers' doublet of complex **1** using ORCA. The reference axis *x*, *y* and *z* of the *g*-tensor are displayed in red, green and blue, respectively. Code colours: dysprosium (pink), zinc (cyan), oxygen (red), chloride (green), nitrogen (blue) and carbon (grey). Hydrogen atoms and counterions have been omitted for clarity.

The computed transverse magnetic moments help to shed light on the relaxation mechanism of **1** (Figure 4.12). Thus, the ground state shows a transverse magnetic moment of 0.12 x 10^{-2} μ_B, which is not large enough in this case to avoid the observation of SMM behavior due to QTM in the ground state. Experimentally, QTM is suppressed upon application of a *dc* magnetic field, which results in the clearer observation of SMM behavior. The transverse moments for the Orbach processes connecting the ground and KD1/KD2 of opposite magnetization is predicted to be 0.48 × 10^{-2} μ_B and 0.15 × 10^{-1} μ_B, respectively, whereas that connecting KD1 and KD2 has a value of 0.57 × 10^{-1} μ_B. These values could point out that these relaxation pathways are operative, in agreement with the experimental results. Additionally, the TA/QTM processes connecting the two KD1/KD2 of opposite magnetization also present quite high

predicted transverse magnetic moments of 0.33 x 10^{-1} μ_B and 0.76 x 10^{-1} μ_B, respectively.

Accordingly, the *ab initio* studies support the magnetic findings, indicating that the Orbach relaxation mechanisms can dominate when QTM is suppressed by applying a *dc* field, together with contributions from Raman and direct relaxation processes.

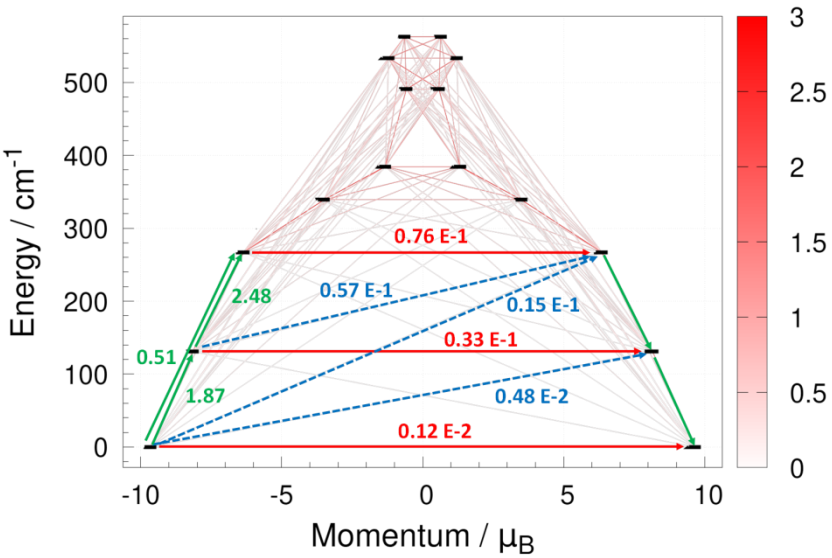

Figure 4.12: *Ab initio* calculated relaxation pathways in compound **1**. The black lines indicate the KDs as a function of the magnetic moments. Red lines denote QTM in the ground state and TA/QTM through the first and second excited states. Blue dashed lines represent possible Orbach processes.

4.4.5 Magnetic properties of compounds 3 and 4

As in the case of compounds **1** and **2**, the magnetic behaviour of **3** and **4** is identical, so only the magnetic properties of **4** will be described. They have been measured in polycrystalline samples, in a temperature range of 2-300 K and an external magnetic field of 0.1 T. The field dependence of the magnetization has been measured at 2 K. The magnetic susceptibility in the form of $\chi_M T$ versus T

(χ_M is the magnetic susceptibility per $Zn^{II}Tb^{III}Zn^{II}$ unit) is given in Figure 4.13 left. At room temperature, the $\chi_M T$ value of 11.49 cm^3 K mol^{-1} for compound **4** is similar with the expected value (11.82 cm^3 K mol^{-1}) for one Tb^{III} ion magnetically isolated (S = 3, g = 3/2). On cooling, the $\chi_M T$ product decreases continuously, first slowly and, from 50 K drastically until to reach a value of 8.79 cm^3 K mol^{-1}. This decrease is due to the depopulation of the excited m_j sublevels of the Tb^{III} ions, which arise from the splitting of the $^7F_6$ ground term by the crystal ligand field.

The field dependence of the magnetization at 2 K (figure 4.13, right) shows a rapid increase in the magnetization at low fields to reach almost saturation at a field of 7 T. The observed saturation value for **4** (4.98 Nβ) is rather lower than the calculated one (9 Nβ), which is due to the existence of significant magnetic anisotropy by crystal field effects.

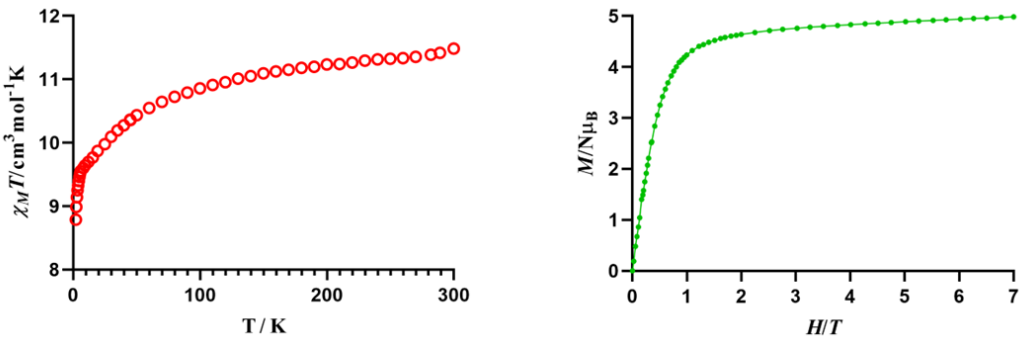

Figure 4.13: (left) Temperature dependence of $\chi_M T$ for **4**. (right) Field dependence of the magnetization at 2 K for **4**.

Compound **4** could exhibit SIM behavior so, temperature and frequency dependence measurements of the magnetic susceptibility in alternating field have been carried out on a polycrystalline sample. Without the presence of an external field (H_{dc} = 0 Oe), compound **4** does not exhibit out-of-phase signals (χ_M''), which indicates that either the thermal energy barrier is very small even at 2 K, or there

exists a fast relaxation of the magnetization originated by QTM. In consequence, to eliminate the QTM, ac measurements were carried out in the presence of an external field of 0.1 T. Under these conditions, compound **4** presents a clear temperature and frequency dependence of the ac magnetic susceptibility (figure 4.14) thus, indicating that **4** exhibit slow magnetisation relaxation.

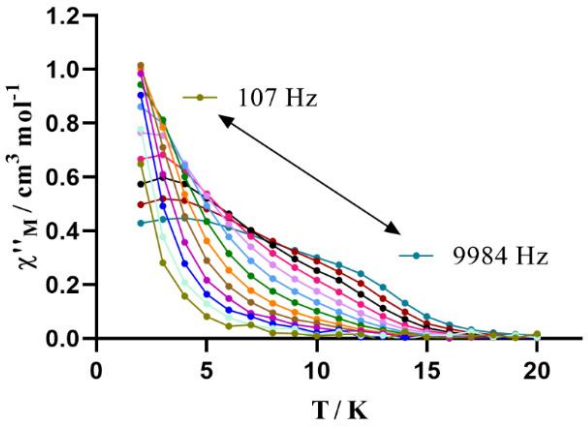

Figure 4.14: Temperature dependence of the out of phase signals (χ_M'') for compound **4** at 0.1 T.

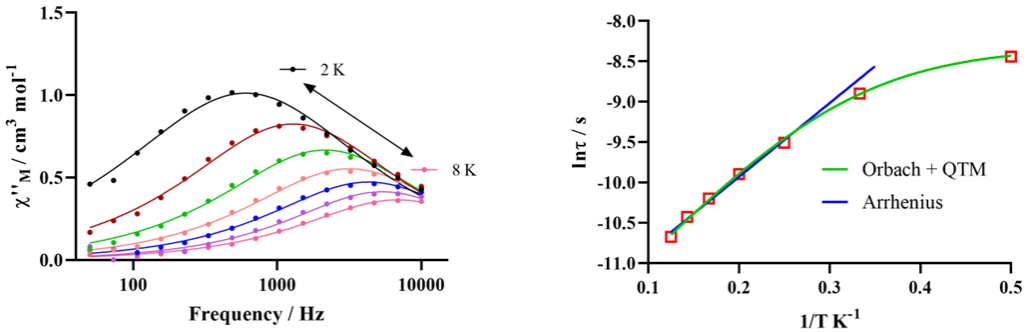

Figure 4.15: (left) Frequency dependence of the χ_M" signals at different temperatures for **4** under a field of 0.1 T. The solid lines represent the best fitting to the Debye model. (right) Representation of Ln τ vs 1/T for **4** at 0.1 T. The solid lines represent the best fit of the experimental data to the Arrhenius equation for a thermally activated process (blue) or for a combination of Orbach and QTM relaxation processes (green).

The relaxation times for **4** have been obtained from the fitting of the frequency dependence of the out of phase ac signals (χ_M'') at different temperatures to the generalised Debye model (figure 4.15, left). The fitting of the linear region in the Ln τ vs 1/T plot (figure 4.15, right) between 4 K – 8 K to an Arrhenius law, for a thermally activated process, leads to an effective energy barrier value of 9.13 K and $\tau_0 = 7.81 \times 10^{-6}$ s.

The Cole−Cole plot (Figure 4.16) shows, in the 2 K-10 K temperature region, semicircular shapes with α values in the range of 0.33−0.1. The wide distribution of the semicircular shapes and α values observed for **4** at low temperature suggested the existence of other competitive relaxation processes.

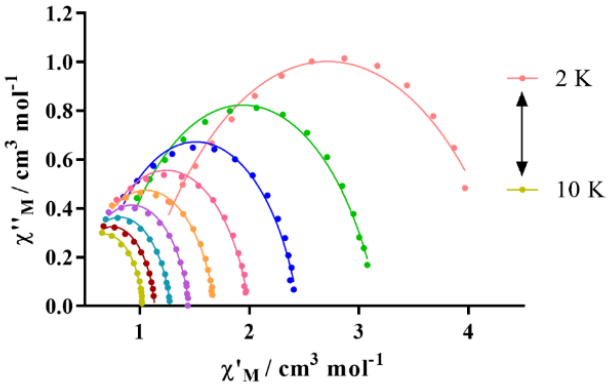

Figure 4.16: Cole-Cole plot for **4**

Moreover, the deviation from the linearity in the ln τ vs 1/T plot at low temperatures also indicates the existence of other additional magnetization relaxation processes that compete with the Orbach one. In view of this, a new fitting has been carried out in the whole temperature range studied (2-8 K) using the equation 1

$$\tau^{-1} = AT + \frac{B_1}{1+B_2H^2} + CT^n + \tau_0 \exp^{\left(-\frac{Ueff}{k_BT}\right)} \quad \text{Equation 1}$$

The fitting using the sum of Orbach and Raman processes, or the sum of Orbach and Direct processes failed, thus suggesting that the QTM process was not completely eliminated (as observed in figure 4.16). Thus, taking into account the sum of orbach and QTM relaxation processes, the fitting of the experimental data was excellent, obtaining the following parameters: U_{eff} = 11.81 K, τ_0 = 6.01 x 10^{-6} s and τ_{QTM} = 2.42 x 10^{-4} s.

In non-Kramers complexes such as compound **4**, the matrix element of the transversal magnetic moment between the two doublet levels is exactly zero, as dictated by Griffiths' theorem, whereas direct QTM arises from an intrinsic tunneling gap present in these complexes in the absence of an external magnetic field.[15] The reason why compound **4** does not exhibit SMM behavior is because only terbium compounds with high symmetry of the complex, close to D_{4d}, can strongly suppress QTM and then exhibit SMM behavior.[15]

4.5 CONCLUSIONS

In this chapter, four heterotrinuclear Zn^{II}-Ln^{III}-Zn^{II} complexes (Ln^{III} = Dy^{III} and Tb^{III}) from two chiral (R,R and S,S) Mannich base ligands have been prepared and structurally characterized by single and/or powder X-ray diffraction. Within the complexes, the cationic trinuclear molecules consist of two dinuclear $[ZnClL_{R,R}]^-$ or $[ZnClL_{S,S}]^-$ units in which the Zn^{II} ions are joined to a central Ln^{III} ion through two phenoxo oxygen atoms from two different chiral ligands. In this arrangement, the Zn^{II} ions occupy the inner N_2O_2 coordination site and the Dy^{III} ion the outer O_2O_2 cavity of the chiral ligands. The Ln^{III} ion presents a LnO_8 coordination environment formed by the phenoxo and aldehyde oxygen atoms belonging to the ligands, giving rise to a distorted square antiprism coordination geometry.

The ac susceptibility measurements have shown that the compounds **1-4** present slow magnetisation relaxation and SIM behavior. For compounds containing Dy^{III} ion (**1** and **2**), the Cole-Cole diagrams indicate the existence of two different relaxation processes, one slow and one fast, with thermal activation barriers of 214.6 K and 157.6 K for the slow and fast relaxation process, respectively. *Ab initio* calculations support the experimental magnetic findings and offer deeper insights into the magnetic dynamics of compound **1**. They confirm that, upon suppression of QTM, such as through the application of a *dc* field, the two relaxation processes primarily proceed *via* Orbach pathways through the two first excited states, with additional contributions from Raman and direct relaxation processes. They provide the corresponding calculated magnetisation U_{cal} barriers of 131.0 cm^{-1} (188.48 K) and 267.2 cm^{-1} (384.44 K), which could correspond to the experimental energy barrier values U_{eff} of 109.5 cm^{-1} (157.6 K) and 149.2 cm^{-1} (214.6 K), respectively. Compound **4** does not exhibit SMM behavior because in non-Kramers complexes direct QTM arises from an intrinsic tunneling gap present in these complexes in the absence of an

external magnetic field. Only terbium compounds with high symmetry of the complex, close to D_{4d}, can strongly suppress QTM and then exhibit SMM behavior.

4.6 REFERENCES

[1] R. Jankowski, M. Wyczesany and S. Chorazy, *Chem. Commun.*, 2023, **59**, 5961-5986.

[2] J. Long, *Front. Chem.*, 2019, **7**, 63.

[3] a) C. Train, M. Gruselle and M. Verdaguer, *Chem. Soc. Rev.*, 2011, **40**, 3297–3312; b) F. Zinna and L. di Bari, *Chirality*, 2015, **27**, 1-13.

[4] a) H. R. Wen, J. J. Hu, K. Yang, J. L. Zhang, S. J. Liu, J. S. Liao and C. M. Liu, *Inorg. Chem.*, 2020, **59**, 2811−2824; b) C. m. Liu, R. Sun, B. W. Wang, X. Hao and X. L. Li, *Inorg. Chem.*, 2022, **61**, 18510−18523.

[5] a) I. Oyarzabal, J. Ruiz, J. M. Seco, M. Evangelisti, A. Camón, E. Ruiz, D. Aravena and E. Colacio, *Chem. Eur. J.*, 2014, **20**, 14262 – 14269; b) I. Oyarzabal, J. Ruiz, E. Ruiz, D. Aravena, J. M. Seco and E. Colacio, *Chem. Commun.*, 2015, **51**, 12353—12356; c) I. Oyarzabal, A. Rodríguez-Diéguez, M. Barquín, J. M. Seco and E. Colacio, *Dalton Trans.*, 2017, **46**, 4278–4286.

[6] M. Llunell, D. Casanova, J. Cirera, P. Alemany and S. Alvarez, SHAPE, v2.1; Universitat de Barcelona: Barcelona, Spain, 2013.

[7] a) D. Reta and N. F. Chilton, *Phys. Chem. Chem. Phys.*, 2019, **21**, 23567; b) W. J. A. Blackmore, G. K. Gransbury, P. Evans, J. G. C. Kragskow, D. P. Mills and N. F. Chilton, *Phys. Chem. Chem. Phys.*, 2023, **25**, 16735.

[8] a) A. Singh and K. N. Shrivastava, *Phys. Status Solidi B*,1979, **95**, 273–277; b) K. N. Shrivastava, *Phys. Status Solidi B*, 1983, **117**, 437–458.

[9] P. A. Malmqvist and B. O. Roos, *Chem. Phys. Lett.*, 1989, **155**, 189.

[10] L. F. Chibotaru and L. Ungur, *J. Chem. Phys.*, 2012, **137**, 064112.

[11] F. Neese, *WIREs Comput. Mol. Sci.*, 2012, **2**, 73–78.

[12] F. Neese, U. B. Wennmohs and C. Riplinger, *J. Chem. Phys.*, 2020, **152**, 224108.

[13] F. Neese, *WIREs Comput. Mol. Sci.*, 2022, **12**, e1606.

[14] J. P. Costes, S. Titos-Padilla, I. Oyarzabal, T. Gupta, C. Duhayon, G. Rajaraman, E. Colacio, *Inorg. Chem.*, 2016, **55**, 4428–4440.

[15] L. Ungur, M. Thewissen, J.-P. Costes, W. Wernsdorfer, L. F. Chibotaru, *Inorg. Chem.*, 2013, **52**, 6328−6337.

CHAPTER 5

CONCLUSIONS

5. CONCLUSIONS

The main goal of the research work carried out in this doctoral thesis are the design, preparation, and characterisation of new multifunctional mononuclear and trinuclear coordination compounds based on lanthanide ions, as well as the experimental and theoretical study of their magnetic and luminescent properties. In order to achieve these objectives, two type of ligands, namely di(1-adamantyl)benzylphosphine, and the chiral Mannich base ligands, R,R'- and S,S'-dimethyl-N,N'-bis(2-hydroxy-3-formyl-5-methyl-benzyl)cyclohexanediamine, were synthesised following reported procedures to achieve mononuclear and trinuclear Ln^{III} compounds, respectively.

The findings and discussions presented in this manuscript allow us to draw the following conclusions:

Chapter 3:

1. A first series of four new mononuclear Ln^{III} complexes were prepared using the di(1-adamantyl)benzylphosphine oxide ($OPAd_2Bz$) ligand. These complexes show the generic formula $[Ln(OPAd_2Bz)_2(H_2O)_4Cl]Cl_2 \cdot xTHF \cdot zH_2O$, where Ln = Dy^{III} (**1**), Yb^{III} (**2**), Tb^{III} (**3**), and Gd^{III} (**4**).

2. A second series of three mononuclear Ln^{III} complexes were prepared using the $OPAd_2Bz$ ligand. These complexes show the generic formula $[Ln(OPAd_2Bz)_2(z)Cl_3] \cdot xTHF$, where Ln = Dy^{III} (**5**, z = THF), Eu^{III} (**6**, z = H_2O) and Gd^{III} (**7**, z = THF).

3. The coordination geometry around the lanthanide ion depends on the employed synthesis method. Complexes **1**-**4**, synthesized by solvothermal methods, exhibit a compressed and distorted pentagonal

bipyramidal coordination geometry (D_{5h}), which is very close to the ideal pentagonal bipyramid polyhedron. Their structures consist of cationic mononuclear $[Ln(OPAd_2Bz)_2(H_2O)_4Cl]^{2+}$ units together with two chloride counteranions and THF solvent molecules. The cationic mononuclear unit shows a LnO_6Cl coordination sphere. Within it, two phosphine oxide ligands coordinate to the Ln^{III} atom in axial positions, whereas one chloride atom and four water molecules are located in the equatorial plane.

4. Complexes **5**-**7**, obtained by reflux in inert atmosphere, exhibit a compressed and distorted octahedral coordination environment (O_h). Their structures are made of mononuclear neutral $[Ln(OPAd_2Bz)_2(THF)Cl_3]$ units without solvent molecules in the crystal structure (**5**, **7**) or with THF solvent molecules (**6**). The neutral mononuclear unit shows a LnO_3Cl_3 coordination sphere. Within it, two phosphine oxide ligands coordinate to the Ln^{III} atom in axial positions again, whereas three chloride atoms and one THF (**5**, **7**) or water (**6**) molecule are located in the equatorial plane.

5. Alternating current (*ac*) magnetic susceptibility measurements were performed on complexes **1**, **2**, **3** and **5** as a function of both frequency and temperature. In the absence of an applied magnetic field (H_{dc} = 0 Oe), for compounds **1** (Dy^{III}, D_{5h}) and **5** (Dy^{III}, O_h), a frequency dependence of the out-of-phase signals (χ''_M), with no clear maxima above 2 K was observed and attributed to significant quantum tunneling of magnetisation (QTM) in the ground state. On the other hand, for compounds **2** (Yb^{III}, D_{5h}) and **3** (Tb^{III}, D_{5h}), no slow relaxation of the magnetization was observed above 2 K at zero field, indicating a very low barrier or a fast QTM. However, when the *ac* measurement was performed in the presence of a small external field of 1000 Oe, complexes **1** (Dy^{III}, D_{5h}), **2** (Yb^{III}, D_{5h}) and **5** (Dy^{III}, O_h) showed typical SIM behaviour, with effective thermal energy barriers of 61.23 K, 18.77 K and

62.41 K, respectively, when considering the Orbach + QTM, Raman + direct and Raman + Orbach processes, respectively. In contrast, complex **3** (Tb^{III}, D_{5h}) showed out-of-phase signals but without reaching a maximum, indicating a weak slow relaxation of the magnetisation above 2 K.

6. It has been demonstrated that the U_{eff} values are influenced by the nature of the lanthanide ion (Dy^{III}, Yb^{III} and Tb^{III}) and the coordinated equatorial ligands (Cl^- or Br^-) (crystal field) in two structurally similar pentagonal bipyramidal complexes, *i.e.* complex **1** and the bromine analogue of **1**. The replacement of bromide atoms with chloride atoms in the equatorial plane in the pentagonal bipyramidal Dy^{III} complex induces a significant decrease in the thermal energy barrier, from 427.7 K to 61.23 K. These observations are supported by *ab initio* calculations, as they indicate that the transverse *g*-tensor components for **1** and **5** are larger (0.01-0.05) than for the bromide analogue of **1** (0.001). The *ab initio* calculated ground-state tunneling demagnetization rate also follows the trend (bromine analogue of **1**) < (**1**) < (**5**). Thus, these results lead us to believe that the observed magnetic behavior of these compounds is intrinsic to the molecular system. Specifically, the presence of heavier halides in the equatorial plane may reduce the transverse ligand field components, thereby suppressing QTM. This is probably due to their weaker donor ability. The significantly lower U_{eff} barrier of complex **2** and the different magnetic behaviour of complex **3** compared to complex **1** is due to the nature of the lanthanide ion (Dy^{III} in **1**, Yb^{III} in **2**, and Tb^{III} in **3**). *Ab initio* calculations also explain the presence of quantum tunneling of magnetization (QTM) in the absence of a magnetic field for compound **2** and indicate that the Orbach process can be ruled out in favor of a combination of Raman and direct processes.

7. A theoretical and experimental photoluminescence study of these complexes demonstrated that the ligand di(1-adamantyl)benzylphosphine oxide acts as an antenna capable of sensitizing the lanthanide emission, and also that different pathways take part in the lanthanide sensitization depending on the compound. Compounds **2** (Yb, D_{5h}), **5** (Dy, O_h) and **6** (Eu, O_h) were sensitized via conventional energy transfer from the ligand's triplet excited state. In contrast, the sensitization of complexes **1** (Dy, D_{5h}) and **3** (Tb, D_{5h}) likely involves ligand-to-metal charge transfer (LMCT), also originating from the triplet state. Notably, compounds **1, 5,** and **6** exhibit dual emission behavior as a function of the excitation wavelength, with an emission band also originating from the ligand, probably due to a partial energy transfer from the T_1 triplet state of the ligand. These results contribute valuable insights to the rational design of dual-emissive materials.

8. These results show that complexes **1**, **2** and **5** are bifunctional compounds, combining field-induced slow relaxation of the magnetisation and luminescent properties.

Chapter 4:

1. Four new heterotrinuclear Zn^{II}-Ln^{III}-Zn^{II} complexes were prepared using the chiral Mannich base ligands, $H_2L_{R,R}$ and $H_2L_{S,S}$, that is, R,R'- and S,S'-dimethyl-N,N'-bis(2-hydroxy-3-formyl-5-methyl-benzyl)cyclohexanediamine, respectively. These complexes show the generic formula $[ZnCl(\mu\text{-}L)Ln(\mu\text{-}L)ClZn](PF_6)$, which corresponds to $[ZnCl(\mu\text{-}L_{\mathbf{R,R}})Ln(\mu\text{-}L_{\mathbf{R,R}})ClZn](PF_6)$ (Ln^{III} = Dy^{III} (**1**) and Tb^{III} (**2**)) and $[ZnCl(\mu\text{-}L_{\mathbf{S,S}})Ln(\mu\text{-}L_{\mathbf{S,S}})ClZn](PF_6)$ (Ln^{III} = Dy^{III} (**3**) and Tb^{III} (**4**)).

2. Their structures consist of cationic trinuclear units $[ZnCl(\mu\text{-}L)Ln(\mu\text{-}L)ClZn]^+$ together with one hexafluorophosphate counteranion. The

cationic trinuclear units are constructed by two $[ZnClL]^-$ units with a central Dy^{III} ion bridged to the Zn^{II} ions through two phenoxo oxygen atoms from two different chiral ligands. The Zn^{II} ions occupy the inner N_2O_2 coordination site, exhibiting a ZnN_2O_2Cl coordination environment with a distorted square-pyramid geometry, while the Ln^{III} ion (Dy^{III} or Tb^{III}) occupies the outer O_2O_2 cavity exhibiting an LnO_8 coordination sphere. This LnO_8 sphere is formed by the phenoxo and aldehyde oxygen atoms from two different ligands, with an intermediate geometry between square antiprism (SAPR-8) and triangular dodecahedron (TDD-8), but closer to square antiprism (SAPR-8).

3. Given the identical magnetic behavior of compounds **1** and **2**, and **3** and **4**, only the magnetic properties of **1** and **4** have been fully measured and studied. Alternating current (*ac*) magnetic susceptibility measurements were performed on complexes **1** and **4** as a function of both frequency and temperature. At zero field, compound **1** exhibited a temperature and frequency dependence of out-of-phase signals (χ''_M) with a well-defined maximum at high temperature and a less well-defined one at low temperature due to a significant QTM. However, compound **4** did not exhibit out-of-phase signals (χ''_M) at zero field, which indicates that either the thermal energy barrier is very small even at 2 K, or there exists a fast relaxation of the magnetization originated by QTM. When the *ac* measurement was performed in the presence of a small external field of 1000 Oe, compounds **1** and **4** showed slow magnetisation relaxation and SIM behaviour. In particular, for compound **4** a fitting of the experimental data considering the sum of Orbach and QTM relaxation processes in the whole temperature range gave rise to an U_{eff} value of 11.81 K.

4. In the case of complex **1**, when the *ac* measurement was performed in the presence of a small external field of 1000 Oe, the temperature

and frequency dependent out-of-phase signals (χ''_M) exhibited two well-defined maxima, indicating the existence of two relaxation processes, one slow and one fast, with effective energy barriers of U_{eff} = 214.6 K and U_{eff} = 157.6 K, respectively, when considering only the Orbach process in the high temperature region. When the full temperature range is considered, the relaxation times were fitted to a combination of Orbach + Direct or Raman + Orbach processes for the slow and fast relaxation processes, respectively.

5. *Ab initio* calculations confirm that the ground Kramers doublet for **1** is highly anisotropic (g_{zz} = 19.32) with very small transverse components ($g_{xx} \sim g_{yy} < 0.005$), in agreement with its zero-field SMM properties. The anisotropy g_{zz} axis lies between the planes formed by the two Dy–O–Zn–O moieties, close to collinearity with the two shortest Dy-O distances. The transverse components of KD2 and KD3 can be large enough to promote magnetic relaxation via the first and second excited states, giving the corresponding calculated magnetisation barrier U_{cal} values of 131.0 cm^{-1} (188.48 K) and 267.2 cm^{-1} (384.44 K), which could correspond to the experimental energy barrier values U_{eff} of 109.5 cm^{-1} (157.6 K) and 149.2 cm^{-1} (214.6 K), respectively. The *ab initio* transverse magnetic moments also support experimental magnetic results indicating that the two relaxation processes mainly proceed *via* Orbach pathways through the two first excited states when QTM is suppressed by applying a *dc* field, together with additional contributions from Raman and direct relaxation processes.

6. Compound **4** does not exhibit SMM behavior because in non-Kramers complexes such as **4** direct QTM arises from an intrinsic tunneling gap present in these complexes in the absence of an external magnetic field. Only terbium compounds with high symmetry of the complex, close to D_{4d}, can strongly suppress QTM and then exhibit SMM behavior.

ANNEX

Throughout the research period for this thesis, various instrumental techniques were employed to fully characterise the synthesised materials. All the instruments and equipment used belong to the Inorganic Chemistry Department or to the Scientific Instrumentation Centre of the University of Granada (CIC-UGR) of the University of Granada. These techniques are described in detail below.

1. Elemental Analysis (EA)

This technique was used to determine the percentage of carbon, hydrogen, nitrogen and sulphur in the samples. For this purpose, a Fisons-Carlo Erba analyser model EA 1108 was used. These analyses were carried out at the Scientific Instrumentation Centre of the University of Granada (CIC-UGR).

2. Proton Nuclear Magnetic Resonance (^{1}H-NMR)

For the characterisation of the ligands, a 400 MHz NMR spectrometer BRUKER Avance Neo of the Scientific Instrumentation Centre of the University of Granada has been used.

3. Fourier Transform Infrared Spectroscopy (FT-IR)

Infrared spectra of the synthetized ligands and compounds have been recorded on a Bruker Tensor 27 spectrophotometer using the ATR accessory.

4. X-ray powder diffraction

Powder X-ray diffractograms have been recorded on a Bruker D8 DISCOVER instrument (2θ) using CuKα radiation (λ = 1.5418 Å) and a DECTRIS PILATUS3R 100K-A detector, from 5 to 50 º (2θ) at a scanning rate of 0.02 º 2θ/min at the Scientific Instrumentation Centre of the University of Granada.

5. Single-crystal X-ray diffraction

For the determination of the crystal structure of the synthesised compounds, crystals suitable for measurement by single-crystal X-ray diffraction were mounted on a glass fibre. X-ray diffraction data were collected at 100 K using a Bruker D8 Venture diffractometer (MoKα radiation, 0.71073 Å) equipped with a PHOTON 100 detector. The unit cell parameters were determined and refined on all observed reflections using APEX4[1] software. The correction for polarisation and Lorentz absorption was applied with SAINT[2] and SADABS[3] programs, respectively. Crystal structure resolution has been carried out using SHELXT[4], and refinement has been performed with the F2 least squares method using the SHELXL-2018[5] and OLEX2[6] programs.

6. Magnetic measurements

Magnetic susceptibility measurements in the temperature range 2-300 K on polycrystalline samples in the presence of a magnetic field of 1000 Oe have been carried out using a DynaCool PPMS-9 physical measurement equipment. Alternating current (*ac*) susceptibility measurements in the presence of different static fields in the temperature ranges used were carried out on a PPMS-9 physical measuring instrument (50-10000 Hz). The susceptibility values have been corrected for the diamagnetism of the molecular constituents and the sample holder.

7. Ultraviolet Visible spectroscopy (UV–Vis)

The UV-Vis spectrum of the $OPAd_2Bz$ ligand in solution was recorded on an AGILENT CARY-100 spectrophotometer. In addition, the solid UV-VIS-NIR of the ligand and lanthanide compounds **1-7** of chapter 3 were measured on a VARIAN CARY-5E spectrophotometer at the Scientific Instrumentation Centre of the University of Granada.

8. Fluorescence spectroscopy

Emission and excitation spectra were measured on a UV-VIS-NIR HORIBA QuantaMaster–8000 spectrofluorometer equipped with a UV-VIS PMT PPD850C Detector (210-870 nm) (**1** and **3**-**7**) or NIR PMT R5509-73 detector (300-1700 nm) (**2**) and a continuous Xenon Short Arc Lamp (190-2000 nm, USHIO). All the spectra (emission and excitation) were corrected with real-time correction functions.

Time Correlated Single Photon Counting (TCSPC) lifetime measurements were performed using a flash lamp (1µs pulse, HORIBA Scientific).

9. Quantum-chemical calculations

For magnetic properties calculations, post–Hartree–Fock *ab initio* calculations were carried out on the crystallographic structures of the compounds using the ORCA 5.0.4 quantum chemistry program package.[7-9] The electronic structure and magnetic properties have been computed using state-averaged complete active space self-consistent field calculations (SA-CASSCF (9,7)) for Dy^{III} and (SA-CASSCF (13,7)) for Yb^{III}.[10] The employed active space includes nine electrons in seven 4f orbitals of Dy^{III} CAS (9,7) and thirteen electrons in seven 4f orbitals of Yb^{III} CAS (13,7). Within this active space, we have computed 21 sextets states, 128 quadruplets and 98 doublets for Dy^{III}, and the 7 doublets for Yb^{III}. The spin-orbit effects were included using the quasi-degenerate perturbation theory (QDPT).[11] Scalar relativistic effects were considered by second-order Douglas–Kroll–Hess (DKH) procedure.[12] In these calculations, all the atoms are described by the def2-TZVPP basis set,[13,14,15] including the corresponding auxiliary basis sets for correlation and Coulomb fitting for all the atoms apart from Dysprosium and Ytterbium, for which the SARC2-DKH-QZVP basis set[16] was used to take into account the relativistic effect. The Single Aniso[17] approach

was also used, which enables calculations of anisotropic magnetic properties and *g* tensors for the ground and first excited Kramers doublets (KD) and the matrix elements of the transition magnetic moments, which gives an estimation of the probability of transition between two different states of the molecules.[18]

In Chapter 3, to study the antenna effect of the di(1-adamantyl)benzylphosphine oxide ligand ($OPAd_2Bz$) and the mechanisms of energy transfer for the lanthanide sensitization the Gaussian 16 program package (revision A.03)[19] was used. The initial minima of the di(1-adamantyl)benzylphosphine oxide ligand ($OPAd_2Bz$) were found with a conformational search by means of molecular mechanics with the MMFF force field.[20] After an adequate conformational energy window (20 kJ/mol) was achieved, 3 conformers were optimized in the ground state in dichloromethane solution and in the gas phase employing the CAM-B3LYP-D3[21] dispersion-corrected[22] (GD3zero damping) functional and the 6-31+G** basis set. As conformer 1 was the most stable in both phases, the rest of the calculations were only performed for it. Thus, full geometry optimizations of the S_0 and S_1 in solution, and S_0, S_1 and T_1 (see below) of conformer 1 in the gas phase were performed using the hybrid exchange–correlation functional wB97xD,[23] and the M062X-D3[24, 25] and CAM-B3LYP-D3[21] dispersion-corrected[22] density functional combinations with the 6-31+G** basis set. The vibrational frequencies were computed for S_0, S_1 and T_1 to check the absence of imaginary frequencies and then verify that the computed minima were real. The effect of the solvent (dichloromethane) was considered implicitly using the polarizable continuum model (PCM).[26]

The vertical electronic transitions were computed using Time-Dependent DFT (TD-DFT) calculations at the same levels of theory. The vertical electronic transitions $S_1 \rightarrow S_0$ in solution were calculated as the difference $ES_1(GS_1)$ -

$ES_0(GS_1)$, where $ES_1(GS_1)$ is the energy of the optimized S_1 state at its equilibrium geometry (state-specific solvation approach)[27] and $ES_0(GS_1)$ is the calculated energy of the S_0 state at the S_1 optimized state geometry and with the static solvation from the excited state.[28]

The optimized S_1 geometries at the three levels of theory were very similar to their respective S_0 geometries. However, full geometry optimization of the T_1 state led to a different geometry with the benzene group tilted (τ (1,2,3,4) = ~ 61º). We tried to mimic the structure of the ligand within the crystal by performing a two-layer ONIOM approach[29,30,31] building a model cluster containing 12 ligands from the crystallographic structure of compound **4**. The two central ligands were treated with PBE0/6-31G** (high level)[32,33] and S_0, S_1 and T_1 electronic state geometries were fully optimized. The two central ligands were surrounded by 10 ligand molecules (low level) treated semi-empirically using PM6[34] to alleviate the computational cost and with their molecular geometries frozen. Lanthanide, chloride, water and tetrahydrofuran molecules were removed from the structure to reduce computational cost. In this case, S_0, S_1 and T_1 geometries were very similar; indicating that no turn of the benzene group takes place in T_1 during full optimization. For this reason, for the T_1 optimization of the isolated ligand molecule, the positions of some atoms were frozen to their corresponding crystallographic coordinates to avoid the benzene group turns, while all other atoms were allowed to relax during optimization.

The molecular geometries of compounds **1**-**3** and **5**-**6** were taken from the crystallographic structures using the cif files and used without optimization to compute the frontier molecular orbitals in the ground state, that is, only single points were performed. When we tried to optimize them, the resulting structures differed from the original ones, leading to a departure from the original crystallographic structure and, for this reason, the structures of the complexes

were not optimized. The 6-31+G** basis set was used for C, H, P and O atoms and SARC-ZORA[35] for Dy (**1** and **5**), Yb (**2**), Tb (**3**), and Eu (**6**) lanthanides to consider the relativistic effect.

REFERENCES

[1] APEX4, Bruker AXS, Madison, Wisconsin (USA), 2022.

[2] SAINT, V8/40b, Bruker AXS, Madison, Wisconsin (USA), 2021

[3] L. Krause, R. Herbst-Irmer, G. M. Sheldrick and D. Stalke, SADABS, Version 2016/2, *J. Appl. Cryst.*, 2015, **48**, 3-10.

[4] G. M. Sheldrick, SHELXT-Integrated Space-Group and Crystal-Structure Determination, *Acta Cryst.*, 2015, **A71**, 3-8.

[5] G. M. Sheldrick, Crystal Structure Refinement with SHELXL, *Acta Cryst.*, 2015, **C71**, 3-8.

[6] O.-V. Dolomanov, L.-J. Bourhis, R.-J Gildea, J-.A. K. Howard, H. Puschmann, *Appl Crystallogr.*, 2009, **42**, 339–341.

[7] F. Neese, *WIREs Comput. Mol. Sci.*, 2012, **2**, 73–78.

[8] F. Neese, U.-B. Wennmohs and C. Riplinger, *J. Chem. Phys.*, 2020, **152**, 224108.

[9] F. Neese, *WIREs Comput. Mol. Sci.*, 2022, **12**, e1606.

[10] P.-A. Malmqvist and B.-O. Roos, *Chem. Phys. Lett.*, 1989, **155**, 189-194.

[11] a) D. Ganyushin, F. Neese, *J. Chem. Phys.*, 2013, **138**, 104113; b) D. Ganyushin, F. Neese, *J. Chem. Phys.*, 2006, **125**, 024103; c) R. Maurice, R. Bastardis, C.-D. Graaf, N. Suaud, T. Mallah, N. Guihéry, *J. Chem. Theory Comput.*, 2009, **5**, 2977-2984; d) F. Neese, *J. Chem. Phys.*, 2005, **122**, 034107.

[12] T. Nakajima, *Chem. Rev.*, 2012, **112**, 385-402.

[13] A. Schäfer, H. Horn, R. Ahlrichs, *J Chem Phys.*, 1992, **97**, 2571–2577.

[14] F. Weigend, R. Ahlrichs, *Physical Chemistry Chemical Physics.*, 2005, **7**, 3297–3305.

[15] A. Schäfer, C. Huber, R. Ahlrichs, *J Chem Phys.*, 1994, **100**, 5829–5835.

[16] D. Aravena, F. Neese and D.-A. Pantazis, *J. Chem. Theory Comput.* 2016, **12**, 1148-1156.

[17] L.-F. Chibotaru, L. Ungur, *J. Chem. Phys*., 2012, **137**, 064112.

[18] L. Ungur and L.-F. Chibotaru, *Inorg. Chem.*, 2016, **55**, 10043-10056.

[19] M.-J. Frisch, G.-W. Trucks, H.-B. Schlegel, G.-E. Scuseria, M.-A. Robb, J.-R. Cheeseman, G. Scalmani, V. Barone, G.-A. Petersson, H. Nakatsuji, X. Li, M. Caricato, A.-V. Marenich, J. Bloino, B.-G. Janesko, R. Gomperts, B. Mennucci, H.-P. Hratchian, J.-V. Ortiz, A.-F. Izmaylov, J.-L. Sonnenberg, D. Williams-Young, F. Ding, F. Lipparini, F. Egidi, J. Goings, B. Peng, A. Petrone, T. Henderson, D. Ranasinghe, V.-G. Zakrzewski, J. Gao, N. Rega, G. Zheng, W. Liang, M. Hada, M. Ehara, K. Toyota, R. Fukuda, J. Hasegawa, M. Ishida, T. Nakajima, Y. Honda, O. Kitao, H. Nakai, T. Vreven, K. Throssell, J.-A. Montgomery, J.-E. Peralta, F. Ogliaro, M.-J. Bearpark, J.-J. Heyd, E.-N. Brothers, K.-N. Kudin, V.-N. Staroverov, T.-A. Keith, R. Kobayashi, J. Normand, K. Raghavachari, A.-P. Rendell, J.-C. Burant, S.-S. Iyengar, J. Tomasi, M. Cossi, J.-M. Millam, M. Klene, C. Adamo, R. Cammi, J.-W. Ochterski, R.-L. Martin, K. Morokuma, O. Farkas, J.-B. Foresman and D.-J. Fox, *Gaussian 16, Revision A.03*, Gaussian, Inc, Wallingford CT, 2016.

[20] T.-A. J. Halgren, *Comput. Chem.*, 1996, **17**, 490–519.

[21] T. Yanai, D.-P. Tew and N.-C. Handy, *Chem. Phys. Lett.*, 2004, **393**, 51–57.

[22] S. Grimme, J. Antony, S. Ehrlich and H. Krieg, *J. Chem. Phys.*, 2010, **132**, 154104.

[23] J.-D. Chai and M. Head-Gordon, *Phys. Chem. Chem. Phys.*, 2008, **10**, 6615–6620.

[24] Y. Zhao and D.-G. Truhlar, *Chem. Phys. Lett.*, 2011, **502**, 1–13.

[25] N. Mardirossian, J.-A. Parkhill and M. Head-Gordon, *Phys. Chem. Chem. Phys.*, 2011, **13**, 19325–19337.

[26] J. Tomasi, B. Mennucci and R. Cammi, *Chem. Rev.*, 2005, **105**, 2999–3093.

[27] R. Improta, V. Barone, G. Scalmani and M.-J. Frisch, *J. Chem. Phys.*, 2006, **125**, 054103.

[28] G. Scalmani, M.-J. Frisch, B. Mennucci, J. Tomasi, R. Cammi and V. Barone, *J. Chem. Phys.*, 2006, **124**, 094107.

[29] S. Dapprich, I. Komáromi, K.-S. Byun, K. Morokuma and M.-J. Frisch, *J. Mol. Struct.: THEOCHEM.*, 1999, **461–462**, 1–21.

[30] T. Vreven, K. Morokuma, Ö. Farkas, H.-B. Schlegel and M.-J. Frisch, *J. Comput. Chem.*, 2003, **24**, 760–769.

[31] H. Lin and D.-G. Truhlar, *Theor. Chem. Acc.*, 2007, **117**, 185–199.

[32] J.-P. Perdew, K. Burke and M. Ernzerhof, *Phys. Rev. Lett.*, 1996, **77**, 3865.

[33] J.-P. Perdew, K. Burke and M. Ernzerhof, *Phys. Rev. Lett.*, 1997, **78**, 1396.

[34] J.-J. P. Stewart, *J. Mol. Model.*, 2007, **13**, 1173–1213.

[35] D.-A. Pantazis and F. Neese, *J. Chem. Theory Comput.*, 2009, **5**, 2229–2238.